

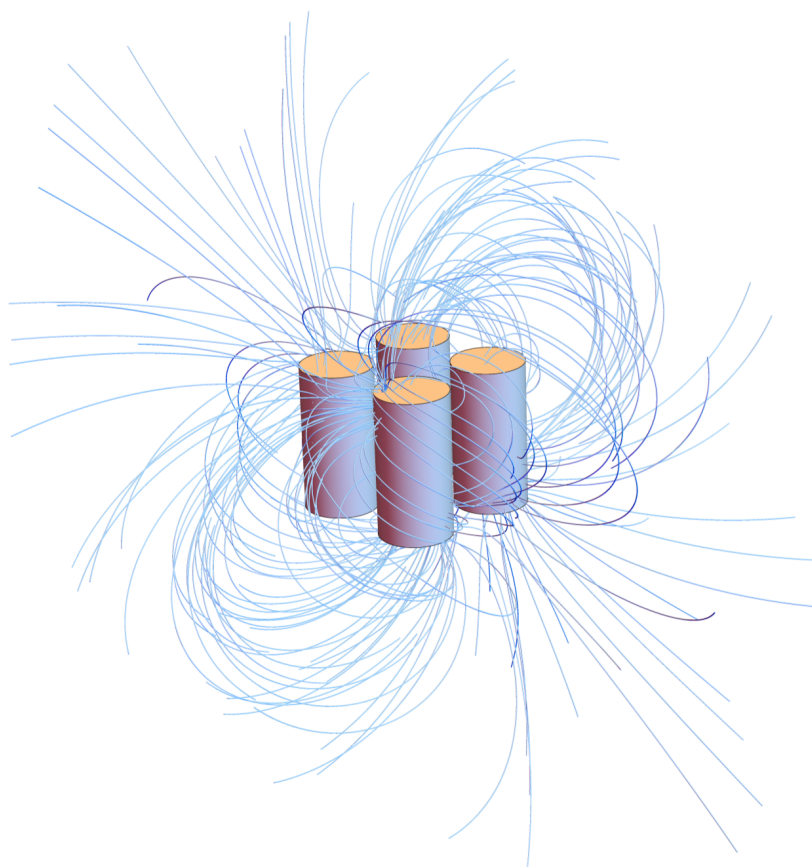


Utrecht University
Van t' Hoff Laboratory for Physical and Colloid
Chemistry

Master Thesis

Magnetic separation

A computer simulation study



Student:
Alessio Caciagli

Thesis advisor:
Prof. Albert Philipse
Research supervisor:
Roel Baars

June 2015

Magnetism, as you recall from physics class, is a powerful force that causes certain items to be attracted to refrigerators.

— Dave Barry

A mia madre e a mio padre.

Contents

Preface	1
1 Magnetic separation: concepts and materials	3
1.1 Introduction to magnetic separation	3
1.1.1 High Gradient Magnetic Separator	4
1.2 Superparamagnetism	6
1.2.1 Magnetic domains and superparamagnetism	10
1.3 Materials	12
1.3.1 Experimental Setup	12
1.3.2 Nanoparticles	13
1.3.3 Ferromagnetic rods	14
1.4 Methods	15
1.4.1 Vibrating Sample Magnetometer	16
1.4.2 Finite Element Method	18
2 Brownian Dynamics: theory and algorithm	21
2.1 Introduction	21
2.2 Static forces	24
2.2.1 Magnetic interaction	24
2.2.2 Hard sphere interaction	25
2.3 Hydrodynamics	25
2.3.1 Hydrodynamic Interactions	25
2.3.2 Drag forces	29
2.4 Simulation algorithm and numerical methods	30
2.4.1 Simulation scheme	31
2.4.2 Reduced units and parameters	32
2.4.3 Speed-ups and cut-offs	33
3 The magnetic field of a cylinder: theory	37
3.1 Introduction	37
3.1.1 The magnetization of a rod in an external field	38
3.2 The field of a longitudinally magnetized cylinder	39
3.3 The field of a transversally magnetized cylinder	41
3.3.1 Limits	43
3.4 Applications	45
4 The magnetic field of a cylinder: validation	47
4.1 Introduction	47
4.2 Single permanently magnetized rod	48
4.2.1 Longitudinal case	49
4.2.2 Transverse case	49
4.2.3 Mixed case	53
4.3 Multiple permanently magnetized rod	61
4.3.1 Results for $M_l = 1$ and $M_t = 1$	62

4.4	Single rod magnetized by an external field	66
4.4.1	Decomposition of the magnetization on the easy and hard axes	67
4.4.2	Comparison between a magnetized rod and a permanent magnet	69
4.5	Multiple rods in a uniform external magnetic field	71
4.5.1	Parallel rods	72
4.5.2	Crossed rods	74
4.6	Conclusions	77
5	Brownian Dynamics simulations and results	81
5.1	Model System	81
5.1.1	Preliminary evaluation of the equations	82
5.2	Optimization study on a single rod	85
5.2.1	Angle optimization	85
5.2.2	Aspect ratio optimization	88
5.2.3	Influence of the rod on far particle	91
5.2.4	Size dependence of the separation time	95
5.3	Efficiency of the rod packing	99
5.3.1	Conclusions	103
5.4	Study of concentrated solutions	104
5.4.1	Chain formation	105
5.4.2	Separation efficiency	106
5.4.3	Conclusions	109
6	Conclusions and Outlook	111
A	Analytical flow fields around a cylinder	115
A.1	Flow perpendicular to the cylinder axis	115
A.2	Flow parallel to the cylinder axis	117
B	Coordinate transformation and rototranslation of a vector field and its derivatives	119
B.1	Coordinate transformation	119
B.2	Rototranslation	122
C	Derivation of the equations for the magnetic field of a transversally magnetized rod	125
C.1	General statement of the problem	125
C.2	The radial component	126
C.3	The angular component	130
C.4	The z component	132
C.5	Limits	134
C.5.1	The radial component	134
C.5.2	The angular component	134
C.5.3	The z component	135
C.5.4	The field on the axis of the cylinder	135
D	Visualization of the magnetic field generated by magnetized rods	137
D.1	Single permanently magnetized rod	137
D.1.1	Longitudinal magnetization	137
D.1.2	Transverse magnetization	139
D.1.3	Mixed magnetization	141
D.2	Multiple permanently magnetized rods	143
	Bibliography	147

Preface

Magnetic nanoparticles are extremely small particles, often comprising of a single magnetic domain that makes them resemble the behavior of a compass needle when subjected to an external field. Nanotechnology which involves magnetic particles has experienced, in the last decades, an impressive boost and magnetic nanoparticles have become an interesting research area on their own. This is due to their possible applications in a rather broad range of techniques and devices, from waste-water treatment to new clinical and biomedical applications. Most notably, they occupy a relevant role in the framework of magnetic separation technology: the possibility to easily separate the magnetic component of a (bio)solution makes them highly suitable for future evolutions of the magnetic separation technology. However, due to their minute size, the actual separation of the magnetic nanoparticles from the solution in which are suspended constitute a real challenge: the separation problem [1]. Understanding the basic mechanisms behind the separation of a dispersion of magnetic nanoparticles subjected to an external field would provide an advance toward the solution of the problem. However, such good understanding is still missing.

In this thesis, we describe our implementation of a simulation algorithm capable of modeling a High Gradient Magnetic Separation (HGMS) process of magnetic nanoparticles in a continuous flow. The simulations are customized to model a separation column made of a random packing of ferromagnetic rods, which is a novel idea in the framework of HGMS. The former has been implemented in a real setup at the Physical and Colloid Chemistry Laboratory (FCC) at Utrecht University: the simulation project is intended to provide a theoretical counterpart to the experiments which are performed with the setup. The study aims to determine the optimal configuration in terms of tunable parameters (strength and orientations of the external magnetic field, flow conditions, packing of the rods, etc.). In order to achieve the main result, an exact expression of the magnetic field generated by the separation matrix is needed. A set of analytical equations describing the magnetic field of a magnetic rod uniformly magnetized in an arbitrary direction have been derived for the purpose.

Chapter 1 provides a general introduction to magnetic separation and outlines the separation system the simulations are intended to model. The materials used in the real setup (nanoparticles, rods in the separation column, etc.) are also described here.

Chapter 2 illustrates the simulation technique implemented in the algorithm. The details of the simulation, such as particle-particle interactions, particles-column interactions and the hydrodynamic description of the problem are reported here.

Chapter 3 and Chapter 4 deal with the exact analytical formulation of the magnetic field created by the ferromagnetic rods in the separation column. The equations and the magnetic field description are stated and their testing and validation against known analytical limits (when possible) and numerical calculations is described.

Chapter 5 presents a summary of the various results which were obtained by the simulations. Different simulation conditions as well as different characterizations of the particles and the rods are explained and the results are examined in the framework of an optimization study on the separation efficiency.

Chapter 6 summarizes the main conclusions related to the different topics covered in this thesis, as well as future implementations and open questions that need to be addressed by further

studies.

Finally, an Appendix containing in-depth analysis of the theoretical work needed for achieving the main results concludes the thesis.

Chapter 1

Magnetic separation: concepts and materials

In this chapter, a general introduction on magnetic separation is provided. After a brief historical perspective, the main characteristics and scopes of magnetic separation are discussed. The discussion will concentrate on High Gradient Magnetic Separation (HGMS), one of the most common approaches and the usual choice when separation of small particles is needed. A brief account of the different classes of magnetic materials is given. Within this, the phenomenon of superparamagnetism and its relevance for nanoparticles is discussed. Finally, the materials and instruments which have been used in the project are described, concluding with the simulation techniques employed in this study.

1.1 Introduction to magnetic separation

A separation process is a process in which the components of a mixture are separated from each other without substantial chemical modification [2]. Separation science is necessary in almost every technological area, from industrial to laboratory applications. The need for it may arise from very different reasons, according to the field in which separation is performed (research, industry, environment, etc.). A common factor is, nevertheless, always present: starting from a mixture, a task which can separate it into its individual components is needed. Nowadays, a broad range of technologies is available for separation purposes. Among the others, filtration, centrifugation and precipitation methods are all well working and established. However, they all presents limitations due to the physical properties involved in their working principle [3]. In this sense, *magnetic separation* has helped to overcome the problems encountered when a part of the mixture is intrinsically magnetic, providing an higher throughput than equivalent traditional methods [4].

Magnetic separation can be formally collocated in the broad field of *magnetophoresis*, which can be understood as the controlled motion of magnetic particles dispersed in a fluid medium by the application of inhomogeneous magnetic fields [4]. Magnetism has been known since ancient times: the identification of the basic properties of magnetic materials dates back to as early as the sixth century BC [5]. However, the phenomenon of materials moved by a magnet remained mysterious until the late 18th century [5]. Its explanation followed in those years from the development of the framework of the classical electromagnetism theory. The use of these “magnetic forces” in chemical and mining industries was then the natural step toward a practical application of magnetism [6].

The birth of magnetic separation dates back to 1792, with a patent filed by William Fullarton describing its use in iron manufacturing [5]. However, the first application occurred in 1852, when magnetite was separated from apatite by a New York iron manufacturer company [5]. From this pioneering application, magnetic separation has found its way into increasingly

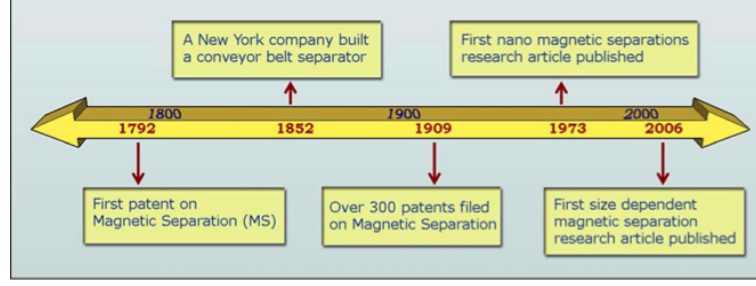


Figure 1.1: The evolution of magnetic separation history (from Yavuz et al.,[6])

complex and diverse industrial processes (Figure 1.1). In addition to chemical and metal industries, magnetic separation has recently become commonplace in biotechnology, where it is successfully used in protein purification and flow cytometry [7].

The working principle of magnetic separation is simple and straightforward, and constitutes the basis of the method since its foundation. Materials that exhibit a magnetic behavior (usually paramagnetic and ferromagnetic media) develop a magnetic moment, either intrinsic (permanent magnets), induced (magnetizable materials) or both. When a magnetic field gradient is present, a force is exerted onto these magnetic moments: an applied field can therefore pick out from a mixture those components who possess distinctive magnetic characteristics [8]. However, magnetic separation has been limited to strong ferromagnetic materials (as iron, magnetite or ferrite) of a relatively large size for quite a long time. In fact, the fields generated by conventional permanent magnets were too low to provide a sufficient force to capture smaller elements or materials exhibiting a weaker magnetic behavior. The method experienced a new birth, however, with the discovery of superconductivity, which led to the creation of new powerful electro-magnets [8]. Since 1960's, the High Gradient Magnetic Separation (HGMS) systems were introduced as a consequence of the breakthroughs in magnet technology [9]. Their main working condition involves the application of a large static magnetic field (1 T) to a column containing ferrous matrices such as steel wool. Due to their irregularity in shapes and surfaces, these matrices give rise to magnetic gradients up to 10^4 T m^{-1} , which are able to capture even weakly magnetic particles [6]. Nowadays, HGMS still constitutes one of the most widely used design in magnetic separation. The following section will illustrate the method more in details.

1.1.1 High Gradient Magnetic Separator

The HGMS concept is based on the fact that the magnetophoretic velocity of a magnetic particle is proportional to the magnetic field gradient [4]. In physical terms, the magnetic force \mathbf{F}_m (N) exerted by a magnetic field \mathbf{B} (T) on a particle which possesses a magnetic moment \mathbf{m} (A m^2) is expressed by the formula:

$$\mathbf{F}_m = (\mathbf{m} \cdot \nabla)\mathbf{B} \quad (1.1)$$

on the assumptions that \mathbf{m} is constant throughout the volume of the particle, such that it is independent of the spatial derivatives [10]. The role of the gradient of the magnetic field in the force expression becomes evident by expanding the RHS in the previous equation:

$$(\mathbf{m} \cdot \nabla)\mathbf{B} = \begin{pmatrix} m_x \frac{\partial B_x}{\partial x} + m_y \frac{\partial B_x}{\partial y} + m_z \frac{\partial B_x}{\partial z} \\ m_x \frac{\partial B_y}{\partial x} + m_y \frac{\partial B_y}{\partial y} + m_z \frac{\partial B_y}{\partial z} \\ m_x \frac{\partial B_z}{\partial x} + m_y \frac{\partial B_z}{\partial y} + m_z \frac{\partial B_z}{\partial z} \end{pmatrix} \quad (1.2)$$

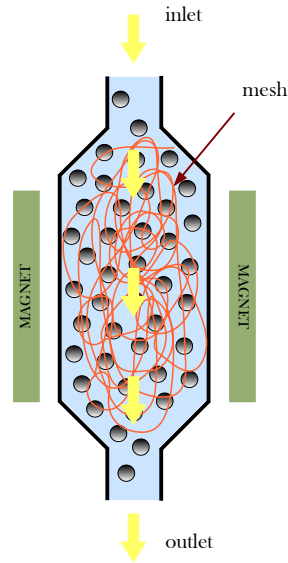


Figure 1.2: Sketch of a HGMS system. The fluid containing the target magnetic particles is passed through the magnetized mesh (in red), which retains the magnetic particles of interest. After separation is accomplished, the magnetic field is removed and the magnetic column is washed in order to recover the magnetic particles captured (from Segura, [4]).

The formula reveals two important aspects. First, the force on the particle is proportional to its magnetic moment, as it is expected from basic physical considerations. Second, and most interestingly, it is proportional to the magnetic field gradient. The field is therefore only responsible of the induced magnetization, but no force is produced unless a magnetic gradient is present [4].

In order to generate these gradients, an HGMS employs a column filled with magnetically susceptible objects, as ferromagnetic wires or beads: under the action of the external static magnetic field, these elements produce high local magnetic fields in their surroundings [4] (Figure 1.2).

In a HGMS setup, the mixture which is intended to be separated assumes the form of a fluid solution, in which the target magnetic particles are suspended. The solution is in fact circulated along the column: the particles passing near the wires are then captured by the local magnetic fields. As a result, the fluid leaving the column at the outlet results separated from its magnetic component. At the end, the column is washed and the particles captured by the ferromagnetic matrix are recovered, thus completing the overall separation process.

As the magnetic gradients at the surface of the matrix elements can be really large, HGMS successfully permits to separate not only ferromagnetic particles, but also weakly paramagnetic particles [11]. This expanded the field of application of magnetic separation to large variety of processes, most notably those in which intrinsically magnetic components are absent as in bio-relevant applications [12]. In this case, the product of interest can be targeted with designer magnetic-beads, making magnetic separation feasible for virtually any system [6].

The claimed benefits of HGMS technology, compared to traditional ones, are [3]:

- Low environmental impact;
- Small dimensions;
- Low pressure drop;
- Long saturation time;
- High selectivity;

- High working speed.

The magnetic force on the particles should be able to overcome the competing forces in play, which are, in general, the gravitational force and the drag force of the surrounding fluid. However, HGMS meets a challenge when the size of the particles is reduced. According to (1.1), the force on the particle is proportional to its magnetic moment, which is roughly dependent on its volume ($|\mathbf{m}| \propto d^3$). As a consequence of decreasing the size of the particles, Brownian motion becomes predominant over the other forces in play: the local magnetic gradients are therefore required to overcome the randomizing effects of the thermal motion of the particles. Other forces become relevant on a sub-micrometric length scale. It is the case of particle-particle interaction forces (Van der Waals, London dispersion, etc.) and frictional forces: they all depend on the size of the particles and on the surrounding conditions, which are rather difficult to describe on a particle scale [13]. All these aspects make the development of a general theory for magnetic separation systems a very challenging problem, and, nowadays, the HGMS is still a complex and not very well understood subject.

However, research focus in magnetic separation is growing, especially in the last few years. Such an interest is often directed toward nanotechnological applications, which represent the most novel and unexplored field in the subject. Using nanoparticles in magnetic separation can provide a solution for several open problems and challenges. For instance, they could be used as scavengers for water contaminants in water purification systems [1]: the target substance adsorbs to the nanoparticle surface via a physico-chemical affinity and, subsequently, the nanoparticles loaded with contaminants are magnetically separated from water. This approach has gained importance as a possible novel technique for arsenic remediation in drinking water [6]. The advantage offered by the use of nanoparticles is, in this specific case, surface area increment (with a consequent cut in terms of waste of magnetic material used for separation) and more reactive surface sites and thus better adsorption properties.

Another promising application is offered by the recent successful employment of magnetic nanoparticles in the biomedical field. In particular, they have been proven to be effective in techniques such as drug and gene delivery [14, 15], hyperthermia [16, 17], MRI imaging contrast enhancement [18] and cell labeling/immunoassay [19]. This last entry can especially benefit from magnetic separation methods, as magnetic nanoparticles can be effectively used to separate entities from their surroundings (Figure 1.3 on the next page). As a first step, the entities are labeled with the magnetic nanoparticles (usually, coated particles are employed). Secondly, a magnetic separation setup ensures that the entities are attracted and hold in specific region, to be successively removed.

Magnetic separation using nanoparticles can be, additionally, incorporated into diagnostic technologies, as for example immunoassays. Their convenient inclusion into microfluidic devices has driven much interest on the subject. Figure 1.4 on page 8 illustrates the concept of a bio-barcode assay to carry out diagnostics of proteins at the attomolar sensitivity [21].

These examples illustrate the more and more important role that magnetic nanoparticles are playing in current research and applications. Magnetic separation efficiently involving them proves therefore to be a valuable technology for the development of such techniques, and an expansion of its usage in waste removal and biotechnological fields can be anticipated in the coming years. A better comprehension of the physical processes that lie behind magnetic separation is, therefore, most desirable. It can lead to more accurate designs as well as an overall optimization of the separation process: as such, it constitutes one of the goals of this current study.

1.2 Superparamagnetism

Ultimately, all magnetic phenomena are due to charges in motion: this applies to common compass needles as well as to the magnetic field of Earth itself. More in details, on an atomic scale magnetism is generated by tiny current loops that can be ascribed to the motion of the electrons. Due to their very small size, they can be simply considered as magnetic dipoles. In general, the fields generated by such dipoles cancel out each other due to the random orientation

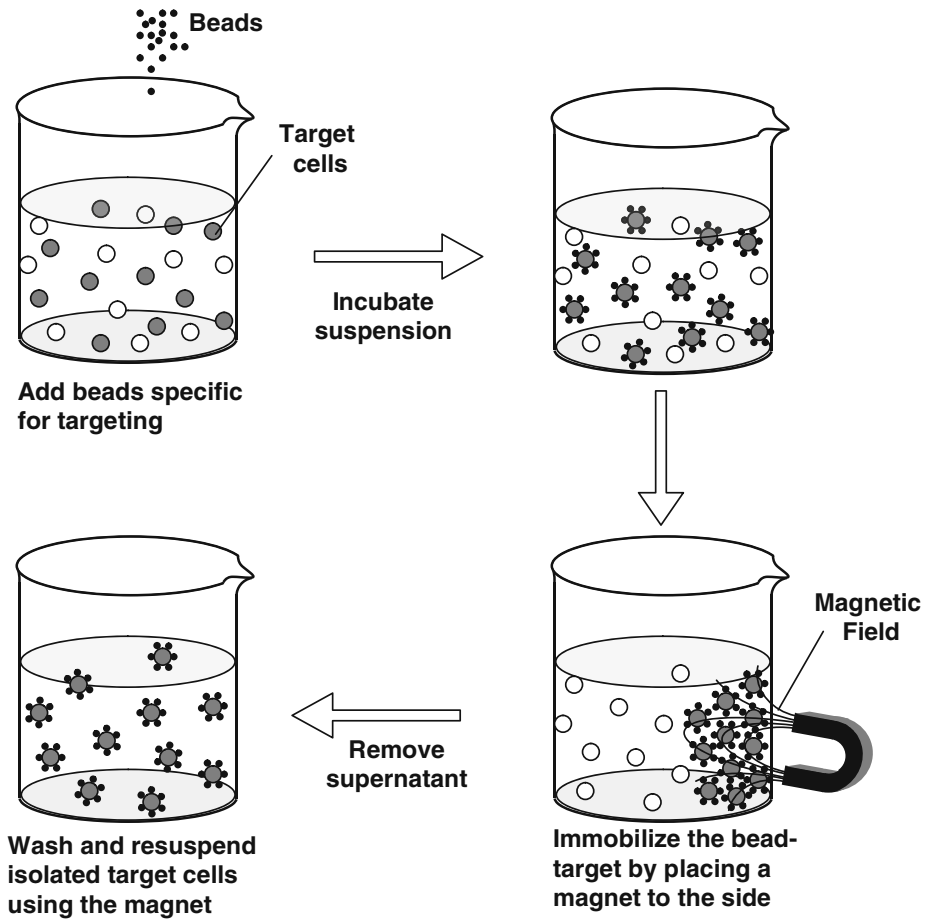


Figure 1.3: Sketch of a possible usage of magnetic separation for biomedical applications (from Ramanujan, [20]).

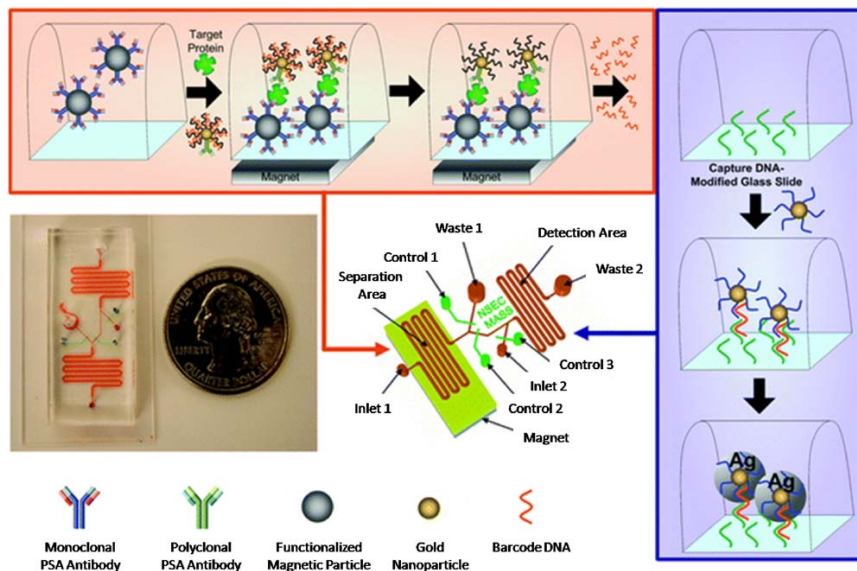


Figure 1.4: Implementation of the bio-barcode assay within a microfluidic device. Functionalized magnetic particles are introduced into the separation area of the chip and immobilized by placing a permanent magnet under the chip. The sample and gold nanoparticles decorated with barcode DNA are introduced. The barcode DNA is then released from the gold nanoparticles and is transported to the detection area of the chip, patterned with capture DNA. A second set of gold nanoparticles functionalized with complementary barcode DNA is introduced into the detection area to allow hybridization. Finally, the signal from the gold nanoparticles is amplified using silver stain (from Goluch et al., [21]).

of atoms. However, when the material is placed in a magnetic field, the dipoles align: the material acquires a *magnetization*.

Materials are classified on the basis of the relationship between the magnetization and the external field. As a note, it is worth to note that *all matter is magnetic*. As the origin of magnetism lies in the orbital and spin motions of electrons, every material exhibits a magnetic response. The main difference between, for instance, aluminum and iron is that the magnetic dipoles align differently between the former and the latter. There are three main classes of magnetic materials:

- Diamagnetism
- Paramagnetism
- Ferromagnetism

In addition, there exist other two classes: ferrimagnetism and anti-ferromagnetism. They represent a type of magnetic ordering exhibited by ionic compounds, such as oxides, where two sublattices are present. Their origin follows from quantum mechanical interactions between the ions. However, they are not relevant for the purpose of this report, and will not be described. Diamagnetism is a fundamental property of all matter. The orbiting electrons are perturbed in the presence of a magnetic field: this causes a change in the magnetic dipole moment. According to Lenz's Law, this change opposes to the external field. The magnetization exhibited by diamagnetic material is thus negative, although the effect is generally very weak (with the notable exception of superconductors). Typical diamagnetic substances, such as silica (SiO_2) or water, possess filled orbital shells and there are no unpaired electrons.

Paramagnetism is shown by substances that possess one or more unpaired electrons. In contrast with diamagnetism, where the electrons do not exhibit a net magnetic moment (the magnetization is caused by the orbit's perturbation), an unpaired electron always carries a

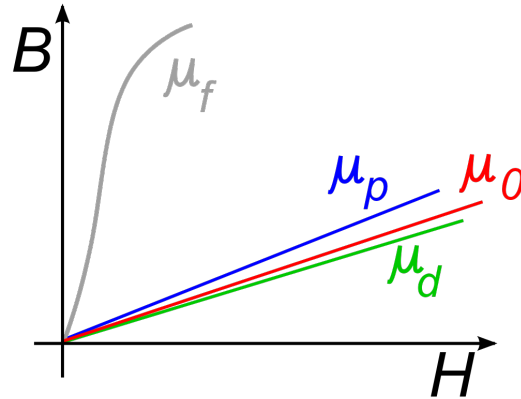


Figure 1.5: Permeability curves of diamagnetic, paramagnetic and ferromagnetic materials. A curve under the linear functions with coefficient μ_0 (vacuum permeability) indicates a negative magnetization. The three principal classes of magnetic materials are illustrated in terms of their typical permeability curves: μ_d stands for diamagnetic materials, μ_p stands for paramagnetic materials and μ_f stands for ferromagnetic material.

dipole moment, which can point in any direction. While in the absence of an external field such dipoles are randomly oriented due to thermal motion, when a magnetic field is applied they align themselves in the direction of the field, thus generating a positive magnetization. The effect is still weak, but is generally larger than the diamagnetic contribution (which is always present): as a result, the net magnetization is positive and linearly depends on the external field (a stronger field is able to align more dipole moments). Typical paramagnetic elements are aluminum (Al), manganese (Mn), platinum (Pt), oxygen (O_2) and rare earth ions.

Ferromagnetism arises from the same basic effect as in paramagnetism: unpaired electron's magnetic moments orient themselves in the presence of an external magnetic field. The difference is that in a ferromagnetic material there is a strong coupling between the dipole moments of the atoms, due to quantum mechanical exchange forces. The net result is that the magnetization induced in such materials is orders of magnitude stronger than in normal paramagnetic materials. Moreover, the atomic moments can exhibit a parallel or anti-parallel alignment with respect to the external field. Figure 1.5 represent the different magnetization curves that apply to the classes of materials described above. The magnetic field \mathbf{B} is plotted against the external field \mathbf{H} ($A\ m^{-1}$). As a recall, the general relation between the two magnetic fields is given by:

$$\mathbf{B} = \mu_0(\mathbf{H} + \mathbf{M}) = \mu\mathbf{H} \quad (1.3)$$

where \mathbf{M} ($A\ m^{-1}$) represents the magnetization generated inside the material of interest and $\mu = \mu_0\mu_R$ represents the *magnetic permeability* of the media, with $\mu_0 = 4\pi \times 10^{-7}\ H\ m^{-1}$. The permeability is a quantity that characterizes the medium and can be a function of various parameters [22]. In the following and in the whole report, \mathbf{H} will always be referred to as the external applied field if not differently specified, while \mathbf{B} will indicate the induced field in which also \mathbf{M} is taken into account.

While for diamagnetic materials (and, for applied fields smaller than 10 T, also for paramagnetic materials) the induced magnetization is a linear function of the applied field, ferromagnetic materials show a highly non-linear behavior. In particular, above a certain value of the applied field \mathbf{H} , the magnetization reaches a limit value above which it cannot increase more. This value is called *saturation magnetization* (M_s) and it is an universal property of the material [23]. Moreover, even when the field is reduced to zero, ferromagnetic materials still retain a non-zero magnetization, referred to as the *remanence magnetization* (M_r). On top of that, ferromagnetic materials conserve a “memory” of the applied field's history, so that there is not an unique correspondence between \mathbf{H} and \mathbf{M} . This behavior is called *hysteresis*. A typical hysteresis loop for a ferromagnetic material is reported in Figure 1.6 on the next page. For a

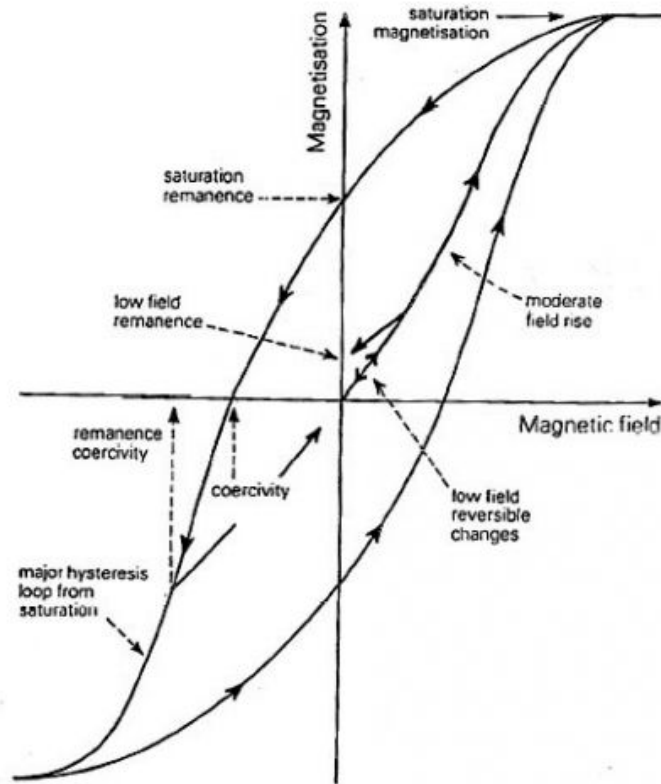


Figure 1.6: Hysteresis loop of a ferromagnetic material.

more detailed description, see [24].

1.2.1 Magnetic domains and superparamagnetism

Even though, in the case of ferromagnetic materials, the atomic moments exhibit a rather strong interaction and tend to align collectively, this behavior is displayed only locally. “Isles” appear throughout the materials, in which the local magnetization is aligned, but it is not necessarily parallel to the other isles. These zones are called *magnetic domains* and are responsible for the typical hysteresis loop of ferromagnetic materials [25]. An external field is able to align the magnetic domains along its direction: a stronger field will result in a higher number of domains sharing the same magnetization direction, until macroscopic magnetic saturation is achieved. All along this process, however, the single domains are *always* locally saturated. The reason for the formation of magnetic domains lies in the fundamental principle of magnetic energy minimization and will not be described here. For a more in-depth description, see [24]. Normally, a magnetic particle exhibits a microscopic multidomain ferromagnetic (FM) structure. However, when the size of the particle is decreased below a critical value D_C , the FM structure becomes energetically unfavorable: the particle shows a single domain (SD) structure. A SD particle is *always* uniformly magnetized to its saturation magnetization. Due to the absence of other domains, the only way to reverse a SD particle’s magnetization is by rotating its atomic spins, which is in general a energetically costly process. This is the reason why SD particles show a high remanence magnetization [26]. If the particle size is further decreased, another critical size limit is reached. At this threshold, D_{SP} , the energy barrier for magnetization flipping is overcome by the thermal energy $k_B T$. The single magnetic moment randomly rotates changing its orientation if no external field is present (thus exhibiting no coercivity), while it aligns with the field behaving effectively as a paramagnet when a magnetic field is applied.

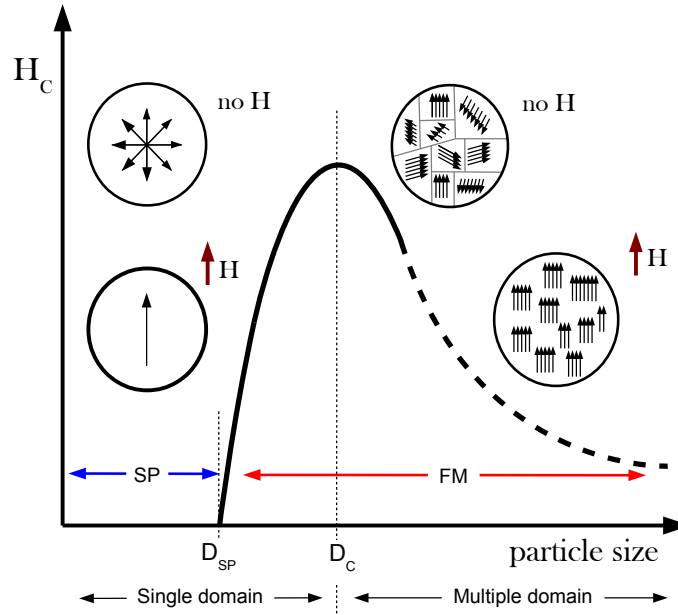


Figure 1.7: Sketch of the change of coercivity as a function of particle size for a magnetic sample. The maximum value is achieved for the critical size D_C , when the particle becomes SD. Below the size D_{SP} , no coercivity and remanence are shown, thus corresponding to a (super)paramagnetic behavior (from Segura, [4])

Table 1.1: Values of the critical sizes D_C and D_{SP} for four different materials that show superparamagnetic behavior. The values are reported from various references (see entries in the table).

	D_C (nm)	D_{SP} (nm)
Fe_3O_4 [28]	80-100	20-30
$\gamma\text{-Fe}_2\text{O}_3$ [29]	100-120	30-40
Ni [30]	50-65	15-25
MgFe_2O_4 [31, 32]	25-30	15

This state is called *superparamagnetic* [27]. The term arises from the fact that, unlike in normal paramagnets where the magnetic moment comes only from a single atom, the dipole moment of a superparamagnetic particle is generated by all the single atoms in the particle. These sum up to a giant (super) moment [26]. A sketch illustrating the different domain transitions of a magnetic particle is provided in Figure 1.7. Some typical values of the critical sizes D_C and D_{SP} for different materials that exhibit superparamagnetism are shown in Table 1.1.

When a magnetic field is applied, superparamagnetic particles align their moments with the field. If this is later removed, thermal fluctuations will relax the magnetization direction to undergo a rotation. A first mechanism responsible for such rotation, called *Neel relaxation*, consists in the reversal of the magnetic dipoles by thermal activation *within* the particle. If the particles are immersed in a fluid (*magnetic colloidal suspension*) a second mechanism also contributes to the magnetization relaxation. This second one, called *Brownian relaxation*, consists of a physical rotation of the particle inside the surrounding fluid due to Brownian motion, while the magnetic moment inside the particle remains blocked. The two mechanisms are competing, with the relaxation time for Neel mechanism being usually slower than that for Brownian relaxation [4]. For a thorough discussion (which is outside the scope of this report) the reader is referred to the relevant literature on the topic [33].

When an external magnetic field is present, on the contrary, the magnetization of superparam-

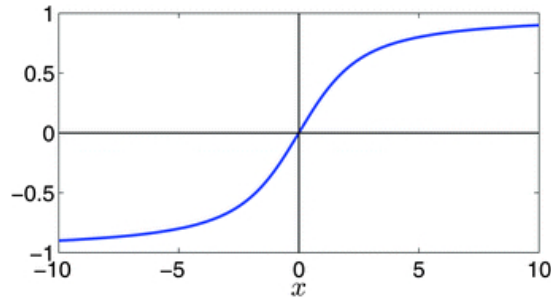


Figure 1.8: Langevin function.

agnetic particles is described according to a treatment analogous to the Langevin theory of paramagnetism. More in details, the dependence of the magnetic moment on the external field is given by [33]:

$$\mu(H) = M_{\text{sat}} \mathcal{L} \left(\frac{\mu_{\text{d}} H}{k_{\text{B}} T} \right) \quad (1.4)$$

where H is the magnitude of the external applied field, M_{sat} represents the saturation magnetization of the particle and μ_{d} (A m^2) represents the magnetic moment of a single magnetic domain. The function $\mathcal{L}(x)$ is the *Langevin function*, defined as:

$$\mathcal{L}(x) = \coth \frac{1}{x} - \frac{1}{x} \quad (1.5)$$

The sketch of the function shape is given in Figure 1.8. For low fields, it exhibits a linear regime, while it reaches saturation for high applied fields. It is possible to express the previous formula in an approximate fashion where the relevant quantities are expressed in terms of the saturation magnetization of the material (rather than that of the single particle) [34]:

$$\mu(H) = n_{\text{d}} M_{\text{S}} V_{\text{d}} \mathcal{L} \left(\frac{V_{\text{d}} M_{\text{S}} H}{k_{\text{B}} T} \right) \quad (1.6)$$

where M_{S} now expresses the saturation magnetization of the constitutive material of the particle and V_{d} (m^3) is the (averaged) volume of a single magnetic domain inside the particles. Throughout the rest of this report, the magnetic moment of a superparamagnetic nanoparticle will be expressed by this final formula.

1.3 Materials

The simulation study which is the object of this report has been performed on the basis of a built-in High Gradient Magnetic Separator setup, located at the Physical and Colloid Chemistry Laboratory (FCC) at Utrecht University. The following subsections will illustrate the principal characteristics of the setup which are of significance for the scope of this report and have been implemented in the simulations.

1.3.1 Experimental Setup

The High Gradient Magnetic Separator on which the simulation study is based is represented in Figure 1.9 on the next page. The setup schematically consists of a magnet that provides the external magnetic field and two sections: the flow input section and the column section. The magnet is a Bruker B-E 25V electromagnet, which generates an uniform external magnetic field throughout the entire column volume. The strength of the field can be tuned up to a



Figure 1.9: HGMS setup at the Physical and Colloid Chemistry Laboratory, Utrecht University

maximum of 1.9 T, depending on the gap between the electromagnet's coils.

The flow input section controls the flow circuit and rate of the setup. Via a system of pipes, valves and directors, the flow of the magnetic solution through the system column is regulated. It is possible to apply an external pressure by nitrogen flow. The magnetic solution flow can be substituted or complemented by a clean water flow.

The column implemented in the setup is a cylindrical tube with an inlet and an outlet through which the magnetic solution flows. Columns of two different dimensions can be mounted. The ferromagnetic matrix which is necessary in the implementation of a HGMS (see 1.1) is provided by a packing of ferromagnetic rods. Details on the rods are given in a following subsection. Figure 1.10 on the following page represents a picture of the real column with the ferromagnetic matrix and a graphical representation of the separation mechanism which takes place in the column. After flowing through the column, the solution exits the system via an output pipe and it is collected in a reservoir for further analysis and collection.

1.3.2 Nanoparticles

The nanoparticles used in the HGMS setup are stabilized colloidal nanoparticles. They are composed of a number of single domains of magnetite (Fe_3O_4) in a coating that ensures stabilization against aggregation. Figure 1.11 on page 15 shows a size distribution and hysteresis curve of the particles. The size distribution shows a mean diameter size of (6.6 ± 2.5) nm, thus exhibiting a relatively peaked shape. For the purpose of this study, therefore, the magnetic

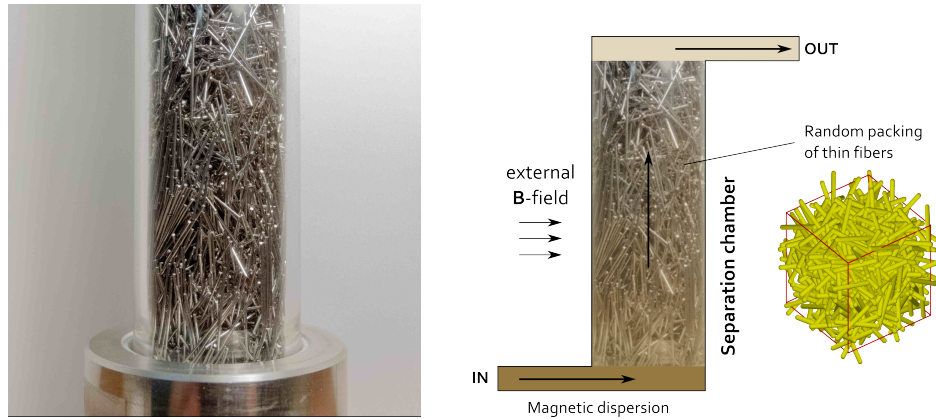


Figure 1.10: Separation column in the HGMS setup. The picture on the left shows a real separation column in the home-built setup at FCC. The picture on the right illustrates the separation mechanism in the matrix, provided by a random packing of ferromagnetic rods.

particles are assumed to be monodisperse.

The particles show no remanence in zero field condition, thus proving to exhibit a superparamagnetic behavior. This aspect is extremely important in a magnetic separator, where a null remanence is required for both the nanoparticles and the ferromagnetic matrix. If this is satisfied, the particles captured by the magnetized rods when the field is on will be released as soon as the external field is switched off. In this way, it is possible to collect them when the separation process is completed. This aspect constitutes one of the many advantages of magnetic separation, as discussed previously in section 1.1.

1.3.3 Ferromagnetic rods

The ferromagnetic matrix in the separation column is composed by a random packing of ferromagnetic rods. These rods are made of an AluchromO® ferrowire, with chemical composition Fe 70%, Cr 25% and Al 5%. The magnetic properties of the rods have been measured via a Microsense EZ9 Vibrating Magnetometer Sample (VSM) (for a description of the technique, see section 1.4 on the facing page). The hysteresis curves relative to different orientation of the rod in the external magnetic field are reported in Figure 1.12 on page 16. From the measurements, we report the saturation magnetization M_s for Aluchrom to be $985\,000\text{ A m}^{-1}$. This value is in agreement with other references in literature [35, 36].

The hysteresis curves in Figure 1.12 on page 16 show that the saturation magnetization is reached for all the angles. The small discrepancies in the saturation magnetization for different angles are due to a shape calibration artifact: the setup was calibrated on a standard reference Yttrium Iron Garnet (YIG) sphere, which does not show shape anisotropy in its magnetic properties. On the contrary, a rod exhibits a cylindrical geometry, thus possessing a magnetization along its easy-axis (longitudinal) and hard-axis (transversal) [38]. This *demagnetization* feature of the cylindrical geometry is visible in the different shape of the curves in Figure 1.12 on page 16 corresponding to different angles. The curve relative to the easy axis ($\theta = 0^\circ$) is very steep and thus it is easy to saturate the rod along its longitudinal axis. The curve relative to the hard axis ($\theta = 90^\circ$) is, on the contrary, quite broad and the rod reaches saturation along its transverse axis only if higher intensity fields are applied, in comparison with the former situation.

This difference between the shape of the calibration sphere and the rod samples introduces an artifact in the magnetic moment measured by the VSM when the sample is rotated, as it is the case for the hysteresis curves reported in this section. However, the discrepancy is small and therefore the effect is negligible: the wire can be confidently assumed to be isotropic.

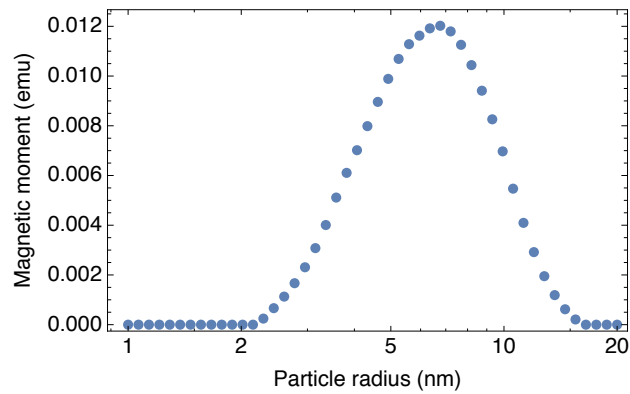
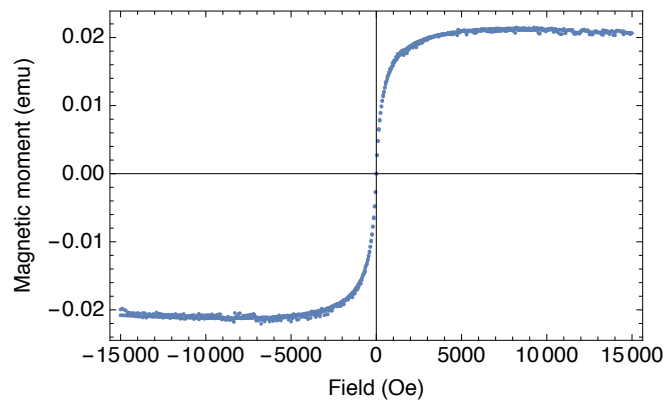
(a) *Size distribution*(b) *Hysteresis curve*

Figure 1.11: Size distribution and hysteresis curve of the nanoparticles used in the setup. The curve refers to a 0.0492 g sample in H₂O with concentration $c = 0.1\% w$. The reported magnetic moment m refers to the whole sample.

The most important aspect of AluchromO[®], confirmed by the measured hysteresis curves, is that it shows no (or very little) magnetic remanence: the magnetization of the rods goes to zero when the external field is removed. As discussed previously for the nanoparticles, this is a very strict requirement in a HGMS setup where collection of the magnetic material after the separation process is desired.

Different sizes of the rods can be obtained via a wire-cutter. This enables for a broad array of possible aspect ratios (L/D) of the ferromagnetic rods in the separation column, thus making it a parameter on which the optimization of the HGMS setup can be assessed. In conclusion, Table 1.2 on the following page reports the geometric specifications of the two different columns and the minimum and maximum sizes of the ferromagnetic rods available for the setup at present.

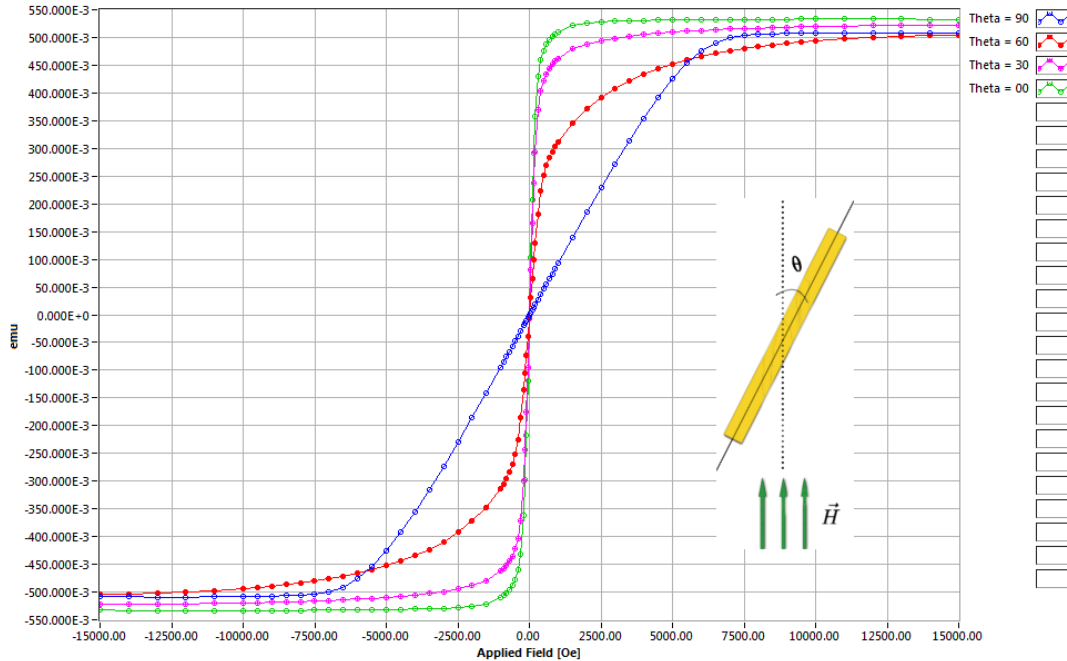


Figure 1.12: Hysteresis curves of a ferromagnetic AluchromO® rod ($D = 0.4$ mm, $L = 12$ mm) for different angles between the external field and the rod longitudinal axis (the inset serves as an explanation). The measurements are done on the shortest rod. The saturation regime reached for the shortest rod ensures that the same regime is reached for larger aspect ratios L/D values [37].

Table 1.2: Sizes and specifics of the columns and ferromagnetic rods implemented in the in-built HGMS present at the FCC laboratory.

	Rods		Columns	
	Maximum size	Minimum size	Big column	Small column
Length (L)	12 mm	4 mm	309 mm	275 mm
Diameter (D)	0.4 mm	0.4 mm	40 mm	20 mm

1.4 Methods

For the purpose of this study, an home-built simulation algorithm was implemented to investigate the underlying physics in a magnetic separation experiment performed on a setup as the one described in the previous section. However, other techniques, both experimental and computational, have been used throughout the duration of the project. The former provided the correct physical parameters and values to be implemented in the simulations. The latter provided a meaningful comparison method for the results obtained via the home-built algorithm. In the following subsections, the two most important techniques used are described.

1.4.1 Vibrating Sample Magnetometer

A *magnetometer* is a measurement instrument used either to measure the strength and direction of a magnetic field in space or the magnetization of a material. Several different kinds of magnetometer exist, depending on the working principle upon which they are based. For measures of the magnetic moment of a material, however, induction methods magnetometers

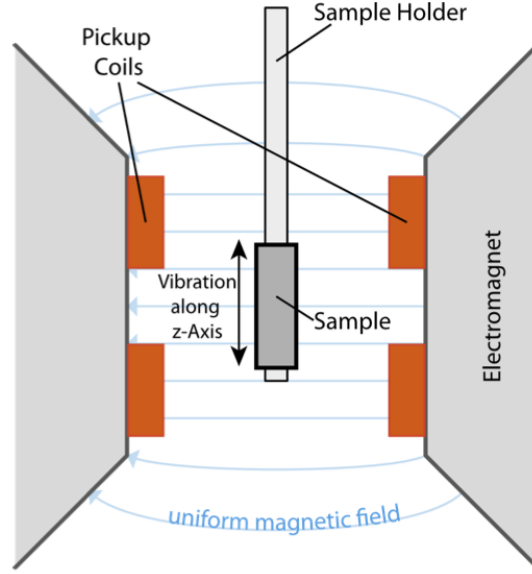


Figure 1.13: Scheme of a Vibrating Sample Magnetometer (VSM) (Image from [40]).

are commonly used. The method is based on the (magnetostatic) Maxwell's equation:

$$\nabla \times \mathbf{E} = \frac{\partial \mathbf{B}}{\partial t} \quad (1.7)$$

where \mathbf{E} is the electric field generated by a temporally varying magnetic field \mathbf{B} . A magnetized body creates an induction field \mathbf{B} . According to Maxwell's equation, the variation of the field in time produces an electromotive force which can be measured by pickup coils. The voltage in the sensing coils is proportional to the magnetic moment of the sample [39]. In practice, static pick-up coils are used, while the sample undergoes vibration. An equivalent vibration of its induction field \mathbf{B} is also generated and, consequently, the electromotive force necessary for measurements. This constitutes the basic principle of the *Vibrating Sample Magnetometer (VSM)*. Commercially available VSM magnetometers have sensitivity below 10^{-9} A m^{-2} [40]. The experiment in this study have been performed on a Microsense EZ9 VSM. The uniform magnetic field necessary to magnetize the sample is usually generated in an electromagnet or a superconducting magnet. A illustrative scheme of the principle of a VSM is given in Figure 1.13.

The high sensitivity reached by the VSM is allowed by the implementation of *lock-in* principle of measurement, that allows to detect signals weaker than noise [40]. Due to demagnetization effects induced by the shape of the samples, one often need to employ correction factors in order to obtain a signal which is independent of the shape [39]. Ideally, a spherical or ellipsoidal sample should be used in a VSM measurement. In this case, the sample can be effectively represented by a point dipole, allowing for an almost null inaccuracy regarding the sample shape. A small sample is often desirable: this allows for a larger signal to noise ratio [40]. However, the maximum size of the sample is limited by the geometrical constraint of the machine, which is dictated by the gap of the external electromagnet.

Due to the directionality of the pair of coils in a typical VSM setup, the magnetic moment is measured with reference to one direction only. However, If an additional set of coils is placed at a right angle respect to the first one, simultaneous measurement of the magnetization among two axes of the sample is possible. This also permits the derivation of the torque on the sample, since torque is equal to the cross product of the field and magnetization vectors, or [39]:

$$\boldsymbol{\tau} = \mathbf{M} \times \mathbf{H}_{\text{ext}} \quad (1.8)$$

where τ is the torque exerted on the sample by a magnetic field \mathbf{H}_{ext} and \mathbf{M} is the sample magnetization.

The most common quantity measured by the VSM is the hysteresis loop of the sample, which has been already described in another section. However, other curves can be inferred, most notably the *remanence curves*. There are principally two different kind of curves. The Isothermal Remanence Magnetization (IRM) curve is measured after the application and removal of a field with the sample initially demagnetized. The DC Demagnetization (DCD) is measured from the saturated state by application of increasingly stronger demagnetizing fields [39]; the DC in the name is due to the fact that the field is generated by a direct current in the electromagnet. The combination of the two curves (i.e., a plot of IRM vs DCD) is called *Henkel Plot* and can give information about the magnetic anisotropy and particle interactions that occurs within the sample which is analyzed [41].

1.4.2 Finite Element Method

Electromagnetism is governed by Maxwell's Equations. According to them, every electromagnetic problem can be expressed in terms of a number of vector and scalar fields [25]. These are the electric field vector \mathbf{E} (V m^{-1}), the magnetic strength field vector \mathbf{H} (A m^{-1}), the electric displacement field vector \mathbf{D} (C m^{-2}), the magnetic field vector \mathbf{B} (T), the current density field vector \mathbf{J} (A m^{-2}), the volume charge density ρ (C m^{-3}), the magnetic permeability μ (H m^{-1}) and the electric permittivity ϵ (F m^{-1}).

The mentioned quantities relate to each other via the following system of differential equations:

$$\nabla \times \mathbf{E} = -\frac{\partial \mathbf{B}}{\partial t} \quad (1.9)$$

$$\nabla \times \mathbf{H} = \mathbf{J} + \frac{\partial \mathbf{D}}{\partial t} \quad (1.10)$$

$$\nabla \cdot \mathbf{D} = \rho \quad (1.11)$$

$$\nabla \cdot \mathbf{B} = 0 \quad (1.12)$$

with the constitutive equations:

$$\mathbf{B} = \mu \mathbf{H} \quad \mathbf{D} = \epsilon \mathbf{E} \quad (1.13)$$

Once that ρ and \mathbf{J} are known, the constitutive relations are stated and the boundary conditions are specified, the electric and magnetic field generated by such configuration can be obtained. However, this approach is in practice unattainable, with the notable exception of a few simple model systems. The reason is that the solution of the problem usually involves the handling of a set of partial differential equations, which is generally non-trivial and, in most cases, not feasible analytically.

However, the problem can be handled by approximate numerical methods. Among the most popular techniques, the Finite Element Method (FEM) offers one of the best option in terms of the balance between flexibility, accuracy and computational time [42]. The central idea behind the method is the simplification of the general electromagnetic problem by discretizing the electromagnetic fields mentioned above. The discretization, also known as meshing, consists in subdividing the spatial geometry into a certain number of elements. These elements are triangular in two dimensional cases and tetrahedral in three dimensional cases.

On each element, the unknown fields are assumed to be of a particularly simple functional dependence. Generally, they are expressed in terms of polynomial functions [42]. The solution is then found by variational analysis, where a proper variational functional is minimized. The minimum corresponds to the solution of Maxwell's Equation over that particular domain element [43, 44].

FEM exhibits a number of strength points. For instance, it can easily deal with complex geometries and configurations in which material inhomogeneities are present. This includes, for instance, dispersive media or frequency-dependent materials (in optics, for example). Moreover, FEM has the advantage to provide a treatment for "multi-physics" problems, where the electromagnetic problem is coupled to thermal or mechanical ones [45]. However, it also presents a few

important drawbacks. First of all, the quality of the solution critically depends on the quality of the mesh. While this can be seen as an advantage (the accuracy can be decided according to the quality of the prepared mesh), especially in 3D problems FEM meshes become very complex. This implies a very intensive computational effort to provide an acceptable solution, which could however be of an extremely approximate nature. Moreover, FEM implementation is extremely complex in terms of coding, both for the meshing algorithm as well as for the iterative solvers needed. This poses severe limits to its use and development and restricts its implementation to individual engineers [42].

The description of FEM in electromagnetism here provided is only intended to serve as a mention. Several excellent texts and monographs on the topic are available [42, 45, 46]. In this study, the commercial FEM software MagNet from Infolytica Corp. [47] for solving electromagnetic problems has been used for two essential reasons. Firstly, it can provide a valid tool of comparison between the results predicted by our in-built algorithm and the results obtained by another simulation method (namely, FEM). Secondly, it is a valuable method for testing the validity of an analytic expression for the magnetic field derived independently, as it is discussed in Chapter 4 of this thesis. Figure 1.14 on the following page provides a MagNet example of a FEM mesh and solution of a three-dimensional problem involving a small ferromagnetic particle in the vicinity of a magnetized cylinder.

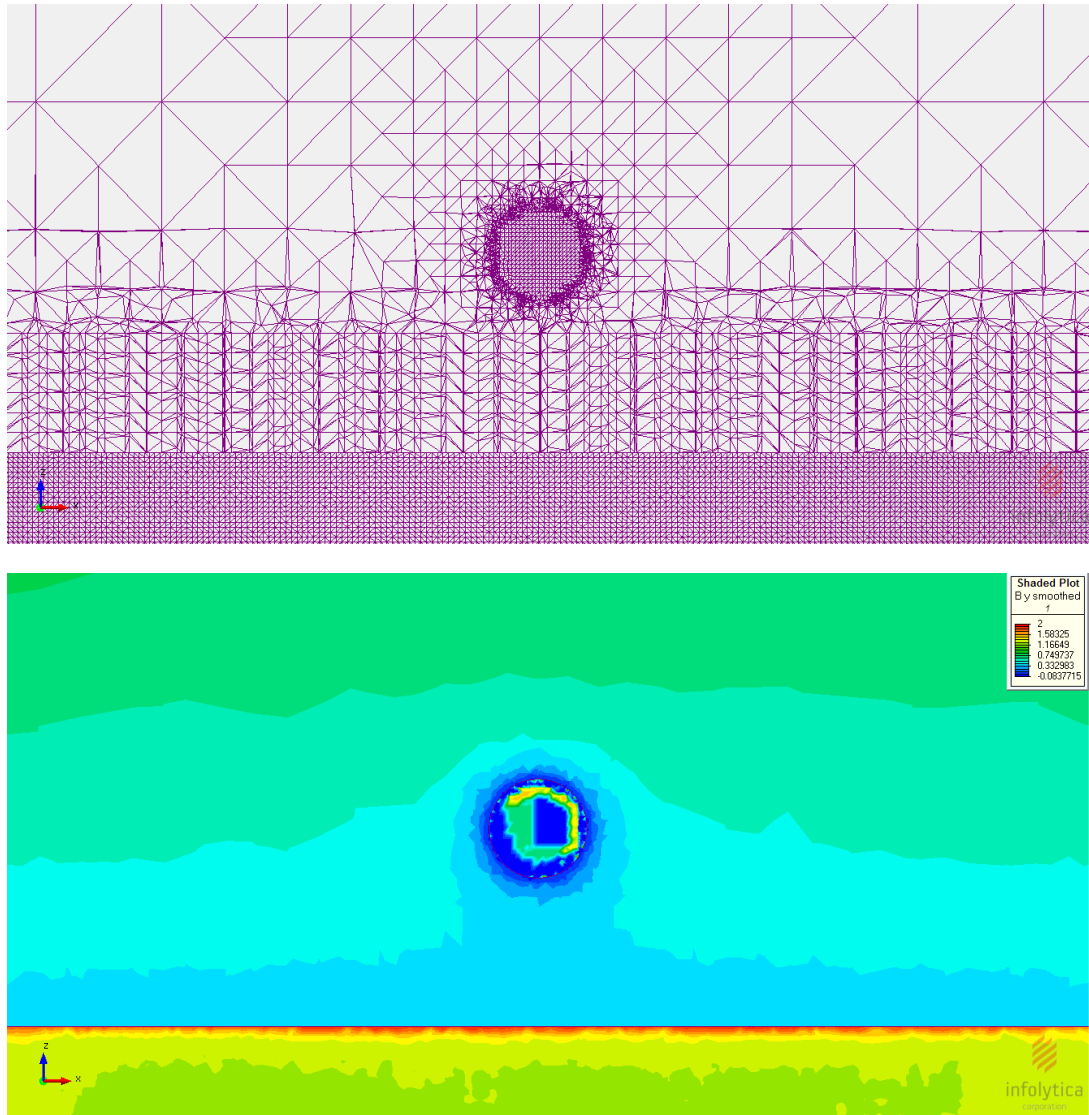


Figure 1.14: FEM three-dimensional modeling of a small ferromagnetic particle in the vicinity of a magnetized cylinder. Top figure: FEM meshing prior to the problem solution. A correct treatment of the gap between the sphere and the cylinder (whose boundary is here visible by its finer mesh) is critical for the overall quality of the solution. Therefore, the mesh in this region is finer than in the surroundings. Bottom figure: FEM solution to the problem. A component of the magnetic field \mathbf{B} is visualized. Despite the presence of a relatively fine mesh and a quite intensive calculation, the solution appear not to be smooth. This constitutes a proof that FEM modeling in 3D can be challenging.

Chapter 2

Brownian Dynamics: theory and algorithm

This chapter illustrates the Brownian Dynamics algorithm which has been implemented for the study of the motion of superparamagnetic nanoparticles in a random packing of magnetic rods. After an introduction on the relevant time and length scales in colloidal suspensions, the central Langevin Equation and its simplification in the Brownian Dynamics framework are stated, with an explanation of why they are appropriate for studying a system as the one presented in this Thesis. The different force terms which have been considered in our implementation of Brownian Dynamics are discussed in their physical justification and in their theoretical description. Finally, the simulation scheme used to solve the Brownian Dynamics equation is presented, with an explanation of the reduced parameters, speed-ups and cut-offs adopted within this study.

2.1 Introduction

Computer simulations provide a strong and established approach to complement both theory and experiments [48–50]. Through a direct control over their complexity, they can be tailored to provide a theoretical framework for ideal systems as well as providing new insights over more realistic complex systems.

The universe of computer simulations is extremely various and several different techniques are available for modeling a very rich “zoo” of physical phenomena. The various methods are generally classified according to the time and length scales of the physical phenomenon of interest [4]. A basic classification scheme is provided in Figure 2.1 on the next page. The time and length scale of interest depend on the system under study. In the case of colloidal suspension, the lengths involved can be divided between the solvent scale (microscopic) and the particle scale (macroscopic). This corresponds to an order of magnitude of 10^{-10} m to 10^{-9} m for the solvent molecules and 10^{-9} m to 10^{-6} m for the colloidal particles. In contrast, there are several relevant times in the case of a colloidal suspension. They range from the solvent scale (collision time between solvent molecules) to the brownian scale (time over which a colloid typically diffuses) [51]. Table 2.1 on page 23 reports a review of the relevant time scales for colloidal suspensions. While relaxation times for the fluid are on the order of 10^{-14} s, a relevant time scale for a colloidal particle under Brownian motion is at least 10^{-9} s. Due to the enormous difference in time and length scales between solvent and particles, it is impossible to provide a molecular model for both solvent particles and colloidal particles and combine them in a single simulation. A form of *coarse graining* is therefore necessary [51].

The separation in time scales (a consequence of the extreme difference in mass between a colloidal particle and a solvent particle) provides the basis of the so-called *Langevin description*, which is central to any Brownian Dynamics (BD) simulation. According to this picture, the

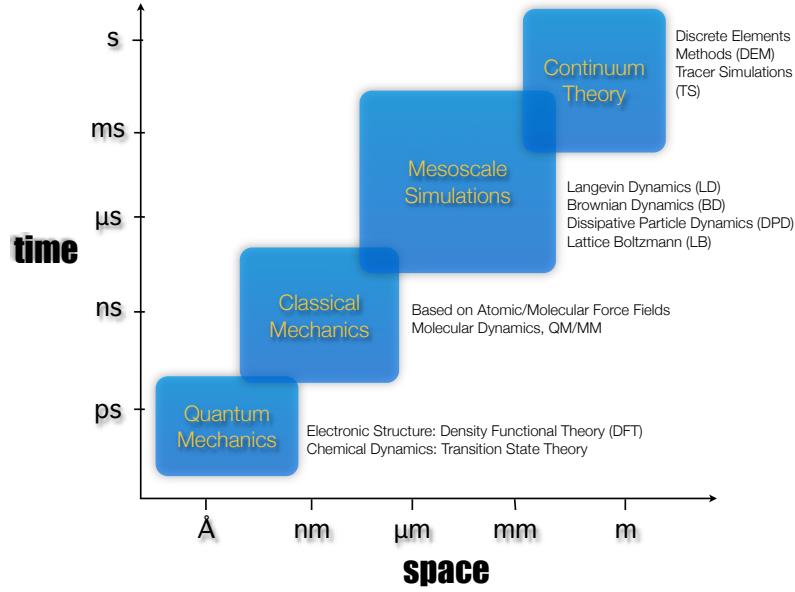


Figure 2.1: Diagram showing the different simulation and computational techniques according to the relevant length and time scales of the processes for which they are designed (from Segura, [4]).

interaction of the colloidal particle with the solvent is separated into two parts. Firstly, there is a fluctuating force due to *random* collisions of solvent molecules with the colloidal particle. Secondly, as the particle attains a certain velocity in the fluid, there is a friction force due to the *systematic* collisions between the solvent molecules [52]. However, as the mass of the particle is orders of magnitude larger than that of the solvent molecules, this last force equals the hydrodynamic friction force of a macroscopic body immersed in a fluid [52]. As a consequence, the equation of motion of a single colloidal particle of mass m can be written as:

$$m \frac{d^2 \mathbf{r}}{dt^2} = \mathbf{F}_f + \mathbf{F}_{\text{ext}} + \mathbf{F}_r \quad (2.1)$$

where \mathbf{r} represents the particle position. As already stated, the particles in this study are assumed to be spherical and superparamagnetic. This means that neither shape anisotropy nor a fixed magnetic dipole moment are present: the rotational degrees of freedom are therefore neglected. Equation 2.1 is commonly referred to as *Langevin Equation* [52]. The term \mathbf{F}_f represents the hydrodynamic forces on the particle. If the velocities are not too large, the term is proportional to the velocity of the particle as given by the Stokes formula:

$$\mathbf{F}_f = -\xi_S \mathbf{v} \quad (2.2)$$

where ξ_S (kg s^{-1}) is the friction coefficient of the particle and \mathbf{v} is its velocity. The term \mathbf{F}_{ext} represents the interaction forces between colloidal particles (dipolar magnetic forces, electrostatic interactions, Van der Waals forces, etc.) and/or external forces. The term \mathbf{F}_r represents the fluctuating force due to random collisions. As this last term only represents the random interaction between solvent and colloidal particles, it obeys the conditions:

$$\langle \mathbf{F}_r(t) \rangle = 0 \quad (2.3)$$

$$\langle \mathbf{F}_r(t) \cdot \mathbf{F}_r(t') \rangle = 2k_B T \xi_S \delta(t - t') \quad (2.4)$$

where the last condition expresses the fluctuation-dissipation theorem [53]. The implementation of this approach for the study of many particle systems is available in several standard simulation software packages [54, 55].

Table 2.1: Relevant time scales for colloidal suspensions. a is the particle radius, ν is the kinematic viscosity of the fluid, v_s is the velocity of the fluid flow, M_c is the mass of a colloidal particle, ξ_S is the friction coefficient of the colloid particle and D is the colloid diffusion coefficient. From Padding et al., [51]

Solvent time scales	<i>Solvent collision time</i> over which solvent molecules interact	$\tau_{\text{col}} \sim 10^{-15} \text{ s}$
	<i>Solvent relaxation time</i> over which solvent velocity correlations decay	$\tau_f \sim 10^{-14} \div 10^{-13} \text{ s}$
Hydrodynamic time scales	<i>Kinematic time</i> over which momentum (velocity) diffuses one colloidal radius	$\tau_\nu = \frac{a^2}{\nu}$
	<i>Stokes time</i> over which a colloid converts over its own radius	$t_s = \frac{a}{v_s}$
Brownian time scales	<i>Brownian relaxation time</i> over which colloid velocity correlations decay	$\tau_B = \frac{M_c}{\xi_S}$
	<i>Colloid diffusion time</i> over which a colloid diffuses over its radius	$\tau_D = \frac{a^2}{D}$

Due to the small mass of the colloidal particles, inertia is negligible. This means that the relaxation time of the colloid to a stationary state is much smaller than the time scale of interest. Therefore, the total force can be assumed to be always zero [48, 56]. Equation 2.1 on the facing page can therefore be simplified by dropping the momentum terms and equating the RHS to zero, giving:

$$\mathbf{F}_f + \mathbf{F}_{\text{ext}} + \mathbf{F}_r = 0 \quad (2.5)$$

With the substitution for the \mathbf{F}_f term as given by 2.2 on the preceding page:

$$\xi_S \mathbf{v} = \mathbf{F}_{\text{ext}} + \mathbf{F}_r \quad (2.6)$$

Finally, by expressing the velocity as the positional derivative, the result for the equation of motion of a single particle is obtained:

$$\frac{d\mathbf{r}}{dt}(t) = \frac{1}{\xi_S} (\mathbf{F}_{\text{ext}}(t) + \mathbf{F}_r(t)) \quad (2.7)$$

A BD simulation is performed by integrating this equation forward in time. The stochastic nature of the equation means that one must produce many independent trajectories that are averaged together, producing the time evolution of an ensemble-averaged property [48, 49]. Obviously, neglecting the inertia terms puts some constraints over the accessible time scale, which cannot be smaller than the relaxation time τ_B (see Table 2.1).

The three different quantities that appear in Equation 2.7, namely ξ_S , \mathbf{F}_{ext} and \mathbf{F}_r , depend on the physical details of the system which is simulated. For the purpose of this study, the following phenomena have been accounted for:

- Intermolecular forces
- Particle-magnet magnetic interaction forces
- Particle-particle magnetic interaction forces
- Drag forces
- Hydrodynamic interactions

2.2 Static forces

In this section, the different models commonly used to describe the interactions between magnetic colloidal particles are described. These interactions enter in Equation 2.7 in the external force term \mathbf{F}_{ext} . For the rest of this chapter, a indicates the radius of the particle, \mathbf{r}_i indicates the position vector of a single particle i , $\mathbf{r}_{ij} = \mathbf{r}_i - \mathbf{r}_j$ and $r_{ij} = |\mathbf{r}_{ij}|$.

2.2.1 Magnetic interaction

The particles in this study are captured by the ferromagnetic matrix. The magnetic field generated by the rods exerts a force on the magnetic dipole exhibited by the particles, which is proportional to the field gradient. Given a magnetic field \mathbf{B} generated by the ensemble of rods, the force experienced by the particles has been already given in Chapter 1 and it is here restated:

$$\mathbf{F}_m = (\mathbf{m} \cdot \nabla)\mathbf{B} \quad (2.8)$$

where \mathbf{m} is the magnetic moment induced on the nanoparticles by the field \mathbf{B} . The ferromagnetic matrix can be modeled as a random packing of magnetic rods, which acquire a uniform magnetization in presence of the external field generated by the electromagnet. The magnetic field of the rods can be analytically expressed in terms of elliptic integrals, as well as its spatial derivatives. The description of the analytical form which has been implemented in the simulations is described in Chapter 3.

In addition to the force exerted by the rods (since the external magnetic field does not exert any force, see Chapter 1), the nanoparticles experience an interaction between their magnetic moments. As previously stated in Chapter 1, the particles are assumed to be superparamagnetic. The magnetic moment intensity acquired by the colloids as a function of the applied field \mathbf{H} is expressed by the Langevin equation (for symbols and units, see Chapter 3):

$$\mu(H) = n_d M_S V_d \mathcal{L} \left(\frac{V_d M_S H}{k_B T} \right) \quad (2.9)$$

As the particles are superparamagnetic, the direction of their magnetic moments will be parallel to the magnetic field \mathbf{H} . The interaction energy between two dipoles at positions \mathbf{r}_i and \mathbf{r}_j is given by [57]:

$$U^{\text{Dip}}(\mathbf{r}_{ij}, \boldsymbol{\mu}_i, \boldsymbol{\mu}_j) = -\frac{\mu_0}{4\pi} \left(\frac{3(\mathbf{r}_{ij} \cdot \boldsymbol{\mu}_i)(\mathbf{r}_{ij} \cdot \boldsymbol{\mu}_j)}{r_{ij}^5} - \frac{\boldsymbol{\mu}_i \cdot \boldsymbol{\mu}_j}{r_{ij}^3} \right) \quad (2.10)$$

where $\boldsymbol{\mu}_i$ and $\boldsymbol{\mu}_j$ represent the magnetic dipole moments of the particles. The force between the dipoles follows by the definition:

$$\mathbf{F}_{ij}^{\text{Dip}} = -\nabla_{\mathbf{r}_i} U(\mathbf{r}_{ij}, \boldsymbol{\mu}_i, \boldsymbol{\mu}_j) \quad (2.11)$$

The field \mathbf{H} in the Langevin equation 2.9 refers to the sum of the external field \mathbf{H}_{ext} and the field generated by the rods random packing. However, the dipole moment $\boldsymbol{\mu}_j$ of each particle will also generate a local magnetic field: if two particles come close to each other, their magnetic moment will be perturbed by the other particle. Schaller *et. al.* studied the dipole interactions by neighboring particles, proposing an iterative method to calculate the effective magnetic moment induced on the particles [34]. However, they showed that the correction factor becomes important only for applied external fields on the order of mT or smaller. Since the external field in the magnetic separation setup is always on the order of 1 T, the magnetic interactions in the calculation of the magnetic moment of the particles by Langevin equation are neglected.

2.2.2 Hard sphere interaction

The hard sphere (HS) interaction is an idealized pair interaction potential that describes impenetrable spheres that cannot overlap in space. Formally, the HS potential between two spheres at positions \mathbf{r}_i and \mathbf{r}_j is defined as follows [48]:

$$U^{\text{HS}}(r_{ij}) = \begin{cases} 0 & r_{ij} \geq 2a \\ \infty & r_{ij} < 2a \end{cases} \quad (2.12)$$

The particles cannot overlap and do not feel any influence by other particles unless they come into direct contact. The nanoparticles used in this study are assumed to exhibit a HS interaction when they are in direct contact. However, the integration of the equation of motion in the BD algorithm outlined in the previous section requires an expression for the force. Due to the discontinuity of the HS potential, U^{HS} as given above is not differentiable and cannot be directly implemented into the simulation algorithm.

A suitable alternative is provided by the so-called Mie(n, m) potential model [58]:

$$U^{\text{MIE}}(r_{ij}) = \left(\frac{n}{n-m}\right) \left(\frac{n}{m}\right)^{\frac{m}{n-m}} \epsilon_{\text{Mie}} \left[\left(\frac{2a}{r_{ij}}\right)^n - \left(\frac{2a}{r_{ij}}\right)^m \right] \quad (2.13)$$

where n and m are two integers with $n > m$. ϵ_{Mie} is the intermolecular energy parameter, for which $U_{\text{min}}^{\text{MIE}} = -\epsilon_{\text{Mie}}$ at position $r_{\text{min}} = 2a \left(\frac{n}{m}\right)^{\frac{1}{n-m}}$. The well known Lennard Jones (LJ) potential is derived from the Mie(m, n) potential by setting $n = 12$ and $m = 6$.

The Mie(m, n) potential presents both an attractive and repulsive part. The latter can be isolated by shifting the potential by the quantity corresponding to its minimum and equating it to zero at larger intermolecular distances. This results in the following potential:

$$u(r_{ij}) = \begin{cases} \left(\frac{n}{n-m}\right) \left(\frac{n}{m}\right)^{\frac{m}{n-m}} \epsilon_{\text{Mie}} \left[\left(\frac{2a}{r_{ij}}\right)^n - \left(\frac{2a}{r_{ij}}\right)^m \right] + \epsilon_{\text{Mie}} & r_{ij} < 2a \left(\frac{n}{m}\right)^{\frac{1}{n-m}} \\ 0 & r_{ij} \geq 2a \left(\frac{n}{m}\right)^{\frac{1}{n-m}} \end{cases} \quad (2.14)$$

The parameter ϵ_{Mie} has to be set according to the relevant energy scale which is to be reproduced in the simulation. The parameters n and m can be adjusted to properly mimic an hard sphere repulsion [59]. Figure 2.2 on the next page illustrates the change in shape of the potential $u(r_{ij})$ for different combinations of the parameters n and m .

2.3 Hydrodynamics

In this section, the different models commonly used to describe the hydrodynamics of a suspension of colloidal particles are described. For the rest of this chapter, a indicates the radius of the particle, \mathbf{r}_i indicates the position vector of a single particle i , $\mathbf{r}_{ij} = \mathbf{r}_i - \mathbf{r}_j$ and $r_{ij} = |\mathbf{r}_{ij}|$.

2.3.1 Hydrodynamic Interactions

A natural choice for the value of the friction coefficient ξ_S comes from the Einstein relation:

$$\xi_S = \frac{k_B T}{D} \quad (2.15)$$

where D ($\text{m}^2 \text{s}^{-1}$) stands for the translational diffusion coefficient of the colloidal particles (the rotational degrees of freedom are neglected, see one of the previous sections). Equation 2.7 on page 23 becomes:

$$\frac{d\mathbf{r}}{dt}(t) = \frac{D}{k_B T} (\mathbf{F}_{\text{ext}}(t) + \mathbf{F}_r(t)) \quad (2.16)$$

However, this choice implies that particles are non-interacting in an hydrodynamic sense. In reality, as a particle moves in the solvent, it exerts a force on it which perturbs the velocity field

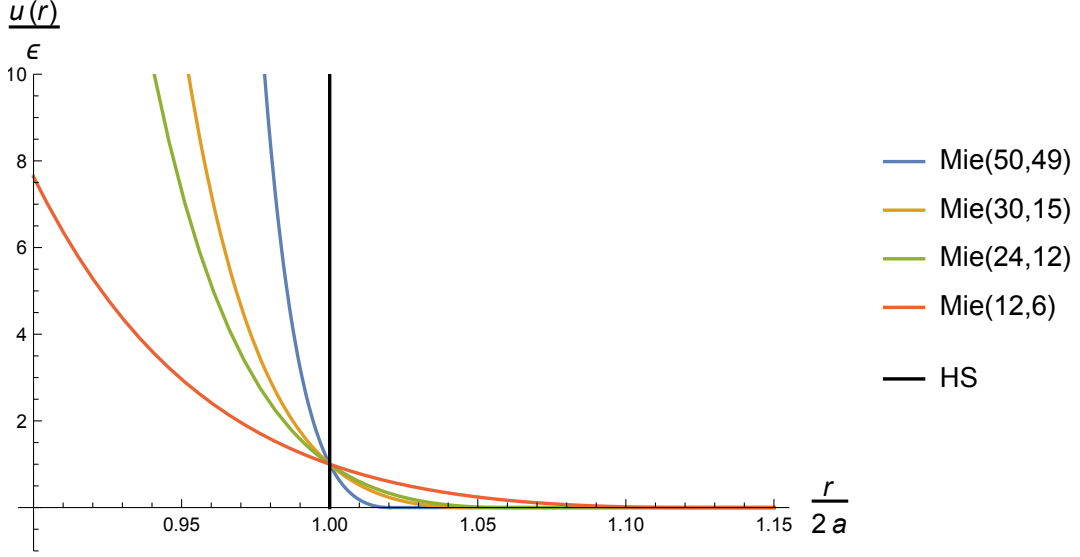


Figure 2.2: Different shifted Mie(n, m) potentials (Equation 2.14 and HS potential).

of the fluid. As a response, this changes the viscous drag force exerted on the other suspended particles. These interactions between particles mediated by the solvent are called *hydrodynamic interactions* (HI). The friction coefficient ξ_S is not a scalar anymore, but becomes a tensor. It must describe the dependence of the hydrodynamic force acting on a particle i as depending on all the other particles velocities. Schaller *et. al.* proved that a non-interacting model is not sufficient to catch the correct physical behavior of a solution of magnetic nanoparticles undergoing magnetophoresis [34]. Therefore, the inclusion of HI in a correct Brownian Dynamics algorithm is necessary.

As the solvent is treated implicitly in the BD simulation scheme, the HI interactions are accounted on the basis of the Navier-Stokes equations. For an incompressible fluid, these reduce to the following [52]:

$$\rho \frac{\partial \mathbf{u}(\mathbf{r}, t)}{\partial t} + \rho \mathbf{u}(\mathbf{r}, t) \nabla \mathbf{u}(\mathbf{r}, t) = \eta \nabla^2 \mathbf{u}(\mathbf{r}, t) - \nabla p(\mathbf{r}, t) + \mathbf{f}(\mathbf{r}) \quad (2.17)$$

with the *continuity equation*:

$$\nabla \cdot \mathbf{u}(\mathbf{r}, t) = 0 \quad (2.18)$$

Here, \mathbf{u} is the velocity field within the solvent, η (Pa.s) is its viscosity, ρ is its density, p is the pressure, and $\mathbf{f}(\mathbf{r})$ is the force density acting at a position \mathbf{r} . Moreover, neglecting inertial terms (the assumption is motivated, as usual, by the predominance of viscous terms for Brownian particles), Equation 2.17 further reduces to [52]:

$$\nabla p(\mathbf{r}, t) - \eta \nabla^2 \mathbf{u}(\mathbf{r}, t) = \mathbf{f}(\mathbf{r}) \quad (2.19)$$

Together with Equation 2.18, this equation fully determines the fluid flow and pressure once the external force and boundary conditions are specified.

Following Green's formalism, it is possible to show that the fluid flow and pressure due to an external force distributed over the fluid is given by [52]:

$$\mathbf{u}(\mathbf{r}) = \int d\mathbf{r}' \mathbf{T}(\mathbf{r} - \mathbf{r}') \cdot \mathbf{f}(\mathbf{r}') \quad (2.20)$$

$$p(\mathbf{r}) = \int d\mathbf{r}' \mathbf{g}(\mathbf{r} - \mathbf{r}') \cdot \mathbf{f}(\mathbf{r}') \quad (2.21)$$

with the Green's functions $\mathbf{T}(\mathbf{r})$ and $\mathbf{g}(\mathbf{r})$ given by:

$$\mathbf{T}(\mathbf{r}) = \frac{1}{8\pi\eta} \frac{1}{r} \left(\hat{\mathbf{I}} + \frac{\mathbf{r}\mathbf{r}}{r^2} \right) \quad (2.22)$$

$$\mathbf{g}(\mathbf{r}) = \frac{1}{4\pi} \frac{\mathbf{r}}{r^3} \quad (2.23)$$

where $\hat{\mathbf{I}}$ indicates the identity matrix. Here, the product $\mathbf{r}\mathbf{r}$ represents a dyadic product, and $\mathbf{T}(\mathbf{r})$ is consequently a tensor of rank 2 (i.e., a matrix).

The boundary conditions are the usual *stick boundary conditions*: it is assumed that the velocity of the fluid at the surface of the Brownian particles is equal to the velocity of the corresponding surface element on the particles' surface [52]. Moreover, the fluid is assumed to be at rest at long distances. In formal terms:

$$\mathbf{u}(\mathbf{r}) = \mathbf{u}' + \boldsymbol{\omega}' \times (\mathbf{r} - \mathbf{r}') \quad \forall \mathbf{r} \in S \quad (2.24)$$

$$\mathbf{u}(\mathbf{r}) \rightarrow 0 \quad \text{for } r \rightarrow \infty \quad (2.25)$$

where S denotes the surface of the particle and \mathbf{u}' and $\boldsymbol{\omega}'$ are the translational and rotational velocities of the particle respect to the fluid.

By solving Equation 2.20 on the preceding page with boundary conditions 2.24 and 2.25, the equations of motion for a colloidal particle can be derived. In particular, Stokes's equation for the drag force over a sphere moving with velocity \mathbf{v} can be retrieved:

$$\mathbf{F}_{\text{drag}} = -6\pi\eta a \mathbf{v} \quad (2.26)$$

The generalization to a system of N spheres follows naturally. The flow field for a many-particle system is given by:

$$\mathbf{u}(\mathbf{r}) = \sum_{i=1}^N \int d\mathbf{r}' \mathbf{T}(\mathbf{r} - \mathbf{r}') \cdot \mathbf{f}_i(\mathbf{r}') \quad (2.27)$$

where \mathbf{f}_i is the force density on the i -particle surface S_i . Boundary condition 2.24 is enforced for each particle surface S_i .

After some mathematical derivation, the equations of motion are given by the linear relation [52, 60]:

$$\mathbf{U} = \mathbf{D}\mathbf{S} \quad (2.28)$$

with:

$$\mathbf{U} = \begin{pmatrix} \mathbf{u}_1 \\ \dots \\ \mathbf{u}_N \end{pmatrix} \quad (2.29)$$

and

$$\mathbf{S} = \begin{pmatrix} \mathbf{F}_1 \\ \dots \\ \mathbf{F}_N \end{pmatrix} \quad (2.30)$$

Here, the quantities refer to the translational velocities and the forces acting on each particle i . The quantity \mathbf{D} is the *diffusion tensor*. The entries in the diffusion tensor have dimensions $\text{m}^2 \text{s}^{-1}$. The diffusion tensor is expressed as a series expansion in the inverse distance r_{ij} between two Brownian particles [52]. Therefore, numerous tensors are proposed in literature [61–63], depending on the leading order in the series expansion.

If HI are neglected, the tensor has the form:

$$\mathbf{D}_{ii} = \frac{k_B T}{6\pi\eta a} \hat{\mathbf{I}} \quad (2.31)$$

and $\mathbf{D}_{ij} = 0$ for $i \neq j$. At the next level, HI can be described by the the tensor 2.31 and:

$$\mathbf{D}_{ij} = \frac{k_B T}{8\pi\eta r_{ij}} \left(\hat{\mathbf{I}} + \frac{\mathbf{r}_{ij}\mathbf{r}_{ij}}{r_{ij}^2} \right) \quad (2.32)$$

for $i \neq j$. This is known as the *Oseen tensor*. It is known, however, that this last tensor is not positive definite when $r_{ij} < 2a$, i.e. when the particles are very close. Therefore, it produces wrong results if the solution is not very dilute and particles are expected to approach each other. The following level in the series expansion accounts for the finite size of the particles. \mathbf{D}_{ii} is given again by Equation 2.31 on the preceding page and:

$$\mathbf{D}_{ij} = \frac{k_B T}{6\pi\eta a} \begin{cases} C_1(r_{ij})\hat{\mathbf{I}} + C_2(r_{ij})\frac{\mathbf{r}_{ij}\mathbf{r}_{ij}}{r_{ij}^2} & r_{ij} > 2a \\ C_3(r_{ij})\hat{\mathbf{I}} + C_4(r_{ij})\frac{\mathbf{r}_{ij}\mathbf{r}_{ij}}{r_{ij}^2} & r_{ij} \leq 2a \end{cases} \quad (2.33)$$

with:

$$\begin{aligned} C_1(r_{ij}) &= \frac{3a}{4r_{ij}} + \frac{a^3}{2r_{ij}^3} & C_2(r) &= \frac{3a}{4r_{ij}} + \frac{3a^3}{2r_{ij}^3} \\ C_3(r_{ij}) &= 1 - \frac{9r_{ij}}{32a} & C_4(r_{ij}) &= \frac{3r_{ij}}{32a} \end{aligned}$$

This is known as the *Rotne-Prager-Yamakawa* (RPY) tensor, commonly used in Brownian Dynamics simulations where the series expansion is truncated at the 3rd order. It must be noted that this still represents an approximation. In the first place, only pairwise interactions between spheres are considered, assuming that three-body and higher order interactions are of negligible probability [52]. Secondly, the RPY still represents a truncation of the series expansion and only accounts for the far-field part of the true hydrodynamic tensor \mathbf{D} . The near-field part, which becomes dominant when the particle separation distance approaches zero, is not included. However, in this regime the dynamics of two neighboring particles moving relative to each other is dominated by *lubrication effects*. These originate from the strong velocity gradients of the flow field in the gap between the two spheres [64]. Neither the near-field or the lubrication effects have been included in this study. However, their inclusion is relatively straightforward as a linear addition to the far-field RPY tensor [65].

A new *Langevin* equation must be formulated for a system of N particles when HI are taken into account. Its derivation is mathematically involved. For the details, see [66]. The equation of motion is:

$$m \frac{d^2 \mathbf{r}}{dt^2} = - \sum_j \boldsymbol{\xi}_{ij} \frac{d\mathbf{r}_j}{dt} + \mathbf{F}_{\text{ext}} + \sum_j \boldsymbol{\alpha}_{ij} \mathbf{f}_j \quad (2.34)$$

with

$$\langle \mathbf{f}_i(t) \rangle = 0 \quad (2.35)$$

$$\langle \mathbf{f}_i(t) \mathbf{f}_j(t') \rangle = 2\delta_{ij} \delta(t - t') \boldsymbol{\delta} \quad (2.36)$$

The last term in the RHS of the previous equation represents the random force due to particle-solvent interaction. The summation is needed since the random forces acting on different particles are coupled, as a consequence of HI. The entries in the friction tensor $\boldsymbol{\xi}$ have dimension kg s^{-1} . The friction tensor is related to the diffusion tensor \mathbf{D} by the relation:

$$\sum_l \boldsymbol{\xi}_{il} \mathbf{D}_{lj} = k_B T \delta_{ij} \quad (2.37)$$

where δ_{ij} is the Kronecker delta. The entries in the tensor $\boldsymbol{\alpha}$ have dimension is related to the friction tensor by:

$$\boldsymbol{\xi}_{ij} = \frac{1}{k_B T} \sum_l \boldsymbol{\alpha}_{il} \boldsymbol{\alpha}_{lj} \quad (2.38)$$

By assuming that the time scales for momentum relaxation and position relaxation of the Brownian particles are well separated, as in the preceding sections, Equation 2.38 can be further

simplified. However, the differentiation in order to obtain a concise expression for $\mathbf{r}_i(t)$ is rather subtle [67]. The final result follows [68]:

$$\frac{d\mathbf{r}_i}{dt} = \sum_j \frac{\mathbf{D}_{ij}\mathbf{F}_j^{\text{ext}}}{k_B T} + \sum_j \nabla_{\mathbf{r}_j} \cdot \mathbf{D}_{ij} + \sqrt{2} \sum_j \mathbf{B}_{ij}\mathbf{w}_j \quad (2.39)$$

with:

$$\langle \mathbf{w}_i(t) \rangle = 0 \quad (2.40)$$

$$\langle \mathbf{w}_i(t)\mathbf{w}_j(t') \rangle = \delta_{ij}\delta(t-t')\boldsymbol{\delta} \quad (2.41)$$

and

$$\sum_l \mathbf{B}_{il}\mathbf{B}_{jl}^T = \mathbf{D}_{ij} \quad (2.42)$$

A numerical discretization scheme for Equation 2.39 is given in the following section.

2.3.2 Drag forces

The hydrodynamic characterization of the problem outlined in the previous section strictly holds for a quiescent fluid. However, in the magnetic separation setup, a constant uniform flow is imposed to the solution (see Chapter 1). Moreover, the presence of the ferromagnetic matrix in the separation chamber creates disturbances to the uniformity of the flow. This flow causes an additional drag force on the particles. If the fluid possesses an inhomogeneous flow field, the problem becomes very involved. The nature of the hydrodynamic interactions is, indeed, changed due to the flow. In general, the hydrodynamic force acting on a particle i becomes [52]:

$$\mathbf{F}_i^h = - \sum_j \boldsymbol{\xi}_{ij} \left(\frac{d\mathbf{r}_j}{dt} - \mathbf{u}_0(\mathbf{r}_j) \right) + \mathbf{C}_i(\mathbf{r}_i, \dots, \mathbf{r}_N, \mathbf{u}_0(\mathbf{r}_i)) \quad (2.43)$$

where \mathbf{u}_0 is the flow field (which is position-dependent) and \mathbf{C}_i quantifies the fluid flow disturbance due to the other Brownian particles. \mathbf{C}_i has the dimension of a force. An analytical expression of \mathbf{C}_i constitutes a challenging hydrodynamic problem: solutions are given, at present, only for linear flows [52, 61, 67].

The inhomogeneity of the field can be however disregarded by assuming a locally uniform flow field. This approximation can be justified by noting that the rod length scale ($\sim 10^{-4}$ m) is separated from the particle length scale ($\sim 10^{-8}$ m). Therefore, the inhomogeneities in the field flow take place on a much larger length scale than the typical interparticle distance. Thus, the particles can be considered to be immersed in a fluid with a homogeneous flow velocity $\mathbf{u}_0(\mathbf{r})$ which depends on the particle positions but is approximately uniform in their vicinity where hydrodynamic interactions with other particles are important. Following this approach, the problem is considerably simplified and the hydrodynamic force acting on a particle i becomes:

$$\mathbf{F}_i^h = - \sum_j \boldsymbol{\xi}_{ij} \left(\frac{d\mathbf{r}_j}{dt} - \mathbf{u}_0(\mathbf{r}_j) \right) \quad (2.44)$$

The form of the equations derived in the previous section remains unaffected by the addition of the solvent flow. The only difference is that the velocities are to be taken relative to the flow velocity field. Therefore, the entire analysis of hydrodynamic interactions between particles in an otherwise quiescent fluid still holds. In terms of Equation 2.39, the addition of the solvent drag forces induced by a flow field reduces to the following result (obtained by substituting the absolute velocities of the particles with the velocities relative to the fluid):

$$\frac{d\mathbf{r}_i}{dt} = \sum_j \frac{\mathbf{D}_{ij}\mathbf{F}_j^{\text{ext}}}{k_B T} + \sum_j \nabla_{\mathbf{r}_j} \cdot \mathbf{D}_{ij} + \sqrt{2} \sum_j \mathbf{B}_{ij}\mathbf{w}_j + \mathbf{u}_0(\mathbf{r}_i) \quad (2.45)$$

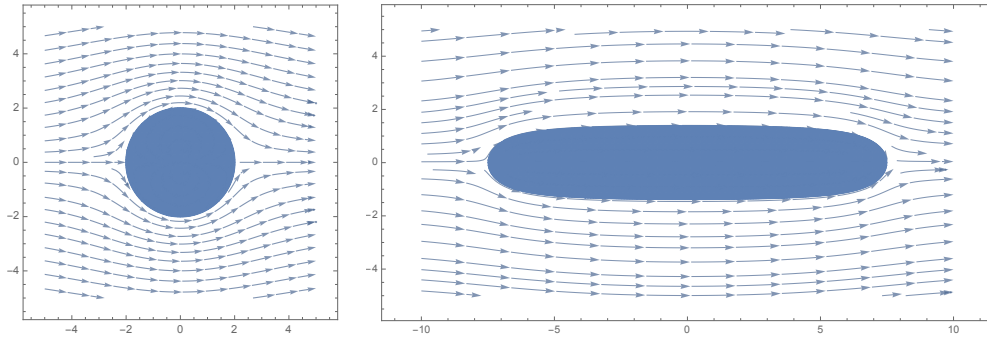


Figure 2.3: Streamlines plot for the 2D flow field past an infinite cylinder placed with its axis perpendicular to the flow (on the left) and a Rankine Oval with its axis parallel to the flow (on the right). For the definition of Rankine Oval bodies, see Appendix A

The flow velocity field can be obtained by solving the Navier-Stokes equations with suitable boundary conditions. The problem is usually involved, although analytical solutions exist for particularly convenient geometries. In this study, magnetic rods are used in the separation matrix. Thus, a solution for a body exhibiting a cylindrical geometry is needed.

Theoretical expressions exist for the limit cases of a flow perpendicular to the cylinder long axis (2D solution) and for a flow parallel to the cylinder long axis (2D solution). The former case can be solved analytically: the derivation is given in Appendix A. For the latter case, however, no analytical solution can be formulated due to the geometry discontinuity at the edges of the cylinder. An approximation for a long cylinder is represented by the *Rankine oval*, for which an analytical solution exists. For the definition of Rankine oval bodies, see Appendix A. For a flow perpendicular to the cylinder long axis, an approximate 3D solution can be obtained under some assumptions. For a flow parallel to the cylinder long axis, a 3D exact solution is available as a generalization of the 2D solution. The discussion and the analytical equations for the velocity fields are given in Appendix A. Figure 2.3 shows the streamlines for the 2D solutions of the two cases presented above.

In this study, an approximate solution to the flow past an array of cylinders is obtained by superimposing the flow fields of the single cylinders and invoking the linearity of Navier-Stokes equations. As the axis of a single rod can have any arbitrary orientation with respect to the flow direction, a suitable combination of the two limit solutions presented above (flow perpendicular and parallel to the cylinder axis) has to be adopted. The cartesian decomposition of the flow direction into two components, respectively parallel and perpendicular to the rod axis, is proposed for a quantitative description of the flow past an arbitrary oriented cylinder. The flow vector \mathbf{u}_0 obtained by such solution strategy is then implemented into Equation 2.45.

2.4 Simulation algorithm and numerical methods

In this section, the simulation scheme implemented to solve the equations of motion outlined in the previous sections is illustrated. Its validation and the numerical methods used within the algorithm (cut-off, speed-ups, reduced units, etc.) are discussed. Without loss of generality, Equation 2.45 will be referred as the equation of motion which is to be integrated. The \mathbf{F}^{ext} term includes the interaction forces as discussed in the section 2.2. Throughout this section, N indicates the number of colloidal particles in the simulation, M the number of rods in order to simulate the ferromagnetic matrix.

2.4.1 Simulation scheme

To obtain an integration scheme for Equation 2.45, the equation is integrated over time. Choosing a suitable time interval Δt , the following is obtained [69]:

$$\mathbf{r}_i(t + \Delta t) = \mathbf{r}_i(t) + \sum_j \frac{\mathbf{D}_{ij} \mathbf{F}_j^{\text{ext}}}{k_B T} \Delta t + \mathbf{u}_0(\mathbf{r}_i(t)) \Delta t + \mathbf{R}_i(\Delta t) \quad (2.46)$$

The RPY tensor is used as the diffusion tensor \mathbf{D} . This tensor has the notable property [69]:

$$\sum_j \nabla_{\mathbf{r}_j} \cdot \mathbf{D}_{ij} = 0 \quad (2.47)$$

thus eliminating one term in the integration of Equation 2.45 and greatly simplifying the calculations.

The term \mathbf{F}^{ext} is calculated as:

$$\mathbf{F}_j^{\text{ext}} = \sum_{l=1}^M \mathbf{F}_l^{\text{magn}} + \sum_{i \neq j} \mathbf{F}_{ij}^{\text{dip}} + \sum_{i \neq j} \mathbf{F}_{ij}^{\text{HS}} \quad (2.48)$$

where $\mathbf{F}_l^{\text{magn}}$ is the interaction of the particle with the ferromagnetic rods (the sum is performed over all the different rods), $\mathbf{F}_{ij}^{\text{dip}}$ represents the dipole interaction term between the particle magnetic moments and $\mathbf{F}_{ij}^{\text{HS}}$ represents the pseudo hard-sphere interaction terms between the particles. The integration scheme is known as the Ermak-McCammon algorithm and is very common in BD simulations with HI.

The random vector \mathbf{R}_i satisfies the properties:

$$\langle \mathbf{R}_i \rangle = 0 \quad (2.49)$$

$$\langle \mathbf{R}_i(\Delta t) \mathbf{R}_j(\Delta t) \rangle = 2\mathbf{D}_{ij} \Delta t \quad (2.50)$$

The standard method for the calculation of these random vectors is by evaluating:

$$\mathbf{R}_i = \sqrt{2\Delta t} \sum_{j=1}^N \mathbf{C}_{ij} \mathbf{v}_j \quad (2.51)$$

where \mathbf{v}_j is a vector of normally distributed random numbers and \mathbf{C} is a lower triangular matrix called *Cholesky factor* that satisfies the relation:

$$\mathbf{D} = \mathbf{C}\mathbf{C}^T \quad (2.52)$$

The Cholesky factor is calculated from the tensor \mathbf{D} via a linear algebra procedure called Cholesky decomposition. Several algorithms are established for performing such operation [70]. As it involves relatively straightforward algebraic operations, an in-built subroutine optimized on the algorithm has been implemented in our simulation algorithm. In the Ermak-McCammon scheme, the determination of the random displacements via the Cholesky decomposition represents the most computationally intensive step, resulting in a runtime of $\mathcal{O}(N^3)$.

The Cartesian coordinate system is adopted. The ferromagnetic matrix is represented by a random array of equal cylinders with arbitrary orientation. A uniform external field $\mathbf{H}_{\text{ext}} = (H, 0, 0)$ is applied to the system. The rods are magnetized according to their orientation respect to the external field, according to the Stoner-Wohlfart magnetization model. For the details of such implementation, see Chapter 3. The magnetic field of the rods is expressed using the elliptic integrals formalism. Numerical methods that compute elliptic integrals of the 1st, 2nd and 3rd kind with good precision are available in literature [70, 71]. The standard Carlson's method has been implemented in the algorithm.

The cylinders are considered impenetrable to the particles. When a particle is captured by one of the rods, its overall force is set to zero and it is considered permanently stuck to the

Table 2.2: Quantities of interest and reduced units

Quantity	Unit
Distance	$x^* = \frac{x}{100a}$
Force	$F^* = \left(\frac{100a}{\epsilon}\right) F$
Viscosity	$\nu^* = \left(\frac{(100a)^2}{(10^6 m \epsilon)^{1/2}}\right) \nu$
Magnetic field	$B^* = \left(\frac{a^2}{100\epsilon}\right) B$
Magnetic dipole moment	$\mu^* = \left(\frac{10^2}{a^2}\right) \mu$
Time	$t^* = \left(\frac{\epsilon}{10^{10} m a^2}\right)^{1/2}$
Diffusion coefficient	$D^* = \left(\frac{10^2 m}{\epsilon a}\right)^{1/2}$

rod for the rest of the simulation. This approach is employed on the basis of the following qualitative argument. Two competing forces act on a particle trapped on the surface of the rod: the viscous drag force exerted by the flowing solvent and the magnetic force exerted by the rod. The drag force can be estimated by [36]:

$$\mathbf{F}_{\text{drag}} = 6\pi\eta a \mathbf{u}_0 \quad (2.53)$$

assuming a constant flow in time. Let us assume that the ferromagnetic rods are ordered in an array: the average distance between them can be estimated by the matrix volume fraction. For the fibers used in the setup, a loose mean pore size is estimated to be in the range 50 μm to 200 μm , depending on the aspect ratio. Furthermore, let us assume that the flow between the rods is parallel to their axes. The pore can be thus modeled as a channel and the flow inside it can be described by a Poiseuille flow [72]:

$$u(s) = u_{\text{max}} - \frac{u_{\text{max}}}{H^2} s^2 \quad (2.54)$$

where H is half the separation distance between the rod's surfaces, s is the distance from the centerline of the channel and $u_{\text{max}} = 2\bar{u}$ with \bar{u} indicating the average flow velocity in the channel. This last quantity can be estimated by a measure of the flow velocity through the separation column. A typical value is 15 mL min^{-1} .

With the correct numerical values, an approximate magnitude of $|\mathbf{F}_{\text{drag}}| \sim 10^{-15}$ N is obtained. On the other hand, simulations give an approximate value of $|\mathbf{F}_{\text{m}}| \sim 10^{-7}$ N for the magnetic force acting on the particle trapped at the rod surface. Due to the difference in magnitude, particles are therefore expected to remain stuck to the magnetic rods. It should be noted, however, that this argument represents a magnitude estimation and it is not intended to provide a quantitative comparison between the magnetic force and the real drag experienced by the particles on the rod's surface.

2.4.2 Reduced units and parameters

In order to reduce the numerical errors associated with the simulations, as well as providing a meaningful comparison between different simulations, reduced units have been implemented for the interesting quantities in the system. Table 2.2 illustrates the principal quantities used in the study with their reduced units. The quantities a , m and ϵ are expressed in SI units of measure. ϵ represents a energy scale for the simulation. It has been set as $\epsilon = 100 k_{\text{B}}T$, where $k_{\text{B}}T$ is expressed in SI units of measure.

Table 2.3: Input parameters

Quantity	Symbol
Length of the rods	L
Radius of the rods	R
Particle diffusion coefficient	D
Saturation magnetization of the particle	M_s^{part}
Saturation magnetization of the rods	M_s^{rods}

The Mie(n, m) parameters have been set to $n = 30$ and $m = 15$. The value of ϵ_{Mie} in the Mie potential formulation represents a typical interaction energy scale and has thus been chosen to be:

$$\epsilon_{\text{Mie}} = \mu_0 \frac{\mu(H)^2}{32\pi a^3} \quad (2.55)$$

which represents the magnetic interaction energy between two particles of radius a in contact. For the stability of the simulation, the time step $\Delta t = 10^{-6}$ s has been chosen. This provides a good balance between a stable algorithm in terms of forces and dynamic steps and a reasonable computational time for meaningful simulation intervals.

A number of parameters are necessarily declared at the beginning of the simulation. These settings configure the cylinders and the particles. Table 2.3 gives the list of input parameters which are assigned to each simulation.

Together with the parameters that set the necessary dimensions and properties for both the rods and the nanoparticles, the initial configuration of the ferromagnetic matrix and the nanoparticles is needed. The initial positions of the nanoparticles are assigned via an initialization algorithm. Several different initial configurations are possible, depending on which region of the ferromagnetic matrix (and which initial concentration) is to be sampled.

The configuration of the ferromagnetic matrix is declared by assigning the number of rods which will form the random packing as well as their orientation in space. Due to the different rod orientations, an efficient way of expressing and superimposing their magnetic fields is needed for calculating the global magnetic field acting on each particle. In the algorithm, a global coordinate system is set. Successively, each rod is assigned a local coordinate integral with the rod's longitudinal axis, in which the relevant equations of the magnetic field are expressed. Once this has been performed, the field is expressed in the global coordinate system. In conclusion, the procedure employed for the calculation of the magnetic field generated by the ferromagnetic matrix is explained in Algorithm 1. In Appendix B the mathematical formulas for the operators R and R^{-1} for the magnetic field vector and the magnetic field derivative matrix are given in their explicit form. For the expression of the field \mathbf{B} and the derivative matrix $d\mathbf{B}$ in different coordinate systems, refer to Chapter 3.

2.4.3 Speed-ups and cut-offs

The algorithm as explained in the previous section, although computationally solid, has a principal drawback in the computational time required for the simulation of even small systems ($N < 100$). In particular, there are three aspects which drastically increase the computing time:

- The calculation of the Elliptic Integrals at every time step. In particular, at each time step there are $3N_{\text{part}}N_{\text{rods}}$ (on for each kind of elliptic integrals) numerical evaluation of the Carlson's routine, which is known to be computationally intensive.
- The evaluation of the pair-wise magnetic and pseudo-HS interactions, which involve $N_{\text{part}}(N_{\text{part}} - 1)$ calculations at each time step.

Algorithm 1 Procedure for the calculation of the magnetic field and derivatives generated by the ferromagnetic matrix on each nanoparticle. \mathbf{B}_i^{tot} stands for the field vector, $d\mathbf{B}_i^{tot}$ stands for the derivative matrix, operator R stands for the rototranslation operation from local to global coordinate system, operator R^{-1} stands for the rototranslation operation from global to local coordinate system, operator B stands for the magnetic field vector calculation, operator dB stands for the magnetic field derivative matrix calculation.

```

for  $i \leftarrow 1, N_{part}$  do
   $\mathbf{B}_i^{tot} \leftarrow 0$  ▷ Set the total field vector and derivative matrix to zero
   $d\mathbf{B}_i^{tot} \leftarrow 0$ 
end for
for  $k \leftarrow 1, N_{rods}$  do
  for  $i \leftarrow 1, N_{part}$  do
     $\mathbf{r}'_i \leftarrow R^{-1}(\mathbf{r}_i)$  ▷ Obtain the particle's coordinates in the local coord system
     $\mathbf{B}_i'^k = B(\mathbf{r}'_i)$  ▷ Calculate the magnetic field and derivatives in the local coord system
     $d\mathbf{B}_i'^k = dB(\mathbf{r}'_i)$ 
     $\mathbf{B}_i^k = R(\mathbf{B}_i'^k)$  ▷ Obtain the magnetic field and derivatives in the global coord system
     $d\mathbf{B}_i^k = R(d\mathbf{B}_i'^k)$ 
     $\mathbf{B}_i^{tot} \leftarrow \mathbf{B}_i^{tot} + \mathbf{B}_i^k$  ▷ Iteratively calculate the total field vector and derivative matrix
  for each particle
     $d\mathbf{B}_i^{tot} \leftarrow d\mathbf{B}_i^{tot} + d\mathbf{B}_i^k$ 
  end for
end for

```

- The evaluation of the hydrodynamic interactions. These are computed with a runtime of $\mathcal{O}(N^3)$ (due to the Cholesky factorization) and are thus known to be the general bottleneck for the Ermak-McCammon scheme in a BD algorithm [73].

In order to optimize the algorithm, implementations have been carried on for each one of these three critical steps.

The Carlson's method for the evaluation of the elliptic integrals has been replaced with a faster method proposed by Fukushima [74, 75]. The equivalence of the two methods, already claimed in the relevant papers, has been tested independently up to the 10th decimal, resulting in a complete agreement.

In order to reduce the HI's evaluation via Cholesky decomposition, Geyer and Winter proposed an approximation that is less computationally involved and only approximates the hydrodynamic coupling for the random forces in the simulation [76]. In this way, HI is computed with a runtime of $\mathcal{O}(N^2)$. The method, called TEA-HI, can however lose accuracy when the particles approach each other. This approach has been implemented in our algorithm, where is possible to choose whether to adopt the Cholesky decomposition or TEA-HI method for computing hydrodynamic interactions. The former will be referred to as the EMC scheme. Tests on the equivalence of the methods have been made on both the implementations in the case of a dilute suspension or a concentrated one.

Figure 2.4 on the facing page shows the computation of the particle diffusion coefficient for a dilute system ($c = 10^{-6}$ mg mL⁻¹) of $N = 100$ particles of radius $a = 125$ nm without any external force applied. The comparison between the measured diffusion coefficient and the theoretical diffusion coefficient of an ideal-non interacting suspension of particles is reported. Both the algorithm correctly retrieve the theoretical result, proving the correctness of the simulations for dilute systems. In particular, the EMC scheme and the TEA-HI scheme are in exceptionally good agreement. In order to compare the TEA and EMC scheme for when the interparticle distance is expected to be small (e.g., in a concentrated suspension), simulations were performed on systems of magnetic nanoparticles in an uniform magnetic field. Several experimental and simulations studies have shown that, under this conditions, the formation of

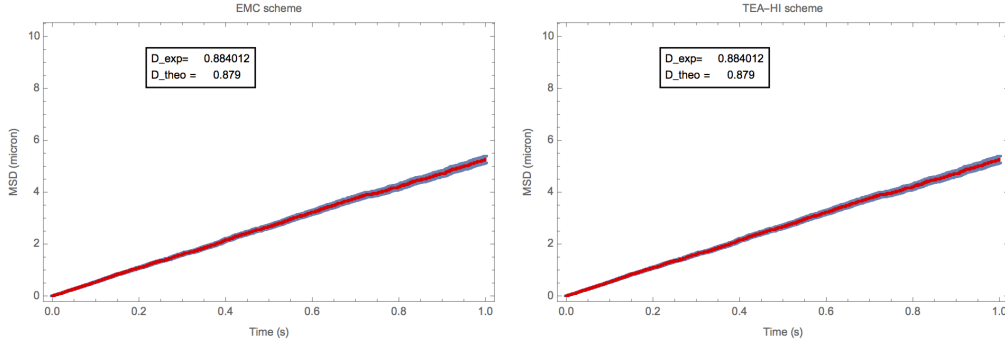


Figure 2.4: Average particle diffusion coefficient for a system of $N = 100$ particles of radius $a = 125$ nm in water ($\eta = 1$ mPas). The standard errors are reported in the graphs. In the box, D_{theo} refers to the Einstein's formula $D = k_B T / 6\pi\eta a$

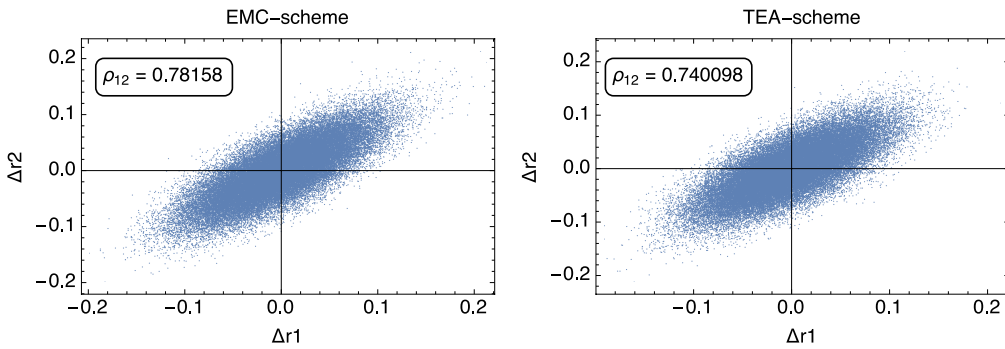


Figure 2.5: Correlation plots of one-dimensional displacements of neighbors in a chain of $N = 8$ particles of radius $a = 100$ nm in water ($\eta = 1$ mPas). The two axes report the displacements of the two particles. In the box, ρ_{12} indicates the correlation coefficient calculated from the scatter data.

linear aggregates (or chains) is observed [77, 78].

The hydrodynamic coupling of the displacements of two particles which are neighbors in the chain provides a good comparison between the EMC and the TEA scheme. A simple measure of it is provided by the correlation coefficient ρ_{12} of two one-dimensional displacements:

$$\rho_{12} = \frac{\text{cov}(\Delta r_1, \Delta r_2)}{\sigma_{\Delta r_1} \sigma_{\Delta r_2}} \quad (2.56)$$

where cov indicates the covariance between the variables and σ indicates the standard deviation. Figure 2.5 shows the correlation coefficients calculated for a chain of $N = 8$ particles of radius $a = 100$ nm. The coefficient for the EMC scheme proves to be slightly higher. This was expected, since the TEA scheme only approximates the true hydrodynamic interactions as evaluated in the EMC scheme, underestimating the coupling between the particles displacements. However, it can be seen that even in the present case of touching spheres, where the correlation is strongest, TEA's underestimation is less than 5%. TEA scheme can therefore also be adopted in simulations of concentrated solutions.

The evaluation of the magnetic interactions can be speeded up by applying a cut-off: if the distance between the particles is larger than a threshold value, the interactions are neglected and the calculations are not performed. The application of a cut-off is well known to be an approximation that often leads to errors, in particular if the interaction energy to which is applied has a long-range nature [48]. However, the magnetic dipole-dipole interaction energy scales as $\sim 1/r^3$. It is therefore possible to apply a cut-off with almost no errors involved.

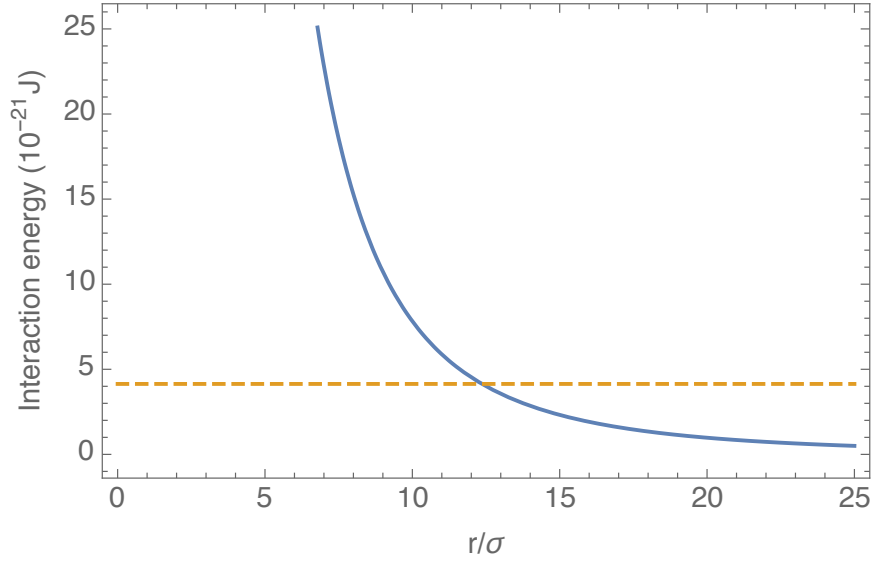


Figure 2.6: Interaction energy between head-tail aligned magnetic dipoles for particles of radius $r = 250 \text{ nm}$ and $\mu = 2.21 \times 10^{-3} \text{ A}\mu\text{m}^{-1}$. The magnitude of μ is evaluated from nanoparticle specifics as given in [34]. The dashed line represents the thermal energy $k_{\text{B}}T$ at room temperature.

A proper threshold value must, however, be set. Figure 2.6 shows a sketch of the maximum interaction energy as a function of the distance between two nanoparticles with magnetic dipoles of the same magnitude μ for particles of radius $r = 250 \text{ nm}$ (the maximum size considered in this current study). The magnitude μ is taken to be the maximum value attainable within the Langevin model for the nanoparticle magnetization, $\mu_{\text{max}} = n_{\text{d}}M_{\text{s}}V_{\text{d}}$. The maximum interaction energy is reached when the dipole moments are placed in a head-tail configuration. The dipole moments are taken to be of the same magnitude because, due to the strong external field applied in the magnetic separation setup, there is an extremely slow variation in space of $\mu(H, \mathbf{r})$.

Figure 2.6 shows that, even for the largest particles studied, the magnetic dipole-dipole interaction energy becomes smaller than the thermal energy for $r > 10\sigma$, where σ is the particles diameter. Therefore, the cut-off radius is set to $r_{\text{cutoff}} = 15\sigma$. This value is in agreement with other cutoff distance as suggested in other studies [78].

Chapter 3

The magnetic field of a cylinder: theory

This chapter illustrates the equations that describe the magnetic field of a cylindrical magnet of finite length with arbitrary uniform magnetization. The final formula represents the exact analytical solution of the magnetostatic problem of finding the magnetic field generated by an assigned uniform magnetization inside a cylindrical domain. The equations make use of the elliptic integrals formulation. Finally, the formula is validated against the well known limits of an infinitely long cylinder and the field on the axis of the cylinder.

The equations here presented are quite general and apply to several different situations and problems. As an example, they can be successfully used to describe bodies with composite geometries, as spherocylinders or hollow cylinders. In addition, the description of complex configurations, as a random packing of cylinders of arbitrary uniform magnetization, is possible.

3.1 Introduction

The simulation of a magnetic separation process is a task that encompasses several different fields and requires the definition of a broad array of details. Apart of the characterization of the magnetic particles and the interaction forces that act between them, it is necessary to give an effective expression for the external magnetic field that acts on the particles. While applying an uniform field (or, more correctly, a uniform field gradient) is the simplest and, by far, the easiest situation to handle, the separation field generated by a random packing of ferromagnetic rods is a really challenging task (Figure 3.1 on the following page). In fact, a proper expression for the magnetic field generated by a single magnetized rod represent the basis: its extension to a multibody configuration constitutes the next step.

While the numerical simulation of the mentioned fields is possible [42], a preference is obvious toward an analytical solution, which should still be suitable for computational purposes. It is clear, though, that the complex geometry represented by a random packing of (several) objects forces to adopt some simplifications, or rather to take some assumptions. We decided to consider our rods as uniformly magnetized cylinders. In this way, we can ignore the highly non trivial problem of determining the exact magnetization pattern of the rod, and we can still make use of a simple geometric form (the cylinder).

The problem to be solved, therefore, is to determine the magnetic field generated by an uniform magnetized cylinder. An arbitrarily oriented magnetization vector can be decomposed on its longitudinal and transverse components. In cylindrical coordinates, this reads:

$$\mathbf{M} = M_l \hat{z} + M_t \hat{\rho} \quad (3.1)$$

where \mathbf{M} represents the magnetization vector and M_l and M_t are respectively the longitudinal and transversal components of the magnetization respect to the cylinder axis of symmetry.



Figure 3.1: Separation matrix in a magnetic separation setup. The matrix is composed by ferromagnetic rods made of AluChrom O® from ThyssenKrupp VDM

The exact solution for the magnetic field created by a longitudinally magnetized cylinder is a standard result in electromagnetism [79] and a number of papers are already present in literature [80–82]. In particular, we make use of the expression reported in [80] due to its effectiveness in computational calculations.

On the other side, the magnetic field of a transversally magnetized is scarcely treated in literature and, to our knowledge, only the two-dimensional analytical result for an infinitely long cylinder is present [10, 11]. We therefore derived the exact analytical solution for the magnetic field created by a uniformly transversally magnetized cylinder making use of the formalism of the elliptic integrals.

The general solution for an arbitrarily magnetized cylinder is then presented as the vectorial sum of the two solutions for the longitudinal and transversal case. In the following sections, the expressions for the field will be stated. Before proceeding with the equations, however, an explanation for the adoption of such model in the framework of this study (a magnetic separation setup) is given.

3.1.1 The magnetization of a rod in an external field

In the current study, the ferromagnetic matrix in the separation chamber is subjected to an uniform external field \mathbf{H}_{ext} : in these conditions, the rods acquire a magnetization, which in turn induce a non-uniform magnetic field \mathbf{B}_{ind} . This last field is responsible for the real separation mechanism. The magnetization direction and intensity will depend on the nature of the material under consideration. The magnetization of linear materials is well discussed in classical electromagnetism [24, 25]. The magnetization \mathbf{M} , in this case, is proportional to the applied external magnetic field \mathbf{H} :

$$\mathbf{M} = \chi \mathbf{H} \quad (3.2)$$

where χ is a constant of the material called *magnetic susceptibility*. On the other side, when the material is ferromagnetic or, in general, non-linear, (3.2) is no longer valid. It is, though, possible to define an effective susceptibility, χ_a [24]. In this case, equation (3.2) can still be applied, provided that the effective susceptibility is used in the formulation.

In general, however, the non-linear magnetization curve is separated into two specific regions [83]: the linear and the saturated region. In the linear region, the magnetization is related to the applied field through equation (3.2). χ_a takes now into account the *demagnetization tensor*

\mathbf{N} [83]. A discussion on the demagnetization tensor will follow in one of the next sections. In the saturated region, the magnetization \mathbf{M} reaches a maximum value M_s since the applied field is high enough to align the maximum number of magnetic dipoles of the materials. The magnetization vector rotates to minimize the magnetic energy of the body [24] and a simple relationship to the external field \mathbf{H} is no longer possible.

Assuming a simple domain inside the magnet (uniform magnetization), it is possible to describe a single rod's magnetization by the Stoner-Wohlfart model [84].

This gives a constrained minimization problem for determining the magnetization vector \mathbf{M} [85]:

$$\min_{\mathbf{M} \in \mathbb{R}^3} \frac{\mu_0}{2} \mathbf{M}^T \mathbf{N} \mathbf{M} - \mu_0 \mathbf{H}^T \mathbf{M} \quad (3.3)$$

$$\text{subject to } \mathbf{M}^T \mathbf{M} - M_s^2 = 0 \quad (3.4)$$

Common numerical software that executes constrained minimization problems can be used to find the magnetization \mathbf{M} given the rod orientation relative to the applied field \mathbf{H} . The demagnetization tensor for the rod is taken as the demagnetization tensor of an infinitely long ellipsoid [86]:

$$\mathbf{N} = \text{diag}\left(\frac{1}{2}, \frac{1}{2}, 0\right) \quad (3.5)$$

in a reference frame where the z axis is the axis of the cylinder. This expression is exact for ellipsoidal bodies but not strictly for a cylinder [24]. However, since the rods which are described here have a very large aspect ratio, they can be viewed as long ellipsoidal bodies: Equation 3.5 is therefore valid to a good degree of approximation. Following this approach, the magnetization can be decomposed in two components. The first one is relative to the axis when the demagnetization tensor shows its minimum, called *easy axis*. In the case in study, it corresponds to the longitudinal component (parallel to the z axis of the rod). The second one is relative to the axis when the demagnetization tensor shows its maximum, called *hard axis*. In the case in study, both the x and the y axis of the rod shows the same demagnetization factor (a conclusion that can be drawn from symmetry reasons). Therefore, the decomposition on the hard axis happens to induce a component on the plane perpendicular to the cylinder long axis, whose direction is parallel to the \mathbf{H} component on the same plane. In summary, given an arbitrary external field \mathbf{H} and a rod with a longitudinal axis \mathbf{u} , the following model for the rod magnetization is adopted:

1. \mathbf{H} is expressed in the local coordinate system of the rod. This local system has its z' axis parallel to \mathbf{u} and arbitrary orientation of x' and y' axis.
2. The new field, \mathbf{H}' induces a magnetization vector \mathbf{M} for the rod according to the Stoner-Wohlfart model with the demagnetization tensor \mathbf{N} as given in Equation 3.5.
3. The vectorial sum of the magnetization vector components on the x' and y' axis gives a vector with direction $\hat{\rho}$ on the plane perpendicular to \mathbf{u} .
4. The magnetization vector can be thus described as $\mathbf{M} = M_l \hat{z} + M_t \hat{\rho}$ with the axes as described.

This procedure outlines a situation as the one described in Equation 3.1. The problem to be solved, therefore, is the determination of the induced field \mathbf{B}_{ind} generated by such configuration. The solution to this problem is presented in the following section.

3.2 The field of a longitudinally magnetized cylinder

The magnetic field of a longitudinally magnetized cylinder is equivalent to the magnetic field of an ideal solenoid. This follows from simple magnetostatics considerations [25]. It is

sufficient to make the following substitution:

$$M \equiv nI \quad (3.6)$$

where $M = |\mathbf{M}|$, n is the number of turns per unit of length and I is the current flowing in the single turn. The magnetic field of the ideal solenoid can, in turn, be calculated directly from the Biot-Savart Law. Without providing the entire derivation, the general results for the radial and longitudinal components are [80] (for convenience, a cylindrical coordinate system is chosen):

$$B_\rho(\rho, \theta, z) = B_0 \int_0^{\pi/2} d\phi (\cos^2 \psi - \sin^2 \psi) \left\{ \frac{\alpha_+}{\sqrt{\cos^2 \psi + k_+^2 \sin^2 \psi}} - \frac{\alpha_-}{\sqrt{\cos^2 \psi + k_-^2 \sin^2 \psi}} \right\} \quad (3.7a)$$

$$B_z(\rho, \theta, z) = \frac{B_0 R}{\rho + R} \int_0^{\pi/2} d\phi \frac{\cos^2 \psi + \gamma \sin^2 \psi}{\cos^2 \psi + \gamma^2 \sin^2 \psi} \left\{ \frac{\beta_+}{\sqrt{\cos^2 \psi + k_+^2 \sin^2 \psi}} - \frac{\beta_-}{\sqrt{\cos^2 \psi + k_-^2 \sin^2 \psi}} \right\} \quad (3.7b)$$

where:

$$\begin{aligned} B_0 &= \frac{\mu_0 M}{\pi} \\ z_\pm &= z \pm L \\ \alpha_\pm &= \frac{R}{\sqrt{z_\pm^2 + (\rho + R)^2}} \\ \beta_\pm &= \frac{z_\pm}{\sqrt{z_\pm^2 + (\rho + R)^2}} \\ \gamma &= \frac{R - \rho}{R + \rho} \\ k_\pm &= \sqrt{\frac{z_\pm^2 + (R - \rho)^2}{z_\pm^2 - (R + \rho)^2}} \end{aligned}$$

and R and L are respectively the radius and the semi-length of the cylinder. It is worth to note that the above expressions are independent of the θ coordinate due to the radial symmetry of the problem.

The formulas can be conveniently coded to be computationally fast and efficient. It is in fact possible to express the formulas via a combination of *generalized complete integrals*:

$$C(k_c, p, c, s) = \int_0^{\pi/2} d\phi \frac{c \cos^2 \phi + s \sin^2 \phi}{(\cos^2 \phi + s \sin^2 \phi) \sqrt{\cos^2 \phi + k_c \sin^2 \phi}} \quad (3.8)$$

Numerical algorithms that computes efficiently this integral are available in several programming languages. For examples, see [70].

The above formula has been already proved to reproduce the field of a current loop for $L \rightarrow 0$ and the field of a point dipole for $|\mathbf{r}| \gg R, L$ [80]. A sketch of the field lines produced by these equations is provided in Figure 3.2 on the next page.

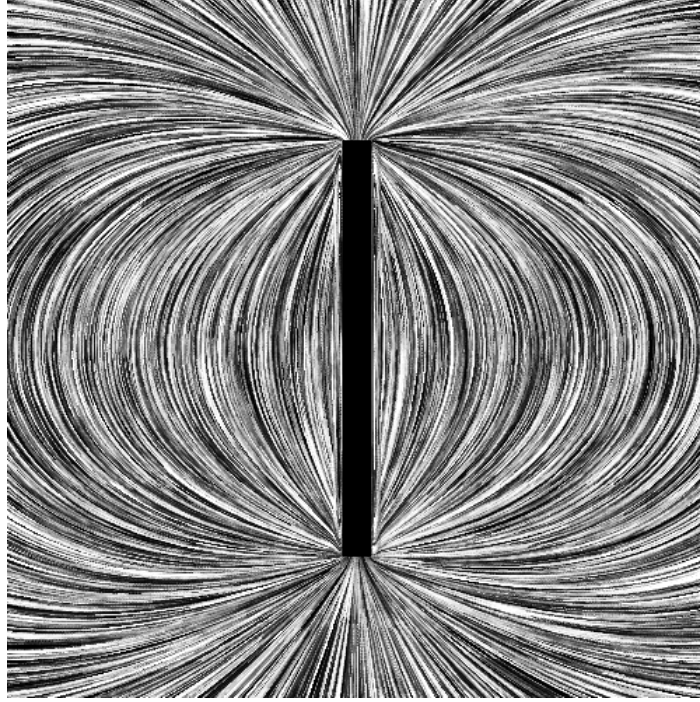


Figure 3.2: Field lines of a longitudinally magnetized cylinder ($R = 0.4$, $L = 6.0$). The lines are obtained via a line integral convolution method.

3.3 The field of a transversally magnetized cylinder

As already outlined, the exact analytical solution for the magnetic field generated by a transversally magnetized cylinder which can be computationally implemented in a convenient way have not been found in literature. The general solution, obtained by solving the associated magnetostatic problem, is valid only for an infinitely long cylinder that carries a magnetization $\mathbf{M} = M_0 \hat{x} = M_0(\cos \theta \hat{\rho} - \sin \theta \hat{\theta})$ [10, 22]:

$$B_{\rho}^{+}(\rho, \theta, z) = \frac{B_0}{2} \frac{R^2}{\rho^2} \cos \theta \quad (3.9a)$$

$$B_{\theta}^{+}(\rho, \theta, z) = -\frac{B_0}{2} \frac{R^2}{\rho^2} \sin \theta \quad (3.9b)$$

$$B_{\rho}^{-}(\rho, \theta, z) = \frac{B_0}{2} \cos \theta \quad (3.9c)$$

$$B_{\theta}^{-}(\rho, \theta, z) = -\frac{B_0}{2} \sin \theta \quad (3.9d)$$

where $B_0 = \mu_0 M_0$ and the subscripts + and - indicates respectively the outside and the inside of the cylinder.

Even though we are interested in long cylinders of aspect ratio $L/R \gg 100$, the modeling of the edges of the cylinder is crucial to us because the magnetic force exerted by the rods on the nanoparticles is proportional to the gradient of the magnetic field components [11] (see Chapters 1 and 2). Therefore, the simple solution for the infinitely long cylinder is not appropriate for our purposes.

We managed to find the exact analytical solution for the magnetostatic problem of finding

the field produced by a finite cylinder with uniform magnetization $\mathbf{M} = M_0 \hat{x}$. The final expressions are given (for a derivation, see Appendix C):

$$B_\rho(\rho, \theta, z) = B_0 \frac{R \cos \theta}{(\rho + R)(\gamma + 1)} \left[-\beta^+(P_1(k^+) - P_2(k^+)) + \beta^-(P_1(k^-) - P_2(k^-)) \right] \quad (3.10a)$$

$$B_\theta(\rho, \theta, z) = B_0 \frac{4R^2 \sin \theta}{(\rho + R)^2(\gamma^2 - 1)} [\beta^+ P_3(k^+) - \beta^- P_3(k^-)] \quad (3.10b)$$

$$B_z(\rho, \theta, z) = B_0 \cos \theta \left[\alpha^-(P_4(k^-) - P_5(k^-)) - \alpha^+(P_4(k^+) - P_5(k^+)) \right] \quad (3.10c)$$

where:

$$\begin{aligned} B_0 &= \frac{\mu_0 M}{\pi} \\ z_\pm &= z \pm L \\ \gamma &= \frac{\rho - R}{\rho + R} \\ \alpha_\pm &= \frac{R}{\sqrt{z_\pm^2 + (\rho + R)^2}} \\ \beta_\pm &= \frac{z_\pm}{\sqrt{z_\pm^2 + (\rho + R)^2}} \\ k_\pm &= \sqrt{\frac{z_\pm^2 + (R - \rho)^2}{z_\pm^2 - (R + \rho)^2}} \end{aligned}$$

and:

$$\begin{aligned} P_1(k) &= \left(1 - \frac{\gamma}{\gamma^2 - 1}\right) K(\sqrt{1 - k^2}) - \frac{1}{1 - k^2} \left(K(\sqrt{1 - k^2}) - E(\sqrt{1 - k^2}) \right) \\ &\quad + \frac{\gamma^3}{\gamma^2 - 1} \Pi(1 - \gamma^2, \sqrt{1 - k^2}) \\ P_2(k) &= \frac{\gamma}{\gamma^2 - 1} K(\sqrt{1 - k^2}) + \frac{1}{1 - k^2} \left(K(\sqrt{1 - k^2}) - E(\sqrt{1 - k^2}) \right) \\ &\quad - \frac{\gamma}{\gamma^2 - 1} \Pi(1 - \gamma^2, \sqrt{1 - k^2}) \end{aligned}$$

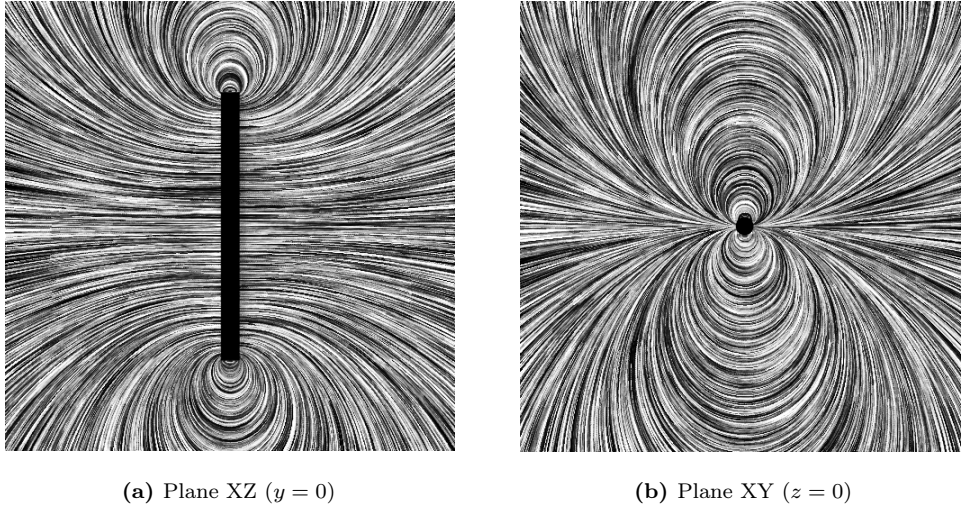


Figure 3.3: Field lines of a transversally magnetized cylinder ($R = 0.4$, $L = 6.0$). The lines are obtained via a line integral convolution method.

$$P_3(k) = \frac{\gamma}{\gamma^2 - 1} K(\sqrt{1 - k^2}) - \frac{1}{1 - k^2} \left(K(\sqrt{1 - k^2}) - E(\sqrt{1 - k^2}) \right) - \frac{\gamma}{\gamma^2 - 1} \Pi(1 - \gamma^2, \sqrt{1 - k^2})$$

$$P_4(k) = K(\sqrt{1 - k^2}) - \frac{1}{1 - k^2} \left(K(\sqrt{1 - k^2}) - E(\sqrt{1 - k^2}) \right)$$

$$P_5(k) = \frac{1}{1 - k^2} \left(K(\sqrt{1 - k^2}) - E(\sqrt{1 - k^2}) \right)$$

and R and L are respectively the radius and the semi-length of the cylinder.

The expressions are quite involved and make use of the special functions $K(k)$, $E(k)$ and $\Pi(N, k)$ which are the first, second and third kind elliptical integrals. However, as these special functions have already been efficiently coded for computation purposes [70], these expressions can still be used with reasonable speed in computational tasks. A sketch of the field lines produced by these equations is provided in Figure 3.3.

3.3.1 Limits

In order to test the correctness of the above formulas, they have been evaluated in the limit of $L \rightarrow \infty$. They correctly resemble the expressions provided by classical magnetostatic [10, 11]. The mathematical proof is reported in Appendix A. Here a numerical test is provided: the Figure 3.4 on the next page shows the ratio between the x-component of the field equations (3.10) and (3.9) as measured in different points in the (x, y, z) space. The cylinder has a unitary radius $R = 1$ and the length L is varied from 1 to 10000. The cylinder is aligned to the z-axis. It is possible to see that the two expressions all agree for $L > 100$ for the different points considered in the study.

Another check can be performed by calculating the magnetic field on the axis of the cylinder. Supposing that the cylinder is magnetized on the x-axis, the following result is retrieved (for a

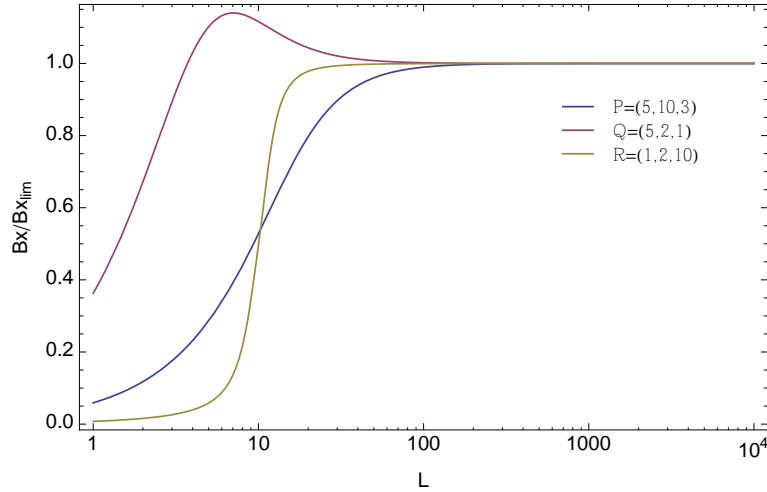


Figure 3.4: Ratio between the analytical expression and the theoretical expression valid for $L \rightarrow \infty$ as a function of the length L of the cylinder. The different lines refer to different points in which the field is measured.

derivation, see Appendix C):

$$B_x(z) = B_r(0, 0, z) = \mu_0 M - \frac{\mu_0 M}{4} \left(\frac{z_+}{\sqrt{R^2 + z_+^2}} - \frac{z_-}{\sqrt{R^2 + z_-^2}} \right) \quad (3.11)$$

which correctly reproduce the analogue result obtained in [87] for the simplified case of the on-axis magnetic field of the magnetized cylinder.

For the field calculated in the origin, the following result is then found:

$$B_x(0) = \mu_0 M - \frac{\mu_0 M}{2} \frac{L}{\sqrt{R^2 + L^2}} \approx \begin{cases} \frac{\mu_0 M}{2} & \text{if } L \gg R \\ \mu_0 M & \text{if } L \ll R \end{cases} \quad (3.12)$$

The results obtained above express the overall magnetic field \mathbf{B} produced both by the external sources and the magnetized body itself. In several occasion, however, it is convenient to separate the two components and have a clear expression for the magnetic field only generated by the magnet, referred as the *demagnetizing field* [24]. In particular, the field generated inside the magnet itself proves useful because of the possibility to link it directly to experimental data. The *demagnetizing field* of a magnetized object is defined as [24]:

$$\mathbf{H}^{\text{int}} = -\mathbf{N} \cdot \mathbf{M} \quad (3.13)$$

where \mathbf{H}^{int} is the internal field, \mathbf{M} is the magnetization and \mathbf{N} is the demagnetization tensor. It is worth to mention that the above formulation is strictly valid for a uniformly magnetized ellipsoid body only: for other shaped (or inhomogeneously) objects, it still can be used provided that the field and the magnetization are intended to be averaged in different fashions (see [24] for a more complete discussion).

As mentioned in one of the previous sections, for an uniformly magnetized ellipsoid the tensor \mathbf{N} is diagonal. Equation (3.13) reduces then to the single component equation:

$$H_i^{\text{int}} = -N_i M_i \quad i = x, y, z \quad (3.14)$$

where the different N_i values are called the *demagnetization factors* of the body.

The demagnetization factors can be meaningfully computed following the method outlined

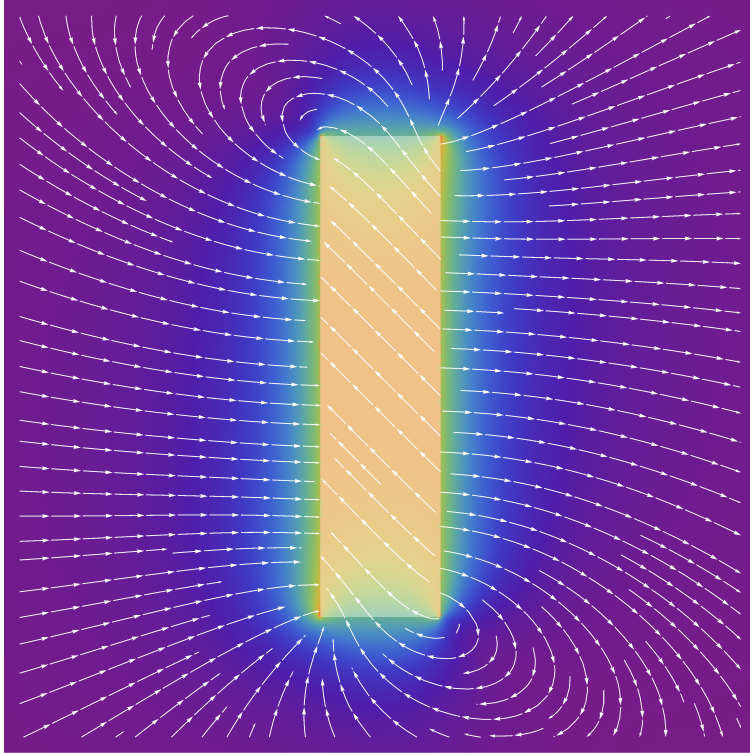


Figure 3.5: Field lines and field intensity plot of a cylinder with off-axis magnetization ($R = 1.0$, $L = 4.0$).

above also for the limits of a infinitely short and long cylinders, as they are both special forms of an ellipsoid. Remembering that [24]:

$$\mathbf{B} = \mu_0 (\mathbf{H} + \mathbf{M}) \quad (3.15)$$

and that the magnetization vector \mathbf{M} is oriented on the x-direction, the above results for the field calculated in the origin translate to the corresponding equations for \mathbf{H} :

$$H_x(0) \approx \begin{cases} \frac{-M}{2} & \text{if } L \gg R \\ 0 & \text{if } L \ll R \end{cases} \quad (3.16)$$

Since we are considering the field \mathbf{H} inside the material, the above result refers to \mathbf{H}^{int} . This gives the value of $N_x = \frac{1}{2}$ for transversally magnetized long cylinder and $N_x = 0$ for a transversally magnetized short cylinder. These results perfectly agree with the literature values reported, for example, in [37].

3.4 Applications

The two sets of equation reported in this chapter ((3.7) and (3.10)) can be efficiently combined together making use of the principle of linear superposition that arises naturally from Maxwell Electromagnetism equations [88]. In this way, it is possible to calculate the magnetic field of a cylinder with an off-axis magnetization. An example of such combination is provided in Figure 3.5.

In this spirit, provided that the linearity of the equations is conserved, the above formulation can be effectively used to solve more complex magnetostatic problems. An example (which is the most meaningful to us) is the magnetic field created by a cylinder that exhibits an

homogeneous magnetization in an arbitrary direction. This case will be discussed and validated more in details in the following chapter. Other examples are:

- *Homogeneously magnetized cylinders with an arbitrary number of holes and voids.* Provided that the geometry of the hollow parts enable an analytical solution for the magnetic field of a correspondent full body, this problem can be solved by conveniently subtracting the magnetic field generated by the void parts assuming they were full;
- *Inhomogeneously magnetized cylinders.* Provided that a functional form of the magnetization is known, this problem can be solved by replacing the constant magnetization in the integral formulation by a magnetization density. As in the equations (3.7) and (3.10) the magnetization appears only as a multiplicative constant, it is possible to decouple the two integrals. This means that the inhomogeneity of the magnetization trivially adds an additional factor represented by the integral of the magnetization density over the domain;
- *Magnetized spherocylinder.* A spherocylinder can be thought about as a cylinder with two spherical caps on the bottom and on the top. The magnetic field generated by this geometrical shape can be obtained by superimposing the fields of the two spherical caps to the field of the cylinders (the field of a homogeneously magnetized sphere is a standard result in classical electrodynamics [25]).

Other examples can be thought about as a combination of the applications suggested. In conclusion, the expressions can be handily used to solve a very general class of magnetostatic problems involving magnetized cylinders.

In addition to the suggestions for applications already presented, the formulation of the solution in terms of elliptic integrals presents an additional advantage. The derivative of the complete elliptic integrals of the 1st, 2nd and 3rd kind can be expressed as combinations of complete elliptic integrals. This means that the derivative of the magnetic fields in the forms presented in this chapter can be analytically computed, without invoking numerical derivatives and other approximation methods. This aspect is particularly convenient for the simulation of the motion of magnetic particles, in which the magnetic force exerted by a magnet is proportional to the derivatives of the magnetic field components B_x , B_y and B_z .

Chapter 4

The magnetic field of a cylinder: validation

This chapter reports the tests that have been performed in order to validate the practical implementation of the analytical equations for the magnetic field of a uniformly magnetized rod. They are described in Chapter 3 and derived in Appendix C. The tests are done by comparing the magnetic field generated by the analytical equations with the corresponding field computed by a commercial finite element method software for magnetostatic problems. The tests are performed at different levels. In a first stage, the field of a permanently magnetized rod is investigated. Both longitudinal and transverse magnetization are investigated, to provide a complete validation. In a second stage, a magnetizable cylinder placed in a uniform magnetic field is studied, in order to reproduce the real condition of a magnetized rod in an external field. In both stages, single and multi-rods system are considered: this allows to assess how the mutual interaction between magnetic bodies affect the results. Our goal is to be able to model the magnetic field generated by a random packing of magnetized rods by simply calculating the field of each rod as they were isolated bodies in a uniform magnetic field. The total field generated by the system is obtained by simply superimposing the fields generated by the rods. We found that the results of our testing confirm (up to numerical discrepancies when the mutual interaction between the magnetized objects is very strong) the validity of this strategy, provided that the rods are saturated by the external field.

4.1 Introduction

The equations derived in Chapter 3 for the magnetic field of a uniformly magnetized rods can be used for model a situation that often occurs in practice: a magnetized body in an external uniform field. In our case, this is needed in order to provide an expression for the magnetic field of a random packing of ferromagnetic rods which can be conveniently used in the framework of a Brownian Dynamics simulation. However, the exact solution for the field of a random rods configuration is far from trivial: besides the difficulties in the analytical form of the equations, the demagnetization effects on the body are induced not only from the external field, but also by the background of the other rods. Micromagnetics can provide a solution for these classes of problems, but its computational costs become soon prohibitive with the scaling of the system [89].

Approximations in the first place are, therefore, needed. We claim that the magnetic field of a random packing of ferromagnetic rods can be calculated via the superposition principle, provided that the rods are saturated by the external uniform field. In our strategy, every rod is independently considered and its magnetic field is calculated according to the equations provided in Chapter 3. The total magnetic field generated by the system is obtained by simply superimposing the fields due to all the rods in the system. In other words, we assume that

no mutual magnetic interaction occurs between the rods. This is, of course, a very strong approximation and several examples exist which proof its general incorrectness [90]. However, we claim that the approximation holds up to an error margin if the rods in exam are saturated by the external magnetic field. In this case, the mutual interactions may be disregarded and the superposition principle can be applied for the calculation of the total magnetic field. In the following sections, we will test this assumption in details. A comparison is established between the results provided by the analytical equations derived in Chapter 3 and the results generated by MagNet v7 (Infolytica Corp.), a commercial Finite Element Method (FEM) software for computing the electromagnetic fields generated by general electromagnetic devices [47].

It is perhaps clarifying to state an important distinction. An ideal permanent magnet conserves its uniform magnetization *independently* from the presence of an external magnetic field. On the contrary, a real magnetizable object acquires a magnetization due to an external field. The magnitude and relative orientation between the rod and the field itself characterizes the magnetization vector of the rod, which could be (and usually it is) non uniform.

The analytical equations formulated in the previous Chapter always assume an *ideal, uniformly magnetized* permanent magnet. The magnetization magnitude and orientation will depend on the external field that induces it, but its uniformity is a direct requirement of the theory developed. On the contrary, MagNet solves the full Maxwell equations, therefore giving realistic results for both uniform and not-uniform magnetizations and for a range of different systems. The testing performed in this Chapter aims to prove that, under suitable conditions and within a certain degree of approximation, a real magnetized object can be effectively represented by an ideal permanent magnet, whose magnetization can be described by our analytical equations. Moreover, it is claimed that this approach can be extended to a collection of magnetizable objects.

The tests reported in this Chapter refer to the comparison of two solutions of a system of rod(s): the one given by our analytical equations and the one obtained by MagNet. The tests are performed on the following systems:

- Single permanently magnetized rod (longitudinal and transversal magnetization);
- Multiple permanently magnetized rods (different mutual orientations and different magnetization conditions);
- Single rod in a uniform external magnetic field (different orientations of the rod axis to the external field);
- Multiple rods in a uniform external magnetic field (different mutual orientations of the rods and different orientations of the rod axis to the external field).

For the case of the rods in an external field, a characterization of the rod's material is needed in order to establish the response of the material to the application of the field. The rod magnetic properties (saturation magnetization and hysteresis curves) are obtained by experimental determination on an AluchromO® ferrowire rod with the same dimensions as the ones used in the Magnetic Separation setup. The experiments are done via a Vibrating Sample Magnetometer (VSM). The rod magnetization orientation respect to the field is described via a Stoner-Wohlfarth model [24]. The details of the method implementation will be described in one of the following sections.

4.2 Single permanently magnetized rod

The first test on the model has been done on a single rod. Three different magnetization \mathbf{M} conditions for the rod have been chosen. They include:

- Pure longitudinal magnetization: $\mathbf{M} = (0, 0, M_z)$;
- Pure transversal magnetization: $\mathbf{M} = (M_x, 0, 0)$;

- Mixed longitudinal and transversal magnetization: $\mathbf{M} = (M_x, 0, M_z)$.

The rod is modeled as a cylinder with radius $R = 0.3$ and height $L = 12$ in dimensionless units. As it is clear from the form of the equations in Chapter 3, the unit of measure of length is arbitrary, as they only contribute for a constant factor. The same consideration holds for the unit of measure of the field, which enter the equation in the form of the constant term M . However, MagNet does make use of the units of measure when setting the geometry of the system. In order to establish a numerical comparison between the two, the $\mu_0 M$ parameter is tuned to 1 T in the analytical equations. The distance are expressed in meters and the magnetic field intensities are expressed in T.

In MagNet, a custom material is created to represent an ideal permanent magnet with fixed magnetization direction. The geometry is the same as the one previously reported. The total magnetization vector is set to the intensity of $800\,000\text{ A m}^{-1}$. This produces a \mathbf{B} field of $\sim 1\text{ T}$ according to the equation $B = \mu_0 M$.

As the field \mathbf{B} is a function of three spatial coordinates, it is impossible to graphically represent the whole field function. The comparison between the analytical equations result and the fields computed by MagNet is therefore done in two ways:

- *Graphically.* The magnetic field components are sampled at different heights z and plotted as a function of the (x, y) coordinates;
- *Statistically.* A linear correlation (Pearson's Correlation) between the two measures is established. A scatter plot is generated together with the R^2 coefficient of the model.

4.2.1 Longitudinal case

The full graphical results are presented in Appendix D. The full statistical results are presented in Figure 4.1, Figure 4.2 and Figure 4.3. Some of the graphical results for relevant cases are included along with the statistical results. The three values of z chosen to sample the field are representative of the spectrum of the possible combinations. $z = -8$ corresponds to a field sampled below the magnet. $z = -3$ corresponds to a field sampled at an height that correspond to half the semi-length of the magnet. Finally, $z = 0$ corresponds to a field sampled on the middle plane of the magnet.

As it can be assessed by both the graphs and the linear correlation plots, the two models are in agreement. MagNet graphs, for $z = -3$, show some noisy behavior at the interface between the Magnet and the surroundings. These are due to meshing problems and, in general, to the discretization issues imposed by the finite element method approach. This is particularly evident by analyzing the case corresponding to $z = 0$. Here, especially for the x and y components, the comparison between the exact analytical result ($B_x = B_y = 0$ on the middle plane of the magnet) shows that a noise is introduced by MagNet. It is, though, of relatively low magnitude ($\sim 10^{-5}\text{ T}$) in comparison with the field inside the magnet ($\sim 1\text{ T}$). The behavior of the linear correlation gives an indeterminate R^2 . This should not be surprising, as the predicted analytical result ($B_x = B_y = 0$) is not matched by the MagNet model, due to the already mentioned noisy behavior.

Looking at the z -component, the linear correlations show that the offset between the model is up to 10% of the field intensity. However, this is due to the initial conditions imposed for the two models, that differ slightly. As a confirmation, $B_{z_{\text{Mag}}}^{\text{max}} = 1.003\text{ T}$ while $B_{z_{\text{Eq}}}^{\text{max}} = 1.000\text{ T}$ where *Mag* refers to the MagNet model and *Eq* to the model that makes use of the analytical equations. This produces the offset observed in the linear correlations plots.

In conclusion, the two models are found to be in very good agreement, except for unimportant offsets due to a slight difference in the magnetization values implemented.

4.2.2 Transverse case

The graphical results are presented in Appendix D. The statistical results are presented in Figure 4.5, Figure 4.6 and Figure 4.7. Some of the graphical results for relevant cases are

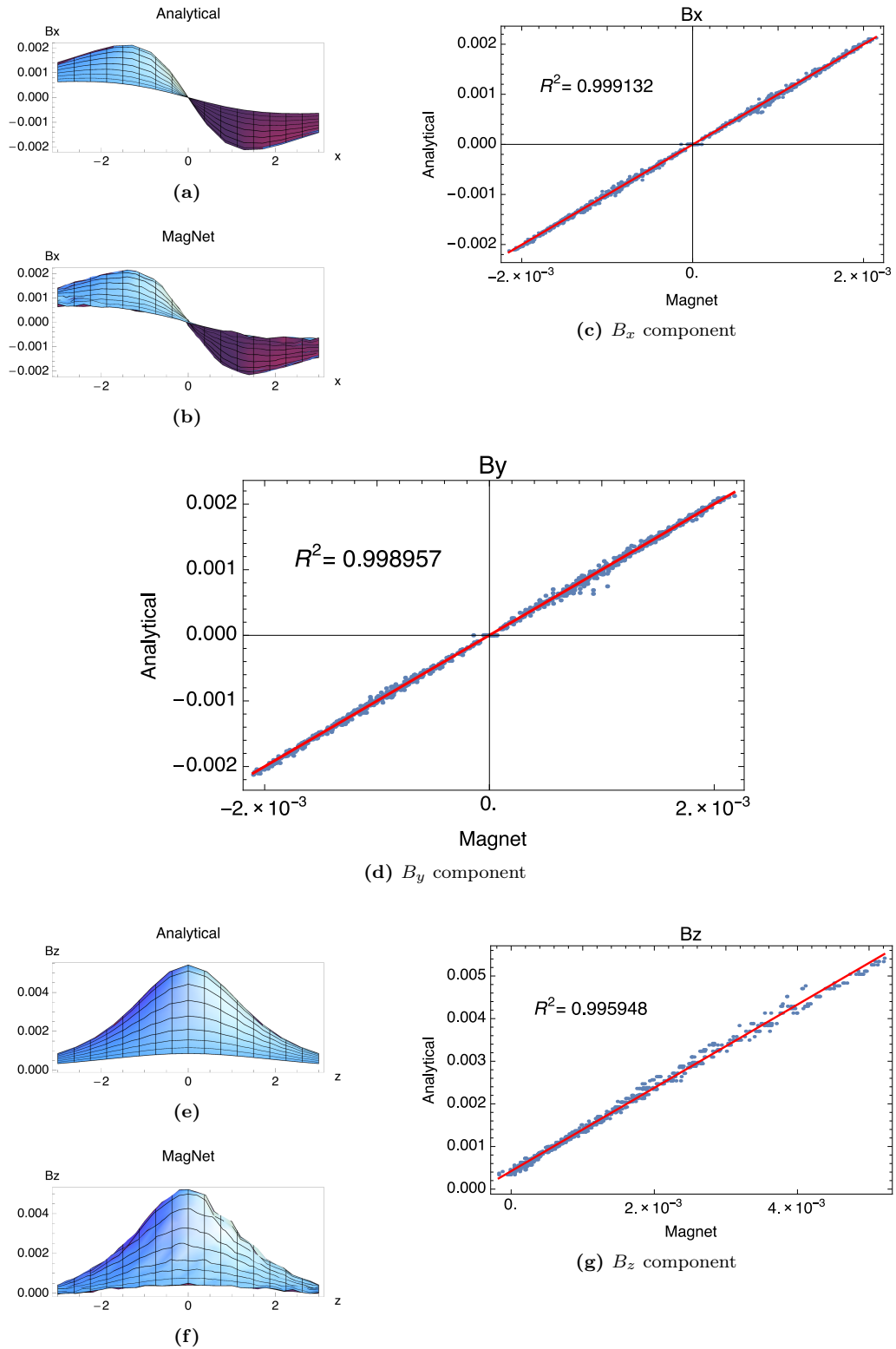


Figure 4.1: Graphical representation and linear correlation of the components of the magnetic field \mathbf{B} for a longitudinally magnetized rod. The field is sampled at $z = -8$. In the statistical plots, blue dots represent the scattered data and the red lines represent the fitted linear models.

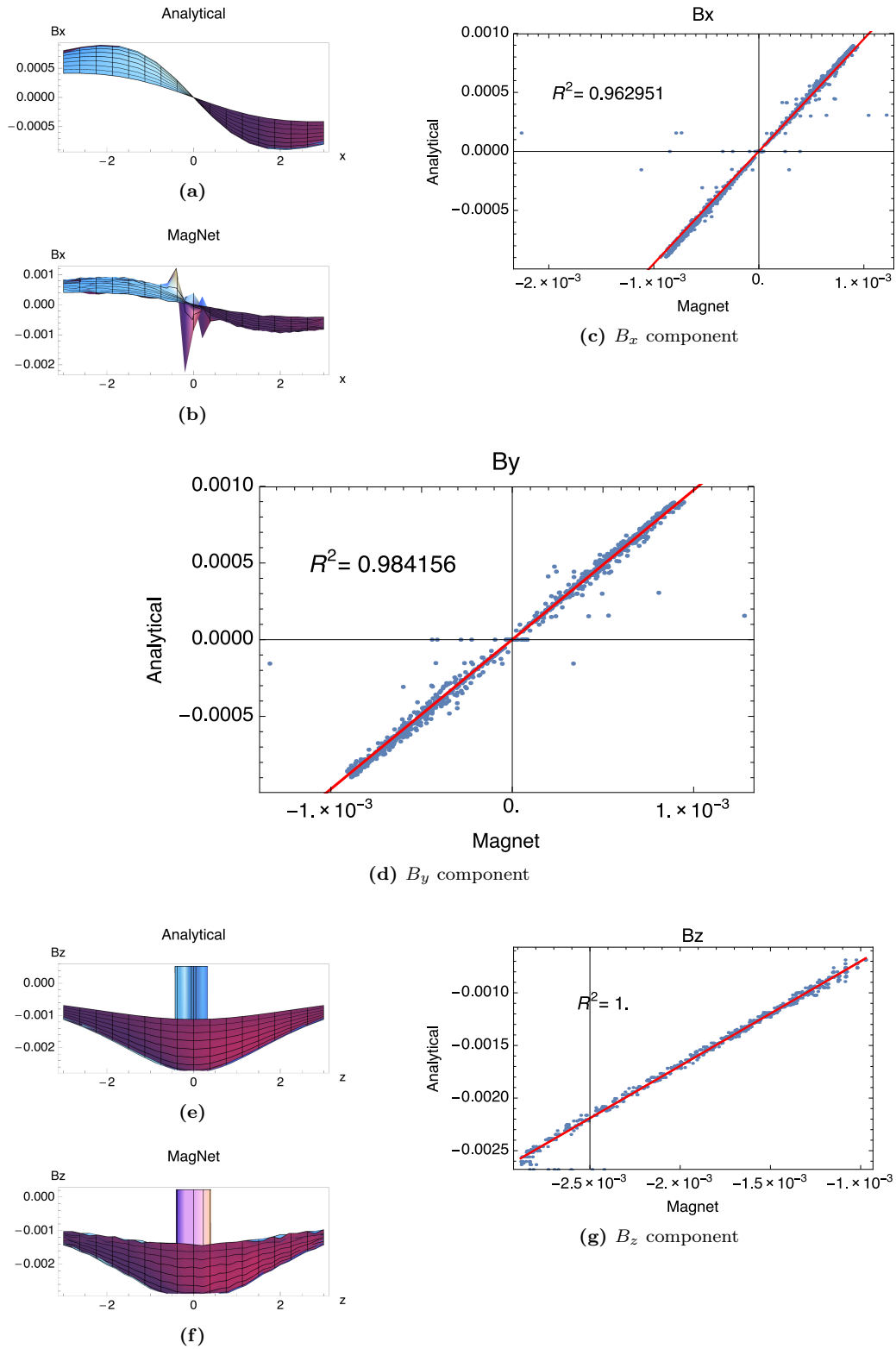


Figure 4.2: Graphical representation and linear correlation of the components of the magnetic field \mathbf{B} for a longitudinally magnetized rod. The field is sampled at $z = -3$. In the statistical plots, blue dots represent the scattered data and the red lines represent the fitted linear models.

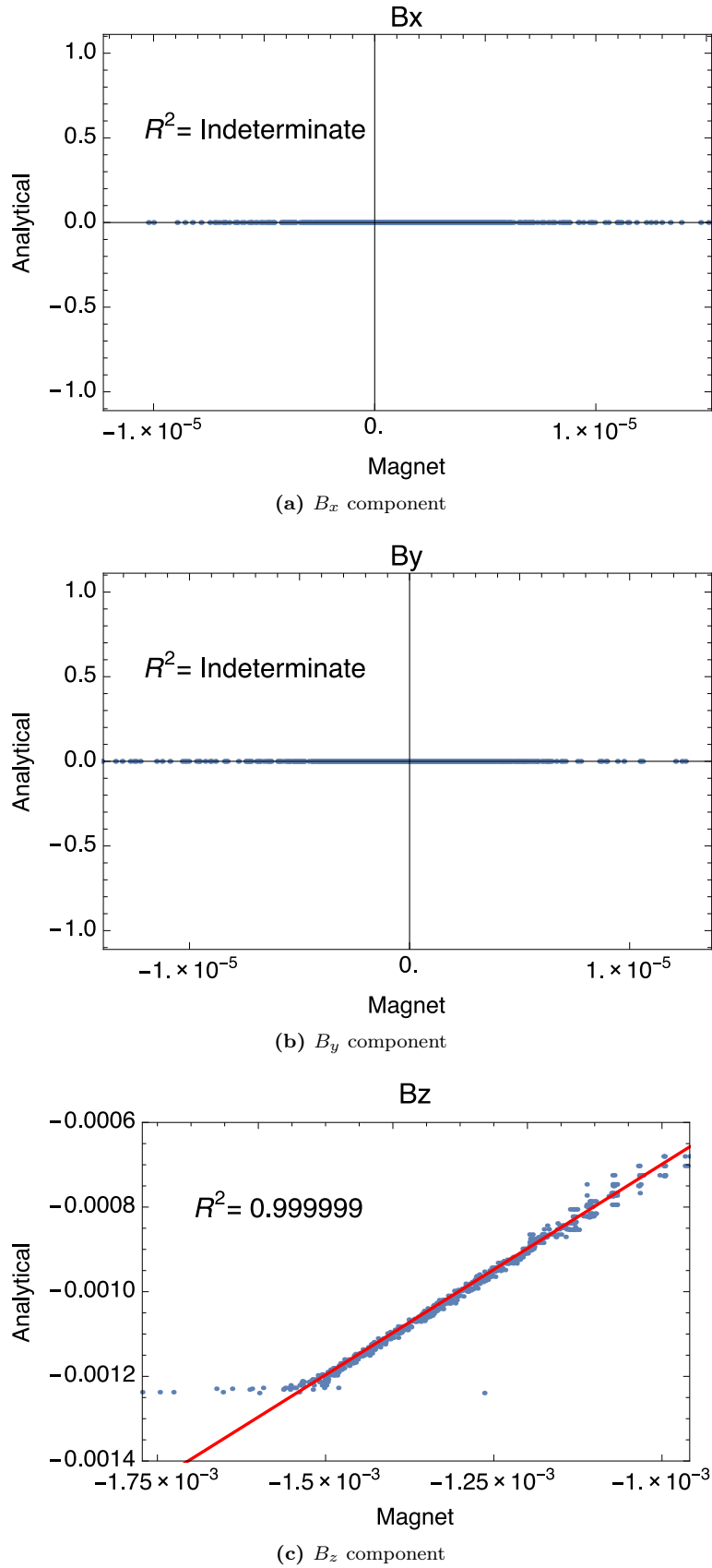


Figure 4.3: Linear correlation of the components of the magnetic field \mathbf{B} for a longitudinally magnetized rod. The field is sampled at $z = 0$. In the statistical plots, blue dots represent the scattered data and the red lines represent the fitted linear models.

included along with the statistical results. The three values of z chosen to sample the field are the same as in the previous section.

As it can be assessed by both the graphs and the linear correlation plots, the two models are in agreement. MagNet graphs for $z = -3$ and $z = 0$ show some noisy behavior at the interface between the MagNet and the surroundings. As already mentioned in the previous section, these are due to meshing problems and, in general, to the discretization issues imposed by the finite element method approach. In particular, the linear correlation plot for B_z sampled at height $z = -3$ shows that the linear fit is not consistent with the data, even though a look at the scatter plot confirms that the relation between the two models is linear (see Figure 4.6). This is due to noise in the MagNet data, which add scattered points that lie outside the linear relationship and gives a poor linear fit. The small inset in Figure 4.6 represents a zoomed out version of the graph. The scattered data (blue dots) which leads to a non correct fit (red line). The linearity of the relationship is however clearly visible in the almost vertical blue line at the center, which is zoomed-in in the bigger graph.

Looking at the x-component, the linear correlations show that the offset between the model is up to 10% of the field intensity for the height $z = -8$. The offset remains of the same absolute value also for $z = -3$ and $z = 0$. This is found again to be due to the initial conditions imposed for the models, that differ slightly. As a confirmation, $B_{x_{Mag}}^{\max} = 0.518$ T while $B_{x_{Eq}}^{\max} = 0.500$ T where *Mag* refers to the MagNet model and *Eq* to the model that makes use of the analytical equations. This produce the offset observed in the linear correlations plots.

In conclusion, the two models are found in very good agreement, except for unimportant offsets due to a slight difference in the magnetization values implemented. As a further example of the very good agreement between the models, 4.4 shows a graph of the B_x component versus the height z as measured on the cylinder axis ($x = y = 0$).

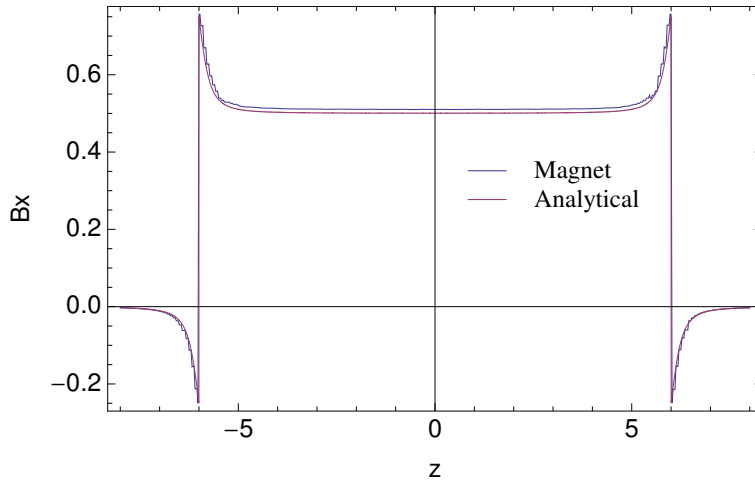


Figure 4.4: Plot of B_x field component in function of the height z measured on the cylinder axis $x = y = 0$.

4.2.3 Mixed case

In this case, the total field generated by the rod has been calculated as the superimposition of a longitudinal and transversal field (see the previous subsections for the separated case). Two situations have been tested: ($M_l = 1$ $M_t = 0.1$) and ($M_l = 1$ $M_t = 1$), where M_l and M_t represent respectively the longitudinal (directed toward the z -axis) and the transversal (directed toward the x -axis) magnetization. They have been normalized for the measurements. The graphical results for the second case are presented in Appendix D. The statistical results are presented in Figure 4.8, Figure 4.9 and Figure 4.10. The first case is not reported because

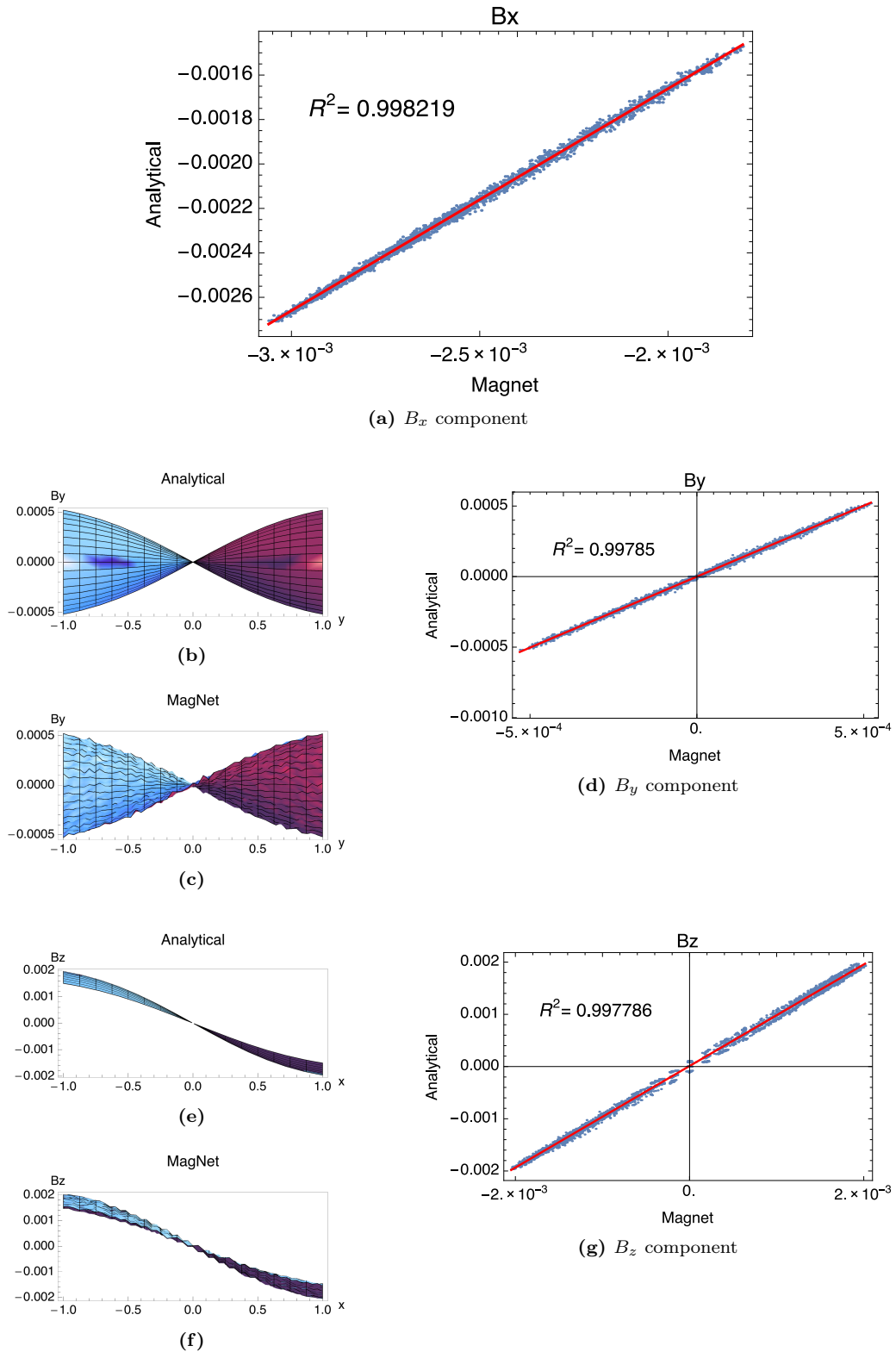


Figure 4.5: Graphical representation and linear correlation of the components of the magnetic field \mathbf{B} for a transversally magnetized rod. The field is sampled at $z = -8$. In the statistical plots, blue dots represent the scattered data and the red lines represent the fitted linear models.

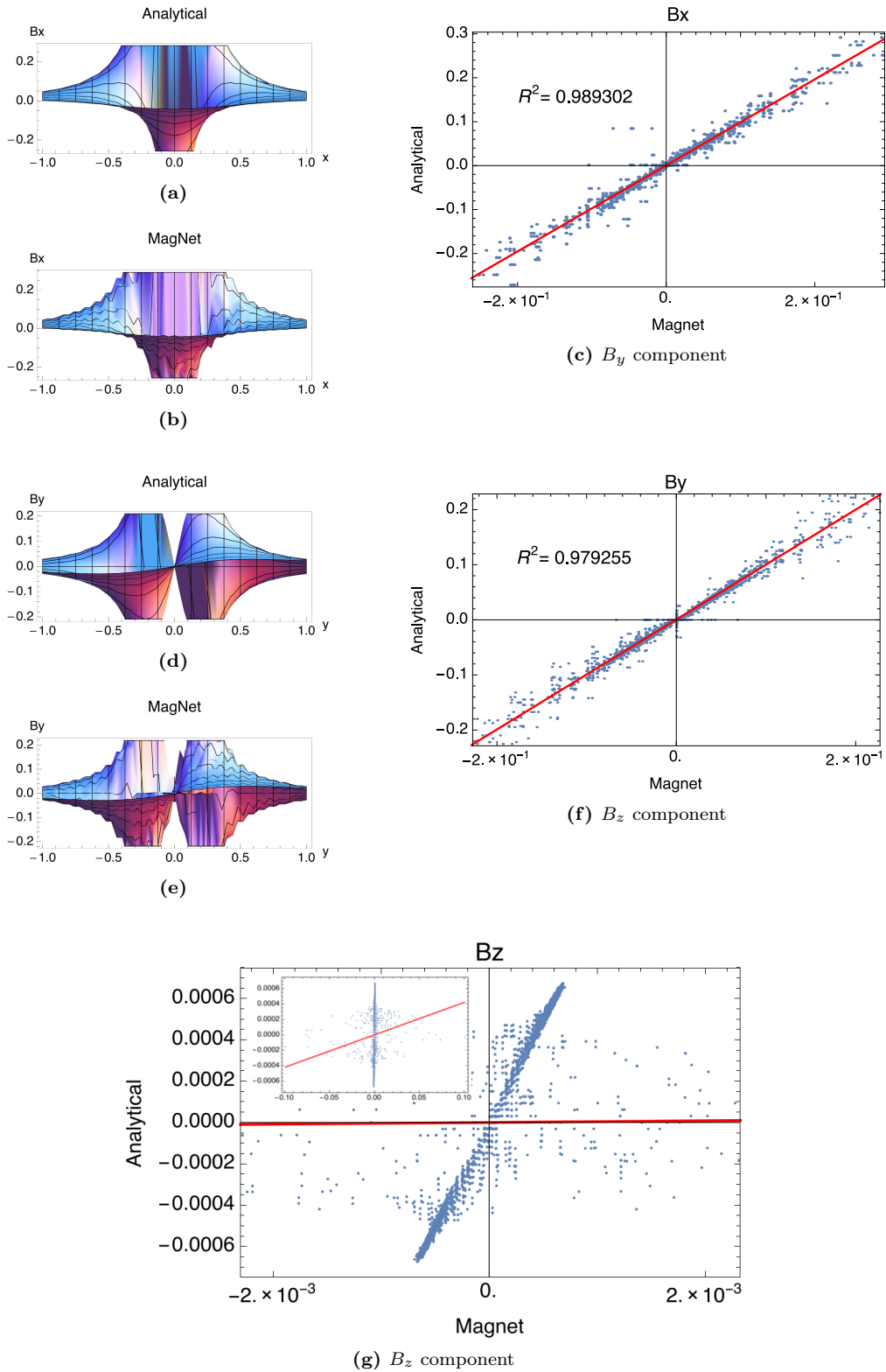


Figure 4.6: Graphical representation and linear correlation of the components of the magnetic field \mathbf{B} for a transversally magnetized rod. The field is sampled at $z = -3$. In the statistical plots, blue dots represent the scattered data and the red lines represent the fitted linear models.

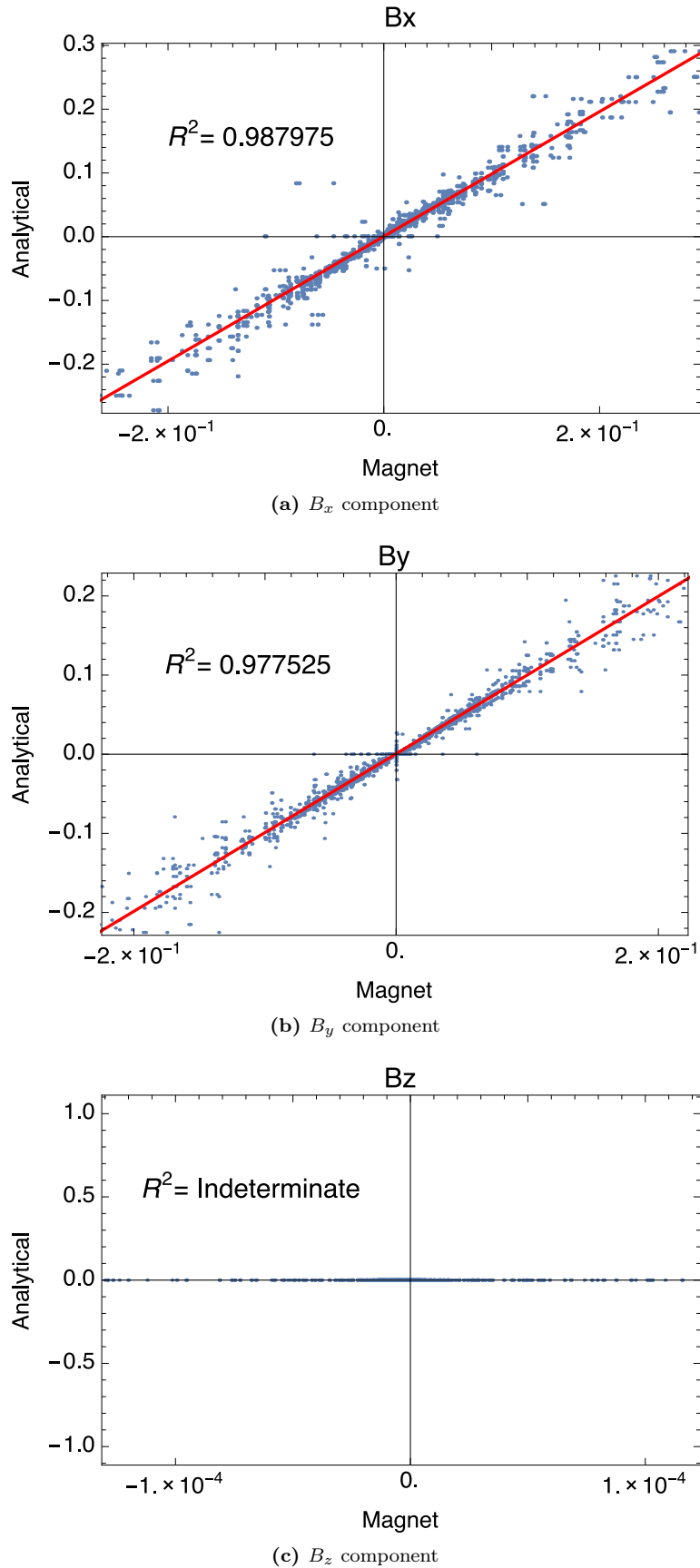


Figure 4.7: Linear correlation of the components of the magnetic field \mathbf{B} for a transversally magnetized rod. The field is sampled at $z = 0$. In the statistical plots, blue dots represent the scattered data and the red lines represent the fitted linear models.

the discussion would be equivalent to the one it will be done in the following paragraphs. The choice of the three values for z follows the same consideration as in the past sections.

As it can be assessed by both the graphs and the linear correlation plots, the two models are in agreement. MagNet graphs, for $z = -3$ and $z = 0$, show some noisy behavior at the interface between the MagNet and the surroundings. The same observations commented for these cases in the previous section can be reproduced for the $z = -3$ and $z = 0$ graphs. Looking at the x-component, the linear correlations show that the offset between the model is up to 10% of the field intensity for the height $z = -8$. The offset remains of the same absolute value also for $z = -3$ and $z = 0$. This is found again to be due to the initial conditions imposed for the models, that differ slightly. As a confirmation, $B_{x\text{Mag}}^{\text{max}} = 0.367$ T while $B_{x\text{Eq}}^{\text{max}} = 0.353$ T. This produces the offset observed in the linear correlations plots. The same reasoning can be applied to the B_y component, which leads to the same observations.

In conclusion, the two models are found in very good agreement, except for unimportant offsets due to a slight difference in the magnetization values implemented.

This section illustrated the comparison between the two models (Analytical equations and MagNet) for a single permanently magnetized rod. The results collected for the three cases provide an additional confirmation of the correctness of the analytical equations for the computation of the magnetic field of the rod. In addition, the section regarding the mixed magnetization case shows that the superposition of the fields (transverse and longitudinal) is exactly valid for a permanent cylindrical magnet with uniform arbitrary magnetization.

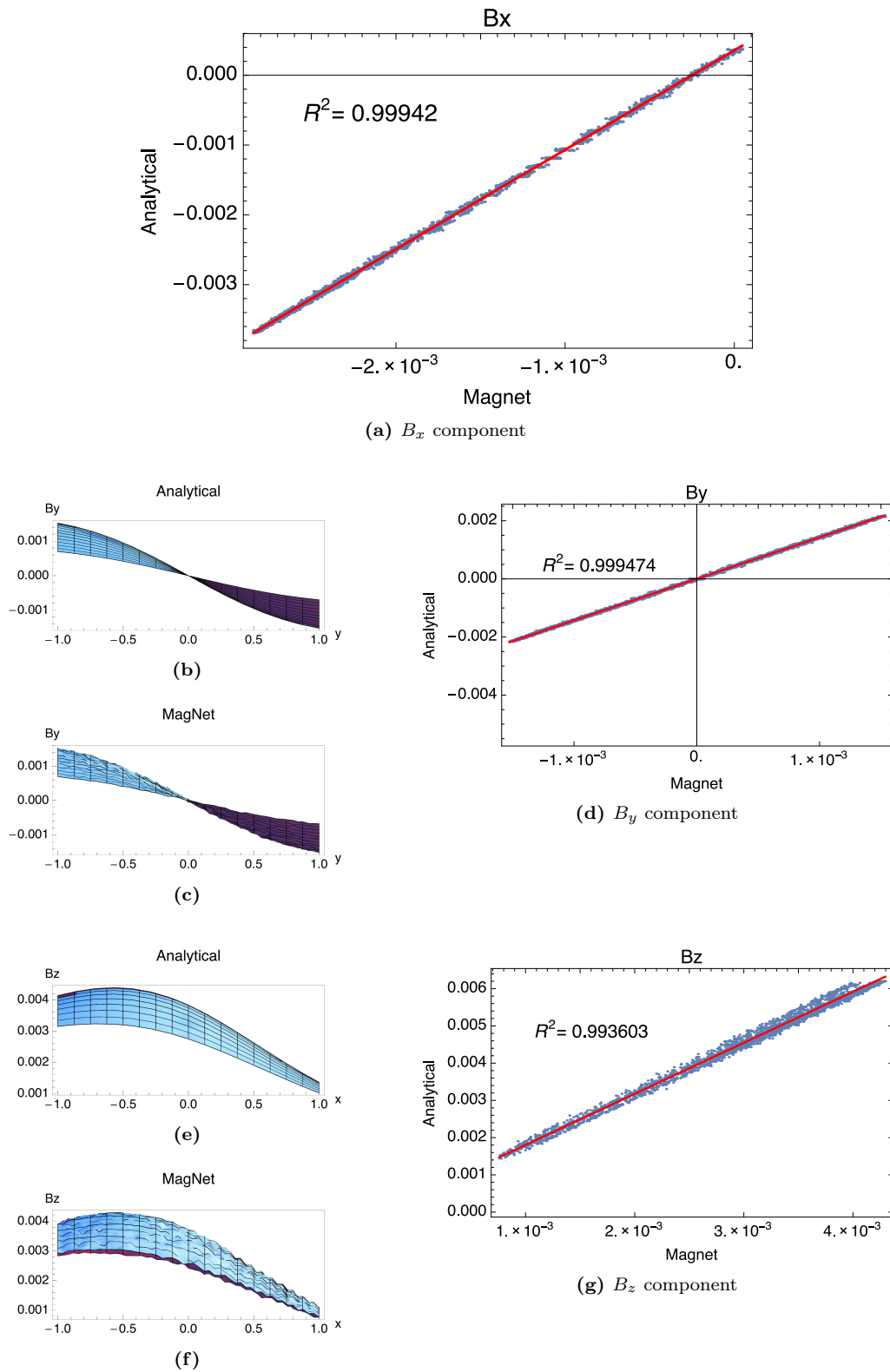


Figure 4.8: Graphical representation and linear correlation of the components of the magnetic field \mathbf{B} for a mixed magnetized rod. The field is sampled at $z = -8$. In the statistical plots, blue dots represent the scattered data and the red lines represent the fitted linear models.

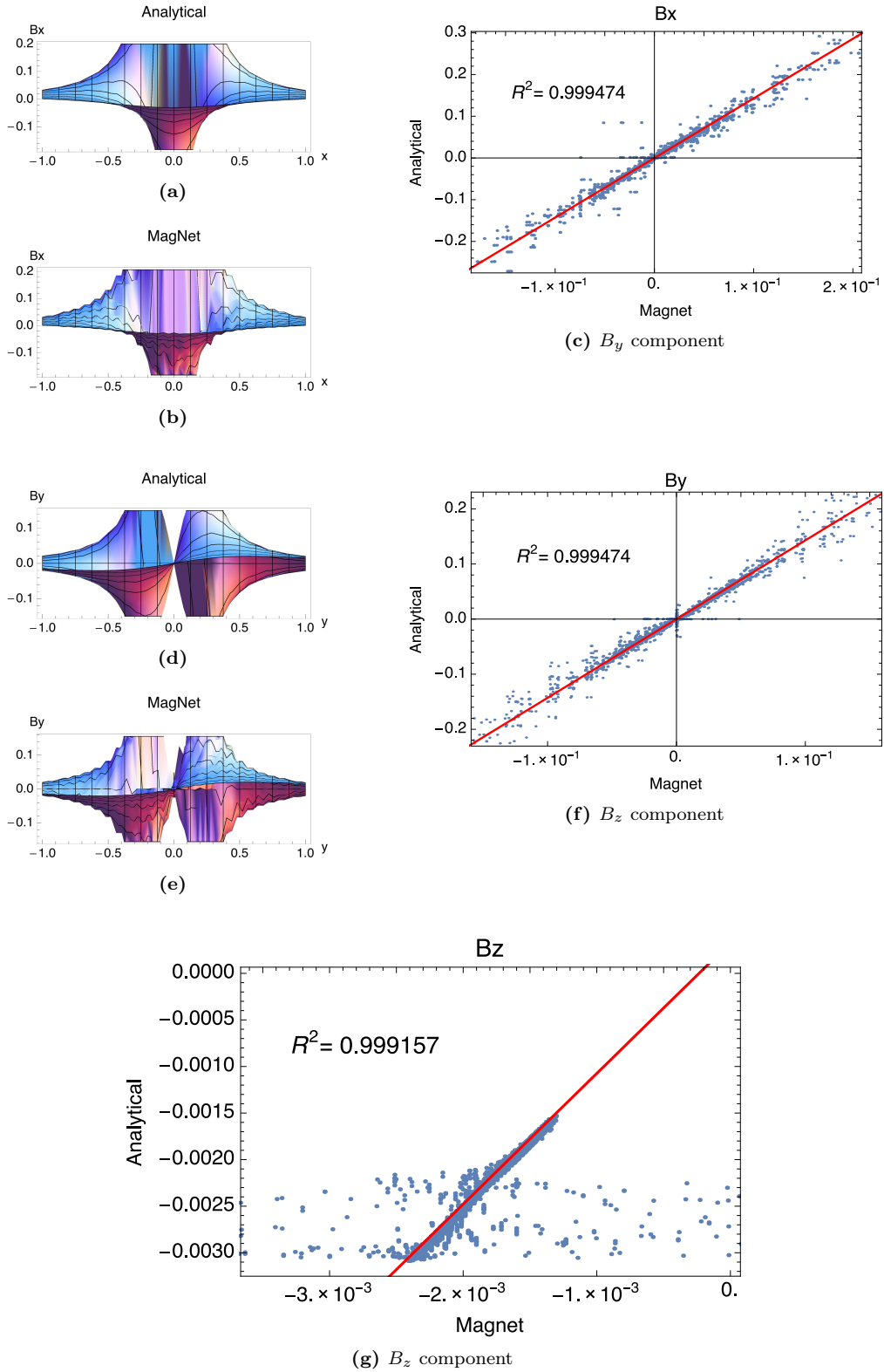


Figure 4.9: Graphical representation and linear correlation of the components of the magnetic field \mathbf{B} for a mixed magnetized rod. The field is sampled at $z = -3$. In the statistical plots, blue dots represent the scattered data and the red lines represent the fitted linear models.

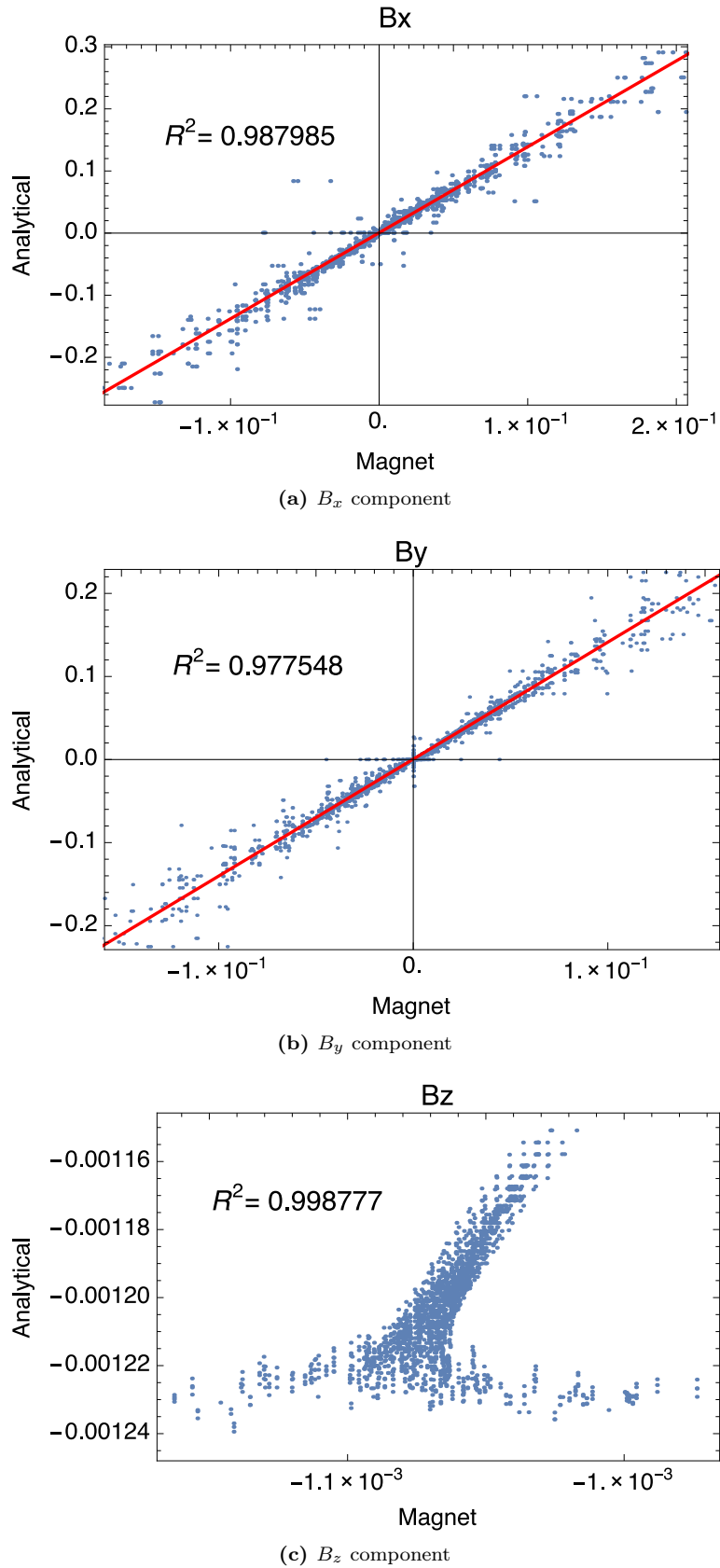


Figure 4.10: Linear correlation of the components of the magnetic field \mathbf{B} for a mixed magnetized rod. The field is sampled at $z = 0$. In the statistical plots, blue dots represent the scattered data and the red lines represent the fitted linear models.

4.3 Multiple permanently magnetized rod

The second test on the model has been done on three non-overlapping rods, mutually rototranslated. A sketch of the system is provided in Figure 4.11. The rods are positioned as

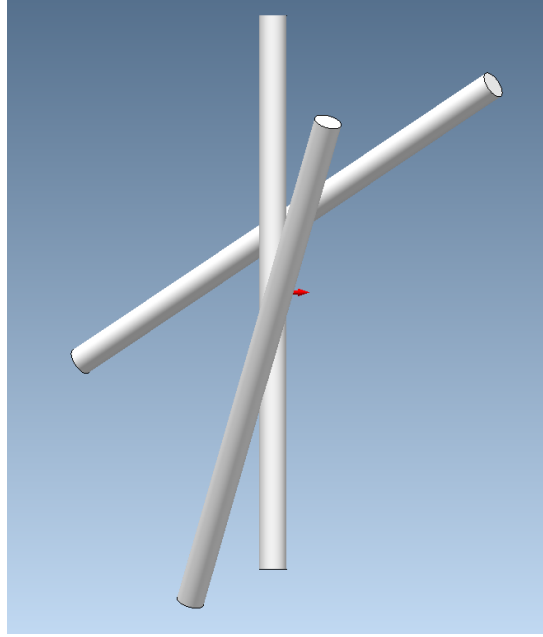


Figure 4.11: Sketch of the system under study for the test on multiple permanently magnetized rods

follows:

1. The first rod is centered in the origin $(0, 0, 0)$. Its axis is parallel to the z-axis;
2. The second rod is centered in $(R, \sqrt{3}R, L/4)$. Its axis is rotated of 30° respect to the x-axis and 30° respect to the z-axis;
3. The third rod is centered in $(-R, -\sqrt{3}R, -L/4)$. Its axis is rotated of 60° respect to the x-axis and 60° respect to the z-axis;

Three different magnetization conditions have been chosen. They include:

- Pure longitudinal magnetization for the three rods. The magnetization vector is \mathbf{M} parallel to the rod axis for all the three cylinders;
- $M_l = 1$ and $M_t = 0.1$ for the three rods. The directions of the two magnetization components are chosen to be the z-axis (M_l) and x-axis (M_t) respective of each rod. In other words: the non-rotated versions of the rods share the same magnetization vectors;
- $M_l = 1$ and $M_t = 1$ for the three rods. The directions of the two magnetization components are chosen to be the z-axis (M_l) and x-axis (M_t) respective of each rod. In other words: the non-rotated versions of the rods share the same magnetization vectors.

The rods and the custom material of which they are made are modeled as in the previous section. The comparison between the analytical equations result and the fields computed by MagNet is done analogously as well. The first case presented above served as a testing routine for the correct implementation of the equations and transformations of the magnetic field of the roto-translated rod. The results will be only presented for the third case, as the second case is equivalent in contents, observations and conclusions.

4.3.1 Results for $M_l = 1$ and $M_t = 1$

The results for the the third case mentioned above are here reported. The graphical results for this case are presented in Appendix D. The statistical results are shown in Figure 4.12 and 4.13. The fields are sampled at five different heights: $z = -8$, $z = -2$, $z = 0$, $z = 2$ and $z = 8$. This differs from the previous section, in which only three values were sampled. The choice is motivated by the fact that, in contrast with the previous situations, this case is not symmetrical respect to the $z = 0$ plane.

As it can be assessed by both the graphs and the linear correlation plots, the two models are in agreement. The correspondence is particularly good even for the domains where the field shows discontinuities. The scatter plots reveal that an offset is often present between the two models, which relative magnitude can reach also high values (up to 25%). As already explained in the previous section, this is due to the slight difference between MagNet and the analytical method regarding the reference values of the magnetization of the rods. While in MagNet it is only possible to set the initial magnetization, from which the \mathbf{B} field is calculated, the analytical method permits to directly set the reference field inside the magnet. The conversion between magnetization and \mathbf{B} is related to the constant factor μ_0 : this gives rise to differences of the order of the second decimal digit between the MagNet and the analytical fields. The accordance between the models remains assessed.

The linear correlation plots show always a very high R^2 coefficient with two notable exceptions: the B_y components for $z = 8$ and $z = -8$. In these occasions, even though the offset between the model is still low in comparison with the other components and the overall scatter plot resemble a linear correlation, there are spurious components that lowers the degree of matching of the two models. This does not seem to be due to the noise introduced by MagNet as in the previous cases, as the xy planes at heights $z = 8$ and $z = -8$ do not intersect the rods.

In order to investigate this observation, graphs of the B_x , B_y and B_z components versus the height z as measured on the cylinder axis ($x = y = 0$) are produced (in analogy with the transverse case discussed in the previous section). The plots are taken for two z-axes: the first one corresponds to the point $(0, 0)$ and the second one to the point $(-1.5, 1.5)$. The first axis is chosen for it is the axis of the first untilted rod. The second axis is chosen because it intersects two of the rods in exam, providing a view of the behavior of the fields on the boundaries. The graphs are shown in Figure 4.14.

The graphs clearly show the noisy behavior of the MagNet model in proximity of the boundaries. For the B_y components at heights $z = \pm 8$, the graphs relative to the $(-1.5, 1.5)$ axis (see Figure 4.14) show that MagNet and the analytical expressions diverge around $z = \pm 6$, that is at the top and bottom ends of the untilted rod. This apparent discrepancy is likely to come from the difficulty of the finite element method to effectively reproduce the boundary zone with a rather coarse mesh as the one used for the testing. The use of a finer mesh was not possible due to the excessive computational time involved in the calculations. In addition, the model in MagNet enforces artificial boundary conditions at the walls of the simulation box. This feature is implicit in the finite element method calculations [42]. The simulation box has dimensions $20 \times 20 \times 20$ to allow a meaningful simulation without an unwanted waste in computational time due to a very large grid, in most part unused. Therefore, it is possible that the points at $z = \pm 8$ display incorrect results due to the proximity of the simulation box boundaries. On the contrary, the analytical equations are believed to give the correct results, as it can be noticed by the smoothness in the curves.

In conclusion, from the graphs and linear correlation plots presented in this section, it can be stated that the superposition principle is exact for a system comprising many permanently magnetized rod. The field generated analytically is consistent with the finite element method even for complex models that involved roto-translated rods with arbitrarily directed uniform magnetization.

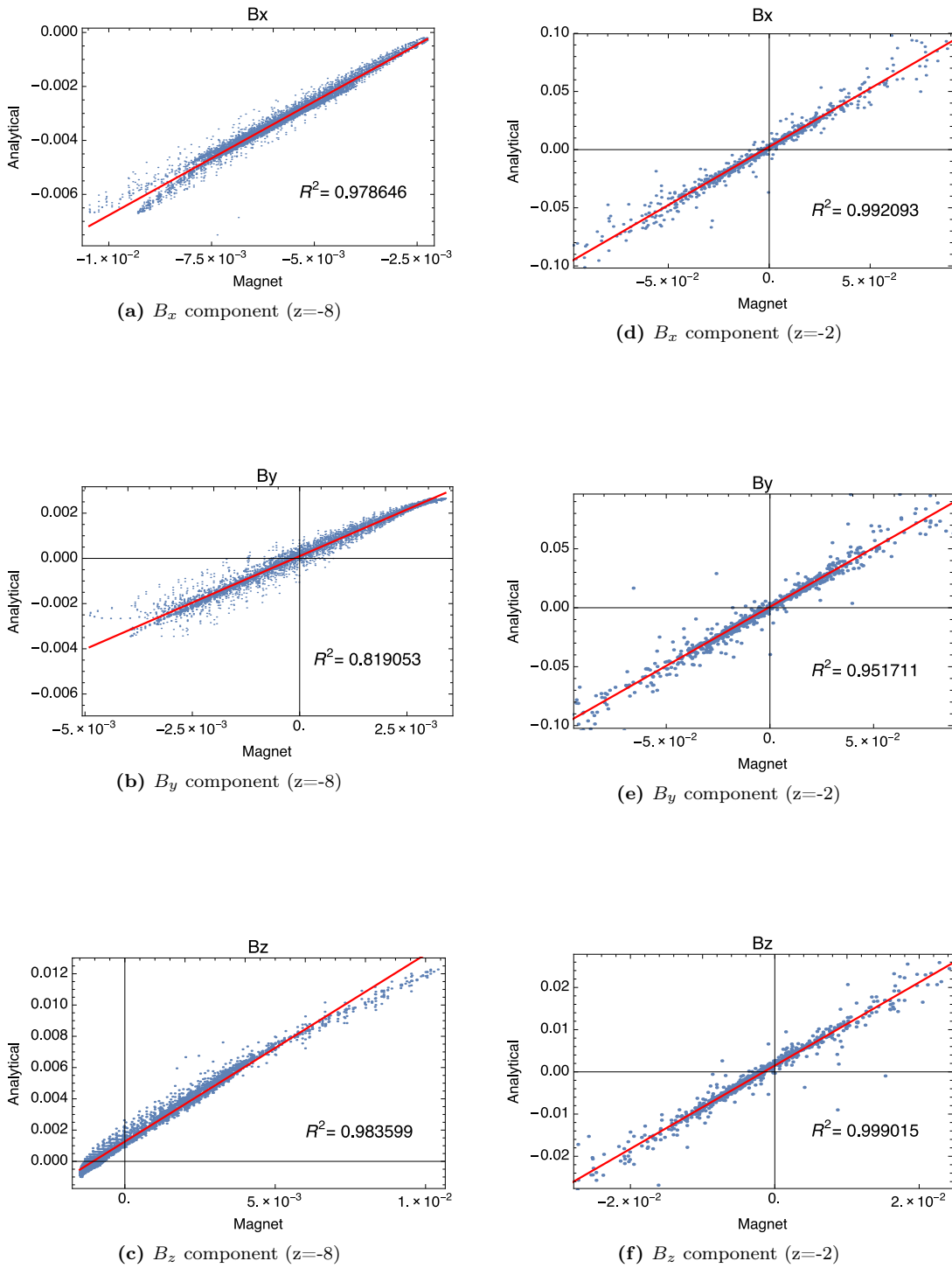


Figure 4.12: Linear correlation of the components of the magnetic field \mathbf{B} for a system of three permanently magnetized rod. Left column (a), (b) and (c): the field is sampled at $z = -8$. Right column (d), (e) and (f): the field is sampled at $z = -3$

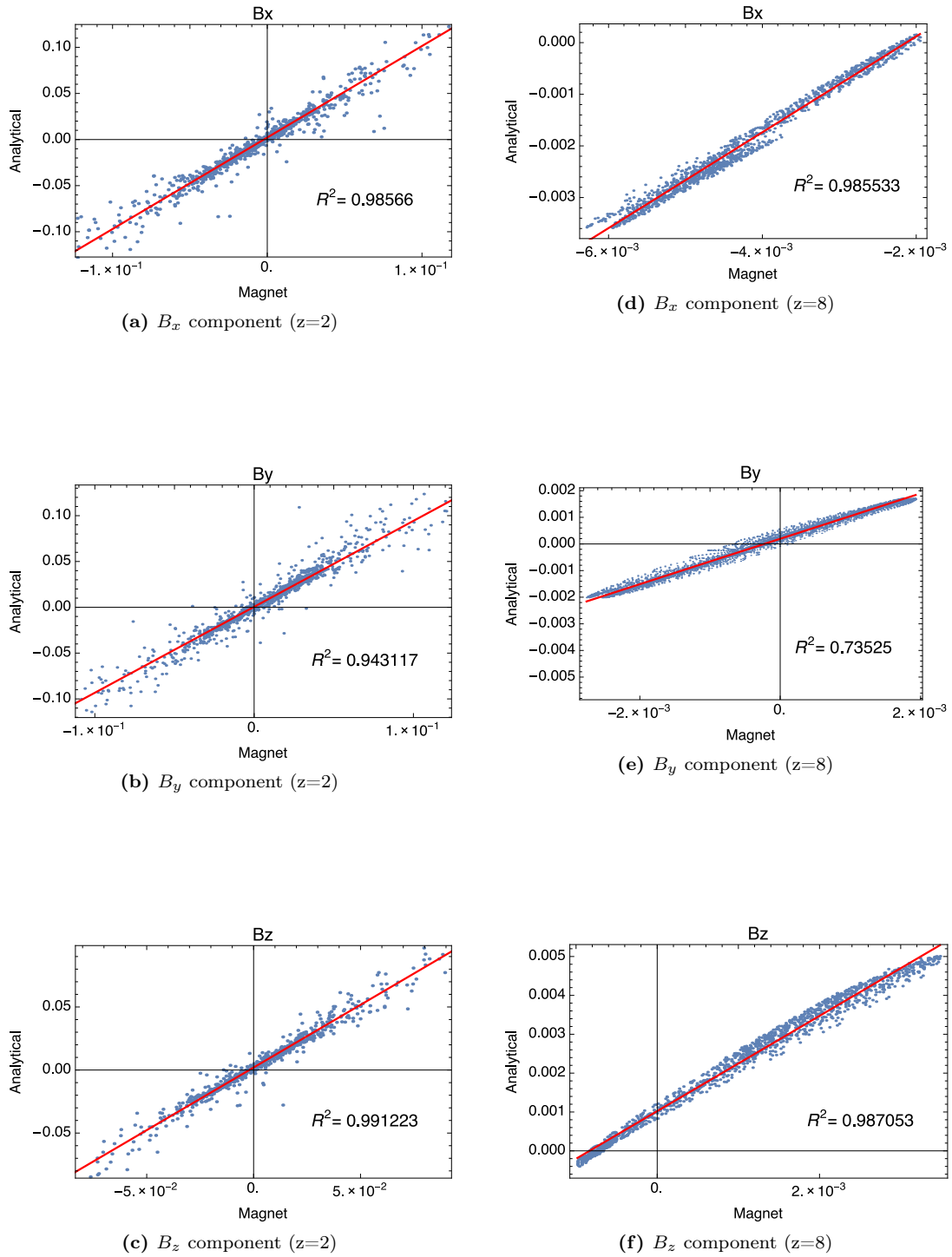


Figure 4.13: Linear correlation of the components of the magnetic field \mathbf{B} for a system of three permanently magnetized rod. Left column (a), (b) and (c): the field is sampled at $z = 2$. Right column (d), (e) and (f): the field is sampled at $z = 8$

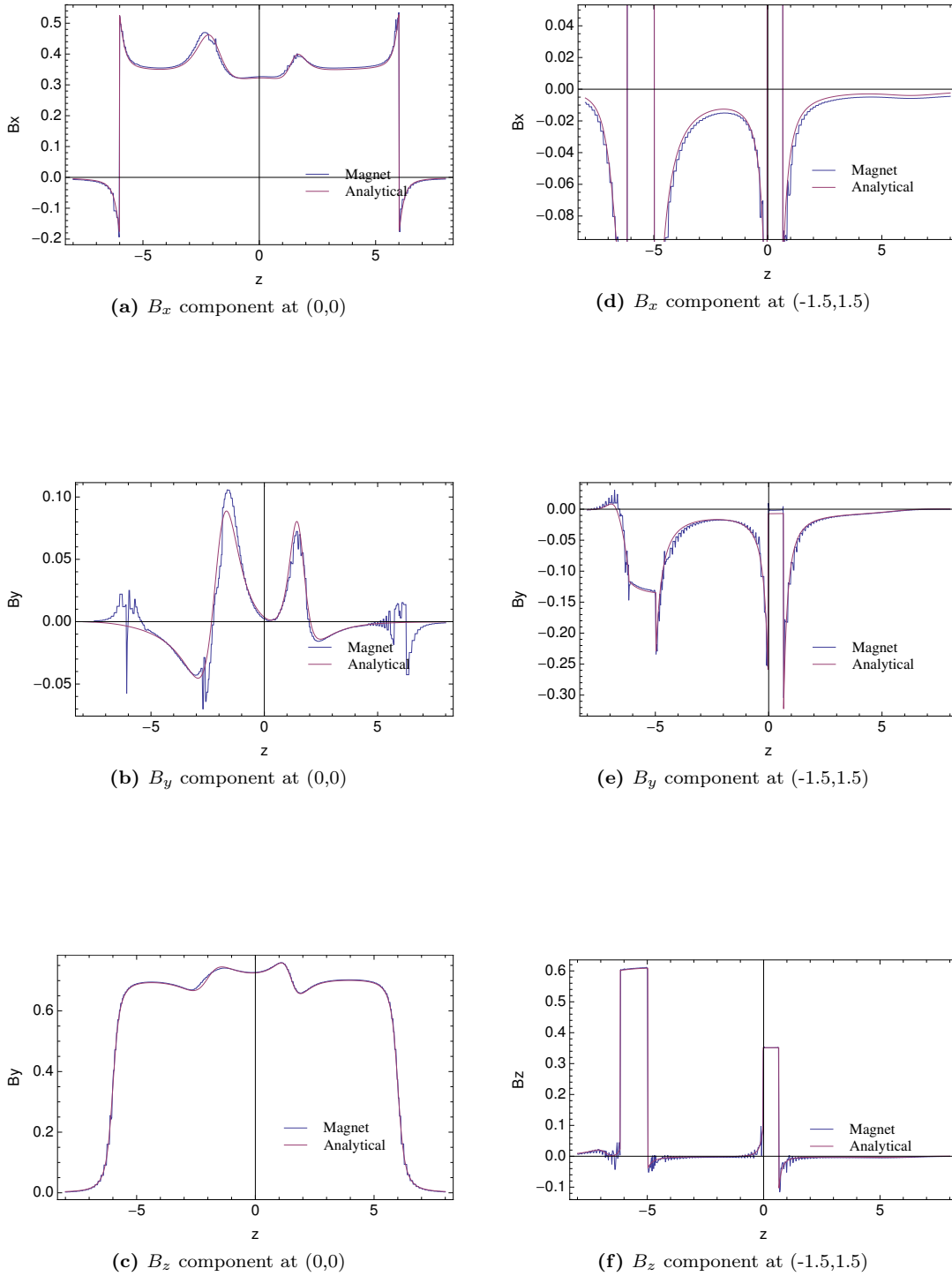


Figure 4.14: Plot of the field components in function of the height z . Left column (a), (b) and (c): the field is sampled at the point (0,0). Right column (d), (e) and (f): the field is sampled at the point (-1.5,1.5).

4.4 Single rod magnetized by an external field

The third test on the model has been done on a single rod placed in an external field. This system is different from the ones analyzed in the previous section. In the latter case, the rods were considered as permanently magnetized along a direction, and no external field was needed to model the system. In this current case, on the contrary, the rods are considered as magnetizable objects. Their magnetization is therefore a direct consequence of the application of an external magnetic field. For the rest of this section, the term *permanent magnet* will always indicate the rod as modeled by our analytical equations, since the equivalence between the analytical model and MagNet model for a permanent magnet has been proven in the previous sections. The term *magnetized rod* will always refer to the rod placed in an external field as modeled by MagNet.

In the analytical model, the condition of an external field magnetizing the rod is simply enforced by assigning a magnetization vector induced by the field. The magnetization vector magnitude and orientation follow from a Stoner-Wohlfarth model. The procedure adopted within the analytical model is outlined in Chapter 3.

In MagNet, the condition of an external field magnetizing the rod must be explicitly modeled.

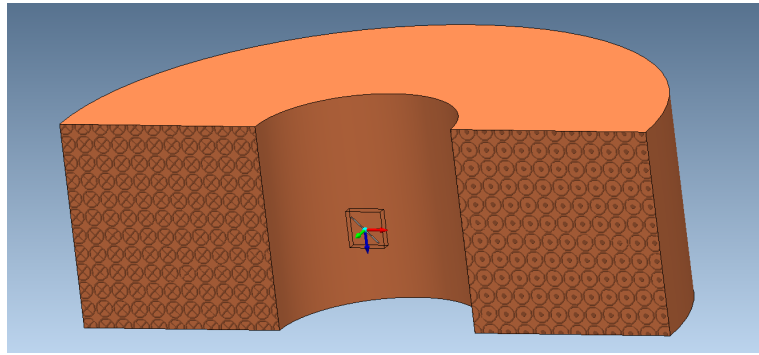


Figure 4.15: Sketch of the system under study for the test on a single rod in an external field

The uniform field is generated by a half-circular coil as in Figure 4.15. The details are the following:

- Material: *Copper 100% IACS* and the specifics are implicitly declared in MagNet.
- Shape: square toroid, $r_{\min} = 3.4$ m and $r_{\max} = 10.1$ m.
- Electric current: stranded, AC/DC source, 3 A *rms* with phase 0

The number of turns N in the coil depends on the desired intensity of the magnetic field. With this geometry, an uniform magnetic field on the central axis of the toroid is created. The field has been proven to be uniform in the surroundings with a good approximation. With $N = 4000000$, the field created between ± 1 m from the central axis varies between 0.950 T to 0.955 T. The number of turns is therefore set to $N = 4000000$. According to the hysteresis curve of the material, the field generated is strong enough to saturate the rod both on the easy-axis (the axis of the cylinder) and the hard-axis (the axis perpendicular to the cylinder). The material used for the ferromagnetic rod in the magnetic separation setup is AluchromO®. The hysteresis curve has been obtained by a Microsense EZ9 VSM (see Figure 1.12 on page 16): the results are then directly implemented into MagNet in the creation of a custom material. The hysteresis curve has been obtained by orienting the field parallel to the easy-axis of the rod (longitudinal axis). In fact, the MagNet input hysteresis curve ideally refers to the bulk properties of the material. The experimental curve relative to the easy-axis of the rod is the closest approximation to a bulk property obtainable by the VSM without taking into account the demagnetization of the sample, which would lead to rather involved corrections [91].

The material for the rod is implemented in MagNet as a non-linear, isotropic material, with $M_{sat} = 985\,000\text{ A m}^{-1}$ and electrical resistivity $\rho = 1.45 \times 10^{-6}\ \Omega\text{ m}$. The rod is modeled as a cylinder with dimensions $D = 0.04\text{ m}$ and $L = 1.2\text{ m}$. These measures are taken via a calibration measurement on the rod used for the VSM measurement, as well as being the ferromagnetic rods effectively used in the magnetic separation setup. The sizes should be scaled by a factor of 0.01 because the real sizes are expressed in mm. This only introduces a scaling factor when distances are involved. It should be noted that the scaling factor of the distance does not affect the magnetic properties of the rod, such as the saturation magnetization or the field necessary to saturate the rods. These are, in fact, intrinsic properties of the material and, as soon as the sample can still be regarded as macroscopic, the results do not depend on the size.

A first test is made to assess the validity of the Stoner-Wohlfarth model in the case in study. The second test involve the usual comparison between the analytical equations result and the fields computed by MagNet. As the previous section already proved the correspondence between the analytical model and the permanent magnet model in MagNet, the comparison has been done entirely in MagNet between a permanent magnet and a magnetized rod. It is done in two ways:

- *Graphically.* The magnetic field components are sampled on a line and plotted again the distance coordinate. This approach is chosen in order to avoid the computational demanding 3D graphs: the magnetization of the rod, in fact, introduces a steep increase of the computational time in MagNet. A small region of study is therefore preferred to an entire plane as done in the previous section. This permits to create a local grid refining in a small spatial region, increasing the efficiency of the simulation. As it will be explained further on, meaningful regions have been chosen for the test;
- *Statistically.* A linear correlation (Pearson's Correlation) between the two measures is established. A scatter plot is generated together with the R^2 coefficient of the model.

4.4.1 Decomposition of the magnetization on the easy and hard axes

As a preliminary test, the rod has been placed with its long axis perpendicular to the field. For the permanent magnet model, the test is trivial as the condition is simply fulfilled by setting a constant transversal magnetization with intensity equal to M_s . For the magnetized rod, on the other side, the test is meant to proof that the rod is saturated in these conditions (external field oriented parallel to the hard axis). The external field created in MagNet has intensity from 0.950 T to 0.005 T. Figure 4.16 shows the magnetization profile on the longitudinal axis as a function of the x-coordinate. The curve is obtained by measuring the field in the series of points $(x, 0, 0)$, where x is the variable that represents the x-coordinate. As a clarification on the reference frame, the z-axis is chosen to be parallel to the external applied field. The x-axis is chosen to be parallel with the long axis of the rod. The frame is centered on the mid-plane of the rod respect to the long axis, with the origin in the rod's geometrical center. The magnetization is obtained by making use of formula (3.15).

As it can be assessed by the picture, the magnetization is constant inside the rod, suggesting that the saturation region is safely reached. The slight parabolic profile between the rod's limits is due to the non-perfect uniformity of the external applied field. The average magnetization on the x-axis profile has an intensity of $974\,985\text{ A m}^{-1}$. It compares well against the saturation value, $M_s = 985\,000\text{ A m}^{-1}$. Other series of points $(x', y', 0)$ that define lines parallel to the x-axes have been investigated, in order to determine the uniformity of the magnetization in the other spatial directions. The results (not reported here) are positive: the profile presented in Figure 4.16 is reproduced with good agreement for the conditions tested.

In conclusion, the field created in MagNet (0.95 T) is able to saturate the rod in every direction, as the saturation on the hard axis is a sufficient condition for this to happen. This is in perfect agreement with the experimental VSM curves obtained for the AluchromO® material and

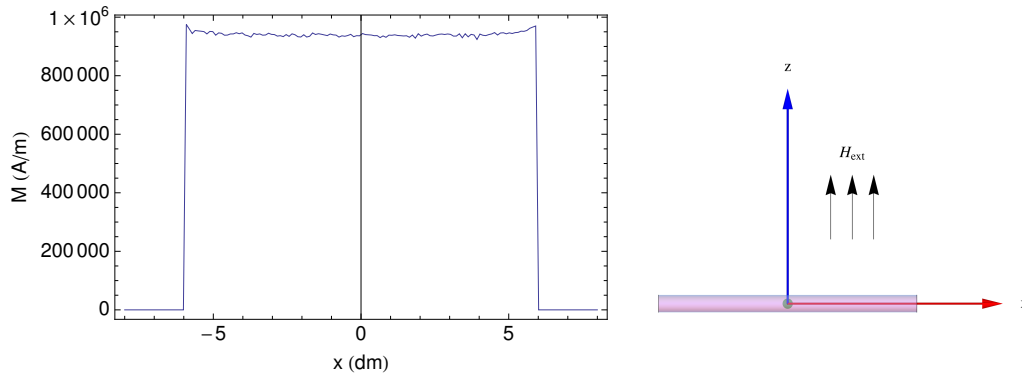


Figure 4.16: Magnetization profile on the long axis of the rod (left) and schematic representations of the reference frame (right). The magnetization reported corresponds to the transversal component, sampled on the x-axis. The length scale on the left figure is not representative (see the text for the discussion on the units of measure adopted in the MagNet model).

confirms that the modeling executed in MagNet is consistent.

In order to study the decomposition of the magnetization vector on the easy and hard axis, the rod has been tilted of 45° respect to the x-axis. This means that the external field has an angle of 45° with the rod. The external field has the same intensity as before. Figure 4.17 shows the magnetization profile on the longitudinal axis as a function of the height coordinate. Both the transversal and longitudinal magnetization are reported. The curve is obtained by measuring the field on the longitudinal axis of the rod. A scheme of the reference is provided in Figure 4.18. The magnetization is obtained by making use of formula (3.15).

The magnetization inside the magnet is constant for both the longitudinal and transverse

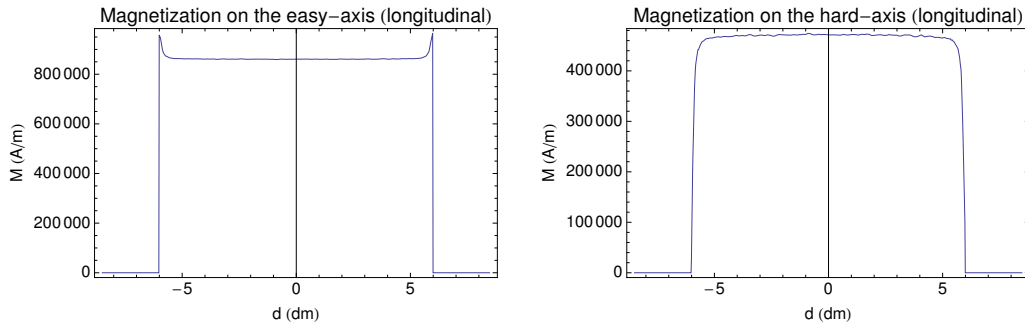


Figure 4.17: Longitudinal (left) and transverse (right) magnetization profile of the rod measured on the long axis of the rod. The coordinate d refers to the length of the rod on its longitudinal axis.

component. Edge effects are visible in correspondence to the top and bottom ends of the rod. They round the corners for the transverse component, while they produce small peaks for the longitudinal component. These effects are interpreted as both an artifact due to the boundary treatment implicit in MagNet when the magnetization effects are taken into account, and as a sign of the non-ideality of the system in study. In fact, as already mentioned, the demagnetizing fields generated by the applied fields are generally non-uniform [38]. Nevertheless, the figure confirms that the assumption of a constant magnetization inside the body is verified to a good degree of approximation.

The values for the longitudinal and transverse magnetization as obtained by the MagNet model are compared to the results obtained by applying the Stoner-Wohlfarth model as described in the previous subsection (Mathematica has been used to solve the constrained minimization

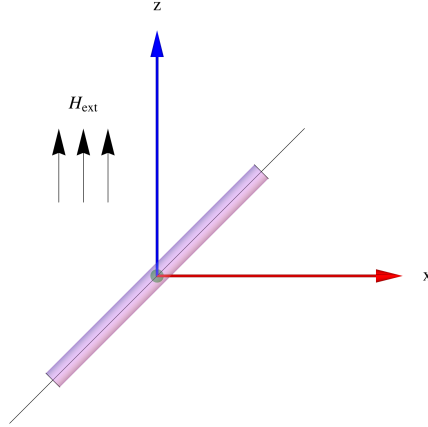


Figure 4.18: Schematic representation of the reference frame. The thin black line represents the locus of points on which the magnetization has been measured.

problem). Table 4.1 illustrates the results. The results prove that the field is properly decom-

	MagNet	Stoner-Wohlfarth
M_z (A/m)	860630	861186
M_x (A/m)	471673	473104
M_y (A/m)	347	1.795×10^{-20}

Table 4.1: Comparison of the magnetization values obtained with MagNet with the values obtained assuming a Stoner-Wohlfarth model for the magnetization. M_z stands for the magnetization on the easy-axis, M_x stands for the magnetization on the hard axis parallel to the field, M_y stands for the magnetization on the hard axis perpendicular to the field.

posed according to the Stoner-Wohlfarth model: the MagNet model is reproduced within a very good range of confidence. The magnetization M_y is correctly negligible in both cases, as zero magnetization component perpendicular to the applied field is expected.

4.4.2 Comparison between a magnetized rod and a permanent magnet

After proving that the Stoner-Wohlfarth model correctly describe the magnetization orientation and magnitude of a magnetizable rod in an external system, the next step is to test whether the analytical equations (which assume an *uniform* magnetization) can correctly reproduce a real magnetized object (which can exhibit *non-uniform* magnetization). The system studied is the same as in the previous subsection. For a sketch of the system, see Figure 4.18. As the study of the fields inside the rod has been already done in the previous subsection, the comparison between the models has been restricted to selected regions in the proximity of the rod's surface. This approach has been chosen because the field is higher in intensity close to the surface: eventual discrepancies between the models are expected to happen at the boundary regions.

Two regions have been examined: the zone close to the center of the rod and the zone close to the corner of the rod. The sketch of the regions are shown in Figure 4.19. The sampling has been done analogously as in the previous subsection: the field is measured on the line of interest as drawn in Figure 4.19. Figure 4.20 shows the magnetic fields for the permanent magnet and the magnetized rod as a function of the distance coordinate as measured for the

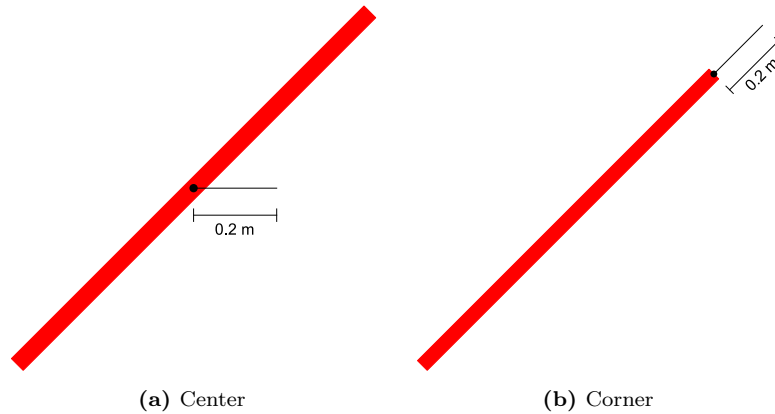


Figure 4.19: Schematic representation of the regions upon which the magnetic field has been sampled. For a sketch of the reference frame, see Figure 4.18.

center case. The x and z subscripts stand respectively for the transverse and longitudinal components relative to the long axis of the rod. Only two components of the field are presented, as the profile is sampled for $y = 0$, implying a null y -component. Only the \mathbf{H} field is reported, as the results for \mathbf{B} and \mathbf{M} are equivalent.

The figures clearly show that the agreement between the magnetized rod and the permanent magnet is almost perfect. The linear plot parameters reveal an offset between the models. This arises most probably from the different saturation magnetization implemented in the two models. This numerical discrepancy, of low relative entity, does not affect the quality of the comparison between the models, as confirmed by the high value of the R^2 coefficient in both graphs.

Figures 4.21 and 4.22 show the magnetic fields for the permanent magnet and the magnetized rod as a function of the distance coordinate as measured for the corner case. The x and z subscripts stand respectively for the transverse and longitudinal components relative to the long axis of the rod. Only two components of the field are presented, as the profile is sampled for $y = 0$, implying a null y -component. The results for \mathbf{M} are not presented, as they are very similar to the pictures presented in Figure 4.17.

A discrepancy between the two models is visible. Even though it is possible to slightly improve the results by refining the mesh used, differences at the critical points in the graphs still remain. In the comparison with the graphs for the center region, it can be seen that the discrepancy arises close to the edge of the rod. In particular, the graphs relative to the B_x and H_x components show the presence of branches, which indicates a non-linearity in the relation between the analytical and MagNet models. For this reason, the correspondent statistical plots do not report the linear fit nor the fitted curve. The origin of these branches lies most probably in the breaking of the agreement between the two models in the small region at the top/bottom ends of the rod. It should be considered, though, that the FEM method often displays unphysical peaks and kinks in the boundary regions due to numerical constraints and instabilities [42]. Therefore, a full study of the agreement of the models in these regions could come only by empirical measurements. It is worth to note, however, that the agreement between the curves is still relatively good. The statistical plots of the B_x and H_x components show that, even though branches are present in the discontinuity at the surface of the rod, the scatter data in the other spatial region follows a linear relation. In the case of the B_z and H_z components, the R^2 values of the linear fits are high. By comparing the graphical and the statistical plots, it can be seen that the deviance from the fitted curve occurs at the discontinuity at the surface of the rod. This means that the region in which the two models show different responses is small in space and that, even there, the discrepancies are small.

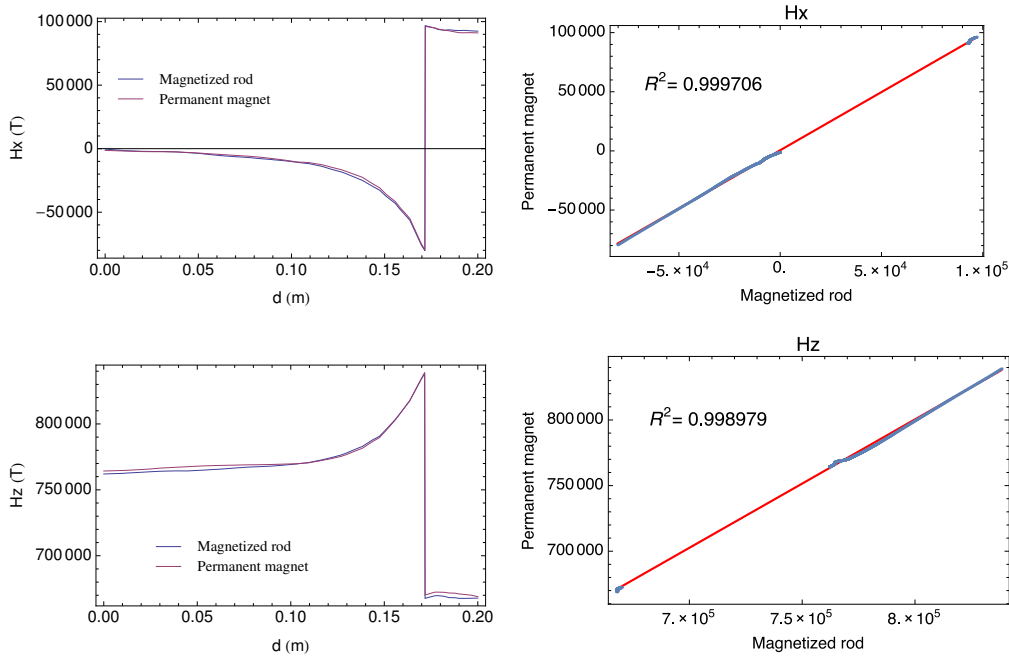


Figure 4.20: Study of the field components in the center region. (Left) Plot of the fields as function of the coordinate d measured on the line as in Figure 4.19. (Right) Linear correlation of the field components between the analytical and MagNet models. The scatter data are shown in blue, while the red line represents the fitted curve.

In conclusion, in this section it has been proved that a magnetized rod can be modeled as a permanently magnetized rod with magnetization components on the easy and hard axis, whose decomposition follows a Stoner-Wohlfarth model. The agreement between the model and an actually magnetized rod is almost perfect for the majority of the space close to the boundaries between the rod and the surroundings, with only small discrepancies at the top/bottom end of the rod.

4.5 Multiple rods in a uniform external magnetic field

The fourth test on the model has been done on two rods placed in an external field. As in the previous case, the comparison is done between a system modeled by our analytical equations and a model fully solved in MagNet. In the former, the mutual magnetization effect is disregarded (as it has been described elsewhere in the Chapter) and the total fields are obtained by a superimposition of the fields generated by the single rods. In the latter, the full Maxwell's equations are solved for the whole system and mutual magnetization effects and non-uniformity in the magnetization are considered. Two relative configurations of the rod have been generated. They include two rods parallel to each other, rotated of 45° degrees respect to the external field, and two rods rotated of respectively -45° and 45° degrees respect to the external field. The rods are placed so that their top/bottom ends are almost touching. The first configuration is chosen because it depicts a non problematic situation, in which large field gradients are not expected. This should provide an optimal check on the validity of the agreement. The second configuration is chosen because, as the rods are almost connected at the top/bottom ends, non-trivial fields are expected to appear in the critical region. Therefore, the configuration depicts a very complex situation in terms of field gradients and magnetizations. The test on the model can be executed to evaluate the extent to which the proposed representation of a magnetized rod as a permanent magnet breaks down when the mutual interaction between the rods is maximum. The schemes of the configurations used are represented in

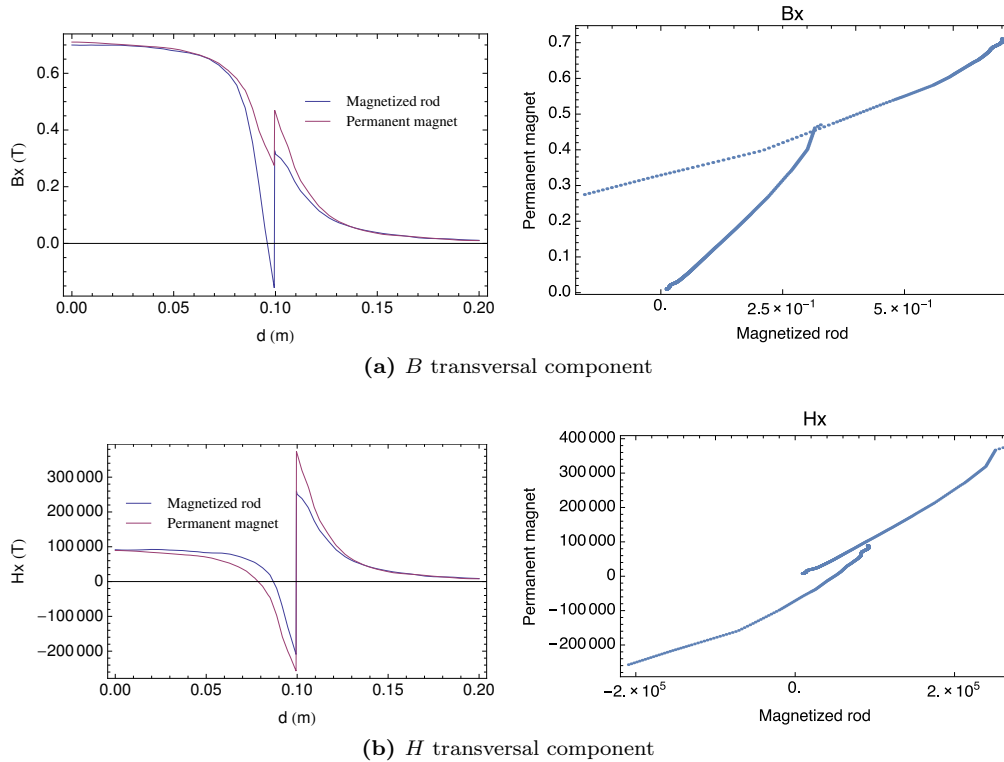


Figure 4.21: Study of the x-components of the field in the corner region. (Left) Plot of the fields as function of the coordinate d measured on the line as in Figure 4.19. (Right) Scatter plot of the field components between the analytical and MagNet models.

Figure 4.23

The setup in MagNet follows the same directives as in the previous section (current coils, external uniform field intensity, material details, rod specifics, ecc.). The permanent magnet is given assigned magnetization on the easy and hard axis, according to the Stoner-Wohlfarth model. The comparison is done in the usual two ways already explained in the previous section.

4.5.1 Parallel rods

The sketch of the configuration is given in Figure 4.23. The field sampling has been done in the same fashion as in the previous sections: the field is measured in the series of points $(x, 0, z)$, where x and z indicate the locus of points that define the line of interest. Two lines have been chosen to be sampled:

- A line that goes from $(0, 0, -0.4)$ to $(0, 0, 0.4)$
- A line that goes from $(-0.42, 0, -0.21)$ to $(-0.42, 0, -0.61)$

The first sampling gives an overall view of the fields in the space region close to the rods. The second sampling gives the fields in the corner zones of both the rods in exam.

Figure 4.24 shows the magnetic fields for a pair of magnetized rods on the function of the distance coordinate as measured on the line of interest in the case of the first sampling.

As the pictures shows, the fields correctly show a symmetry around the distance $d = 0.4$. The slight variations from the uniformity of the fields inside the rods, centered in $d = 0.2$ and $d = 0.6$, arises from the rather coarse mesh applied. This is necessary for a characterization of a broad zone as the one sampled. The magnetization components, not shown in the graphs,

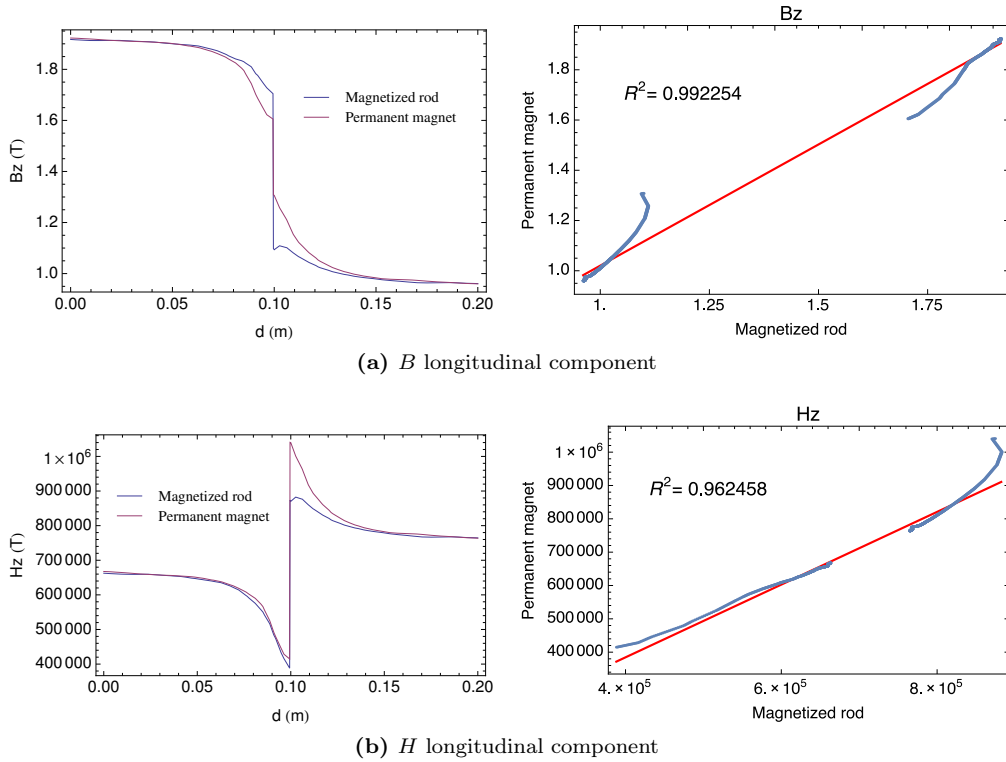


Figure 4.22: Study of the z -components of the field in the corner region. (Left) Plot of the fields as function of the coordinate d measured on the line as in Figure 4.19. (Right) Linear correlation of the field components between the analytical and MagNet models. The scatter data are shown in blue, while the red line represents the fitted curve.

are proven to give equal uniform magnetization inside the two rods. The magnetic field intensity decays in the outer regions ($0.0 < d < 0.2$ and $0.6 < d < 0.8$) and the inner region ($0.2 < d < 0.6$) quantify the rod mutual interaction. If the interaction is important, in fact, the inner region is expected to give different curve shapes in comparison with the outer region, which is less affected by the presence of the second rod. From the pictures, it can be seen that the profiles are very similar, except of a slight superposition of the fields of the two rods in proximity of $d = 0.4$. Therefore, it can be concluded that the rods do not show an appreciable mutual interaction.

The comparison with an equivalent configuration that features a permanently magnetized rod has not been made for this sampling, due to the already satisfying results discussed in the previous subsections.

Figure 4.25 shows the magnetic fields and the magnetization curves for a pair of magnetized rods as a function of the distance coordinate measured on the line of interest in the case of the second sampling.

The two models show an essential agreement for most of the profile sampled, with some discrepancies at the boundary regions between the rods and the surrounding background. From a comparison with figures 4.21 and 4.22, it can be seen that the discrepancies resembles the differences between a magnetized rod and a permanent magnet already shown for a single rod. In that occasion, an explanation was already hypothesized in terms of a combination of FEM inaccuracies and simple non-ideal behavior of the rod. This last statement is confirmed by the magnetization curves: both M_x and M_z show a discrepancy between a magnetized rod and a permanent magnet at the boundaries. However, as already stated for the case of a single rod, the region in which the two models show different responses is small in space and the

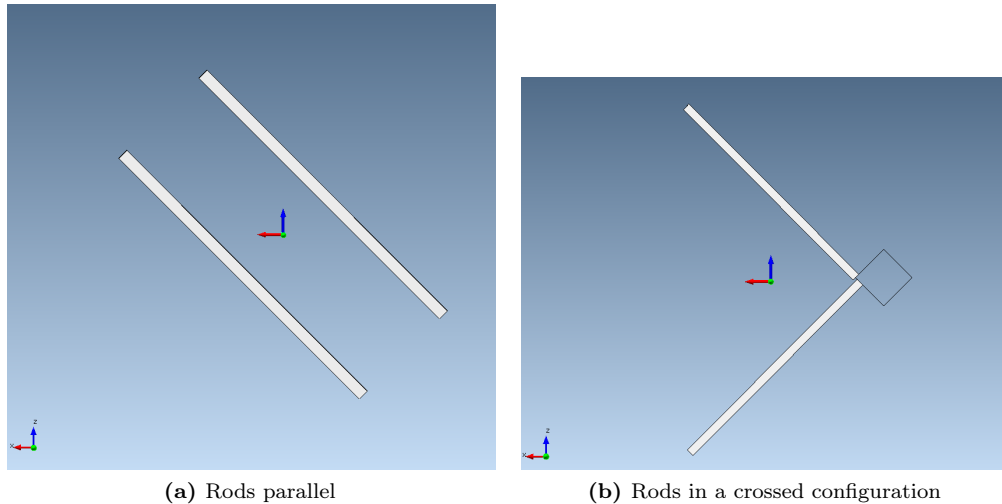


Figure 4.23: Sketch of the systems studied for the case of multiple rods in an external uniform field.

differences are not large.

The agreement between the models is otherwise pretty good for the region between the rod edges. In this sense, the mutual interaction between the rods is shown to be not particularly appreciable.

The statistical correlation plots collected for this configuration are not shown, because they are found to give similar information and insights as the ones for the case of a single tilted rod. In this sense, they confirm that the region in which a discrepancy between the models occur is limited in space. The results prove that, except for the very edges of the rods in which the magnetization pattern is no longer perfectly uniform, the description of the system in terms of permanent magnets is appropriate.

4.5.2 Crossed rods

The sketch of the configuration is given in Figure 4.23. The small squared box visible close to the edges of the two rods represents the spatial zone where mesh refinement has been implemented: the field measures are constrained to that zone because it is the most interesting to assess the non ideality of the system's behavior. The configuration is created as following, starting with two rods centered in $(0, 0, 0)$ and with the long axis parallel to the z axis:

- The first rod is rotated of 45° on the y -axis. The second rod is rotated of -45° on the y -axis.
- The first rod is translated of $(0, 0, 0.45)$. The second rod is translated of $(0, 0, -0.45)$.
- The second rod is translated of $(0.15, 0, 0.25)$. This creates the “crossed-shifted” configuration as in Figure 4.23

The field sampling has been done on a line of interest. The line chosen for this case goes from $(-0.34, 0, 0.11)$ to $(-0.46, 0, -0.01)$. A sketch is provided in Figure 4.26.

Different combinations of permanent magnets and magnetized rod have been used. They include:

- Two magnetized rods (MM configuration);
- A magnetized rod and a permanent magnet (MP configuration);
- Two permanent magnets (PP configuration).

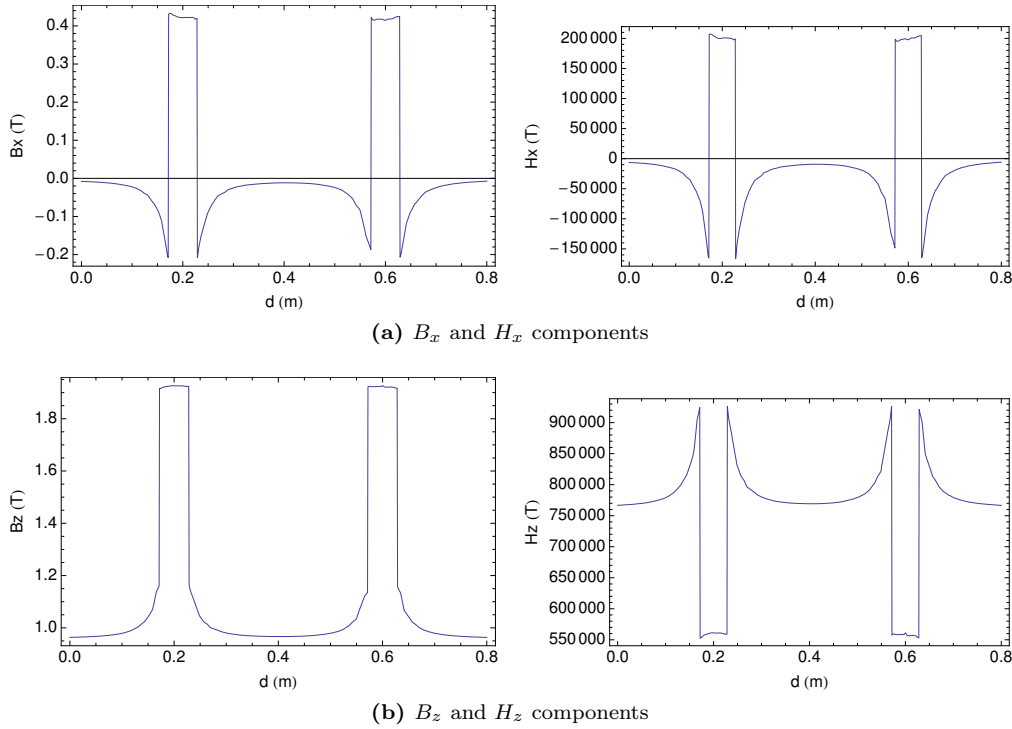


Figure 4.24: Plot of the field components in function of the coordinate d measured on the line $(0, 0, -0.4)$ to $(0, 0, 0.4)$. The reference frame chosen is shown in Figure 4.23

This approach has been adopted in order to provide a comparison between different situations and investigate the magnitude of the mutual interactions of the objects. Nevertheless, the ultimate comparison to be accounted for is the one between two magnetized rods and two permanent magnets, which constitute the objective of this overall testing section.

Figure 4.27 shows the x and z components of the magnetic fields and the magnetization. The pictures clearly show that a discrepancy arises between the different models. In particular, the PP configuration produces a higher value for the fields in the proximity of the surface of the rod. This behavior can be understood by looking at the magnetization curves: both the other configurations (MP and MM) show a divergence from the ideal step function of the magnetization for the PP configuration. This is believed to be the principal cause of the discrepancy observed. By comparing the MM and the MP configurations, it can be seen that the MP configuration is (as expected) more similar to the PP case. In particular, the MP configuration behaves like the MM one for small distances from the rod surface ($d \sim 0.12$) while it resembles the PP configuration at greater distances from the rod. To clarify further, the curves for the MP case show the field and the magnetization in the proximity of the magnetized rod (and not of the permanent magnet). Therefore, the higher values of the fields shown by the PP configuration at the rod's surface are ultimately to be due to the permanent magnet. This conclusion is in agreement with similar observations already made for a single magnetized rod and for the parallel rods of the previous subsection.

The discrepancies are smaller for the z-components. The curves in Figure 4.27 are, in fact, converging as the distance from the rod's surface increase. On the contrary, the x-component shows a worse agreement. It can be seen from Figure 4.27 that the MM case and PP one actually agree well for closer distances to the rod's surface, while they show an offset for larger ones. However, their profiles converge for even higher distances.

Figure 4.28 shows the linear correlation plots for the different field components between the two models. As in the case of a single magnetized rod, a discrepancy between the models is visible. The x-components of the fields show again the presence of branches, remarking the

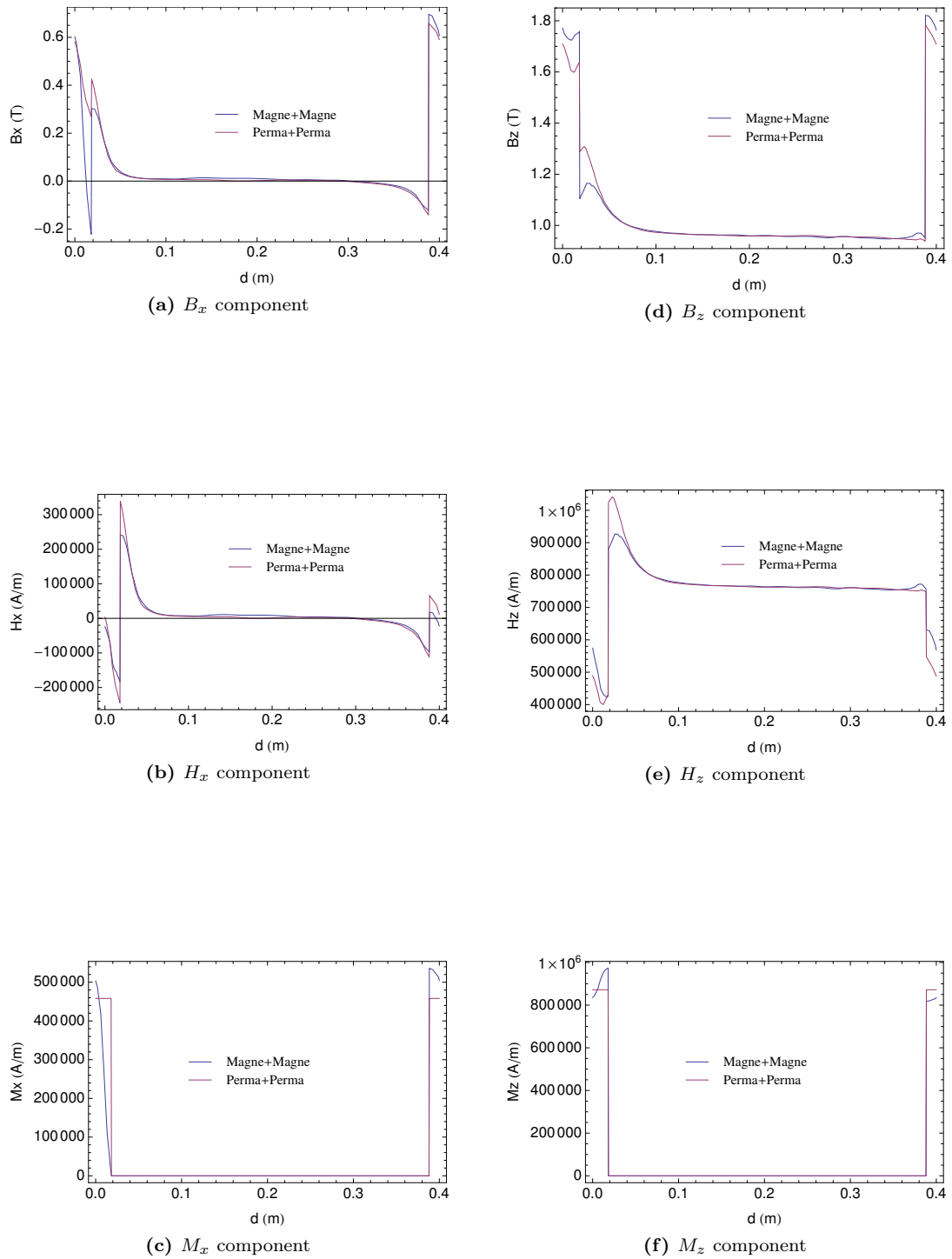


Figure 4.25: Plot of the field components and magnetization in function of the coordinate d measured on the line of interest. (a), (b) and (c) refer to the x-component. (d), (e) and (f) refer to the z-component. The reference frame chosen is shown in Figure 4.23 (parallel configuration)

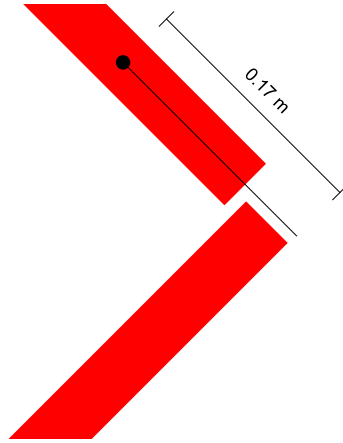


Figure 4.26: Schematic representation of the reference frame. The thin black line represents the locus of point on which the fields have been measured.

non-linear relation between the two models. For this reason, the R^2 and the fitting curve are not shown. As already pointed out, this confirms that the mutual magnetization effects cannot be disregarded in the small region very close to the top/bottom end of the rod.

The agreement for the z -components is better: the linear coefficients are higher, confirming the observations already made previously in the case of a single magnetized rod. Overall, the two models qualitatively exhibit the same behavior, though some numerical discrepancies are present. At a distance $d_{ref} = 0.3$ from the rod surface ($d = 0.15$ in the graphs) the numerical difference is estimated to be less than 10% of the field intensity for the z -components, while they are up to 25% of the field intensity for the x -components.

In conclusion, the comparison between a model consisting of two permanently magnetized rods and an equivalent one consisting of two magnetized rods in an external field shows that some discrepancies appear when the distance between the two rods is very small. These effects are produced because the magnetization curve for the magnetized rods does not follow the ideal step function displayed by the permanently magnetized rod. Nevertheless, it has been shown that the agreement between the two models is qualitatively good even in the proximity of the rods, where the non-ideal behavior is most expected. Even though a quantitative agreement in the numerical values is not reached, the two configurations displays the same curve profile, Most notably, the maxima and minima of the curves occur at the same points, confirming that the two models are in good agreement.

4.6 Conclusions

This overall chapter deals with the explanation of the different tests performed to validate the analytical equations for the magnetic field of an uniformly magnetized rod. In the first sections, it has been shown that the analytical equations can be effectively used to model a system of arbitrarily oriented rods which display a permanent arbitrary uniform magnetization. For a single rod, the correlation between the models resulted in linear coefficients higher than 96% for 26 out of the 27 cases presented. The last case's apparent discrepancy between the models has been motivated as solely due to the inaccuracy of the FEM model. For multiple rods, the correlation between the models resulted in linear coefficients higher than 95% for 10 out of the 12 cases presented. The apparent discrepancy in the last two cases has been motivated again as solely due to the inaccuracy of the FEM model. The graphical representations of the magnetic field components confirm this conclusion.

The second part of the chapter shows that a magnetic rod in an external field can be modeled by an equivalent permanent magnet, the magnetization of which can be obtained by solving a

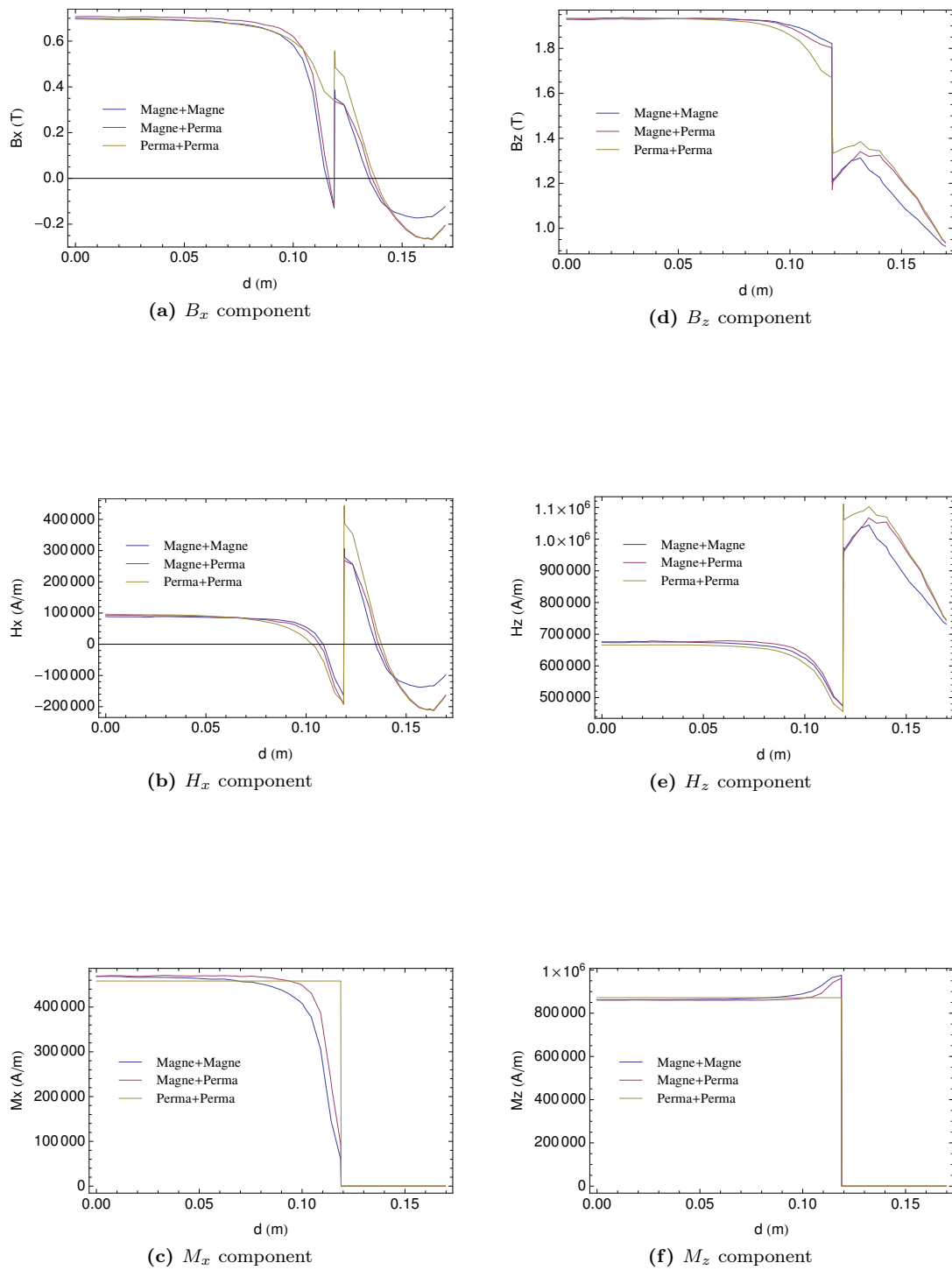


Figure 4.27: Plot of the field components and magnetization in function of the coordinate d measured on the line of interest. (a), (b) and (c) refer to the x-component. (d), (e) and (f) refer to the z-component. The reference frame chosen is shown in Figure 4.23 (crossed configuration)

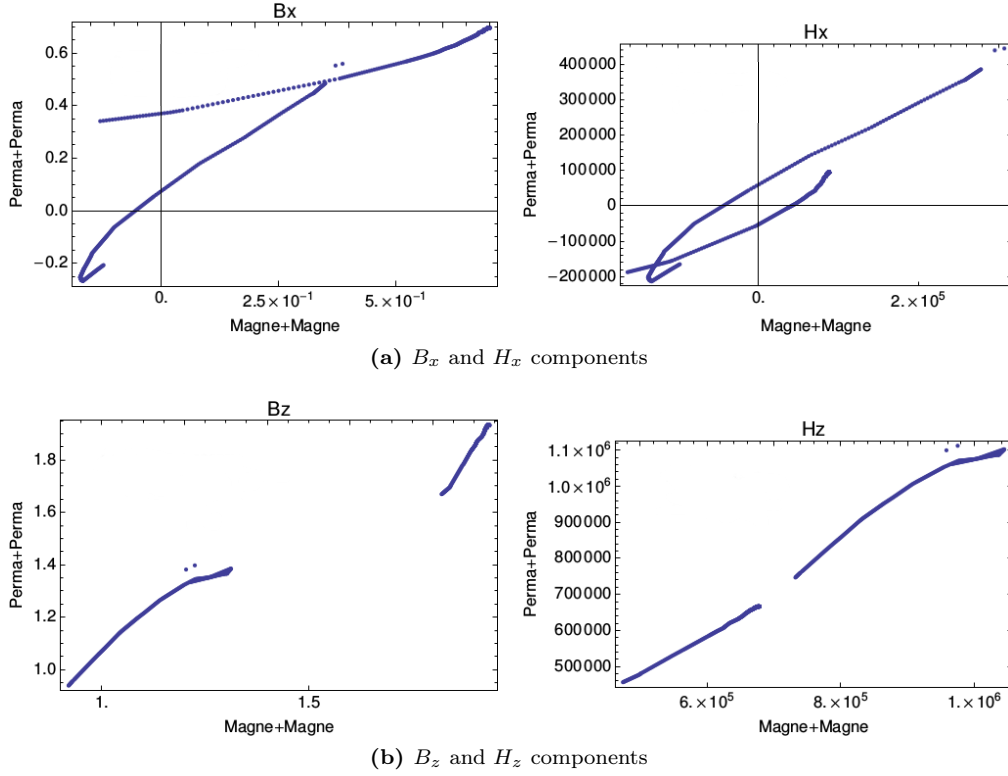


Figure 4.28: Linear correlation plots for the x and z field components. The comparison is done between the PP and MM models as described in the text.

constrained minimization problem, according to the Stoner-Wohlfarth model for a magnetized body. For a single rod, the correlation between the analytical model and the MagNet model resulted in linear coefficients higher than 99% for fields sampled in the center region. The presence of branches as well as the graphical plots show that a non-linear relation between the models exists for fields sampled in the corner region. The relative error between the field values outside the rod remains below 10% except that for a small region (less than 1% of the rod's length in extension) at the corner.

The last part of the chapter provides the comparison between the two different descriptions (real magnetized objects and analytical equations for magnetized objects) of a system of arbitrarily oriented magnetic rods placed in an external field. For parallel rods, the correlation between the analytical model and the MagNet model resulted in small discrepancies at the boundary surfaces. The discrepancies are the same as discussed for the single rod's case. For crossed rods, the correlation between the two models resulted in discrepancies localized at the region in which the rods almost come in touch. The relative error between the models remains below 25% in this critical region. Therefore, the description of the system via the analytical equations is qualitatively correct even in the regions where the mutual interaction between the rods plays a dominant role.

This proves that the analytical equations derived in Chapter 3 are suited to model an array of magnetized rods with long aspect ratio with good accuracy. The rods are assumed to be saturated by the external field, which leads to an analytical expression for the magnetic field generated by a random packing of ferromagnetic rods. This is handy to compute and very convenient for implementations in situations where an explicit formulation of the fields in functional forms is required (for example, in Molecular Dynamics simulations).

Chapter 5

Brownian Dynamics simulations and results

In this Chapter, the Brownian Dynamics simulations of a magnetic separation process on nanoparticles are presented. In the first section, the model system, comprising both the rod and the nanoparticles, and the preliminary studies are explained. In the second part, the simulations performed on a single rod are presented and the different rod's parameters on which the separation process has been optimized (namely, the angle between the rod and the external field and the rod's aspect ratio) are discussed. Moreover, the influence of the particle's size and its initial distance from the rod is investigated. In the third part, the strategy used for simulating the separation process for a collection of rods is explained and the results for two different configurations are compared and discussed. A connection between these observations and the liquid flow in the separation column is proposed and an estimation of the optimal column flow is given. The last part illustrates the studies performed on concentrated solutions of nanoparticles. The formation of chains and the separation efficiency as a function of the concentration and the rod's angle with the external field are investigated. Our results show that a power-law provides a good fit for the dependence of the separation time on the sample concentration. Moreover, the obtained data and its comparison with the available literature suggest that a magnetic separation process on superparamagnetic nanoparticles may follow an universal behavior.

5.1 Model System

The nanoparticles under investigation are modeled as Fe_3O_4 uncharged, almost hard-spheres, in order to match the real nanoparticles used in the experiments. Their density is taken to be $\rho = 5 \text{ g cm}^{-3}$ [92]. According to Equation 2.9 on page 24, the parameters n_d , M_S and V_d must be specified in order to have a complete description of the magnetic moment of the particles. M_S is taken to be 350 kA m^{-1} [34]. For the other details, we referred to the experimental data available on an ensemble of magnetic nanoparticles used in a previous study on magnetic separation by Schaller et al. [34]. Table 5.1 on the following page presents the complete magnetic properties for each particle diameter considered in the present study. Due to the similarity between the values of r_d for different particles, a value of 12 nm has been adopted for all the different particles considered.

The rods in the ferromagnetic matrix, according to the analytical model derived in Chapter 3, are characterized by their length L , their diameter D and their magnetization M . The saturation magnetization is taken to be $M_S = 985 \text{ kA m}^{-1}$: the value has been obtained by experimental measures on the rods that compose the actual separation column in the setup (see Chapter 1). The external magnetic field, oriented on the x-axis as discussed in Chapter 2, has been set to 1 T, which is a typical value used in the experiments. When subjected to this field, the rods reach saturation according to their hysteresis loop in Figure 1.12. The direction

Table 5.1: Magnetic properties for different Fe_3O_4 magnetic particles. a represents the particle radius. n_d represents the number of single magnetic domains. r_d represents the mean diameter of the single domains.

a (nm)	r_d (nm)	n_d
25	11.8	5
50	12.3	101
75	12.7	232
100	11.9	215
125	12.4	1489
212	11.7	6523

of the magnetization with respect to the rod axis is calculated via the method discussed in Chapter 3.

The solvent is considered to be water, for which a standard viscosity of $\eta = 1$ mPa s has been set. The friction coefficient of the particles is evaluated from the Stokes formula $\gamma = 6\pi\eta a$, where a represents the radius of the particle. The simulations are intended to be performed at room temperature $T = 298$ K. This sets the value of the thermal energy of the system to $k_B T = 4.14 \times 10^{-21}$ J. The diffusion coefficient of the particles is then evaluated via the Einstein formula $D = \frac{k_B T}{\gamma}$.

If not differently specified, the details given have been adopted for all the computations and results that will be reported in the following sections.

5.1.1 Preliminary evaluation of the equations

As a preliminary evaluation of the action of the rods in magnetic separation, the spatial zone in which a single rod exerts a notable attractive magnetic force has been studied. Such zone has been called *capture zone*. Its extension depends on the chosen threshold value of the magnetic force: a larger threshold value corresponds to a wider capture zone. The shape is, however, independent on the threshold value. Various orientations of the magnetization (i.e., various orientations of the rod with respect to the external field) have been considered. Figure 5.1 on the next page shows the capture zones as shown by rods with different aspect ratios, for a threshold value for the magnetic force of 0.15 in dimensionless units (the rod's radius is set to $R = 1$ and the magnetization magnitude is set to $M = 1$). Three angles with respect to the external field have been investigated: $\alpha = 0^\circ$, 45° and 90° .

The capture zones relative to different angles show a trend in the shape. For a rod oriented parallel to the external field ($\alpha = 0^\circ$), two ellipsoidal regions of high activity only appears at the top and bottom edges of the rod. The side region does not show an appreciable magnetic force. When the rod gets an inclination ($\alpha = 45^\circ$), the ellipsoids turn into two angular lobes, oriented opposite to each other. The side region starts to show a certain activity. Finally, when the rod is placed perpendicularly to the field ($\alpha = 90^\circ$), the lobes turn into a shape symmetric respect to the rod's axis, that encloses the entire rod. The side region becomes very active. Comparing the bottom and top rows of Figure 5.1, relative to two different aspect ratios, we see that the shape is basically conserved. However, the ellipsoidal regions for ($\alpha = 0^\circ$) become spherical for an higher aspect ratio.

From the preliminary analysis of the capture zones, it appears that the side region shows a prominent magnetic force only when the rod is not placed parallel to the field: its extent grows with the angle, with a maximum at $\alpha = 90^\circ$. Consequently, when placed parallel to the field, a rod with a larger aspect ratio presents a larger volume in which almost no magnetic force is generated. These two preliminary predictions (a small magnetic activity on the side region of the rod and a better performance from a short rod than from a long one) will be validated in the following sections.

The capture zones shown in Figure 5.1 on the facing page are calculated only taking into

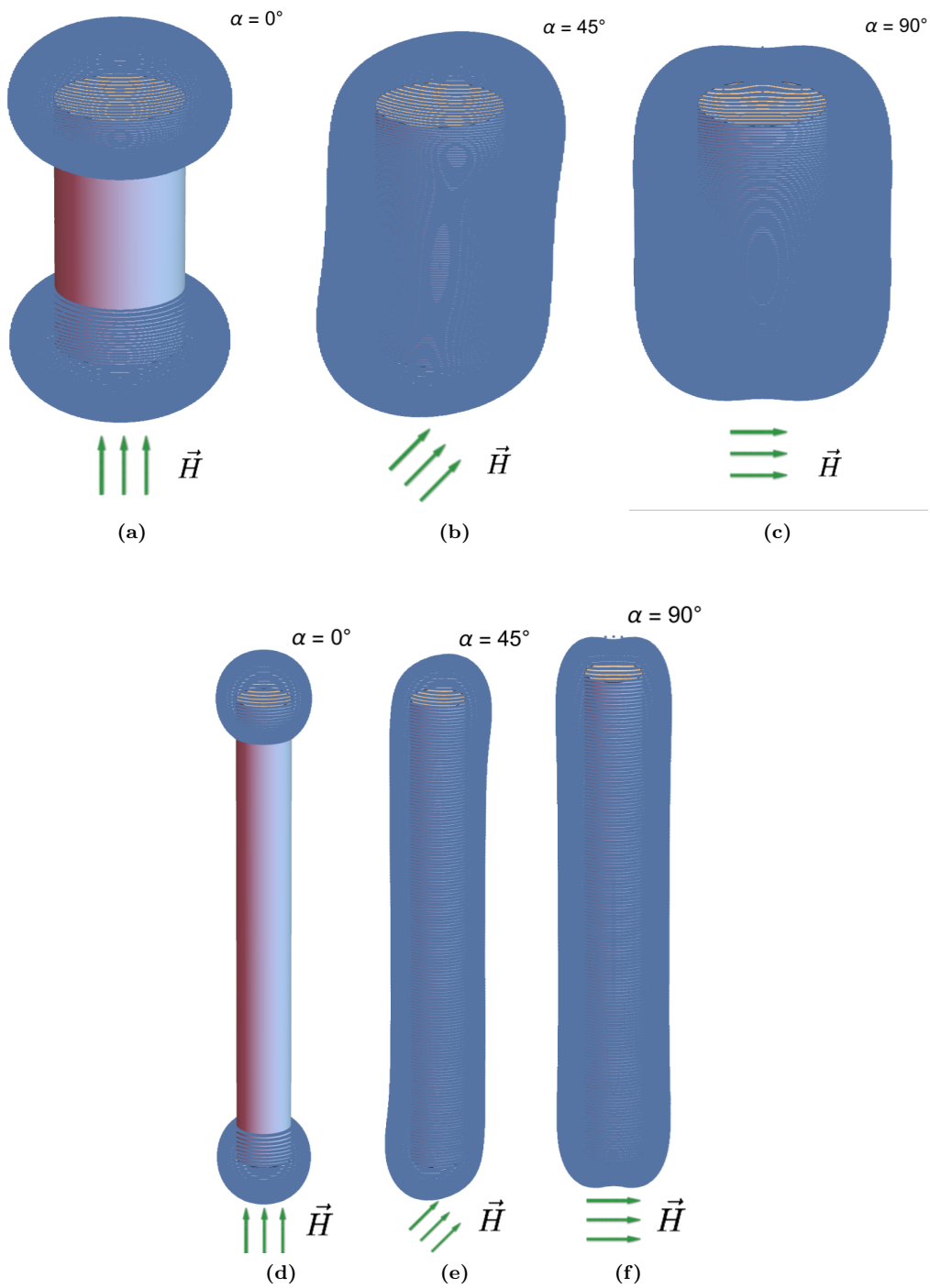


Figure 5.1: Capture zones for different rods angles and aspect ratios. The top row refers to a rod with $L/D = 2$. The bottom row refers to a rod with $L/D = 6$. The capture zones are evaluated for a threshold value of 0.15 in dimensionless units (where $R = 1$ and $M = 1$). The angle express the orientation of the rod with respect to the external field.

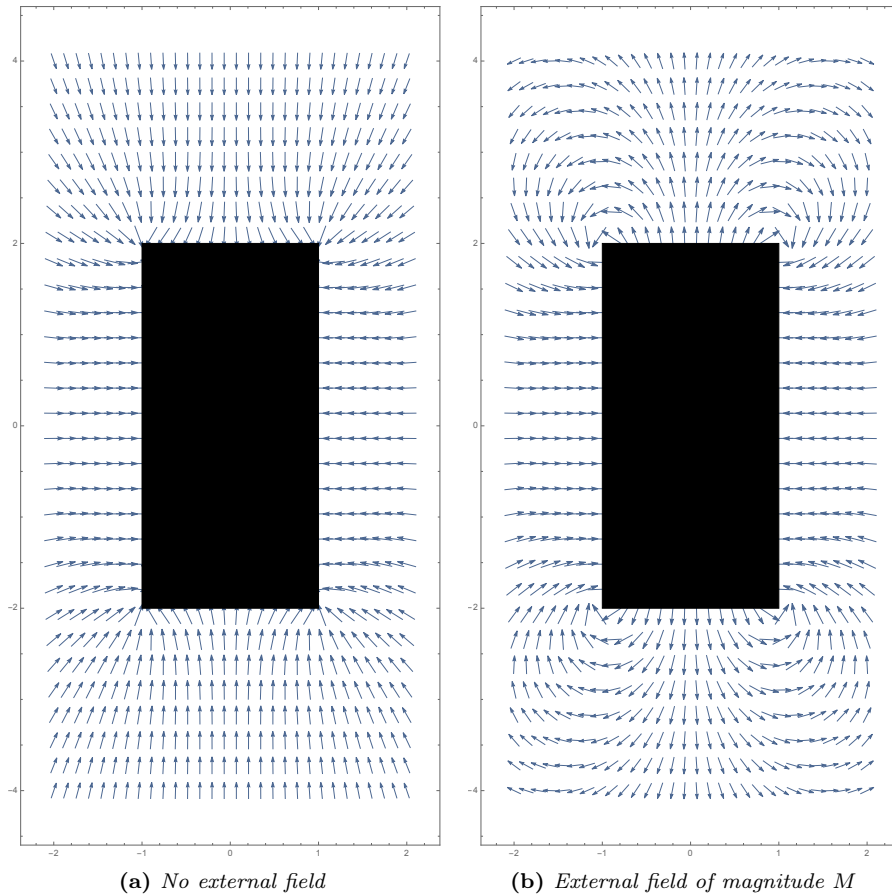


Figure 5.2: Field lines of the magnetic force vector field taken on the $y = 0$ axis of a $L/D = 2$ rod. Two situations in which the external field is included or not are compared.

consideration the field created by the rod. More in details, the rod is assumed to be magnetized by the external field and thus to acquire a certain magnetization. This magnetization produces in turn a non-homogeneous field, which is the responsible for the actual separation process. The capture zones refer to this final field. This could suggest that there is no need to specifically include the external field in the system description: the specification of the magnetization acquired by the rod appears to be sufficient. However, we note that the presence of the external field has a rather great impact on the magnetic force on the particles. Figure 5.2 shows the field lines, taken on the plane $y = 0$, of the magnetic force vector field for a rod. The configuration when the field is added in the description is compared to a situation in which only the field generated by the rod is considered.

It is evident that the explicit presence of the external field in the system description is of crucial importance, even though it only adds a uniform contribute. In particular, it is possible to see that, while the field lines for the *no-field* situation describe an attractive force everywhere in space, the field lines for the *field* situation shows a contrasting picture. Some field lines close to the top and bottom edges are even depicting a repulsion from the rod. The reasons behind this counterintuitive behavior can be traced back to the equation for the magnetic force, Eq 1.1 on page 4. As the magnetic moment of a superparamagnetic particle (according to the Langevin Model used in this study) is oriented in the same direction of the total magnetic field, the external field strongly affects the magnetic force field lines. We expect to confirm this preliminary investigation via the simulations of the particle motion, illustrated in the following sections. In conclusion, the external field must be added to the description of the system, even though it is a uniform field: its presence has a profound influence on particles motion in the

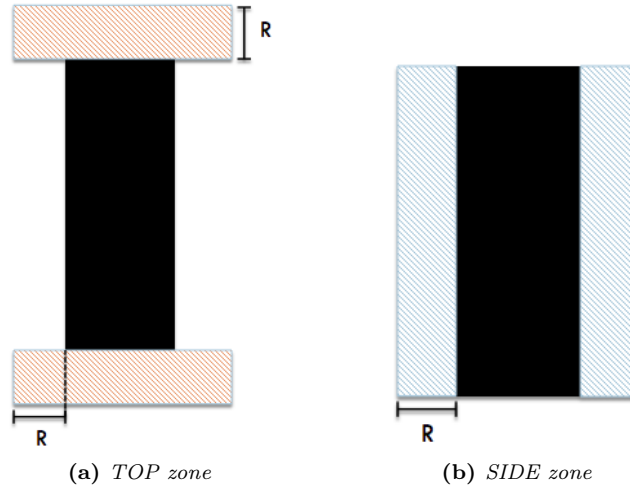


Figure 5.3: Different initial particle configurations. R represents the radius of the rod.

field gradient generated by the ferromagnetic matrix, even though the external field is not directly responsible for such gradient.

5.2 Optimization study on a single rod

The results obtained from the preliminary evaluations of the activity of a single rod demonstrate that the latter is already able to exert a reasonable magnetic force on the particles, according to the space region covered by the capture zone. This means that a single rod is expected to be already able to separate the nanoparticles.

We investigated the capture of nanoparticles on a single rod by varying two macroscopic parameters: the aspect ratio L/D of the rod and the angle that its axis has with respect to the external field. In order to compare the separation efficiency also for different particle sizes, nanoparticles with radii mentioned in Table 5.1 on page 82 have been studied. To the extent of our knowledge, no other similar study has been conducted before.

The use of a single rod has been preferred over implementing a full multi-rod matrix (which is nevertheless possible in the algorithm developed by us) for two principal reasons. The first one is that simulating a single rod can dramatically scale down the computational time needed to perform the calculations, which has a dependence $\mathcal{O}(N_{\text{rods}})$. The second one is that a single rod is the first step in a quantitative study of the performance of the matrix in the separation process. The implementation of a full multi-rod system can follow this first study as a second step and upgrade.

The particles are generated randomly in a space portion around the rod (see Figure 5.3). We distinguish two zones: a TOP zone, in which the particles are generated close to the top and bottom surfaces of the rod, and a SIDE zone, in which the particles are generated close to the lateral surface of the rod. A dilute system of $N = 100$ particles has been studied. For each zone, 30 different simulations have been run in order to obtain a good statistics on the system. As the system is dilute, the simulation time step has been increased to $\Delta t = 5 \times 10^{-5}$ s. Each simulations has been run for a maximum separation time of $t_{\text{max}} = 50$ s.

5.2.1 Angle optimization

The orientation of the rod with respect of the external field has been varied between 0 and 90 degrees. The fraction of particles captured at the end of the separation process has been investigated. Figure 5.4 on the following page shows the time evolution of the capture fraction for two different particle sizes and a specific value of L/D . The curve referring to both the

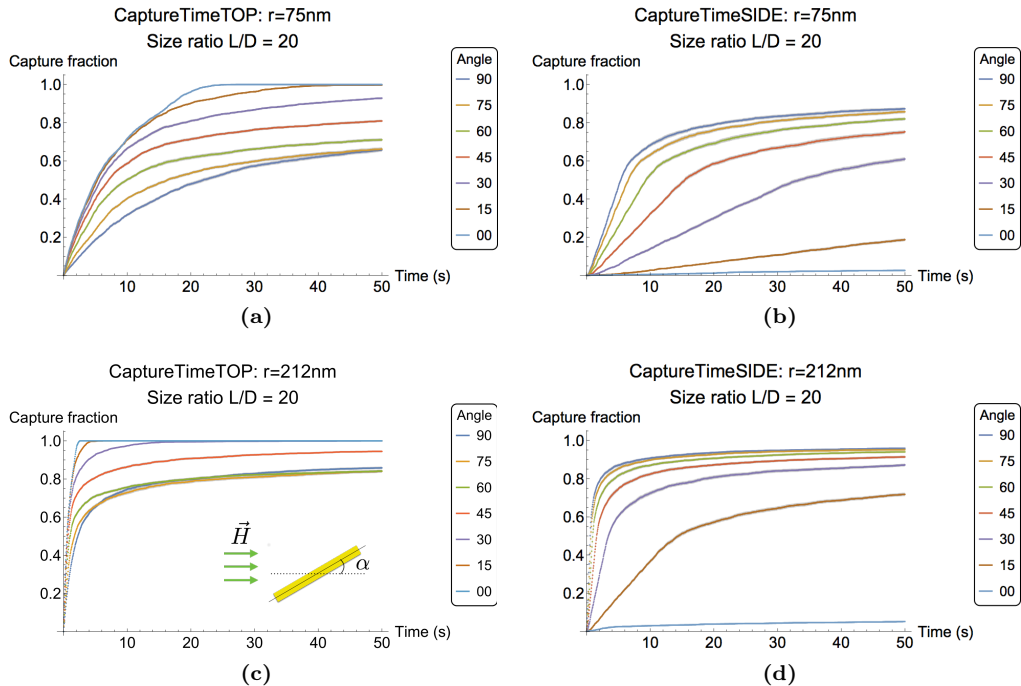


Figure 5.4: Time evolution of the capture fraction for different particle sizes. Different curves correspond to different angles. The labels *TOP* and *SIDE* refer to the initial configuration of the particles. The standard error relative to each curve is reported: in most of the cases, it is smaller than the size of the marker in the graph.

SIDE and *TOP* zones graphs are shown.

We observe a radically different behavior between the two zones investigated. For the *TOP* zone, the final capture fraction for low inclination angles of the rod approaches unity. For high angles, on the contrary, the capture fraction is slightly larger than 0.5 (Subfigures 5.4a and 5.4c). Lower angles are therefore more efficient in separating particles in the *TOP* zone. The behavior is inverted when considering the *SIDE* zone, for which the low angles show almost no efficiency at all (Subfigures 5.4b and 5.4d). This confirms our preliminary evaluations: the rods with low inclination angles concentrate their capture activity exclusively on the edges, while the lateral surface is mostly inert.

For both the *TOP* and *SIDE* zones, the low efficiency can be understood by observing the time trajectories of the particles. Figure 5.5 on the next page shows the trajectories of $N = 200$ particles of size $r = 125$ nm for the two limit angles considered in the study (0 and 90).

It can be seen that, due to the force field generated by the rod, some particles experience a depletion from the surface, thus being not captured within the time frame of the separation process. This is also a confirmation of one of the preliminary evaluations made in the previous section. The disordered pattern shown by the depleted particles at the end of their time trajectories (red in the color gradient) is due to the Brownian motion. In fact, when driven away from the rod, the particles experience anymore a weaker magnetic force and Brownian motion starts to dominate their dynamics.

In order to assess the dependence of the separation efficiency with the orientation of the rod in the external field, the capture fraction at the end of the separation process is plotted against the different angles. This is done by combining the *TOP* and *SIDE* data sets in a total set for the L/D value of interest. By varying the aspect ratio of the rod and keeping the total number of particles in the system fixed, it is evident that the ratio between the *TOP* and *SIDE* volumes changes and it is not correct to simply add the two data sets together. For a

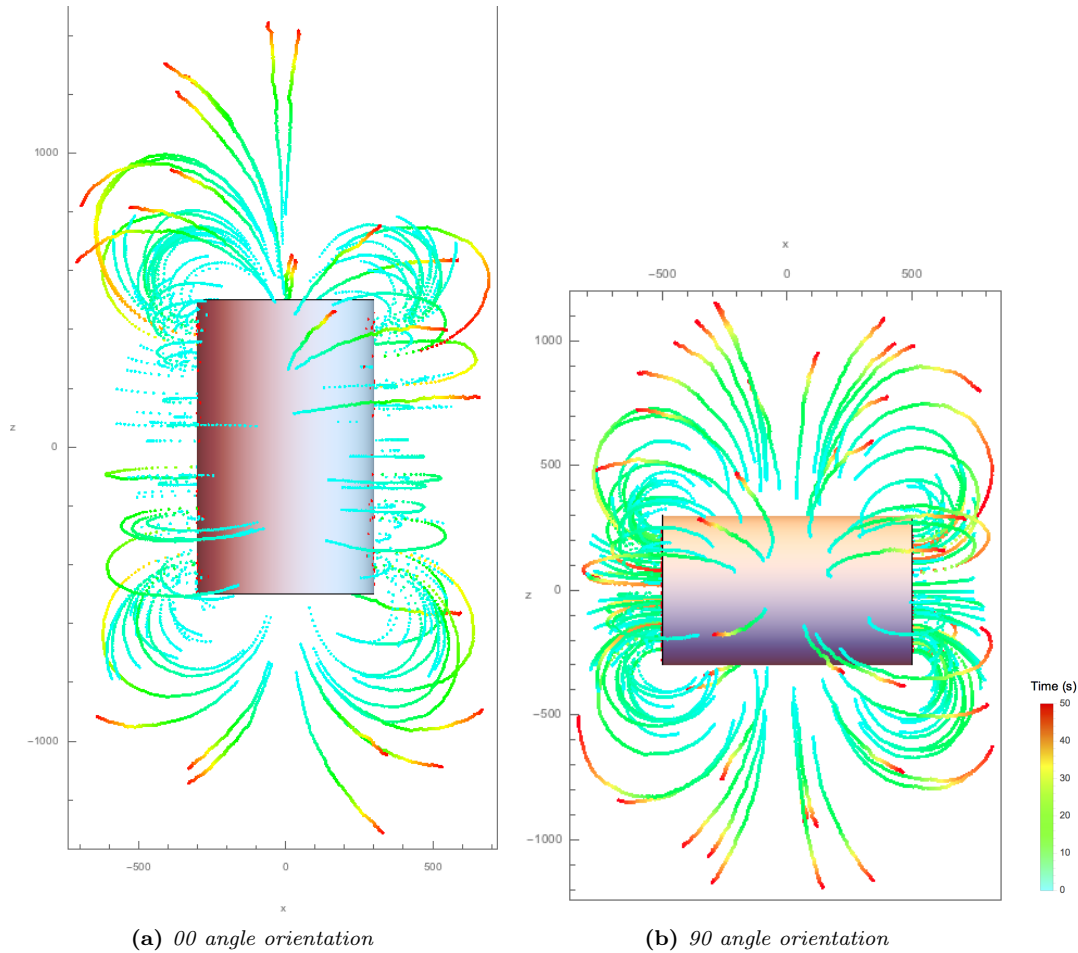


Figure 5.5: Time trajectories of $r = 125$ nm particles for a rod with $L/D = 1.66$. Time is shown via a color gradient. The external field is applied on the x -axis direction.

correct combination, a total set is built by including the *TOP* and *SIDE* sets with a proper weight determined by the fraction of the overall volume occupied by the single zone (*TOP* or *SIDE*). Such method for combining different data sets is also adopted for the angles, assuming an equal weight for all of them as no angle is to be preferred on the other. In the following, when referring to a total set of data (either built from *TOP* and *SIDE* zones or from the different angles), we always assume that the weighting procedure has been adopted. Figure 5.6 on the following page shows the obtained efficiency curves for the six different particle sizes considered in this study.

The curves show a very low capture fraction for the case of a rod parallel the field (0° angle). The largest sizes show a steep curve that reaches saturation already at low angles (30°). The other sizes show a rising curve as well, but they exhibit a different behavior. For the sizes from $r = 100$ nm to $r = 50$ nm, the curve shows an initial low increase in the capture fraction with the angle. Between $\alpha = 15^\circ$ and $\alpha = 30^\circ$, however, the steepness of the curve becomes larger and the saturation regime is reached upon $\alpha > 45^\circ$. A similar behavior could be expected for the larger sizes as well: the low sensitivity in the angle variation (15°) probably hinders the transition between the low and high increase regimes.

The smallest size investigated ($r = 25$ nm) shows a different behavior. Here, the capture fraction remains low (under 0.4) for the whole range of angles considered. However, it is possible to recognize a low increase regime when $0^\circ < \alpha < 30^\circ$ and a higher increase regime for larger angles. The saturation limit is not approached in this last case. There are two main reasons for this behavior: either the maximum separation time (50 s) is too short or Brownian

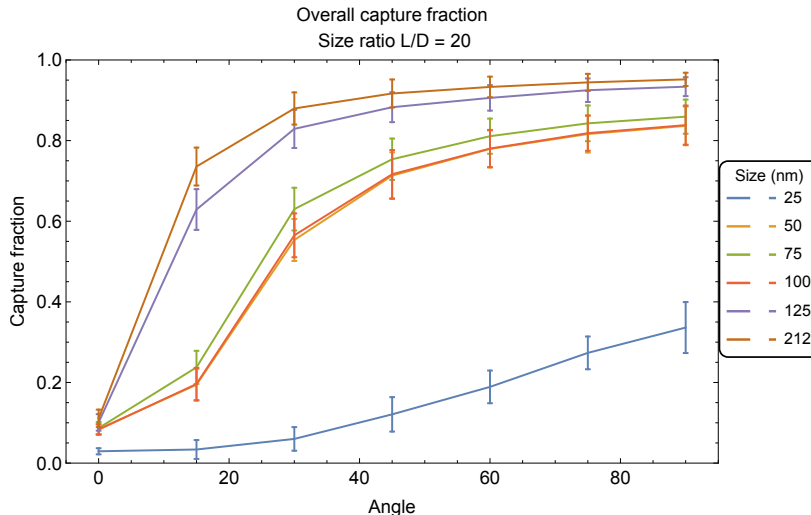


Figure 5.6: Plot of the overall (for both *SIDE* and *TOP* zones) maximum capture fraction on different angles. The error bars express the standard deviation of the plot points.

motion dominates the dynamics of many particles. This aspect will be investigated in the next subsection.

For the purpose of our optimization study, the curves clearly show that the efficiency is at its minimum when the inclination angle of the rod respect to the field is small. Therefore, we conclude that, for efficiency purposes, the best orientation of a single rod is perpendicular to the external field: in such configuration, the maximum capture fraction is obtained for all the particle sizes considered.

5.2.2 Aspect ratio optimization

The aspect ratio the rod has been varied between 1.66 and 20. The diameter of the rod was kept at a constant value $D = 600 \mu\text{m}$ while the length L is varied. The value of 20 is given by the longest rod currently available in the separation setup. A rod with aspect ratio 1.66 is not yet available in the experimental setup: however, it has been chosen to investigate a full range of different aspect ratios, from the limit of a long rod ($L/D = 20$) to a cylinder almost as thick as its height ($L/D = 1.66$). The differences in the fraction of particles captured at the end of the separation process have been investigated. Figure 5.7 on the next page shows the time evolution of the capture fraction for a particle size of $r = 125 \text{ nm}$ and two different values of L/D . Both the *SIDE* and *TOP* zones graphs are reported.

By varying the aspect ratio of the rod and keeping the total number of particles in the system fixed, it is evident that rods with larger L/D will handle systems with lower concentrations. This does not introduce a bias in the separate results for the *TOP* and *SIDE* zones, as the capture fraction is not dependent on the actual value of the concentration as soon as the system is considered dilute, which is here satisfied (see Section 5.2).

We observe a slightly different behavior between the two aspect ratios curves. For the *TOP* zone (Subfigures 5.7a on the facing page and 5.7c on the next page), the aspect ratio does not seem to affect the separation efficiency. On the contrary, the *SIDE* zone shows a dramatic increase in the final capture fraction for low angles values when the aspect ratio is reduced (Subfigures 5.7b on the facing page and 5.7d on the next page). This confirms the preliminary evaluations on the capture zone of the rod made in the previous section: due to their reduced length, the rods with small aspect ratios will have a larger activity on the side because the capture zones on the edges will extend to include part of the rod's small length. We also note

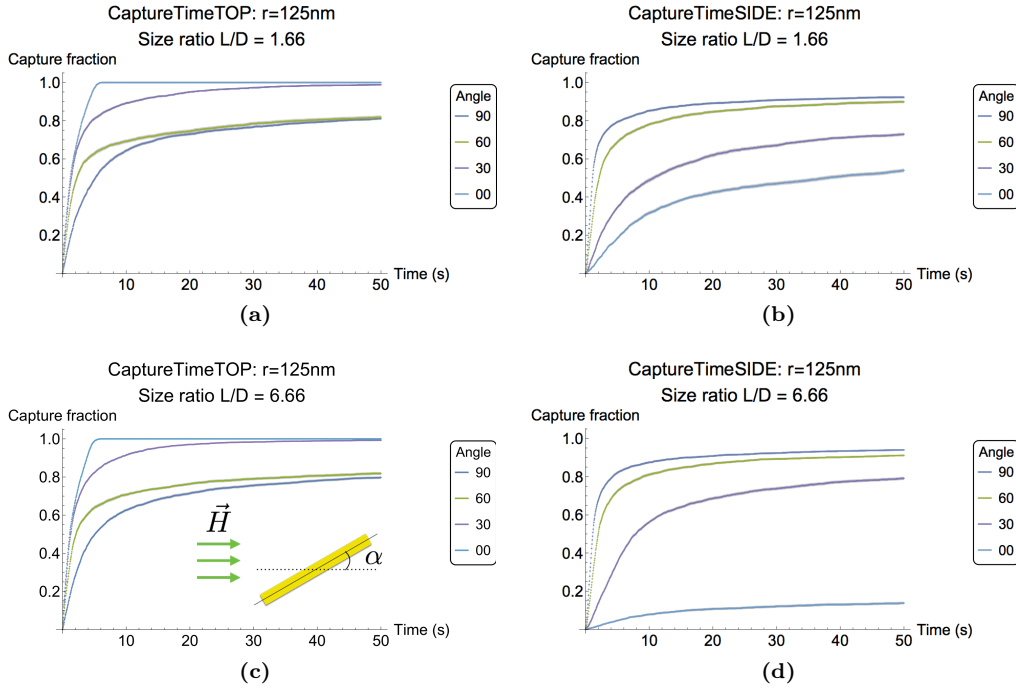


Figure 5.7: Time evolution of the capture fraction for different aspect ratios. Different curves correspond to different angles. The labels *TOP* and *SIDE* refer to the initial configuration of the particles. The standard error relative to each curve is reported: in most of the cases, it is smaller than the size of the marker in the graph.

that the final capture fraction for high angles values decreases when the aspect ratio becomes smaller, in contrast with the behavior observed for low angles. We explain this observation by considering that the small rods will also generate a magnetic field which possesses a larger spatial decay. Therefore, a small rod influences far particles less than a long rod.

For the low angles in the *SIDE* zone, the change in efficiency between different aspect ratios can be understood by observing the time trajectories of the particles. Figure 5.8 on the following page shows the trajectories of $N = 200$ particles of size $r = 125$ nm with an angle of 0° for the two aspect ratios considered previously.

It can be seen that, for the case $L/D = 20$, all the particles along the side of the rod does not feel any influence by the rod. On the contrary, the shorter rod ($L/D = 1.66$) is able to capture the particles on the side thanks to its force field, which depletes particles along the lateral surface to collect them on the edges. It is evident, therefore, that the length of the rod largely influences the motion of the particles at small angles inclinations with respect to the external field.

In order to assess the dependence of the separation efficiency with the aspect ratio of the rod, the capture fraction at the end of the separation process is plotted against the different values of L/D . Figure 5.9 on page 91 shows the obtained efficiency curves for the six different particle sizes considered in the study.

The curves all show a similar behavior: the maximum capture fraction increases when the aspect ratio decreases. The effect is particularly visible for the larger sizes considered, for which the maximum capture fraction increases from a value of around 0.7 ($L/D = 20$) to a value of around 0.9 ($L/D = 1.66$). For smaller particle sizes, the rise is less evident, giving an overall increase of about 0.1 between the two extrema in the curves.

The smallest size investigated ($r = 25$ nm) exhibits also the smallest increase in the capture fraction, with a value rising of just above 0.05. The reason of this low improvement is to be

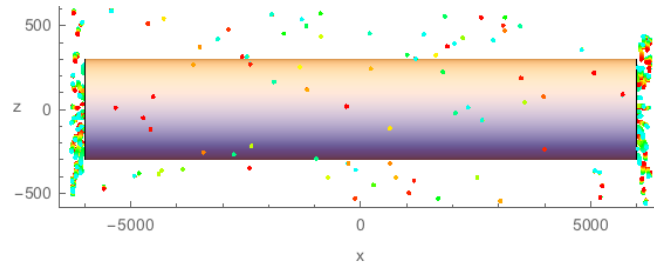
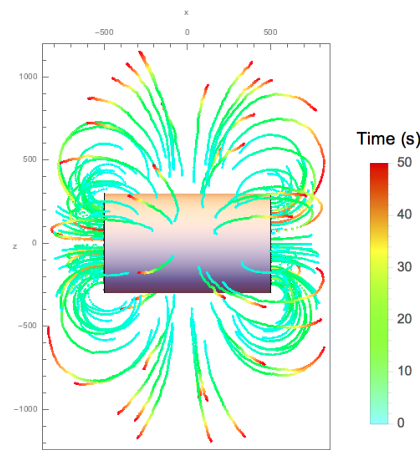
(a) $L/D = 20$ (b) $L/D = 1.66$

Figure 5.8: Time trajectories of $r = 125$ nm particles for two rods with different aspect ratios. Time is shown via a color gradient. The external field is applied on the x-axis direction. Note that, for the graph relative to $L/D = 20$, the axes are not proportional (because of length constraints).

probably accounted for the overall very limited capture fraction values which are obtainable with the $r = 25$ nm size. As already mentioned, this aspect will be investigated in the next subsection.

The overall small rises in the capture efficiency do not confirm the observation outlined above when the different curves for the *TOP* and *SIDE* zones were discussed. It has to be noticed that, however, the overall curves refer to an average on the different angles. It is interesting to see the behavior of the capture fraction as a function of the aspect ratio for the different angles considered. Figure 5.10 on page 92 shows the maximum capture fraction at different values of L/D for various orientation angles. The particle size is taken to be $r = 125$ nm. The graphs referring to both the *SIDE* and *TOP* zones are reported.

The *TOP* graph shows that, for all the angles considered, the variation in the capture fraction is almost negligible upon varying the aspect ratio, with only a slight dependence for the small angles curves. The *SIDE* graph shows a much more interesting picture. Considering the single values, all the angles except 0° give better capture fraction when the aspect ratio is larger. On the contrary, the 0° angle shows a steep decrease in the maximum efficiency when the aspect ratio is increased. This last observation is in agreement with the considerations about the increase in the *SIDE* curves capture fractions when L/D is decreased, as shown in Figure 5.7 on the previous page. It explains, therefore, why the performance of the shorter rods is only slightly better than the longer ones, as observed in Figure 5.9 on the facing page. As in the latter plot the results are obtained as an average of both the zones and the angles, the dramatic increase in the capture fraction observed for the *SIDE* zone in the specific case of $\alpha = 0^\circ$ is smoothed. Finally, it has been investigated whether the shape of the curves in Figure 5.10 on page 92 is size-dependent. Figure 5.11 on page 93 shows the comparison between the *SIDE*

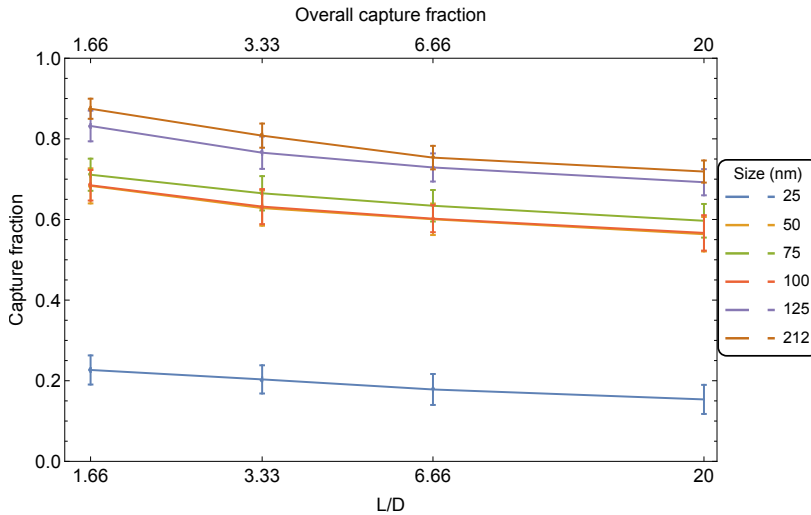


Figure 5.9: Plot of the overall (for both *SIDE* and *TOP* zones and the angles considered) maximum capture fraction on different aspect ratios. The error bars express the standard deviation of the plot points.

curves for different particle sizes.

The *TOP* curves are not shown because they are less significant than their *SIDE* counterpart. It is possible to see that the $r = 25$ nm curve shows a very mild dependence of the capture fraction on L/D , in contrast with the $r = 125$ nm curve. We conclude that the increase in efficiency with L/D is to be limited to large particle size, while the capture fraction for small particles is not significantly enhanced by shorter rods.

For the purpose of our optimization study, the curves show that there is an overall mild increase in the maximum capture fraction for lower L/D values. Therefore, we conclude that shorter rods are more efficient than longer rods in the separation process. We also observe that, however, this improvement is extremely dependent on the angle: an appreciable increase in capture fraction is only observed for the 0° case. Moreover, there is also a strong size dependence, in the sense that large particles are more affected than small particles by this increase in the rod's capture efficiency. In conclusion, we state that the L/D parameter is less important than the angle of the rod with the external field for the optimization study on a single rod.

5.2.3 Influence of the rod on far particle

The study of the rod's capture efficiency on the two parameters considered in the past sections revealed a low performance for the smallest particle considered, $r = 25$ nm. Two reasons have been proposed to account for it: a too small separation time or a too high percentage of particles for which Brownian motion dominates over the magnetic force. In order to assess how many particles do not feel the influence of the rod, their mean displacement at the end of the separation process (50 s) has been evaluated. Indicating with $\langle x \rangle$ the time averaged displacement of the particle, if the following criteria holds:

$$\langle r^2 \rangle < 2\langle r^2 \rangle_{\text{Brown}} \quad (5.1)$$

the particle motion does not show an appreciable drift, and therefore Brownian motion dominates the particle dynamics. $\langle r^2 \rangle_{\text{Brown}} = \sqrt{6Dt}$ is the Einstein equation for the mean quadratic displacement of a Brownian particle [52]. We will refer to the (normalized) number of particles that satisfies the above mentioned criteria as the Brownian particles percentage.

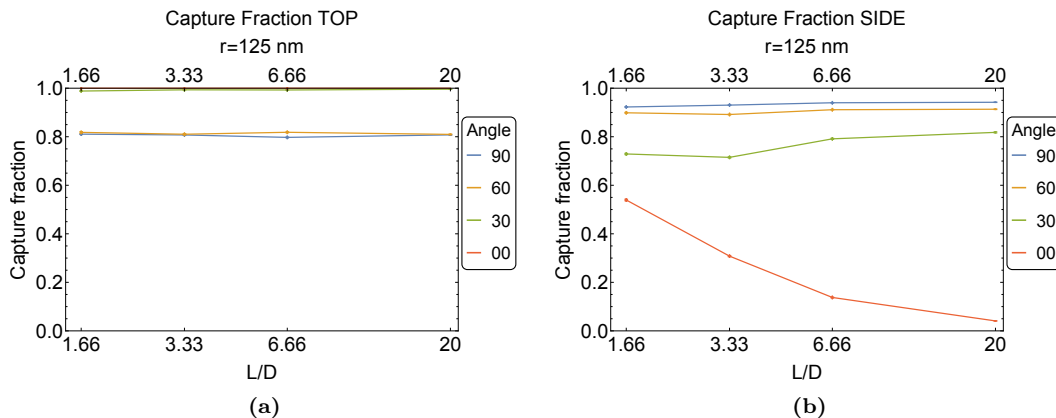


Figure 5.10: Maximum attainable capture fractions for different aspect ratios. Particle size is taken to be $r = 125$ nm. Different curves correspond to different angles. The labels *TOP* and *SIDE* refer to the initial configuration of the particles. The standard error relative to each curve is reported: in most of the cases, it is smaller than the size of the marker in the graph.

Figure 5.12 on page 93 shows the dependency of the Brownian particles percentage on the angles. The study refers to a size ratio $L/D = 20$. Both the *SIDE* and *TOP* zones graphs are reported. The *TOP* case shows an interesting behavior. Except that for the smallest size investigated, the Brownian particles percentage is always zero, irregardless of the angle. This is a confirmation of what was previously stated: the *TOP* zone of the rod is more active than the *SIDE* zone during the separation process. The case $r = 25$ nm shows a finite percentage of Brownian particles above 20%, which increases as the angle increases. This means that a rod placed perpendicularly to the field is less active in capturing particles on the *TOP*. The behavior reflects what has already been observed for the angle optimization study case (see Subsection 5.2.1). The *SIDE* case, on the contrary, displays an opposite behavior: small angles show higher Brownian percentages, demonstrating again that a rod placed parallel to the field is less active in capturing particles on the *SIDE*. It is interesting to note that all the sizes considered show high Brownian percentage in the limit case $\alpha = 0^\circ$, independently of the zone (*TOP* or *SIDE*). This observation suggests that in the *SIDE* region of a rod with $\alpha = 0^\circ$, diffusion dominates the dynamics of every particle.

In order to give a complete analysis of the dependence of the Brownian particles percentage on the orientation of the rod, an overall curve in which the results for the *TOP* and *SIDE* are combined is plotted. The combination was done accordingly to a weighting procedure for the two spatial regions analogously to that discussed in the previous sections. Figure 5.13 on page 94 shows the obtained percentage curves for the six different particle sizes considered in the study.

The graph shows, as expected, that the *SIDE* behavior dominates the overall dependence of the Brownian percentage with the angle, due to the larger spatial volume of the *SIDE* zone with respect to the *TOP* zone. For all the particle sizes except for $r = 25$ nm, a high percentage of Brownian particles is observed only for low angles. According to the size of the particles, the number of Brownian particles goes to 0 already for small angles (15°) or for slightly larger angles (30°). For the smallest size ($r = 25$ nm), the Brownian particle percentage remains high for almost all the angular range investigated, being lower than 20 % only for angles larger than 60° . It is also interesting to note that, even for $\alpha = 90^\circ$, the Brownian percentage does not reach zero, as observed for the other sizes.

The percentage of Brownian particles in the system is directly correlated with the maximum capture fraction obtainable in the separation process, independently of the separation time. It

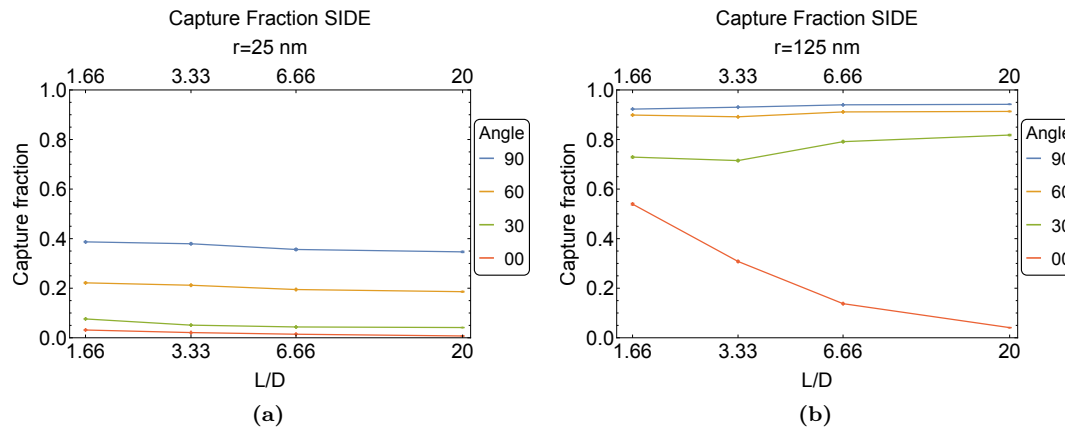


Figure 5.11: Maximum attainable capture fractions for different aspect ratios. Different curves correspond to different angles. The standard error relative to each curve is reported: in most of the cases, it is smaller than the size of the marker in the graph. The particle size to which each graph refers is given in the plot labels.

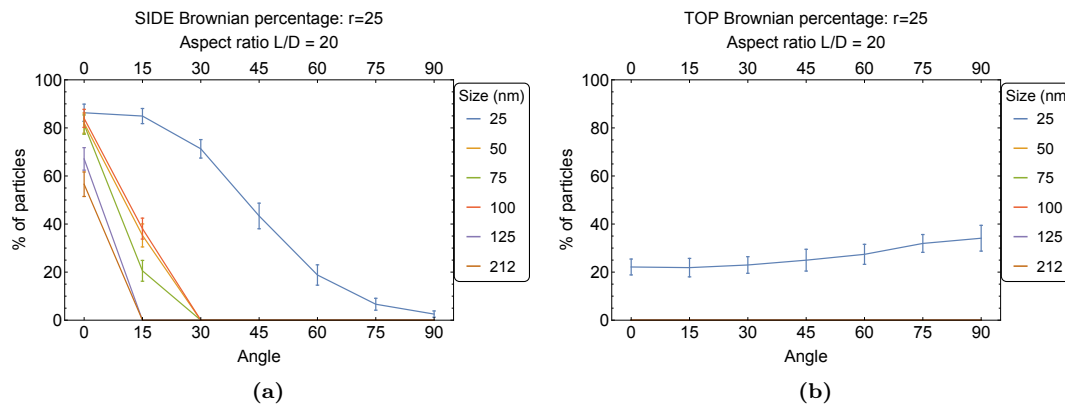


Figure 5.12: Brownian particle percentage in the separation process for different orientation angles of the rod with the external field. Different curves correspond to different angles. The standard error relative to each curve is reported.

will not be possible to obtain a capture fraction higher than $(1 - \%_{\text{Brownian}})$, as those particles will not feel the rod. However, it is possible that those particles, by means of free diffusion, are able to enter a region in which the rod exerts an active magnetic force. However, as diffusion is not driven by external forces in this case, the average number of particles captured due to random walking into a region in which the magnetic force is stronger is considered to be negligible.

Figure 5.14 on page 95 shows the total percentage of Brownian particles in the system for the different particle sizes considered in this study. The overall results are obtained by combining the *TOP* and *SIDE* zones in the same fashion as described above. Again, the results are an average over the different angles, assuming an equal weight for all of them as no angle is to be preferred on the others.

A low percentage (below 10%) of Brownian particles is present even for the larger sizes ($r = 125$ nm and $r = 250$ nm). As seen in the previous figures, this contribute comes exclusively from the low angle configurations. A percentage of around 15% is observed for the other sizes except the smallest. It is due to the same reason as the one mentioned for the larger particles. For the lowest size, the percentage of Brownian particles is observed to be above 40%. This precludes the possibility, for a separation process with a single rod, to obtain a capture fraction

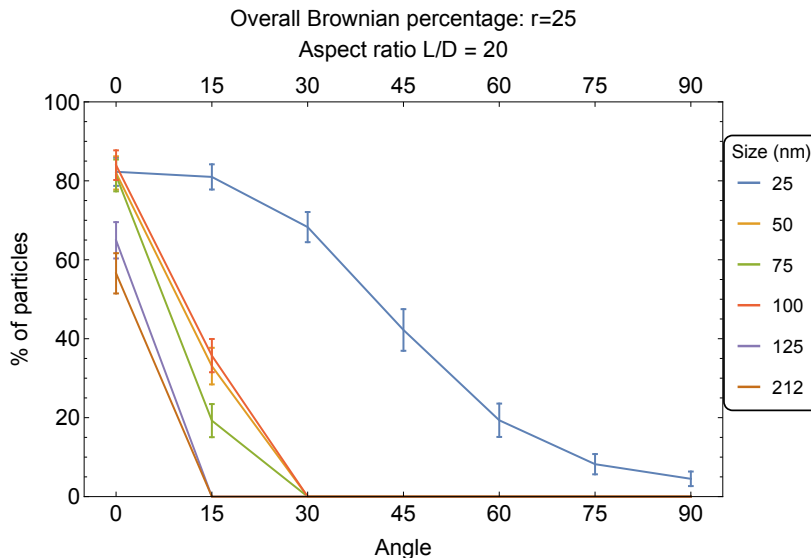


Figure 5.13: Plot of the overall (for both *SIDE* and *TOP* zones) Brownian particle percentage for different angles. The error bars express the standard deviation of the plot points.

higher than 0.6 for the particle size $r = 25$ nm, irregardless of the duration of the separation. Lastly, it is interesting to note that, for the size $r = 100$ nm, there is an apparent inversion of the observed trend according to which larger sizes lead to smaller brownian percentage: this particular size shows, on the contrary, a percentage comparable with the $r = 50$ nm case. This observation will be further investigated in the following section.

To investigate how the aspect ratio influences the percentage of Brownian particles, the same analysis as described in the previous section for an aspect ratio $L/D = 20$ has been extended to the other aspect ratios considered in this study. Figure 5.15 on page 96 shows the dependence of the Brownian percentage on the angle for two different aspect ratios. Plots for all the six different particle sizes are reported. The two curves show that the aspect ratio plays an important role. For all the particles sizes except the smallest, the Brownian percentage at low angles is seen to be smaller than the equivalent in the graph for $L/D = 20$ (see Figure 5.13). However, the smallest aspect ratio ($L/D = 1.66$) shows that this percentage goes to zero. This suggests that, as observed in the Subsection 5.2.2 on page 88, a short rod is more active in capturing particles which are in the proximity of its lateral surface.

The smallest size ($r = 25$ nm) shows a similar trend as observed above: even though it does not go to zero, the percentage at low angles decreases when the aspect ratio is decreased as well. It is interesting to note, however, that the percentage of Brownian particles for the orientation $\alpha = 90^\circ$ is slightly higher for $L/D = 1.66$ than for $L/D = 6.66$. This aspect can be explained by noting that, even though a shorter rod has proven to be more active than a long one around the *SIDE* surface, the spatial decay of the field gradients is also shorter due to the reduced dimensions. Therefore, the rod is less able to capture far particles, in comparison with long rods.

Lastly, it is interesting to see the overall dependence of the Brownian particles in the system on the particle sizes for the different aspect ratios considered in this study. Figure 5.16 shows the different overall curves for each of the four aspect ratios which have been investigated. The plot rationale is the same as for Figure 5.14 on the next page. The graph clearly show that, even though variations could be observed in the percentage of Brownian particles for different angulations (see Figure 5.15 on page 96), the overall results (obtained as an average over different angles) smoothen those differences. The curves for the smallest aspect ratios show that, except for the smallest size, the percentage of Brownian particles in the system is zero. The curve for

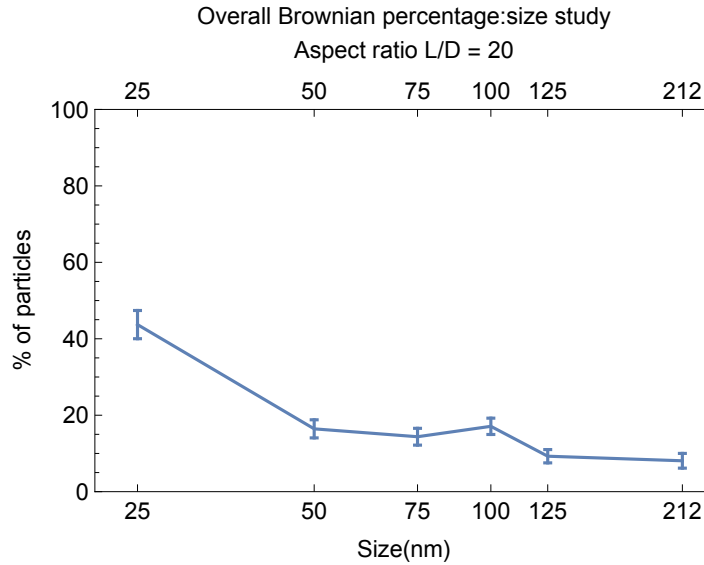


Figure 5.14: Plot of the overall (for both *SIDE* and *TOP* zones) Brownian particle percentage for different sizes. The error bars express the standard deviation of the plot points.

$L/D = 6.66$ shows that a minimal percentage is observable for all the sizes, with the exception of the largest ($r = 250$ nm). It is possible to spot that the $r = 100$ nm particles show again a larger Brownian percentage in comparison with smaller sizes: the observation confirms the equivalent one made previously (see Figure 5.14 on the next page). The curve for $L/D = 20$ is equivalent to the one of Figure 5.14. From this graph, we can draw the overall conclusion that a shorter aspect ratio rod shows a slightly smaller percentage of Brownian particles in the system. This is especially visible for the $r = 25$ nm size on the graph, for which the points corresponding to different L/D show a sequence raising from under 30% to over 40%. The other particle sizes show an almost negligible percentage for aspect ratios under $L/D \sim 5$, which is considered to be the limit under which all the particles (except $r = 25$ nm) feel the influence of the rod.

For the purpose of our optimization study, the results illustrated in this subsection show that the number of Brownian particles in the system depends on several factors. If the rod is short enough ($L/D < 5$) almost all the particles experience a magnetic force regardless of the angle or their position respect to the rod (*TOP* and *SIDE* regions), with the exception of $r = 25$ nm particles. For rods with larger aspect ratios, the *SIDE* zone starts to display an appreciable percentage of Brownian particles. The largest contribute to the overall percentage is given by rods oriented with low angles respect to the field, most notably from $\alpha = 0^\circ$. Overall, larger particles show a smaller percentage than smaller ones. This confirms the logic conclusion that larger particles's dynamics are dominated by magnetic forces rather than by thermal motion. A curious inversion of this trend has been observed for the $r = 100$ nm particles, which show a percentage comparable to the $r = 50$ nm case. This note is left for further investigation in the following section. Finally, even though the $r = 25$ nm particles are separated more efficiently by the shorter rods, a percentage of around 30% is displayed even by the shortest L/D investigated. It has been shown that, except that for the largest particles, high angles show a finite percentage of Brownian particles, which does not reach zero. Therefore, we can conclude that a separation process with a single rod performs better with smaller rods, as they increase the number of particles that are actively attracted to the rod. However, it is not possible to achieve a capture fraction of 1 in the case of small particles ($r = 25$ nm) due to the presence of a still relevant fraction of particle freely diffusing.

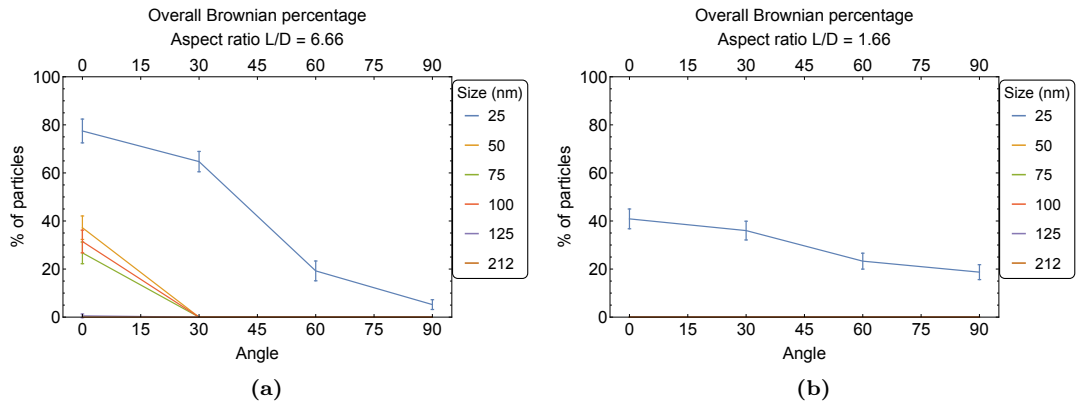


Figure 5.15: Brownian particle percentage in the separation process for different orientation angles of the rod with the external field. Different curves correspond to different angles. *SIDE* and *TOP* zones have been averaged out. The standard error relative to each curve is reported.

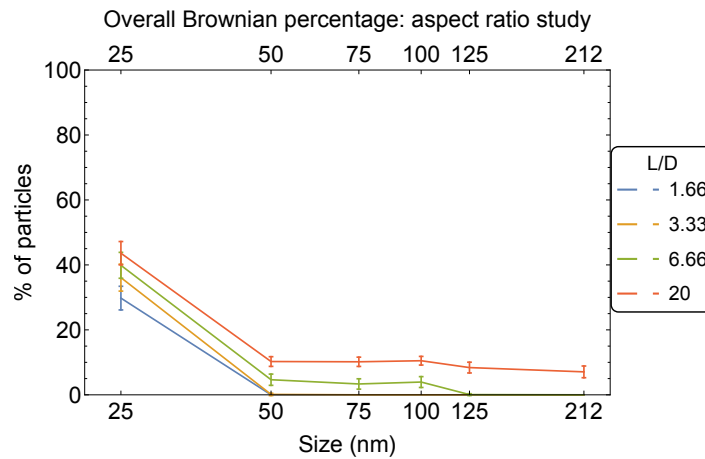


Figure 5.16: Plot of the overall (for both *SIDE* and *TOP* zones) Brownian particle percentage for different sizes. The error bars express the standard deviation of the plot points.

5.2.4 Size dependence of the separation time

Figure 5.4 on page 86 shows the capture fraction plotted against the separation time, for a specific size. In analogy with the data analysis performed in the past sections, it is interesting to see the evolution of the capture fraction in time, irregardless on the rod's orientation. An average on the different orientation angles of the rod is thus again considered, with the modality described in the previous sections. Figure 5.17 on the facing page shows the separation curves in time for the six particle sizes investigated in this study. The curves for the two limit aspect ratios are compared.

The two different aspect ratios do not show an appreciable difference between each other. The shorter rod, $L/D = 1.66$, shows an higher capture fraction for the maximum separation time investigated (50 s) and a slightly higher rate in the first seconds of the separation process. The capture rate is defined as $\Delta f_{\text{Cap}}/\Delta t$, where Δf_{Cap} is the capture fraction. Even though the aspect ratio optimization has shown that a shorter rod is more active, the curves obtained from a combination of the *TOP* and *SIDE* zones, as well as of the orientation angles, smoothen the differences between long and short rods. They show capture dynamics which are quite comparable.

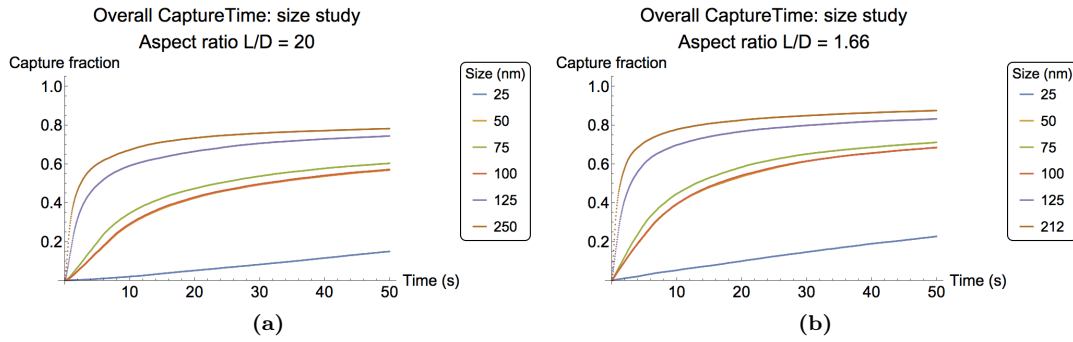


Figure 5.17: Time evolution of the capture fraction for different particle sizes. Different curves correspond to different sizes. The standard error relative to each curve is reported: in most of the cases, it is smaller than the size of the marker in the graph.

The curves show that, for the largest sizes (250 nm and 125 nm), a threshold capture fraction of 0.5 is obtained in a time of the order of 5 s or less while smaller sizes (except 25 nm) exhibit times on the order of 40 s. A comparison with other experimental and simulation studies is difficult due to the different setup considered in this study. However, the time scale predicted for a single rod roughly matches the order of magnitude of previous separation experiments and simulations when a magnetic wire or wool is used as the separation matrix [93–95], thus confirming the consistency of the obtained results.

The time dependence in the curves reveals the presence of two principal regimes. The first dynamic regime corresponds to the initial stage of the separation: the capture fraction shows a *linear* increase in time. The capture rate is almost constant and depends on the size of the particle. For the particles between 50 nm and 100 nm the rate is found to be between 0.03 and 0.04 *fraction points per second (f.p.p.s.)* while for the largest sizes the rate is found to be between 0.2 and 0.4 *f.p.p.s.*, being thus approximately 10 times larger.

The second dynamic regime is characterized by the capture fraction reaching a limit value: the capture rate becomes very small, and the curve slowly approaches a constant value. In this regime, most of the particles have already been captured, while the particles that started further away from the rod are still being separated. A certain percentage of particles is also freely diffusing without any influence by the rod. The actual limit value is dictated by this percentage, called here $\%_{\text{Brown}}$. More in details, the limit value corresponds to all the particles which are not freely diffusing, i.e. $1 - \%_{\text{Brown}}$. From the Brownian percentage curves shown in the past section, the saturation capture fraction is expected to be on the order of 0.9 for all the particles considered.

The saturation regime starts after a time of approximately 20 s for the largest sizes. For the smaller sizes, this time is found to be on the order of a minute or more: its estimation is not possible with more accuracy due to the limited time interval investigated during the simulations, which extend to 50 s at its most.

The smallest particle investigated, $r = 25$ nm, only displays the linear regime. The capture rate is found to be on the order of 0.003 *f.p.p.s.*, thus being approximately 10 times smaller than for the particles between 50 nm and 100 nm. Moreover, taking into the account the Brownian percentage curves shown in the past section, the saturation capture fraction is expected to be on the order of 0.6.

In general, the curves confirm a trend that was expected: larger sizes lead to a faster separation process, as well as a higher saturation value. It is however difficult to give a quantitative scaling of the separation time with the particle size. For instance the 100 nm particles shows an inversion of the scaling trend just outlined, as already mentioned previously. This is especially visible in Figure 5.17: the 100 nm curve is found to be almost equivalent to the 50 nm curve.

This fact can be explained by taking into account not only the size but also the other different contributes to the dynamic of the particles.

Assuming that the particle is captured, the two contributes to the dynamics come from the magnetic force, actively driving the separation, and the viscous friction force, opposing to the particle motion. The hydrodynamic friction, according to Stokes equation (see Section 5.1 on page 81), scales linearly with the radius of the particles: $F_h \propto a$. The magnetic force, assuming magnetically saturated particles, scales with the particle magnetic properties (see Chapter 2 on page 21): $F_m \propto n_d V_d$. The V_d parameter, that stands for the volume of a single superparamagnetic domain, has been assumed to be the same for the different particle sizes. This leaves the magnetic force depending only on n_d . This parameter is expected to scale with the volume of the particles. However, this prediction has been found not to be correct in some cases. From Table 5.1 on page 82, it can be seen that, in the case of 100 nm, n_d is comparable to the value for 50 nm and is smaller than the value for 75 nm. This proves that the n_d strongly depends on the individual nanoparticle and its synthesis, and it is a critical parameter for the magnetic separation process.

Going back to the two contributes to the dynamics, the n_d parameter for the 100 nm particles is found to be roughly two times the equivalent for the 50 nm ones. Therefore, the 100 nm is experiencing a magnetic force which is twice stronger, while being subjected to a friction which is also twice stronger than the 50 nm case. The two competing terms are therefore balanced and the overall resulting dynamics is the same for the two sizes, thus explaining the equivalence between the separation time curves observed. However, it should be noted that larger particles will also exhibit a lower percentage of particles freely diffusing, as the thermal fluctuations amplitude scales inversely with the size. Therefore, the saturation value obtained for the 100 nm case is expected to be higher than that of the 50 nm one. This has not been observed due to the time constraints on the maximum separation time obtainable in the simulations. The non-trivial dependence of the parameter n_d on the particles radius makes it challenging to do a quantitative study of the separation process efficiency on the particle's magnetic moment. An alternative approach, more suited for the scope, would be to assume that the particles have a fixed magnetization per volume. This value could be obtained experimentally by a statistic on a large number of particles with different sizes. On this basis, a dependence of n_d on the particle radius could be approximated, e.g. $n_d = n_d(r)$. While this dependence of n_d cannot be generalized to nanoparticle of different materials (since the magnetic properties are strictly material-dependent), it could still give an easier interpretation of the results for the specific material under study. Due to time constraints, this approach has not been followed.

Looking again at the graphs in Figure 5.17 on the previous page, all the curves display a similar shape, with the exclusion of the 25 nm curve which differs greatly. Therefore, it can be argued that, by a proper rescaling of the time, an universal curve for the magnetic separation in the presence of a single rod can be obtained. This result has been proposed in literature [34, 96]. However, only time has been rescaled in those specific case. Our study, on the contrary, shows that there are other factors which have to be included. One is the saturation limit, which differs from size to size and depends on the percentage of Brownian particles in the system. A second one is represented by the magnetic properties of the particle, and more specifically by their magnetic moment at saturation. Its role has been properly discussed in the previous section. Here we just mention that considering both the particle size and magnetic properties is necessary for a correct description of the rescaling quantities. In conclusion, we hypothesize the existence of an universal curve, based on a rescaling of the separation time by taking into consideration both the magnetic properties and the size of the particles. The saturation limit should also be subjected to such rescaling. In particular, regarding the simple system composed by a single rod, it can be argued whether a description similar to the problem of sedimenting particles in a gravitational or electrostatic field can be made. A *magnetic length* l_m may be obtained, with a dependence on the particle size and magnetic properties. It could have the same physical meaning of the well known gravitational and electrostatic counterpart. A particle displaying a long l_m will be subjected to free diffusion, while a short l_m implies their separation by the rod. However, this considerations were not further investigated due to time constraints

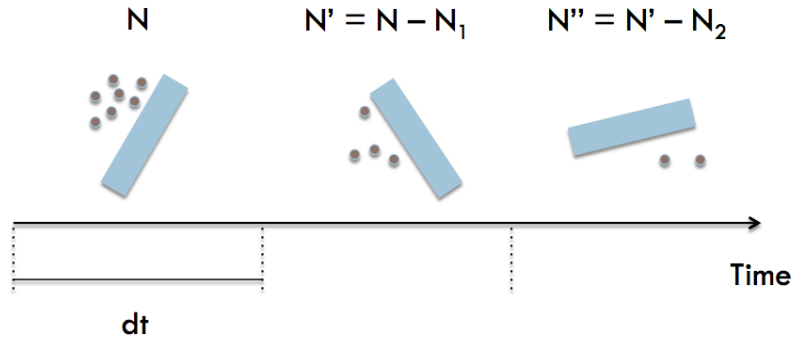


Figure 5.18: Schematic representation of the cascade procedure used to model a separation process in which more than one rod is involved. dt is the maximum time allowed for each single separation process in the sequence. N and subsequents indicate the number of particles at the initial stage of each single separation process.

on the project. They are left as a possible and interesting outlook of this study.

5.3 Efficiency of the rod packing

In the previous section, the optimization study of a magnetic separation process with a single ferromagnetic rod has been discussed. The orientation angle of the rod with respect to the field and the aspect ratio L/D of the rod have been varied and their impact on the separation efficiency has been extensively assessed.

In order to perform a similar study on a system of multiple rods (therefore modeling a real separation matrix as the one used in the experimental setup), a complete description of the system and the dynamics of the particles would require the use of the multi-rod version of our algorithm. Even though this feature is already implemented in the algorithm (see Appendix B), a study with a multi-rod setup has not been performed due to time constraints.

However, we investigated the effect on the separation curves induced by adding more rods to the system. In order to do so, we used a procedure in which a number of single rod separation processes are performed in series. We called it the *cascade procedure*. Figure 5.18 gives a graphical illustration of the method. A dilute system of N particles is considered as the initial configuration of the overall procedure. In each of the processes that compose the sequence, the simulations are performed with the same methodology as described above. However, the separation process only lasts for a specified time Δt and the capture fraction obtained after this time is calculated. The correspondent number of captured particles is then subtracted from the total that underwent the process. The net N' , which corresponds to the number of particles which were not captured, is then used as the new initial number of particles for the next separation process in the sequence. The procedure is iterated until a capture fraction close to one is obtained. For instance, if N is the initial number of particles and N_1 is the number of particles that were captured during the first process, then $(N - N_1)$ particles will undergo the second separation process. If N_2 is the number of particles captured during this process, then $(N - N_1 - N_2)$ particles will undergo the third process. During the procedure, the capture fraction will approach the saturation value of unity. The overall process will reach this value only if it is possible to achieve a capture fraction of 1 during a single separation process. On the contrary, if Δt allows for a maximum capture fraction lower than 1 during the single process, the overall sequence will not be able to separate all the particles. This resembles the saturation regime in the separation time curves discussed in the previous section (see Section 5.2.4). The advantage offered by this procedure is the possibility to model different setups of the rod in the sequence. For instance, a random packing configuration can be obtained by allowing the rods in the sequence to have each one an arbitrary orientation with respect to the field.

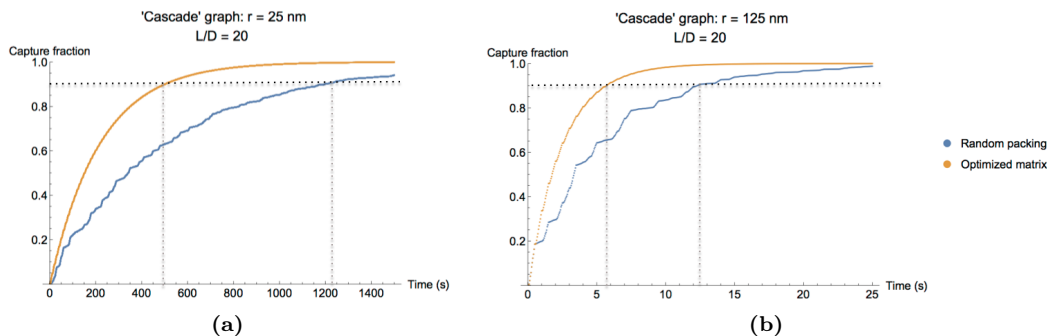


Figure 5.19: Separation curves of the cascade procedure. The black horizontal line marks a capture fraction of 0.9. The gray dashed lines are a guide for the eye. For $r = 25$ nm, a Δt of 10 s has been used. For $r = 125$ nm, a Δt of 0.5 s has been used.

On the contrary, a pre-determined rod configuration inside the column can be obtained by constraining the angle to specified value(s).

Figure 5.19 shows the time separation curves obtained by the *cascade procedure*. Two different setups have been investigated: a sequence of rod with random orientation and a sequence of rods that are always perpendicular to the external field. This last configuration is referred to as the optimized setup, as $\alpha = 90^\circ$ gave the best efficiency in the optimization study on a single rod that. Two different sizes for the nanoparticles are considered.

The curves for the different setups show a similar form, equivalent to the one already described in Section 5.2.4 on page 95. However, the random configuration curve is less smooth than the optimized setup one. This is due to the presence of several single separation processes in the overall curve, where each process refers to a different orientation angle of the corresponding rod. The overall curve shows, therefore, a sequence in which sections with high capture rate alternate to sections where the rate is almost zero.

The curves show that, as expected, the random packing setup performs worse than the equivalent optimized setup. As a quantitative measure of the performance, the time at which a capture fraction of 0.9 is obtained has been calculated for both the setups. For the curve referring to the 25 nm size, the time obtained for the random configuration is around 1300 s, being 2.5 times larger than the corresponding for the optimized setup. For the curve referring to the 125 nm size, the time obtained for the random configuration is around 12 s, being 2 times larger than the one for the optimized setup. Therefore, the performance of the former is better for the 125 nm case, as the scaling factor relatively to the latter is smaller. Moreover, the random configuration setup proves to be able to reach a capture fraction of almost 1 in reasonable times. This holds also for the $r = 25$ nm particles, for which magnetic separation has been showed to be challenging.

For the two different sizes considered previously, two different Δt values have been used. In particular, Δt for the 25 nm size was rather large. This is due to the fact that the single rod separation curves for times smaller than Δt were found not be continuous but composed of little steps in the capture fraction over time. This effect is observed because not many particles are captured in the desired time lapse due to the too short separation times considered. This does not permit a statistically meaningful description of the very first instants of the separation process and larger times (for instance, the chosen $\Delta t = 10$ s) are needed for drawing more accurate time curves. On the contrary, the 125 nm particles experience a faster separation, and the curves are accurate even for short times (for instance, the chosen $\Delta t = 0.5$ s).

Only for the larger particles, the effect of the Δt parameter on the separation curves has been evaluated. Figure 5.20 on the next page shows the comparison between separation curves obtained with four different Δt values. It can be noted that the choice of the parameter Δt modifies the correspondent separation curve. For the highest value taken (Subfigure 5.20a), the

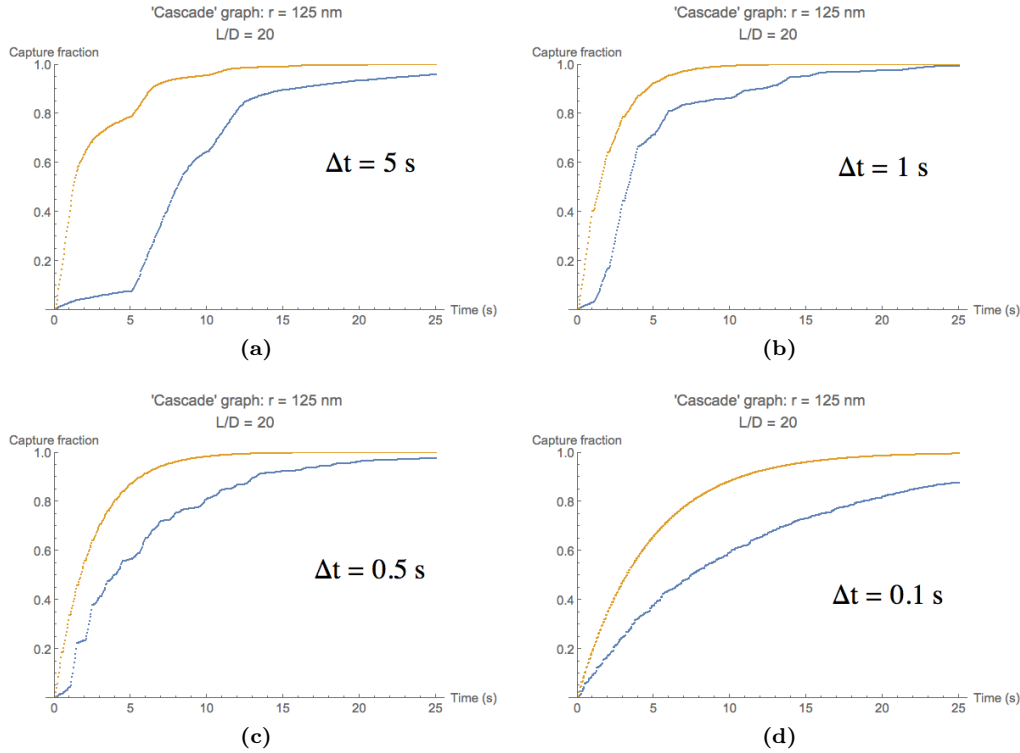


Figure 5.20: Separation curves of the cascade procedure. The different Δt used are indicated in the inset. The curves refer to a particle size of 125 nm.

curves for the two setups are very different. The random configuration appears to be slower than the optimized setup by a factor larger than the results previously discussed. However, the presence of several steps in the plots indicates that the description is rather poor: the value of Δt chosen is too large and almost saturation is reached within the first separation process in the sequence. Therefore, this choice is not appropriate for the system under study.

The curves for smaller Δt (Subfigures 5.20b and 5.20c), are, on the contrary, well characterized. The separation times for the random configuration and the optimized setup reach the same values as in the previous analysis. It is possible to see a small decrease in the capture efficiency for $\Delta t = 0.5$ s in comparison with $\Delta t = 1$ s. This may be explained by the analysis on the separation curve shape, which has been done in one of the previous sections. In particular, the initial linear regime assumes, in this case, a more parabolic behavior during the first instants of the separation process. Reducing Δt will enhance the first part of this regime, which has a slow rise at the beginning due to its parabolic dependence. The resulting overall curve, therefore, shows a slower approach toward the saturation regime.

Lastly, the last curve (Subfigure 5.20d) shows a considerably slower development in time in comparison with the other curves. This can be explained by the same considerations as before. However, Δt might be too small: only the very initial particle dynamics toward the rods is considered, and the resulting curves lack of a better characterization. For this reason, the plots for higher Δt values have a rougher appearance. A too small Δt is thus not fully appropriate for the system under study.

The considerations about the parameter Δt show that its choice can greatly modify the resulting separation curves. It can be questioned whether a correct choice of the parameter can be made. The mistakes occurring when Δt is either too short or too long have been explained. However, the range of possible values for the parameter still remains wide. It is possible to physically associate the choice of Δt to the residence time of the particles in the vicinity of a

single rod. This time can be assumed to be due to the flow of the suspension in the system. A long residence time implies a slow flow, while a high residence time means that the particles are quickly transported along the sequence of rods. Therefore, the variations in Δt might be associated to the variations in the flow velocity. In this sense, an interplay between the separation speed and the flow can be seen. If Δt is high (Subfigure 5.20a on the previous page) the system approaches saturation even for the first rod in the sequence. However, this also means that the system will mostly be in the separation regime. As the percentage of Brownian particles in a single rod system prevents the capture fraction to reach unity during a single process, this means that the overall initial capture rate is high, but the approach to the saturation value is slow. This situation correspond to a slow flow.

On the contrary, if Δt is small (Subfigure 5.20d on the preceding page), the particles are transported to a successive rod in the setup without being able to be captured within the single process separation time. In order to reach saturation, therefore, more rods in the sequence needs to be explored. As it has been discussed above, the dynamics for such small separation times is slower due to a parabolic behavior of the time curve in the very beginning of the separation process. This means that the overall capture rate is small: the situation corresponds to a high flow.

The optimal range for the flow (i.e., the parameter Δt) is therefore associated to the interval of Δt for which the curves show fast separation but are still well defined. For the case under study, we conclude that an optimal choice for Δt lies between 0.5 and 1.0. Assuming that the particles travel a length equivalent to that of the rod, L , this means that the Δt parameter may be associated to a flow velocity of:

$$v = \frac{L}{\Delta t} \quad (5.2)$$

The length of the rod under consideration is $L = 12 \text{ mm s}^{-1}$. According to this naive model, the optimal range for the flow in the separation column is estimated to be between $1 \text{ cm}^3 \text{ s}^{-1}$ and $3 \text{ cm}^3 \text{ s}^{-1}$. However, experimental and theoretical studies on the separation efficiency in a HGMS setup with a separation matrix composed by ferrowires indicates an increase of the number of particles lost from the separation column up to 50% for flows of the order of magnitude of $1 \text{ cm}^3 \text{ s}^{-1}$ [95]. This is due to the fact that the magnetic force may not be able to keep the particles on the rod's surface: they are dragged away by the flow. The estimation of the optimal flow velocity by our naive model does not take into account this effect. As a consequence, the results given here for the optimal flow might be overestimated.

The effect of the aspect ratio on the separation curves for the cascade procedure has been investigated. Figure 5.21 shows the comparison between the separation curves for two different aspect ratios. The curves refer to a particle size of 125 nm and a value $\Delta t = 0.5 \text{ s}$ has been chosen. As a comparison parameter, the time at which a capture fraction of 0.9 is obtained is considered. The two curves for the random configuration both show an efficiency higher than the one of the previous curves for $L/D = 20$. Using shorter rods seem to enhance the general performance of all the angulations, so that the random packing efficiency raises. This was expected according to the conclusions reached in the optimization study section.

By comparing the two curves, the random configuration becomes similar to the optimized setup for $L/D = 1.66$. The two setups perform the separation process in roughly the same time. This may suggest that the overall performance of the random configuration is enhanced when shorter rods are used.

However, considering the optimized setup, the time at which a fraction of 0.9 is achieved is calculated to be 7.5 s for $L/D = 1.66$ and 7 s for $L/D = 6.66$. Therefore, the performance of the optimized setup decreases when shorter rods are considered. For $L/D = 6.66$, the optimized setup shows a separation time of 4.5 s, while $L/D = 1.66$ shows a separation time of 6 s. The slight decrease is explained by taking into consideration the optimization study on L/D which has been done in the previous section. It was shown that, by using a short rod, the capture efficiency greatly improves for low angles but decreases for high angles.

As the optimized setup is composed by rods with an orientation of $\alpha = 90^\circ$ with respect to

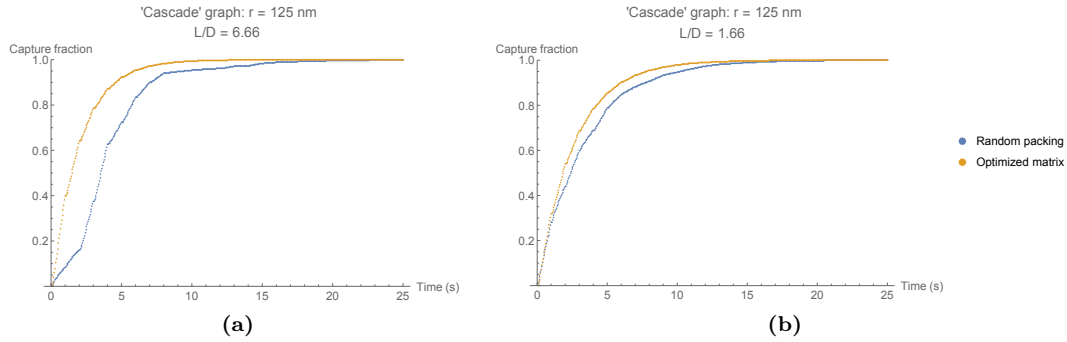


Figure 5.21: Separation curves of the cascade procedure for two different aspect ratios. $\Delta t = 0.5$ s for both the graphs. The curves refer to a particle size of 125 nm.

the field, this setup performs better when longer rods are used. On the contrary, the random configuration benefits from using shorter rods. According to the optimization study, the slight decrease in efficiency for high angles is balanced by a dramatic increase of the performance for low angles. Therefore, as the random configuration employs a sequence of arbitrarily oriented rods, the overall separation curves reach saturation in a shorter time. It is interesting to see, however, that the increase in the absolute performance of the random configuration occurs between $L/D = 20$ and $L/D = 6.66$. The smaller rods considered in this study ($L/D = 3.33$ and $L/D = 1.66$) show comparable separation times, all between 7 s and 7.5 s. Investigating aspect ratios in the range between 6 and 20 may show the value of L/D which gives the best performance.

5.3.1 Conclusions

In this section, an analysis of a system comprising several rods has been performed by a *cascade procedure*, in which the particles undergo magnetic separation in a single rod system for a sequence of rods. A sequence in which the rods are randomly oriented has been compared to a sequence in which the rods are optimally oriented with respect to the external field. The performances of the two sequences have been compared. For long rods, the optimized setup is found to be approximately two times faster than the random configuration. The latter separates 125 nm particles within a time of 12 s, while small 25 nm particles are separated in a time of 1300 s. The separation curves show that it is possible to achieve efficiencies of the order of 100% in reasonable times with a random configuration, even though the optimal setup performs better.

A study on the choice of the Δt parameter shows a possible relationship between such parameter and the flow of the suspension in the system. A flow velocity of the order of 1 cm s^{-1} to 3 cm s^{-1} has been estimated as optimal for the separation process of particles with size 125 nm. However, the evaluation follows from a simple model that does not take into account the drag force of particles already captured by the rods, which might remove them if the flow is too fast.

Finally, it has been found that a small aspect ratio of the rods initially increases the efficiency of the random configuration. After a threshold value is reached, however, reducing the aspect ratio only lowers the performance of the optimal setup. In conclusion, the random configuration may not be an optimal choice when long rods are used. When the matrix is composed by shorter rods, however, the random packing configuration is enhanced and becomes even comparable to the optimized setup. Therefore, taking into account the advantages offered by implementing a random packing in comparison with a matrix of fixed wires, we conclude that the former offers a valuable alternative without losses in efficiency when rods with an aspect ratio smaller than $L/D = 7$ are used.

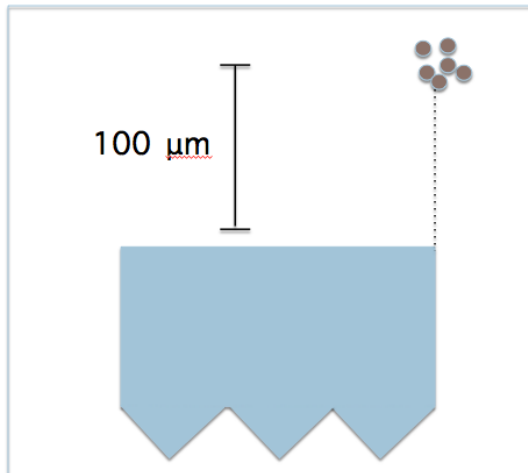


Figure 5.22: Initial configuration of the particles in the simulations performed on concentrated samples. The relative dimensions of the rod and the particles and the distances are not in scale.

5.4 Study of concentrated solutions

The previous studies and results refer to dilute solutions. This means that the particles will only experience an hydrodynamic perturbation (which has a very long range decay) from the motion of the other particles. No magnetic interaction nor hard sphere repulsion is however experienced by them.

However, it can be argued that the study of concentrated samples would give different results. One of the features that appears when concentrated solutions of magnetic nanoparticles are subjected to an external magnetic field is their aggregation into chain-like structures. This happens both in uniform and non-uniform external fields [34, 77, 97, 98].

The chain formation is driven by the magnetic interactions between the particles. Due to the magnetic field, the particles acquire large magnetic dipoles and arrange head-to-tail. In the framework of a magnetic separation process, chains are also supposed to be captured by the matrix: due to the presence of several particles in the aggregate, the resulting kinetics is cooperative. Moreover, the total magnetic moment of the chain is composed by the moments of the particles that form the aggregate. For this reason, longer chains exhibit larger dipole moments. We expect, therefore, that the separation process is faster for concentrated solutions in comparison with the dilute systems treated so far.

Unlike the previous case, particles are now generated in a specific zone in the vicinity of the rod. The choice of the zone is very important because, as shown in the optimization study, *TOP* and *SIDE* zones perform differently. We chose to generate the particles in a region which is located at top edge of the rod (see Figure 5.22). Our thought is that this zone, as it is influenced by both the *TOP* and *SIDE* behavior, may give the most insightful results.

A system of $N = 500$ particles has been studied. Particles are randomly generated in a cubic box centered in the position specified by the initial configuration region (see Figure 5.22). They are then left free to be captured by the rod. As in the previous case, flow is not considered. The side of the box is chosen accordingly to the resulting concentration. Given a desired number concentration c (g cm^{-3}), the side of the box results to be:

$$\Delta = \sqrt[3]{\frac{\rho V_p}{c}} \quad (5.3)$$

where ρ (g cm^{-3}) indicates the density of the particles and V_p (cm^3) indicate the volume of the single particle.

The concentrations have been varied in the range 0.5 g mL^{-1} to 2.0 g mL^{-1} . For each zone, 10 different simulations were run for obtaining a good statistic on the system. As the system is concentrate and aggregates occur, a small time step is required to model the collective motion of the particles in the aggregate. A time step of $\Delta t = 10^{-6} \text{ s}$ has been chosen. Each simulations was run for a maximum separation time of $t_{\text{max}} = 1 \text{ s}$.

5.4.1 Chain formation

In the initial phase of the separation process, the particles are found to aggregate into chains, in agreement with the expectations pointed out in the previous discussion. According to the classical theory on ferrofluids, a criterion for chain formation is given by the *magnetic parameter* [24]:

$$\Gamma = \frac{\mu_0 m^2}{2\pi d^3 k_B T} \quad (5.4)$$

where m is the magnetic moment of the particles (here assumed to be the same for two interacting particles) and d is the particle diameter. Γ essentially expresses the ratio between the dipole interaction energy (which induces chain formation) and thermal energy (which tends to dismantle the aggregates). If $\Gamma \gg 1$ is verified, chains are formed within the suspension. However, for superparamagnetic nanoparticles, the criterion is found not to be appropriate. Another dimensionless parameter has been proposed [78]:

$$N^* = \sqrt{\phi_0 e^{\Gamma-1}} \quad (5.5)$$

with ϕ_0 being the magnetic particles volume fraction and Γ being the magnetic parameter as specified above. Again, when $N^* \gg 1$ is verified, chains are expected to appear in the system. Therefore, the chain formation for superparamagnetic nanoparticles can be seen as regulated by both the concentration and the parameter Γ . For the particles used in our study, Γ varies between a value of 1700 for $r = 125 \text{ nm}$ to a value of 1 for $r = 25 \text{ nm}$. For large particles, therefore, N^* assumes very high values for almost the complete concentration range attainable, while for $r = 25 \text{ nm}$ we obtain $N^* = \sqrt{\phi_0}$. According to this picture, chains are expected for all the particles except for $r = 25 \text{ nm}$, for which chain formation is predicted to be hindered by thermal motion. Figure 5.23 on the following page shows the chains which are observed in the system for different simulation conditions.

The picture shows that, as expected, the 25 nm system does not experience chain formation. Increasing the concentration does not involve the formation of aggregates, confirming that the magnetic parameter is too small for chain structures to appear. On the contrary, a few chain structures are visible for the 75 nm case. The comparison between curves for different concentrations shows that the number of particles in the chains does not change, and an average number $\langle N \rangle = 3$ is observed during the separation process. Increasing the size of the particles does not appreciably increase their number in the chain. Simulations performed with $r = 125 \text{ nm}$ showed an average number $\langle N \rangle = 4$. On the contrary, simulations performed in uniform fields show that the number of particles in the chain depends on the size via the parameter N^* [78].

The apparent discrepancy can be explained by considering that, for non-homogeneous fields, the magnetic force exerted by the rod ($\approx 10^{-6} \text{ N}$) is stronger than the magnetic interparticle interaction ($\approx 10^{-12} \text{ N}$ for particles $1 \mu\text{m}$ apart). Therefore, the particles assemble into relatively small chains with the closest neighbors, and similar small aggregates occur for the majority of the particles in the system. The small chain's motion, due to the stronger magnetic force generated by the rod, follows a trajectory that leads it toward the rod rather than toward other aggregates. This behavior is confirmed by simulations performed in similar non-uniform conditions, in which aggregates with a similar average number of particles are obtained [34]. We argue that a higher number of particles in the system, or the implementation of boundary conditions in order to better reproduce a concentrated sample, may show an increase of the

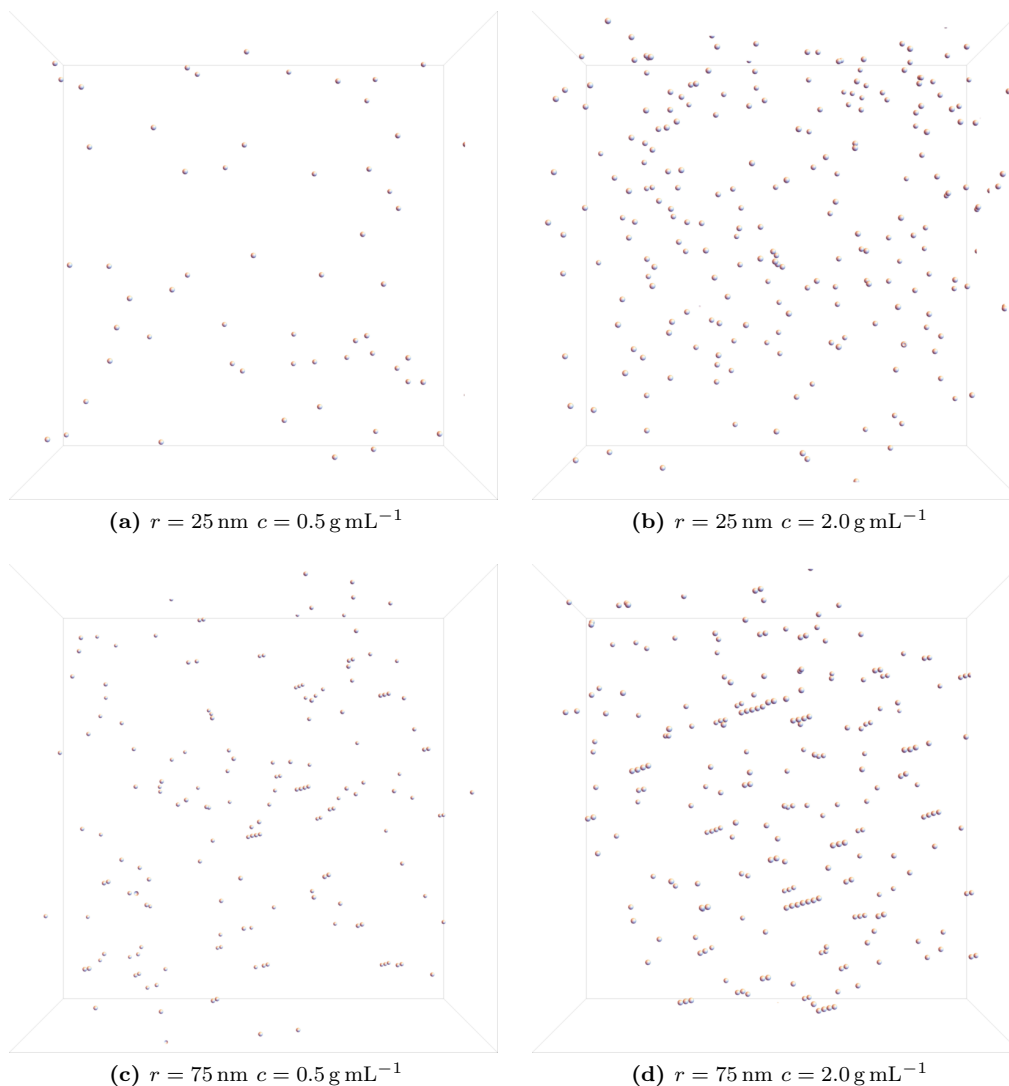


Figure 5.23: Snapshot of the nanoparticles during the separation process, for different sizes and concentrations of the samples.

average chain length with the size of the considered particles.

5.4.2 Separation efficiency

In analogy with the studies performed for the optimization of a single rod, we investigated the capture fraction evolution in time for the concentrated sample under study. With the same methodology as for dilute systems, the influence of the angle of the rod with respect to the external field has been assessed. Moreover, the performances obtained for different sample concentrations have been compared. Figure 5.24 on the next page shows the separation curves obtained for two different angle configurations. The particle size is $r = 75 \text{ nm}$. By comparing the curves, it is possible to see that they both display the same shape. In the initial phase of the separation process, no particle is captured. After a certain time, a sudden rise in the curves is visible. This marks the temporal instant at which most of the particles are captured. We can refer to this temporal instant as to the *separation time*, as most of the particles get separated at this point during. The great majority of the captured particles are chain structures: this

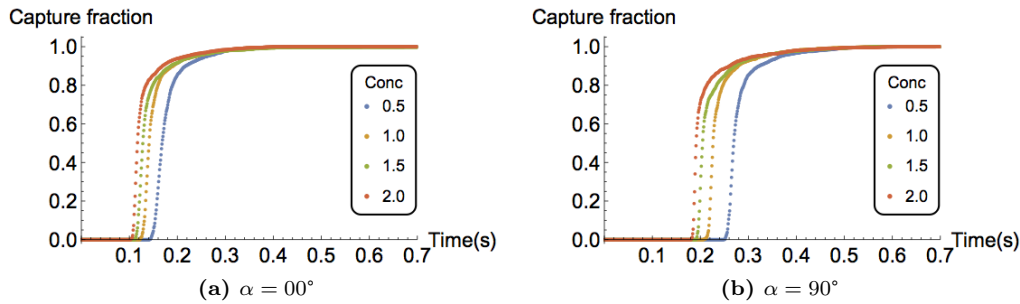


Figure 5.24: Time curves for different sample concentrations. $r = 75$ nm and $L/D = 20$.

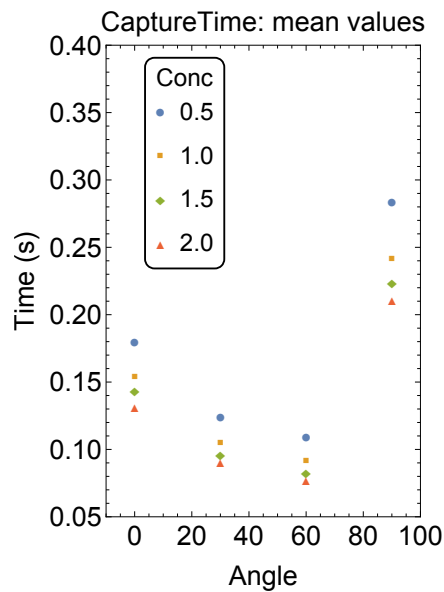


Figure 5.25: Separation times dependence on the angle of the rod with the external field. The different colors refer to different concentrations

confirms that the separation process is faster for chain-like aggregates. For subsequent times, the curve slowly approaches the saturation limit of unity. In this last stage, the single particles that did not aggregate into chains are captured. As already stated, the curves for angles $\alpha = 0^\circ$ and $\alpha = 90^\circ$ do not differ. This is not in contrast with the optimization study performed in the previous sections. The initial configuration of the particles system consists in a very specific zone in the vicinity of the rod. As the capture time for a dilute system has been proved to be heavily dependent on the zone investigated, a different variation of the temporal evolution of the capture fraction with the orientation angle is expected. In Figure 5.25, the separation time is plotted against the various orientation angles.

A peculiar pattern can be recognized. Surprisingly, the large angle $\alpha = 90^\circ$ shows the longest separation time. However, the minimum occurs for the next large angle ($\alpha = 60^\circ$). Smaller angles show again an increase of the separation time. The parabolic shape arises because of the initial configuration of the system. Referring to Figure 5.22 on page 104, the particles start in the proximity of the rod's corner. According to 5.1 on page 83, when the rod is rotated respect to the field, lobes of strong activity appear at the top. The lobes collapse to single spherical regions centered on the extremities for $\alpha = 0^\circ$. In the system studied, however, the initial position of the particles is in one of the active lobes when the rod is tilted (e.g., $\alpha = 60^\circ$). The particles therefore feel a stronger magnetic force and their separation is faster. It is interesting to compare the separation times obtained for different concentrations. Fig-

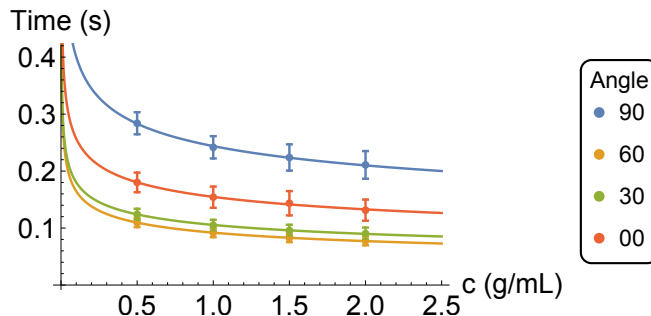


Figure 5.26: Separation time dependence on the concentration. The different colors refer to different angles. The solid lines represents the power-law fits for the various angle values.

Table 5.2: Results of the experimental fitting procedure on the power-law equation for different angles. The particles have size $r = 75$ nm.

<i>Angle</i> ($^{\circ}$)	t_0 (s)	α
90	0.2438 ± 0.0008	0.215 ± 0.007
60	0.0919 ± 0.0002	0.253 ± 0.002
30	0.1054 ± 0.0002	0.232 ± 0.005
00	0.1545 ± 0.0009	0.22 ± 0.01

ure 5.24 shows that all the concentrations investigated show a similar time curve, with the regimes outlined above. For higher concentrations, however, the system performs faster. This can be explained by noting that, in the more concentrated systems, more chain structures appear in the system. Therefore, the separation proceeds faster for the reasons already discussed above. We conclude that, in agreement with experimental studies on magnetophoresis [99], a higher concentration of the sample leads to a faster separation process. Following [99], a fit of the separation times for different concentrations has been attempted with a power-law equation of the type:

$$t_s = t_0 c^\alpha \quad (5.6)$$

where t_0 and α are parameters to be fitted. The simulations data and the power-law fit are plotted in Figure 5.26. The results of the fit are reported in Table 5.2. The results for α are all found to be in fair agreement with a value of 0.25 reported in [99] for a magnetic separation process in a uniform gradient setup. Indeed, the most accurate data set (the one relative to $\alpha = 60^\circ$) has the best agreement with the reported value. Further confirmation of this scaling law, both from simulations and experimental results, would be highly desirable.

From the separation time, we can derive the average magnetophoretic velocity of the particles when they are captured by the rod. If Δr is the absolute distance travelled by the particles and Δt is the separation time, the average magnetophoretic velocity is given by:

$$v = \frac{\Delta r}{\Delta t} \quad (5.7)$$

In our case, the particles are all generated at $\sim 100 \mu\text{m}$ from the rod's edge, according to their initial configuration. The values for Δt are obtained from the separation curves. For reference, the values for t_0 reported in Table 5.2 are taken: they refer to a concentration of $c = 1.0 \text{ g mL}^{-1}$. The obtained magnetophoretic velocities for the different angles range from a minimum of 0.41 mm s^{-1} to a maximum of 1.09 mm s^{-1} . The reported velocities are higher than the magnetophoretic velocity for concentrated samples reported in [96], which predicts a value of 0.26 mm s^{-1} . Their study, however, refers to separation experiments conducted in an uniform gradient magnetic separator. That setup provides some advantages over HGMS in

Table 5.3: Results of the experimental fitting procedure on the power-law equation for different angles. The particles have size $r = 125$ nm. The fit errors for the parameter t_0 are not reported as they are too small.

<i>Angle</i> (°)	t_0 (s)	α
90	0.0513	0.254 ± 0.002
60	0.0201	0.265 ± 0.001
30	0.0228	0.265 ± 0.001
00	0.0331	0.264 ± 0.002

terms of parameter controls and reproducibility, but is known to perform slower. Our simulation study therefore confirms the better performance of HGMS in terms of separation times.

The previous study has been repeated for sizes $r = 25$ nm and $r = 125$ nm. The separation curves for the 125 nm are very similar in shape to the ones already shown, and are not reported. Table 5.3 shows the results of the fitting procedure for this system. Again, the values obtained for α are in good agreement with the value 0.25 reported elsewhere [99]. However, the fit results are slightly larger in comparison with the equivalent ones for $r = 75$ nm. This may imply that a scaling of the power-law parameter α with the size of the particles may exist. Confirmation of this hypothesis, both from new simulations and experimental results, constitutes a possible future line of research.

The $r = 25$ nm did not show an appreciable capture fraction in the maximum separation time allowed for the simulation. Therefore, we could not extend the size analysis to small particles. It is still possible to evaluate the magnetophoretic velocity of the particles. In this case, the distance Δr travelled during the simulation time (1 s) is evaluated. Averaging over the number of particles gives the estimation of the magnetophoretic velocity. As no chains are observed for this system, we expect that the velocity does not depend on the concentration. The analysis effectuated for $\alpha = 0^\circ$ confirms that the velocities vary from a minimum of $18.4 \mu\text{m s}^{-1}$ for the smallest concentration up to a maximum of $20.1 \mu\text{m s}^{-1}$ for the highest concentration. The velocity does not display, therefore, a dependence on the concentration.

Lastly, the separation velocity for the concentrated sample has been compared with the corresponding result for a dilute system. Again, as no chains are observed, the results are expected to be comparable. The overall velocity is calculated by averaging the results obtained for different angles and concentrations. We obtain a magnetophoretic velocity of $19.6 \mu\text{m s}^{-1}$ for the concentrated sample and of $15.2 \mu\text{m s}^{-1}$ for the dilute system. The value are found to be comparable, as expected.

Similarly, the performance of a concentrated sample and a dilute one have been compared for the other particle's sizes. The separation times for the two systems have been considered. For the concentrated sample, the parameter t_0 of the power-law equation is taken. The values are averaged over the different angular configurations. We obtain separation times of $\Delta t_{\text{conc}}^{75} = 0.15$ s and $\Delta t_{\text{dil}}^{75} = 3.78$ s for $r = 75$ nm, and $\Delta t_{\text{conc}}^{125} = 0.05$ s and $\Delta t_{\text{dil}}^{125} = 0.81$ s for $r = 125$ nm. The dramatic decrease of the separation time for the concentrated system is clear in both cases: the separation proceeds almost 30 times faster. The order of magnitude of the estimated increase agrees with a similar prediction stated in [96]. The predicted values for the separation times for concentrated samples compare also to experimental evidences. In conclusion, it appears that the separation process is dominated by a collective motion of the particles, which aggregate into chains that undergo faster separation due to their enhanced magnetic moment.

5.4.3 Conclusions

In this section, we have discussed a case in which the separation process of a concentrated sample is simulated. The aggregation of particles into chain structures has been observed, in agreement with both experimental and simulations results. The separation curves were found to be dependent on the sample concentration. In particular, a power-law fits this dependence.

The value of the exponent is in agreement with analogous results in literature. From a first estimation, the exponent has been found to be dependent on the size of the particles. However, as only two sizes have been considered, new simulations are required. Lastly, the separation times for the concentrated sample have been compared to the equivalent quantities obtained for a dilute sample. The concentrated system is found to separate at least one order of magnitude faster, in agreement with similar observations made in other studies on the topic.

The fact that the data obtained in this study refers to a different separation setup may suggest that a magnetic separation process involving superparamagnetic nanoparticles follows an universal behavior. However, the present study has been conducted for a very specific initial configuration. Therefore, more simulations exploring different initial conditions, as well as investigating more sizes and concentrations, are required in order to obtain a full understanding of the separation time *versus* concentration dependence.

Chapter 6

Conclusions and Outlook

A simulation study of the feasibility and efficiency of magnetic separation using superparamagnetic nanoparticles was performed. The study aimed to reproduce the conditions which are really occurring in an existing separation setup, in which the separation matrix is composed by a random packing of ferromagnetic rod. An algorithm has been developed for the purposes. The algorithm is based on a Brownian Dynamics technique in which hydrodynamics effects, arising from the motion of the nanoparticles in the solution, are explicitly taken into account. In order to simulate the magnetic field generated by a rod in the matrix, exact analytical equations have been derived for the magnetic field generated by a rod with uniform magnetization transverse to its axis. Together with the known result for magnetization parallel to the rod's axis, our equations can effectively model a rod which gets uniformly magnetized in an arbitrary direction when placed in an external field. The equations have proved to give equivalent results to numerical calculations when applied to permanent magnets. In the conditions experienced in the separation setup, the analytical model developed in this study has proven to give an accurate, albeit approximate, description of magnetizable objects even when the mutual magnetization between them is taken into consideration.

The separation process of superparamagnetic nanoparticles in presence of one single rod has been studied by varying the rod's angle respect to the external field and the aspect ratio of the rod. The minimum separation time and the maximum fraction of captured particles are reached when the rod is placed perpendicularly respect to the external field. The regions on the top and bottom of the rod proved to be more active during the separation process than the lateral surface. In general, a short rod has been seen to give better performances. However, the aspect ratio has been found to affect the separation efficiency less than the angle respect to the field.

The separation process in presence of a single rod has been simulated for different particle sizes. Particles with a radius bigger than $r = 50 \text{ nm}$ has been seen to undergo effective separation even when only one rod is considered. The dominant mechanism in the particle dynamics is the attractive force exerted by the rod, with only a minor fraction of particles for which thermal fluctuations overcome the magnetic force (mostly located in the proximity of the lateral surface of the rod). On the contrary, particle as small as $r = 25 \text{ nm}$ have shown to be poorly captured. For a relevant number of them, brownian motion has been seen to dominate the dynamics, as the magnetic force exerted by the rod is not strong enough to trigger the capture. However, the use of a shorter rod has been proven to slightly improve the separation efficiency even for small particles.

A first estimation of the efficiency of the random packing configuration for the separation matrix has been performed on the basis of the study on single rods. When long rods are considered, the random packing has proven to perform worse than an array of cylinders disposed perpendicularly to the external field (therefore, at the optimum angle). On average, the random packing performs separation twice longer: the times vary from the order of $\approx 10 \text{ s}$ for particles above 100 nm to $\approx 1000 \text{ s}$ for particles on the order of 25 nm . When shorter rods are used, however, the random packing has been seen to perform separation on the same time scale of the

optimized setup, therefore offering a valid design for the separation matrix of a HGMS setup. Finally, the influence of the concentration of the superparamagnetic particles has been evaluated by performing a simulation with a single rod on a concentrated suspension. Chain aggregates are reported to form in these conditions: the chains enhance the separation speed of a factor of at least one order of magnitude, in comparison with a dilute system. The dependence of the separation time on the concentration has been empirically described by a power law equation. The obtained results correspond well with the predictions from theory and simulations obtained by other research groups. Furthermore, they hint to the possibility of the existence of a general scaling law for the separation time of superparamagnetic nanoparticles with different sizes.

The study presented in this thesis suggests new analysis and research lines in order to better characterize the efficiency of the magnetic separation setup and further optimize it on the available parameters. Among the most important, the following could be considered:

- Study of a multi-rod system. The algorithm is designed to simulate also a multi-rod configuration: the simulations have not been done for time constraints. A multi-rod system would provide an optimization on the system geometry, after the single rod optimization has been performed in this study.
- Possibility of a universal curve. As mentioned in the relevant section of the optimization study, the separation time curves for different particle sizes suggest that, upon proper rescaling, a universal curve may exist. Even though a similar result has been reported in literature, no mention has been made so far upon its dependence on both the size and the magnetic properties. Its evaluation would provide an interesting theoretical result as well as a practical and immediate tool for determining the separation time of an arbitrary superparamagnetic particle.
- Magnetic length. As mentioned in the relevant section, the occurrence of essentially two kinetics regimes (one dominated by the magnetic attraction force and one dominated by the thermal fluctuations) may suggest the existence of a general *magnetic length* of the particles and system. In perfect parallel with the electrostatic and gravitational counterpart, its determination could provide an easy criterion to assess whether magnetic separation, for a specific particle size and rod, will take place or if Brownian motion (or eventually drag) would be the dominant mechanism.
- Study of concentrated systems. So far, the concentrated systems analyzed are limited to a single initial configuration. More simulations for different conditions would refine the power-law dependence which has been formulated, as well as providing more insights on the difference between the separation of dilute (ideal) systems and their concentrated (real) counterpart.

For further research, the following improvement on the developed algorithm could be considered:

- Inclusion of other interparticle forces (e.g., electrostatic interactions) in order to simulate other particle systems.
- Implementation of a general flow pattern inside the separation column. A flow configuration for the porous matrix could be, for instance, generated via a preliminary Lattice Boltzmann simulation.
- Implementation of lubrication effects when the particles get almost in touch. Considering lubrication would provide a better characterization of the chain formation mechanism and dynamics.
- Inclusion of a contact interaction between the captured particles and the ferromagnetic rods. Considering such interaction would describe quantitatively the effect of flow on the captured particle, stating if they keep separated by the rod or get dragged by the flow.

Finally, it is evident that, in the field of magnetic separation, the theory develops at a way slower pace in comparison with the impressive evolutions in both technological implementations and new particle types and sizes. However, this study proves that simulations can provide an actual insight into the physics involved in such a rich and complex field, as well as providing a very valuable tool for the design of new setups and interpretation of experimental results. Therefore, the results obtained via the simulations should be compared with the experiments performed with a similar setup and a mixed approach to the separation problem is suggested. In the view of the author, the suitable combination of designed experiments and tailored simulations offers the most efficient way to address the yet many open questions concerning magnetic separation with superparamagnetic nanoparticles. In turn, this would provide a better understanding of the functioning details of the existing separation setups, and would lead the way to a new generation of setups and applications of the magnetic separation technology.

Appendix A

Analytical flow fields around a cylinder

In this Appendix the analytical formulas that express the solvent steady flow fields around a cylinder are presented. Two kinds of flow are considered: a flow perpendicular to the cylinder axis and a flow parallel to the cylinder axis. The solutions presented are two-dimensional, but can be extended to the 3D case by symmetry arguments.

In both cases, the flow is considered inviscid ($\rho = 0$), incompressible ($\nabla \cdot \mathbf{u} = 0$) and irrotational ($\nabla \times \mathbf{u} = 0$). In mathematical terms, the flow obeys Laplace's equation [72]:

$$\nabla^2 \phi = 0 \tag{A.1}$$

where $\mathbf{u} = \nabla \phi$. The boundary conditions are given [72]:

$$\mathbf{u}_\infty = U \hat{x} \tag{A.2}$$

$$\mathbf{u} \cdot \hat{n} = 0 \tag{A.3}$$

where \hat{n} is a vector normal to the body surface. These correspond to an uniform flow far from the body and a flow tangential to the body's surface.

A.1 Flow perpendicular to the cylinder axis

The cylinder has radius a and it is centered in the origin. Its axis is oriented along the \hat{z} axis: therefore, in the two-dimensional case considered here, the cylinder consists of a disk. The flow far from the cylinder has uniform value U along the \hat{x} axis. The solution for the function ϕ in polar coordinates is [72]:

$$\phi(r, \theta) = U \left(r + \frac{a^2}{r} \right) \cos \theta \tag{A.4}$$

The velocity components in polar coordinates are found by differentiating the previous result:

$$u_r = U \left(1 - \frac{a^2}{r^2} \right) \cos \theta \tag{A.5}$$

$$u_\theta = -U \left(1 + \frac{a^2}{r^2} \right) \sin \theta \tag{A.6}$$

Figure A.1 represents the streamlines of the solution given by these equations. This solution is valid in 3D if the cylinder is infinitely long. In this case, the complete flow field consists of the stated 2D solution in cylindrical coordinates (without, therefore, any explicit dependence on z). A rather crude approximation can be obtained for a finite cylinder by disregarding the end

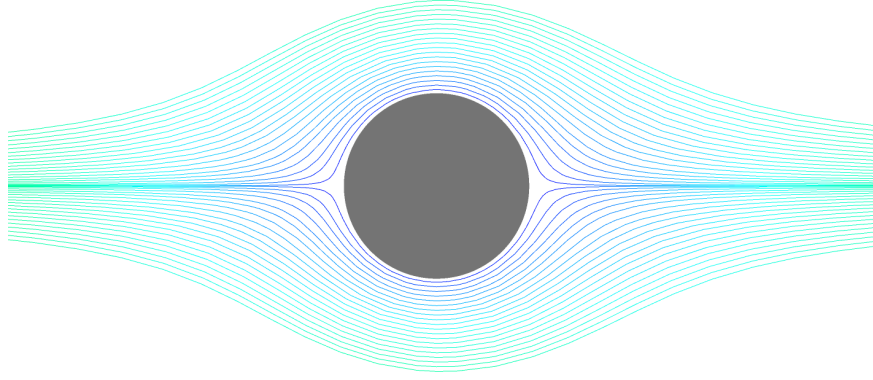


Figure A.1: Velocity field past a cylinder with its long axis perpendicular to the flow (streamlines). The solution is valid for an inviscid, incompressible and irrotational fluid [72].

effects. In that case, the 3D solution for a finite cylinder of radius a and length L in cylindrical coordinates is:

$$\begin{cases} \mathbf{u}(r, \theta, z) = (u_r, u_\theta, 0) & |z| < L/2 \\ \mathbf{u}(r, \theta, z) = (U \cos \theta, U \sin \theta, 0) & |z| \geq L/2 \end{cases} \quad (\text{A.7})$$

with u_r and u_θ as given above. This solution has the disadvantage to be discontinuous at $|z| = L/2$. Unfortunately, is not possible to cure the discontinuity for a cylinder in an analytic solution without considering turbulence effects, which would contradict the assumptions made on the flow condition at the beginning of this Appendix. A better solution is provided by regarding the cylinder as a sphero-cylinder: for sufficiently large L/D ratios, the approximation of a cylinder to a sphero-cylinder holds. In this way, the caps are modeled as hemispheres. The field around the hemisphere can be computed starting from the solutions u_r and u_θ already found for the cylinder. Let us consider the top cap. As we are considering an hemisphere, we limit to $z \geq L/2$. The solution in the plane $(x, 0, z)$ is given by:

$$u_x = U \left(1 - \frac{a^2}{x^2 + z^2} \frac{x^2 - z^2}{x^2 + z^2} \right) \quad (\text{A.8})$$

$$u_y = 0 \quad (\text{A.9})$$

$$u_z = U \frac{a^2}{x^2 + z^2} \frac{2xz}{x^2 + z^2} \quad (\text{A.10})$$

These solutions for u_x and u_z are obtained by expressing Equations A.5 and A.6 in cartesian coordinates with the proper axis orientation. Cylindrical symmetry around the \hat{x} axis can be then enforced. A new cylindrical system of coordinate can be set for the top hemisphere:

$$y = \rho \cos \psi \quad (\text{A.11})$$

$$z = \pm \rho \sin \psi \quad (\text{A.12})$$

$$x = h \quad (\text{A.13})$$

where the signs \pm take into account the sign inversion in the z coordinate between the top and bottom hemispheres. With regards to these new definitions, the flow field solution for the hemisphere is:

$$u_\rho^\pm = U \frac{a^2}{h^2 + \rho^2} \frac{2h\rho}{h^2 + \rho^2} \quad (\text{A.14})$$

$$u_\psi^\pm = 0 \quad (\text{A.15})$$

$$u_h^\pm = U \left(1 - \frac{a^2}{x^2 + z^2} \frac{x^2 - z^2}{x^2 + z^2} \right) \quad (\text{A.16})$$

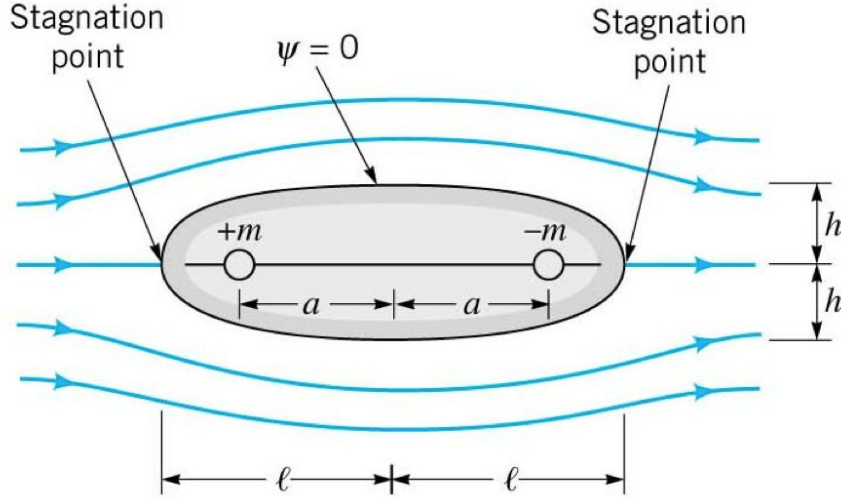


Figure A.2: Rankine oval. The parameters m and a , together with the uniform flow velocity U far from the body, determines the shape and dimension of the oval.

The flow field for the whole cylinder can be thus expressed:

$$\begin{cases} \mathbf{u}(\rho, \psi, h) = (u_{\rho}^-, 0, u_h^-) & z < -L/2 \\ \mathbf{u}(r, \theta, z) = (u_r, u_{\theta}, 0) & |z| \leq L/2 \\ \mathbf{u}(\rho, \psi, h) = (u_{\rho}^+, 0, u_h^+) & z > L/2 \end{cases} \quad (\text{A.17})$$

where the superscript signs \pm take into account the sign inversion in the z coordinate between the top and bottom hemisphere. This solution is continuous at the edge planes $(x, y, \pm L/2)$, being thus preferable to the first 3D solution proposed above. Using a 2D solution and enforcing cylindrical symmetry to model the flow around the hemisphere is still not exact, since the 3D solution for a flow past a sphere slightly differs for that of a 2D cylinder.

A.2 Flow parallel to the cylinder axis

The flow past a cylinder oriented with its axis parallel to the flow implies the presence a very sharp boundary at the edges of the cylinder. This leads to the creation of vortexes and other complex turbulence fluid features, which ultimately are not discussed in the frame of this study. An analytical solution for the flow past a cylinder which does not require such involved analysis is therefore not obtained. However, if the aspect ratio L/D of the cylinder is large enough, the cylinder can be approximated by an oval body, for which analytical solutions exist. In particular, a class of convenient bodies which can be exactly modeled under the assumed flow conditions (inviscid, incompressible steady flow) are called *Rankine Ovals* [100]. They are cylindrical shapes which are long compared to their heights. Unlike a cylinder, they are not physical bodies. They are, on the contrary, exact solutions for potential flows involving ideal fluid sinks and sources: the body surface is given by the solution of an exact mathematical equation [100]. As a consequence, the dimensions of a Rankine Oval is dependent on some constituent parameters. Figure A.2 is a representation of a Rankine Oval: the relevant parameters are shown.

In 2D, setting a cartesian coordinate system with its origin in the center of the oval and the x-axis oriented parallel to the body long axis, the solution for the function ϕ is [100]:

$$\phi(x, y) = Ux - \frac{m}{2\pi} \left(\log \frac{\sqrt{(x-a)^2 + y^2}}{\sqrt{(x+a)^2 + y^2}} \right) \quad (\text{A.18})$$

and the velocities u_x and u_y follow from differentiating the potential function ϕ . The body's half-width and length result to be [100]:

$$l = \sqrt{\frac{ma}{\pi U} + a^2} \quad (\text{A.19})$$

$$h = \frac{h^2 - a^2}{2a} \tan \frac{2\pi U h}{m} \quad (\text{A.20})$$

The expression for h is intended to be solved iteratively. It is possible to invert the parameters declaration problem: giving l and h to be known and U to be a fixed parameter, m and a can be found. In this way, it is possible to find an approximate analytical solution for a 2D cylinder of radius h and half-length l .

A generalization to 3D, unlike the previous case, is possible for a Rankine Oval: the resulting solid shape is obtained by a revolution of the 2D oval around its major axis. Setting a cartesian coordinate system with its origin in the center of the body and the x-axis oriented parallel to the long axis, the solution for ϕ is:

$$\phi(x, y, z) = Ux + \frac{m}{4\pi} \left(\frac{1}{\sqrt{(x-a)^2 + y^2 + z^2}} - \frac{1}{\sqrt{(x+a)^2 + y^2 + z^2}} \right) \quad (\text{A.21})$$

The velocity components in are found by differentiating the previous result:

$$u_x = U - \frac{m}{4\pi} \left(\frac{x-a}{((x-a)^2 + y^2 + z^2)^{3/2}} - \frac{x+a}{((x+a)^2 + y^2 + z^2)^{3/2}} \right) \quad (\text{A.22})$$

$$u_y = -\frac{m}{4\pi} \left(\frac{y}{((x-a)^2 + y^2 + z^2)^{3/2}} - \frac{y}{((x+a)^2 + y^2 + z^2)^{3/2}} \right) \quad (\text{A.23})$$

$$u_z = -\frac{m}{4\pi} \left(\frac{z}{((x-a)^2 + y^2 + z^2)^{3/2}} - \frac{z}{((x+a)^2 + y^2 + z^2)^{3/2}} \right) \quad (\text{A.24})$$

The body's half-width h and length l are solutions of the equations:

$$(l^2 - a^2)^2 - \frac{mla}{\pi U} = 0 \quad (\text{A.25})$$

$$\pi U h^2 \sqrt{1 + h^2/a^2} = m \quad (\text{A.26})$$

As before, it is possible to invert the parameter's declaration problem: giving l and h to be known and U to be a fixed parameter, m and a can be found. In this way, it is possible to find an approximate analytical solution for a 3D cylinder of radius h and half-length l .

Appendix B

Coordinate transformation and rototranslation of a vector field and its derivatives

In this Appendix the numerical formulas for the change of coordinate system and for the rototranslation of a vector field are given. The formulas were directly implemented into the BD algorithm as discussed in Chapter 2.

B.1 Coordinate transformation - From cylindrical to cartesian coordinates

Let us consider a vector field \mathbf{B} . Its expression in cylindrical coordinates reads:

$$\mathbf{B} = (B_\rho, B_\theta, B_z) \quad (\text{B.1})$$

The matrix of the derivatives in cylindrical coordinates reads:

$$d\mathbf{B} = \begin{pmatrix} \frac{\partial B_\rho}{\partial \rho} & \frac{\partial B_\rho}{\partial \theta} & \frac{\partial B_\rho}{\partial z} \\ \frac{\partial B_\theta}{\partial \rho} & \frac{\partial B_\theta}{\partial \theta} & \frac{\partial B_\theta}{\partial z} \\ \frac{\partial B_z}{\partial \rho} & \frac{\partial B_z}{\partial \theta} & \frac{\partial B_z}{\partial z} \end{pmatrix} \quad (\text{B.2})$$

We look for an expression of the field \mathbf{B} and the derivative matrix $d\mathbf{B}$ in a cartesian coordinates reference frame opportunely oriented respect to the cylindrical one.

The basis vectors of the two coordinate systems are related by the following equations:

$$\hat{\mathbf{e}}_\rho = \cos \theta \hat{\mathbf{e}}_x + \sin \theta \hat{\mathbf{e}}_y \quad (\text{B.3})$$

$$\hat{\mathbf{e}}_\theta = -\sin \theta \hat{\mathbf{e}}_x + \cos \theta \hat{\mathbf{e}}_y \quad (\text{B.4})$$

$$\hat{\mathbf{e}}_z = \hat{\mathbf{e}}_z \quad (\text{B.5})$$

The following identity holds for the vector field:

$$B_x \hat{\mathbf{e}}_x + B_y \hat{\mathbf{e}}_y + B_z \hat{\mathbf{e}}_z = B_\rho \hat{\mathbf{e}}_\rho + B_\theta \hat{\mathbf{e}}_\theta + B_z \hat{\mathbf{e}}_z \quad (\text{B.6})$$

From this, the following relations can be derived:

$$B_x(x, y, z) = B_\rho(\rho, \theta, z) \frac{x}{\rho} - B_\theta(\rho, \theta, z) \frac{y}{\rho} \quad (\text{B.7})$$

$$B_y(x, y, z) = B_\rho(\rho, \theta, z) \frac{y}{\rho} + B_\theta(\rho, \theta, z) \frac{x}{\rho} \quad (\text{B.8})$$

$$B_z(x, y, z) = B_z(\rho, \theta, z) \quad (\text{B.9})$$

with $\rho = \sqrt{x^2 + y^2}$ and $\theta = \arctan x/y$. These relation connects the vector field \mathbf{B} components from a cylindrical to a cartesian coordinate system.

Before starting the derivation of the connecting equations between cylindrical and cartesian coordinates for the derivative matrix, it is useful to recall the chain rule for partial derivatives. If $\mathbf{f}(\mathbf{x})$ and $\mathbf{g}(\mathbf{y})$ are vector fields in a three dimensional space and $\mathbf{h} = \mathbf{g} \circ \mathbf{f}$, then:

$$\frac{\partial h_i}{\partial x_j}(\mathbf{x}) = \sum_{l=1}^3 \frac{\partial g_l}{\partial y_l}(\mathbf{f}(\mathbf{x})) \frac{\partial f_l}{\partial x_j}(\mathbf{x}) \quad (\text{B.10})$$

Matrix formulation is perhaps more elegant:

$$\begin{pmatrix} \frac{\partial h_i}{\partial x_1}(\mathbf{x}) \\ \frac{\partial h_i}{\partial x_2}(\mathbf{x}) \\ \frac{\partial h_i}{\partial x_3}(\mathbf{x}) \end{pmatrix} = \mathbf{J}^\top \begin{pmatrix} \frac{\partial g_i}{\partial y_1}(\mathbf{y}) \\ \frac{\partial g_i}{\partial y_2}(\mathbf{y}) \\ \frac{\partial g_i}{\partial y_3}(\mathbf{y}) \end{pmatrix} \quad (\text{B.11})$$

where \mathbf{J} represents the Jacobian matrix of the function \mathbf{f} :

$$\mathbf{J} = \begin{pmatrix} \frac{\partial f_1}{\partial x_1} & \frac{\partial f_1}{\partial x_2} & \frac{\partial f_1}{\partial x_3} \\ \frac{\partial f_2}{\partial x_1} & \frac{\partial f_2}{\partial x_2} & \frac{\partial f_2}{\partial x_3} \\ \frac{\partial f_3}{\partial x_1} & \frac{\partial f_3}{\partial x_2} & \frac{\partial f_3}{\partial x_3} \end{pmatrix} \quad (\text{B.12})$$

and the subscript T stands for the transposition operation. For the case under study, the vector field \mathbf{g} represents the field \mathbf{B} while the field \mathbf{f} represents the coordinate system transformation. Let us call this transformation ϕ for notation clarity. In going from cartesian to cylindrical coordinates, ϕ is defined as:

$$(\rho, \theta, z) \xrightarrow{\phi} (\rho \cos \theta, \rho \sin \theta, z) = (x, y, z) \quad (\text{B.13})$$

The matrix $T\phi$ is the transpose of the Jacobian $\frac{\partial(x, y)}{\partial(\rho, \theta)}$ of the coordinate transformation. It can be shown that it results to be:

$$T\phi = \left(\frac{\partial(x, y)}{\partial(\rho, \theta)} \right)^T = \begin{pmatrix} \cos \theta & \sin \theta & 0 \\ -\rho \sin \theta & \rho \cos \theta & 0 \\ 0 & 0 & 1 \end{pmatrix} \quad (\text{B.14})$$

Going the other way (cylindrical to cartesian) simply implies inverting the matrix $T\phi$. It can be proved that:

$$T\phi^{-1} = \begin{pmatrix} \cos \theta & -\frac{\sin \theta}{\rho} & 0 \\ \sin \theta & \frac{\cos \theta}{\rho} & 0 \\ 0 & 0 & 1 \end{pmatrix} \quad (\text{B.15})$$

Therefore, the following result holds for an arbitrary component B_i with $i = (x, y, z)$ for the field \mathbf{B} :

$$\begin{pmatrix} \frac{\partial B_i}{\partial x} \\ \frac{\partial B_i}{\partial y} \\ \frac{\partial B_i}{\partial z} \end{pmatrix} = \begin{pmatrix} \cos \theta & -\frac{\sin \theta}{\rho} & 0 \\ \sin \theta & \frac{\cos \theta}{\rho} & 0 \\ 0 & 0 & 1 \end{pmatrix} \begin{pmatrix} \frac{\partial B_i}{\partial \rho} \\ \frac{\partial B_i}{\partial \theta} \\ \frac{\partial B_i}{\partial z} \end{pmatrix} \quad (\text{B.16})$$

The partial differentiation in the last matrix should be carried on in the cylindrical coordinate system. E.g., with the notation $\frac{\partial B_x}{\partial \rho}$, it is intended $\frac{\partial B_x}{\partial \rho}(\rho, \theta, z)$. Finally, the overall derivative matrix in cartesian coordinates is given in compact notation:

$$d\mathbf{B}^{\text{cart}} = T\phi^{-1} \begin{pmatrix} \frac{\partial B_x}{\partial r} & \frac{\partial B_y}{\partial r} & \frac{\partial B_z}{\partial r} \\ \frac{\partial B_x}{\partial \theta} & \frac{\partial B_y}{\partial \theta} & \frac{\partial B_z}{\partial \theta} \\ \frac{\partial B_x}{\partial z} & \frac{\partial B_y}{\partial z} & \frac{\partial B_z}{\partial z} \end{pmatrix} \quad (\text{B.17})$$

This equation relates all the nine entries in the derivative matrix $d\mathbf{B}^{\text{cart}}$ in cartesian coordinates to the nine partial derivatives of the matrix $d\mathbf{B}^{\text{cyl}}$ in cylindrical coordinates. As the notation can generate confusion, the actual calculation of one of the entries of $d\mathbf{B}^{\text{cart}}$ in cartesian will be performed.

Let us consider the entry $\frac{\partial B_x}{\partial x}$. According to Equation B.17:

$$\frac{\partial B_x}{\partial x} = \cos \theta \frac{\partial B_x}{\partial \rho} - \frac{\sin \theta}{\rho} \frac{\partial B_x}{\partial \theta} \quad (\text{B.18})$$

In order to perform the derivatives $\frac{\partial B_x}{\partial \rho}$ and $\frac{\partial B_x}{\partial \theta}$, let us rewrite Equation B.7 on the facing page as:

$$B_x(x, y, z) = B_\rho(\rho, \theta, z) \frac{x}{\rho} - B_\theta(\rho, \theta, z) \frac{y}{\rho} = B_\rho(\rho, \theta, z) \cos \theta - B_\theta(\rho, \theta, z) \sin \theta \quad (\text{B.19})$$

Therefore, we can rewrite Equation B.18 as:

$$\frac{\partial B_x}{\partial x} = \cos \theta \frac{\partial}{\partial \rho} (B_\rho \cos \theta - B_\theta \sin \theta) - \frac{\sin \theta}{\rho} \frac{\partial}{\partial \theta} (B_\rho \cos \theta - B_\theta \sin \theta) \quad (\text{B.20})$$

Now, the RHS only contains derivatives that are entries of the matrix $d\mathbf{B}^{\text{cyl}}$, which are known. A little bit of algebra gives the final result:

$$\begin{aligned} \frac{\partial B_x}{\partial x} &= \frac{\sin^2 \theta}{\rho} B_\rho + \cos \theta \sin \theta \left(B_\theta - \frac{\partial B_\rho}{\partial \theta} \right) + \frac{\sin^2 \theta}{\rho} \frac{\partial B_\theta}{\partial \theta} \\ &\quad + \cos^2 \theta \frac{\partial B_\rho}{\partial \rho} - \cos \theta \sin \theta \frac{\partial B_\rho}{\partial \theta} \end{aligned} \quad (\text{B.21})$$

As a final observation, the above expression is independent of the choice of the coordinate system, provided that the transformation function ϕ between the systems is observed: the quantities (x, y, z) and (ρ, θ, z) in the coefficients can be even mixed. However, it is important to note that the functions $\frac{\partial B_\rho}{\partial \theta}$ are entries of $d\mathbf{B}^{\text{cyl}}$ and, therefore, the partial derivatives are calculated in the (ρ, θ, z) plane. The substitution $(x, y, z) = (\rho \cos \theta, \rho \sin \theta, z)$ is performed only *after* the differentiation.

B.2 Rototranslation of vector fields and derivatives between two Cartesian coordinate systems

Let us consider a vector field \mathbf{B} . Its expression in a cartesian coordinate reference (x, y, z) frame reads:

$$\mathbf{B} = B_x \hat{\mathbf{x}} + B_y \hat{\mathbf{y}} + B_z \hat{\mathbf{z}} \quad (\text{B.22})$$

Let be a second cartesian reference frame (x', y', z') . This new frame is rototranslated within respect to the former one.

The translations are intended to be performed respect to the origin $(0, 0, 0)$ of the former frame. A translation can be expressed by a vector $\mathbf{v} = (v_x, v_y, v_z)$. If the original coordinates of a point are (x, y, z) , after the translation they will be:

$$(x', y', z') = (x + v_x, y + v_y, z + v_z) \quad (\text{B.23})$$

A rotation can be expressed by a matrix R . If the original coordinates of a point are $\mathbf{r} = (x, y, z)$, after the rotation they will be:

$$\mathbf{r}' = R\mathbf{r} \quad (\text{B.24})$$

The form of the rotation matrix R depends on the formalism chosen to express it. In this study, the rotations are intended to be *basic rotations*, i.e. rotations about one of the axes of a coordinate system. Basic rotations are expressed in matrix notation [101]. According to this formalism, a general rotation can be obtained as a sequence of basic rotations:

$$R = R_x(\alpha)R_y(\beta)R_z(\gamma) \quad (\text{B.25})$$

where the subscript x , y and z represent the axes on which the rotation is performed and α , β and γ represent the rotation angles. The expression of the standard rotation matrices $R_x(\theta)$, $R_y(\theta)$ and $R_z(\theta)$ are [101]:

$$R_x(\theta) = \begin{pmatrix} 1 & 0 & 0 \\ 0 & \cos \theta & -\sin \theta \\ 0 & \sin \theta & \cos \theta \end{pmatrix} \quad (\text{B.26})$$

$$R_y(\theta) = \begin{pmatrix} \cos \theta & 0 & \sin \theta \\ 0 & 1 & 0 \\ -\sin \theta & 0 & \cos \theta \end{pmatrix} \quad (\text{B.27})$$

$$R_z(\theta) = \begin{pmatrix} \cos \theta & -\sin \theta & 0 \\ \sin \theta & \cos \theta & 0 \\ 0 & 0 & 1 \end{pmatrix} \quad (\text{B.28})$$

It should be noted that the order in which the matrix multiplication is performed matters, as a rotation $R_x R_y R_z$ will be different from a rotation $R_y R_x R_z$ even if the rotation angles are the same.

Returning to our cartesian frames (x, y, z) and (x', y', z') , let \mathbf{v} be the translation vector and (α, β, γ) be the rotation angles of the latter respect to the former. The rotation matrix is $R = R_z(\gamma)R_y(\beta)R_x(\alpha)$. The vector field $\mathbf{B} = (B_x, B_y, B_z)$ in the first coordinate system will be rototranslated into the vector field $\mathbf{B}' = (B'_{x'}, B'_{y'}, B'_{z'})$ in the second reference frame. The components $(B'_{x'}, B'_{y'}, B'_{z'})$ are a results of two operations: a rototranslation of the *coordinates* (x, y, z) and a rototranslation of the *components* (B_x, B_y, B_z) . Particular care has to be taken in the correct order of the operations involved, as the components (B_x, B_y, B_z) are theirselve functions of the coordinates (x, y, z) . The rototranslation of the field is done according to the following equation:

$$\begin{pmatrix} B'_{x'}(x', y', z') \\ B'_{y'}(x', y', z') \\ B'_{z'}(x', y', z') \end{pmatrix} = R \begin{pmatrix} B_x(x, y, z) \\ B_y(x, y, z) \\ B_z(x, y, z) \end{pmatrix} \quad (\text{B.29})$$

with:

$$\mathbf{r}' = R\mathbf{r} + \mathbf{v} \quad (\text{B.30})$$

The rototransformation of the derivatives is more involved, as, in addition to the aforementioned two operations, a third one must be added: the differentiation respect to the new variables (x', y', z') . The procedure for calculating one entry of the derivative matrix $d\mathbf{B}'$ starting from $d\mathbf{B}$ will be given in the following. Let us consider B_x . According to Equation B.29 on the facing page, the following holds:

$$B'_{x'} = R_{11}B_x + R_{12}B_y + R_{13}B_z \quad (\text{B.31})$$

where R_{ij} indicates the opportune entry in the rotation matrix R . Consequently:

$$\frac{\partial B'_{x'}}{\partial x'} = R_{11} \frac{\partial B_x}{\partial x'} + R_{12} \frac{\partial B_y}{\partial x'} + R_{13} \frac{\partial B_z}{\partial x'} \quad (\text{B.32})$$

According to the chain rule for partial derivatives:

$$\frac{\partial B_x}{\partial x'} = \frac{\partial B_x}{\partial x} \frac{dx}{dx'} + \frac{\partial B_x}{\partial y} \frac{dy}{dx'} + \frac{\partial B_x}{\partial z} \frac{dz}{dx'} \quad (\text{B.33})$$

The terms $\frac{dx}{dx'}$ and similar can be obtained via Equation B.30. As the translation does not contribute to the derivative, the general rule is:

$$\frac{dx_i}{dx'_j} = R_{ij}^{-1} \quad (\text{B.34})$$

where R^{-1} is the inverse matrix of R . Now, all the elements of Equation B.33 can be expressed in terms of entries of the matrices R and $d\mathbf{B}$. The entries of the matrix $d\mathbf{B}'$ can be thus obtained by carrying on all the algebra involved by the procedure just illustrated. In compact notation, it can be proved that the final results is given by:

$$d\mathbf{B}' = R d\mathbf{B} R^{-1} \quad (\text{B.35})$$

As a final remark, given the matrix R there is no real need to effectuate the inversion operation to retrieve R^{-1} , as the rotation matrices have the property $R^{-1} = R^T$, thus greatly simplifying the calculation of the coefficients.

Appendix C

Derivation of the equations for the magnetic field of a transversally magnetized rod

In this Appendix, the derivation of the equations for the magnetic field produced by a transversally magnetized cylinder (Equation (3.10) in the text) is provided. Following the derivation of the equations, the limiting cases for an infinitely long cylinder will also be obtained.

C.1 General statement of the problem

Suppose we have a circular cylindrical magnet of radius R and length L magnetized along the x-direction (this is not a loss of generality, as any other transverse magnetization direction is obtainable simply rotating the reference frame). The magnetization vector is therefore:

$$\mathbf{M} = M\hat{x} \quad (\text{C.1})$$

The magnetostatic potential generated by an arbitrary magnetization vector is given by [10]:

$$\Phi(\mathbf{r}) = \int_V d\mathbf{r}' \frac{\rho(\mathbf{r}')}{4\pi|\mathbf{r} - \mathbf{r}'|} \quad (\text{C.2})$$

in which the *bound magnetic charge* formulation is used. The previous equation can be more conveniently reformulated in terms of the potential of a point charge. Using therefore the Green's function:

$$G(\mathbf{r}) = \frac{1}{4\pi|\mathbf{r}|} \quad (\text{C.3})$$

the magnetostatic potential now reads:

$$\Phi(\mathbf{r}) = \int_V d\mathbf{r}' G(\mathbf{r} - \mathbf{r}')\rho(\mathbf{r}') \quad (\text{C.4})$$

In the problem of interest, the volume charge density $\rho(\mathbf{r})$ reduces to a surface charge distribution on the outer surface of the cylinder (excluding the top and bottom ends). In cylindrical coordinates where $\theta = 0$ corresponds to the x-axis, this results in:

$$\sigma(\theta) = M \cos \theta \quad (\text{C.5})$$

The integral in Equation (C.4) reduces to the integral over the lateral surface of the cylinder:

$$\Phi(\mathbf{r}) = \frac{M}{4\pi} \int_0^{2\pi} d\theta' \int_{-L}^L dz' \frac{R \cos \theta'}{\sqrt{r^2 + R^2 - 2rR \cos(\theta - \theta') + (z - z')^2}} \quad (\text{C.6})$$

The magnetic field \mathbf{H} can be obtained by:

$$\mathbf{H} = -\nabla\Phi \quad (\text{C.7})$$

The problem now reduces to the calculations of the three components of the field:

$$H_r(r, \theta, z) = -\frac{\partial\Phi}{\partial r} \quad (\text{C.8a})$$

$$H_\theta(r, \theta, z) = -\frac{1}{r} \frac{\partial\Phi}{\partial\theta} \quad (\text{C.8b})$$

$$H_z(r, \theta, z) = -\frac{\partial\Phi}{\partial z} \quad (\text{C.8c})$$

C.2 The radial component

Performing the derivation in (C.8a), the component becomes (the variables of the function will be omitted for simplicity):

$$H_r = -\frac{MR}{4\pi} \int_0^{2\pi} d\theta' \int_{-L}^L dz' \cos\theta' \left(-\frac{r - R \cos(\theta - \theta')}{(r^2 + R^2 - 2rR \cos(\theta - \theta') + (z - z')^2)^{3/2}} \right)$$

Performing the first integral gives:

$$H_r = \frac{MR}{4\pi} \int_0^{2\pi} d\theta' \cos\theta' \frac{r - R \cos(\theta - \theta')}{r^2 + R^2 - 2rR \cos(\theta - \theta')} \left(\frac{z + L}{\sqrt{(z + L)^2 + r^2 + R^2 - 2rR \cos(\theta - \theta')}} - \frac{z - L}{\sqrt{(z - L)^2 + r^2 + R^2 - 2rR \cos(\theta - \theta')}} \right)$$

The following substitution of variable can be done:

$$2\psi = \pi - (\theta - \theta')$$

This leads to the following simplifying expressions:

$$\begin{aligned} r^2 + R^2 - 2rR \cos(\theta - \theta') &= (r + R)^2 \left[\cos^2 \psi + \left(\frac{r-R}{r+R} \right)^2 \sin^2 \psi \right] \\ r - R \cos(\theta - \theta') &= (r + R) \left[\cos^2 \psi + \left(\frac{r-R}{r+R} \right) \sin^2 \psi \right] \\ (z \pm L)^2 + R^2 + r^2 - 2rR \cos(\theta - \theta') &= \cos^2 \psi [(z \pm L)^2 + (r + R)^2] + \\ &\quad \sin^2 \psi [(z \pm L)^2 + (r + R)^2] \left(\frac{(z \pm L)^2 + (r - R)^2}{(z \pm L)^2 + (r + R)^2} \right) \end{aligned}$$

With the substitutions:

$$\begin{aligned} z_\pm &= z \pm L \\ \gamma &= \frac{\rho - R}{\rho + R} \\ \alpha_\pm &= \frac{R}{\sqrt{z_\pm^2 + (\rho + R)^2}} \\ \beta_\pm &= \frac{z_\pm}{\sqrt{z_\pm^2 + (\rho + R)^2}} \\ k_\pm &= \sqrt{\frac{z_\pm^2 + (R - \rho)^2}{z_\pm^2 + (R + \rho)^2}} \end{aligned}$$

the following expression is obtained:

$$H_r = \frac{MR}{2\pi(r+R)} \int_{\frac{\pi}{2}-\frac{\theta}{2}}^{\frac{3}{2}\pi-\frac{\theta}{2}} d\psi [\cos 2\psi \cos(\pi-\theta) + \sin 2\psi \sin(\pi-\theta)] \frac{\cos^2 \psi + \gamma \sin^2 \psi}{\cos^2 \psi + \gamma^2 \sin^2 \psi} \left(\frac{\beta_+}{\sqrt{\cos^2 \psi + k_+^2 \sin^2 \psi}} - \frac{\beta_-}{\sqrt{\cos^2 \psi + k_-^2 \sin^2 \psi}} \right) \quad (\text{C.9})$$

The term in the squared bracket can be decomposed as:

$$\begin{aligned} & \cos 2\psi \cos(\pi-\theta) + \sin 2\psi \sin(\pi-\theta) \\ &= \cos(\pi-\theta) [\cos^2 \psi - \sin^2 \psi] + \sin(\pi-\theta) 2 \sin \psi \cos \psi \\ &= \cos(\pi-\theta) \cos^2 \psi - \cos(\pi-\theta) \sin^2 \psi + \sin(\pi-\theta) 2 \sin \psi \cos \psi \end{aligned}$$

The overall integral in equation (C.9) can be therefore seen as comprised of three different terms.

The first term is evidently:

$$\int_{\frac{\pi}{2}-\frac{\theta}{2}}^{\frac{3}{2}\pi-\frac{\theta}{2}} d\psi \cos(\pi-\theta) \cos^2 \psi L(\psi)$$

where $L(\psi)$ is simply a contraction for the remaining terms of equation (C.9).

A new substitution $x = \sin \psi$ leads to:

$$- \int_{-\cos \frac{\theta}{2}}^{\cos \frac{\theta}{2}} dx \cos(\pi-\theta) \frac{(1-x^2)(1-(1-\gamma)x^2)}{1-(1-\gamma^2)x^2} \left(\frac{\beta_+}{\sqrt{(1-x^2)(1-(1-k_+^2)x^2)}} - \frac{\beta_-}{\sqrt{(1-x^2)(1-(1-k_-^2)x^2)}} \right) \quad (\text{C.10})$$

Leaving apart the minus sign, some constant factors, the subscripts + and - and the factor β_{\pm} , which can be retrieved later on, the essential integral to be solved becomes:

$$\begin{aligned} & \int_{-\cos \frac{\theta}{2}}^{\cos \frac{\theta}{2}} dx \frac{(1-x^2)(1-(1-\gamma)x^2)}{1-(1-\gamma^2)x^2} \frac{1}{\sqrt{(1-x^2)(1-(1-k^2)x^2)}} \\ &= \int_{-\cos \frac{\theta}{2}}^{\cos \frac{\theta}{2}} \frac{dx}{1+\gamma} \left[\left(1 - \frac{\gamma}{\gamma^2-1} \right) - x^2 + \left(\frac{\gamma^3}{(\gamma^2-1)(1+(\gamma^2-1)x^2)} \right) \right] \\ & \quad \frac{1}{\sqrt{(1-x^2)(1-(1-k^2)x^2)}} \\ &= \int_{-\cos \frac{\theta}{2}}^{\cos \frac{\theta}{2}} \frac{dx}{1+\gamma} R(x) \end{aligned} \quad (\text{C.11})$$

where $R(x)$ is introduced to make the notation shorter.

The last integral can be split as:

$$\int_{-\cos \frac{\theta}{2}}^{\cos \frac{\theta}{2}} = \int_0^{\cos \frac{\theta}{2}} - \int_0^{-\cos \frac{\theta}{2}}$$

Using the formalism of the elliptic integrals:

$$\begin{aligned} \int_0^{\cos \frac{\theta}{2}} \frac{dx}{1+\gamma} R(x) &= \left(1 - \frac{\gamma}{\gamma^2 - 1}\right) K\left(\frac{\pi}{2} - \frac{\theta}{2} \middle| \sqrt{1-k^2}\right) \\ &- \frac{1}{1-k^2} \left(K\left(\frac{\pi}{2} - \frac{\theta}{2} \middle| \sqrt{1-k^2}\right) - E\left(\frac{\pi}{2} - \frac{\theta}{2} \middle| \sqrt{1-k^2}\right) \right) \\ &+ \frac{\gamma^3}{\gamma^2 - 1} \Pi\left(1 - \gamma^2; \frac{\pi}{2} - \frac{\theta}{2} \middle| \sqrt{1-k^2}\right) \end{aligned}$$

where the forms used correspond to the incomplete elliptic integrals of the 1st, 2nd and 3rd kind, according to the definitions:

$$\begin{aligned} K(x|k) &= \int_0^x \frac{dt}{\sqrt{(1-t^2)(1-k^2t^2)}} \\ E(x|k) &= \int_0^x dt \frac{\sqrt{1-k^2t^2}}{\sqrt{1-t^2}} \\ \Pi(n; \phi|k) &= \int_0^{\sin \phi} \frac{dt}{1-nt^2} \frac{1}{\sqrt{(1-t^2)(1-mt^2)}} \end{aligned}$$

An analogue formulation can be done for the second part of the previously split integral, $\int_0^{-\cos \frac{\theta}{2}}$ considering that

$$\cos\left(-\frac{\theta}{2}\right) = \sin\left(\frac{3}{2}\pi - \frac{\theta}{2}\right)$$

The following identities hold for the complete and incomplete forms of the elliptic integrals:

$$\begin{aligned} K(z + \pi | k) &= 2K(k) + K(z | k) \\ E(z + \pi | k) &= 2E(k) + E(z | k) \\ \Pi(n; z + \pi | k) &= 2\Pi(n | k) + \Pi(n; z | k) \end{aligned}$$

As the two parts of the integral considered before differs of a period π and they differ for a minus sign, the incomplete elliptic integral forms vanish and only complete elliptic integral forms remain. The final result for the first term is then:

$$\int_{\frac{\pi}{2} - \frac{\theta}{2}}^{\frac{3}{2}\pi - \frac{\theta}{2}} d\psi \cos(\pi - \theta) \cos^2 \psi L(\psi) = \frac{2 \cos(\pi - \theta)}{\gamma + 1} [\beta_+ P_1(k_+) - \beta_- P_1(k_-)] \quad (\text{C.12})$$

where all the factors and minus signs are retrieved and:

$$\begin{aligned} P_1(k) &= \left(1 - \frac{\gamma}{\gamma^2 - 1}\right) K(\sqrt{1-k^2}) - \frac{1}{1-k^2} \left(K(\sqrt{1-k^2}) - E(\sqrt{1-k^2}) \right) \\ &+ \frac{\gamma^3}{\gamma^2 - 1} \Pi(1 - \gamma^2, \sqrt{1-k^2}) \quad (\text{C.13}) \end{aligned}$$

The second term is:

$$- \int_{\frac{\pi}{2} - \frac{\theta}{2}}^{\frac{3}{2}\pi - \frac{\theta}{2}} d\psi \cos(\pi - \theta) \sin^2 \psi L(\psi)$$

It is possible to treat this integral with the same substitutions and proceedings as used for the first term. The essential integral to be solved is in this case:

$$\begin{aligned} & \int_{-\cos \frac{\theta}{2}}^{\cos \frac{\theta}{2}} dx \frac{x^2(1 - (1 - \gamma)x^2)}{1 - (1 - \gamma^2)x^2} \frac{1}{\sqrt{(1 - x^2)(1 - (1 - k^2)x^2)}} \\ &= \int_{-\cos \frac{\theta}{2}}^{\cos \frac{\theta}{2}} \frac{dx}{1 + \gamma} \left[\frac{\gamma}{\gamma^2 - 1} + x^2 - \left(\frac{\gamma}{(\gamma^2 - 1)(1 + (\gamma^2 - 1)x^2)} \right) \right] \\ & \quad \frac{1}{\sqrt{(1 - x^2)(1 - (1 - k^2)x^2)}} \end{aligned} \quad (\text{C.14})$$

The result leads again to a form that only contains complete elliptic integrals, according to the same procedure followed above. The final result for this second term is therefore:

$$- \int_{\frac{\pi}{2} - \frac{\theta}{2}}^{\frac{3}{2}\pi - \frac{\theta}{2}} d\psi \cos(\pi - \theta) \sin^2 \psi L(\psi) = - \frac{2 \cos(\pi - \theta)}{\gamma + 1} [\beta_+ P_2(k_+) - \beta_- P_2(k_-)] \quad (\text{C.15})$$

where:

$$\begin{aligned} P_2(k) = \frac{\gamma}{\gamma^2 - 1} K(\sqrt{1 - k^2}) + \frac{1}{1 - k^2} \left(K(\sqrt{1 - k^2}) - E(\sqrt{1 - k^2}) \right) \\ - \frac{\gamma}{\gamma^2 - 1} \Pi(1 - \gamma^2, \sqrt{1 - k^2}) \end{aligned} \quad (\text{C.16})$$

The third term is:

$$\int_{\frac{\pi}{2} - \frac{\theta}{2}}^{\frac{3}{2}\pi - \frac{\theta}{2}} d\psi \sin(\pi - \theta) 2 \sin \psi \cos \psi L(\psi)$$

Proceeding as usual and leaving temporarily apart the constant factors, the essential integral to be solved is in this case:

$$\begin{aligned} & \int_{-\cos \frac{\theta}{2}}^{\cos \frac{\theta}{2}} dx \frac{x\sqrt{1 - x^2}(1 - (1 - \gamma)x^2)}{1 - (1 - \gamma^2)x^2} \frac{1}{\sqrt{(1 - x^2)(1 - (1 - k^2)x^2)}} \\ &= \int_{-\cos \frac{\theta}{2}}^{\cos \frac{\theta}{2}} dx \frac{x(1 - (1 - \gamma)x^2)}{1 - (1 - \gamma^2)x^2} \frac{1}{\sqrt{1 - (1 - k^2)x^2}} \end{aligned} \quad (\text{C.17})$$

With a new substitution $t = x^2$ the integral becomes:

$$\frac{1}{2} \int_{\sin^2(\frac{\pi}{2} - \frac{\theta}{2})}^{\sin^2(\frac{3}{2}\pi - \frac{\theta}{2})} dt \frac{1 - (1 - \gamma)t}{1 - (1 - \gamma^2)t} \frac{1}{\sqrt{1 - (1 - k^2)t}}$$

As:

$$\begin{aligned} \sin^2\left(\frac{3}{2}\pi - \frac{\theta}{2}\right) &= \left(-\cos \frac{\theta}{2}\right)^2 = \cos^2 \frac{\theta}{2} \\ \sin^2\left(\frac{\pi}{2} - \frac{\theta}{2}\right) &= \cos^2 \frac{\theta}{2} \end{aligned}$$

the two integration extrema in the past integral are the same and the integral is null. Therefore, the third term does not contribute. In conclusion, we can now express the radial component as the sum of the first and the second term computed above.

The final result can be obtained by simply summing the contributes for the three terms just evaluated, with all the constants and the correct signs entering again the expression. It is:

$$H_\rho(\rho, \theta, z) = \frac{M}{\pi} \frac{R \cos \theta}{(\rho + R)(\gamma + 1)} \left[-\beta^+(P_1(k^+) - P_2(k^+)) + \beta^-(P_1(k^-) - P_2(k^-)) \right] \quad (\text{C.18})$$

C.3 The angular component

Performing the derivation in (C.8b), the component becomes (the variables of the function will be omitted for simplicity):

$$H_\theta = -\frac{MR}{4\pi r} \int_0^{2\pi} d\theta' \int_{-L}^L dz' \cos \theta' \left(-\frac{rR \sin(\theta - \theta')}{(r^2 + R^2 - 2rR \cos(\theta - \theta') + (z - z')^2)^{3/2}} \right)$$

Performing the first integral gives:

$$H_\theta = \frac{MR}{4\pi r} \int_0^{2\pi} d\theta' \cos \theta' \frac{rR \sin(\theta - \theta')}{r^2 + R^2 - 2rR \cos(\theta - \theta')} \left(\frac{z + L}{\sqrt{(z + L)^2 + r^2 + R^2 - 2rR \cos(\theta - \theta')}} - \frac{z - L}{\sqrt{(z - L)^2 + r^2 + R^2 - 2rR \cos(\theta - \theta')}} \right)$$

Applying the usual substitution of variable:

$$2\psi = \pi - (\theta - \theta')$$

and the simplifying expression:

$$rR \sin(\theta - \theta') = 2rR \sin \psi \cos \psi$$

and using the compact forms as already defined in the previous section, the following expression is obtained:

$$H_\theta = \frac{MR^2}{\pi(r + R)^2} \int_{\frac{\pi}{2} - \frac{\theta}{2}}^{\frac{3}{2}\pi - \frac{\theta}{2}} d\psi [\cos 2\psi \cos(\pi - \theta) + \sin 2\psi \sin(\pi - \theta)] \frac{\cos \psi \sin \psi}{\cos^2 \psi + \gamma^2 \sin^2 \psi} \left(\frac{\beta_+}{\sqrt{\cos^2 \psi + k_+^2 \sin^2 \psi}} - \frac{\beta_-}{\sqrt{\cos^2 \psi + k_-^2 \sin^2 \psi}} \right) \quad (\text{C.19})$$

Performing the decomposition as in the previous case, the overall integral in equation (C.19) can be seen as comprised of three different terms.

The first term is:

$$\int_{\frac{\pi}{2} - \frac{\theta}{2}}^{\frac{3}{2}\pi - \frac{\theta}{2}} d\psi \cos(\pi - \theta) \cos^2 \psi L(\psi)$$

where $L(\psi)$ is simply a contraction for the other part of equation (C.19).

The usual substitution $x = \sin \psi$ leads to:

$$-\int_{-\cos \frac{\theta}{2}}^{\cos \frac{\theta}{2}} dx \cos(\pi - \theta) \frac{x(1 - x^2)\sqrt{1 - x^2}}{1 - (1 - \gamma^2)x^2} \left(\frac{\beta_+}{\sqrt{(1 - x^2)(1 - (1 - k_+^2)x^2)}} - \frac{\beta_-}{\sqrt{(1 - x^2)(1 - (1 - k_-^2)x^2)}} \right) \quad (\text{C.20})$$

Leaving apart the minus sign, some constant factors, the subscripts + and – and the factor β_{\pm} , which can be retrieved later on, the essential integral to be solved becomes:

$$\int_{-\cos \frac{\theta}{2}}^{\cos \frac{\theta}{2}} dx \frac{x(1-x^2)}{1-(1-\gamma^2)x^2} \frac{1}{\sqrt{(1-(1-k^2)x^2)}} \quad (\text{C.21})$$

With a new substitution $t = x^2$ the integral becomes:

$$\frac{1}{2} \int_{\sin^2(\frac{\pi}{2}-\frac{\theta}{2})}^{\sin^2(\frac{3}{2}\pi-\frac{\theta}{2})} dt \frac{1-t}{1-(1-\gamma^2)t} \frac{1}{\sqrt{1-(1-k^2)t}}$$

As pointed out in the previous section, the integration extrema are the same and therefore the integral is zero.

The second term is:

$$- \int_{\frac{\pi}{2}-\frac{\theta}{2}}^{\frac{3}{2}\pi-\frac{\theta}{2}} d\psi \cos(\pi-\theta) \sin^2 \psi L(\psi)$$

Proceeding as usual and leaving temporarily apart the constant factors, the essential integral to be solved is in this case:

$$\int_{-\cos \frac{\theta}{2}}^{\cos \frac{\theta}{2}} dx \frac{x^3}{1-(1-\gamma^2)x^2} \frac{1}{\sqrt{(1-(1-k^2)x^2)}} \quad (\text{C.22})$$

With a new substitution $t = x^2$ the integral becomes:

$$\frac{1}{2} \int_{\sin^2(\frac{\pi}{2}-\frac{\theta}{2})}^{\sin^2(\frac{3}{2}\pi-\frac{\theta}{2})} dt \frac{t}{1-(1-\gamma^2)t} \frac{1}{\sqrt{1-(1-k^2)t}}$$

As pointed out in the previous section, the integration extrema are the same and therefore the integral is zero.

The third term is:

$$\int_{\frac{\pi}{2}-\frac{\theta}{2}}^{\frac{3}{2}\pi-\frac{\theta}{2}} d\psi \sin(\pi-\theta) 2 \sin \psi \cos \psi L(\psi)$$

The essential integral to be solved is in this case:

$$\begin{aligned} & \int_{-\cos \frac{\theta}{2}}^{\cos \frac{\theta}{2}} dx \frac{x^2(1-x^2)}{1-(1-\gamma^2)x^2} \frac{1}{\sqrt{(1-x^2)(1-(1-k^2)x^2)}} \\ &= \int_{-\cos \frac{\theta}{2}}^{\cos \frac{\theta}{2}} \frac{dx}{\gamma^2-1} \left[\frac{\gamma^2}{\gamma^2-1} - x^2 - \left(\frac{\gamma^2}{(\gamma^2-1)(1+(\gamma^2-1)x^2)} \right) \right] \\ & \quad \frac{1}{\sqrt{(1-x^2)(1-(1-k^2)x^2)}} \end{aligned} \quad (\text{C.23})$$

The result leads again to a form that only contains complete elliptic integrals, according to the same procedure followed above. The final result for the third term is therefore:

$$\int_{\frac{\pi}{2}-\frac{\theta}{2}}^{\frac{3}{2}\pi-\frac{\theta}{2}} d\psi \sin(\pi-\theta) 2 \cos \psi \sin \psi L(\psi) = \frac{4 \sin(\pi-\theta)}{\gamma^2-1} [\beta_+ P_3(k_+) - \beta_- P_3(k_-)] \quad (\text{C.24})$$

where:

$$\begin{aligned} P_3(k) &= \frac{\gamma}{\gamma^2-1} K(\sqrt{1-k^2}) - \frac{1}{1-k^2} \left(K(\sqrt{1-k^2}) - E(\sqrt{1-k^2}) \right) \\ & \quad - \frac{\gamma}{\gamma^2-1} \Pi(1-\gamma^2, \sqrt{1-k^2}) \end{aligned} \quad (\text{C.25})$$

The final result is therefore only represented by this last third term, as the first two terms vanish. With all the constants and the correct signs entering again the expression, it reads:

$$H_\theta(\rho, \theta, z) = \frac{M}{\pi} \frac{4R^2 \sin \theta}{(\rho + R)^2(\gamma^2 - 1)} \left[\beta^+ P_3(k^+) - \beta^- P_3(k^-) \right] \quad (\text{C.26})$$

C.4 The z component

Performing the derivation in (C.8c), the component becomes (the variables of the function will be omitted for simplicity):

$$H_z = -\frac{MR}{4\pi} \int_0^{2\pi} d\theta' \int_{-L}^L dz' \cos \theta' \left(-\frac{z - z'}{(r^2 + R^2 - 2rR \cos(\theta - \theta') + (z - z')^2)^{3/2}} \right)$$

Performing the first integral gives:

$$H_z = \frac{MR}{4\pi} \int_0^{2\pi} d\theta' \cos \theta' \left(\frac{1}{\sqrt{(z + L)^2 + r^2 + R^2 - 2rR \cos(\theta - \theta')}} - \frac{1}{\sqrt{(z - L)^2 + r^2 + R^2 - 2rR \cos(\theta - \theta')}} \right)$$

Applying the usual substitution of variable:

$$2\psi = \pi - (\theta - \theta')$$

and using the compact forms as already defined in the previous section, the following expression is obtained:

$$H_z = \frac{M}{2\pi} \int_{\frac{\pi}{2} - \frac{\theta}{2}}^{\frac{3}{2}\pi - \frac{\theta}{2}} d\psi [\cos 2\psi \cos(\pi - \theta) + \sin 2\psi \sin(\pi - \theta)] \left(\frac{\alpha_-}{\sqrt{\cos^2 \psi + k_-^2 \sin^2 \psi}} - \frac{\alpha_+}{\sqrt{\cos^2 \psi + k_+^2 \sin^2 \psi}} \right) \quad (\text{C.27})$$

Performing the decomposition as in the previous case, the overall integral in equation (C.27) can be seen as comprised of three different terms.

The first term is:

$$\int_{\frac{\pi}{2} - \frac{\theta}{2}}^{\frac{3}{2}\pi - \frac{\theta}{2}} d\psi \cos(\pi - \theta) \cos^2 \psi L(\psi)$$

where $L(\psi)$ is simply a contraction for the other part of equation (C.27).

The usual substitution $x = \sin \psi$ leads to:

$$\int_{-\cos \frac{\theta}{2}}^{\cos \frac{\theta}{2}} dx \cos(\pi - \theta) (1 - x^2) \left(\frac{\alpha_-}{\sqrt{(1 - x^2)(1 - (1 - k_-^2))}} - \frac{\alpha_+}{\sqrt{(1 - x^2)(1 - (1 - k_+^2)x^2)}} \right) \quad (\text{C.28})$$

Leaving apart the minus sign, some constant factors, the subscripts + and – and the factor α_{\pm} , which can be retrieved later on, the essential integral to be solved becomes:

$$\int_{-\cos \frac{\theta}{2}}^{\cos \frac{\theta}{2}} dx (1-x^2) \frac{1}{\sqrt{(1-x^2)(1-(1-k^2)x^2)}} \quad (\text{C.29})$$

The result leads again to a form that only contains complete elliptic integrals, according to the same procedure followed above. The final result for the first term is therefore:

$$\int_{\frac{\pi}{2}-\frac{\theta}{2}}^{\frac{3}{2}\pi-\frac{\theta}{2}} d\psi \cos(\pi-\theta) \cos^2 \psi L(\psi) = 2 \cos(\pi-\theta) [\alpha_- P_4(k_-) - \alpha_+ P_4(k_+)] \quad (\text{C.30})$$

where:

$$P_4(k) = K(\sqrt{1-k^2}) - \frac{1}{1-k^2} \left(K(\sqrt{1-k^2}) - E(\sqrt{1-k^2}) \right) \quad (\text{C.31})$$

The second term is:

$$- \int_{\frac{\pi}{2}-\frac{\theta}{2}}^{\frac{3}{2}\pi-\frac{\theta}{2}} d\psi \cos(\pi-\theta) \sin^2 \psi L(\psi)$$

Proceeding as usual and leaving temporarily apart the constant factors, the essential integral to be solved is in this case:

$$\int_{-\cos \frac{\theta}{2}}^{\cos \frac{\theta}{2}} dx x^2 \frac{1}{\sqrt{(1-x^2)(1-(1-k_+^2)x^2)}} \quad (\text{C.32})$$

The result leads again to a form that only contains complete elliptic integrals, according to the same procedure followed above. The final result for the second term is therefore:

$$- \int_{\frac{\pi}{2}-\frac{\theta}{2}}^{\frac{3}{2}\pi-\frac{\theta}{2}} d\psi \cos(\pi-\theta) \sin^2 \psi L(\psi) = -2 \cos(\pi-\theta) [\alpha_- P_5(k_-) - \alpha_+ P_5(k_+)] \quad (\text{C.33})$$

where:

$$P_5(k) = \frac{1}{1-k^2} \left(K(\sqrt{1-k^2}) - E(\sqrt{1-k^2}) \right) \quad (\text{C.34})$$

The third term is:

$$\int_{\frac{\pi}{2}-\frac{\theta}{2}}^{\frac{3}{2}\pi-\frac{\theta}{2}} d\psi \sin(\pi-\theta) 2 \sin \psi \cos \psi L(\psi)$$

The essential integral to be solved is in this case:

$$\int_{-\cos \frac{\theta}{2}}^{\cos \frac{\theta}{2}} dx \frac{x}{\sqrt{(1-(1-k^2)x^2)}} \quad (\text{C.35})$$

With a new substitution $t = x^2$ the integral becomes:

$$\frac{1}{2} \int_{\sin^2(\frac{\pi}{2}-\frac{\theta}{2})}^{\sin^2(\frac{3}{2}\pi-\frac{\theta}{2})} dt \frac{t}{\sqrt{1-(1-k^2)t}}$$

As pointed out in the previous section, the integration extrema are the same and therefore the integral is zero.

The final result is obtained by summing the first two terms just evaluated, as the third one vanish. With all the constants and the correct signs entering again the expression, it is:

$$H_z(\rho, \theta, z) = \frac{M}{\pi} \cos \theta \left[\alpha^- (P_4(k^-) - P_5(k^-)) - \alpha^+ (P_4(k^+) - P_5(k^+)) \right] \quad (\text{C.36})$$

C.5 Limits

For a very long cylinder ($L/R \rightarrow \infty$) the following limits hold:

$$\begin{aligned} k_{\pm} &\rightarrow 1 \\ \alpha_{\pm} &\rightarrow 0 \\ \beta_{\pm} &\rightarrow \pm 1 \end{aligned}$$

This simplify considerably the integrals in the previous section, enabling to retrieve the proper theoretical analytic expression for the magnetic of an infinite cylinder [10, 11].

C.5.1 The radial component

The integral in the first term, Equation (C.9), for the limits outlined above reduce to:

$$H_r = \frac{MR}{\pi(r+R)} \int_{\frac{\pi}{2}-\frac{\theta}{2}}^{\frac{3}{2}\pi-\frac{\theta}{2}} d\psi [\cos 2\psi \cos(\pi-\theta)] \frac{\cos^2 \psi + \gamma \sin^2 \psi}{\cos^2 \psi + \gamma^2 \sin^2 \psi}$$

where it has been also make use of the fact that the term in $\sin(\pi-\theta)$ vanishes as demonstrated in the previous analysis. Without invoking the formalism of the elliptic integrals, the previous integral is solvable in terms of elementary function. The final result is then:

$$H_r = -\frac{MR \cos \theta}{\pi(r+R)} \frac{\pi(|\gamma|^3 - 2|\gamma|^2 + |\gamma|)}{\gamma(\gamma-1)(\gamma+1)^2}$$

where the absolute value represents the two possible zones, respectively inside ($\gamma < 0$) and outside ($\gamma > 0$) the magnet. With the substitution of γ with its value in terms of r and R , the theoretical limit is correctly retrieved:

$$H_r^+(r, \theta, z) = \frac{M}{2} \frac{R^2}{r^2} \cos \theta \quad (\text{C.37a})$$

$$H_r^-(r, \theta, z) = -\frac{M}{2} \cos \theta \quad (\text{C.37b})$$

where the + and - subscripts indicates the component respectively outside and inside the cylinder. The minus sign in the second expression correctly comes from considering the \mathbf{H} field, that gives two fields of opposite sign outside and inside the magnet due to the magnetization present in the latter case. Converting the previous equation to an expression for the field \mathbf{B} using (3.15), the expressions (3.9a) and (3.9c) are retrieved.

C.5.2 The angular component

The integral in the first term, Equation (C.19), for the limits outlined above reduce to:

$$H_{\theta} = \frac{MR^2}{\pi(r+R)^2} \int_{\frac{\pi}{2}-\frac{\theta}{2}}^{\frac{3}{2}\pi-\frac{\theta}{2}} d\psi [2 \sin 2\psi \sin(\pi-\theta)] \frac{\cos \psi \sin \psi}{\cos^2 \psi + \gamma^2 \sin^2 \psi}$$

where it has been also make use of the fact that the term in $\cos(\pi-\theta)$ vanishes as demonstrated in the previous analysis. Without invoking the formalism of the elliptic integrals, the previous integral is solvable in terms of elementary function. The final result is then:

$$H_{\theta} = \frac{2MR^2 \sin \theta}{\pi(r+R)^2} \frac{\pi(|\gamma|^2 - 2|\gamma| + 1)}{(\gamma^2 - 1)^2}$$

where the absolute value represents again the two possible zones, respectively inside ($\gamma < 0$) and outside ($\gamma > 0$) the magnet. With the substitution of γ with its value in terms of r and R , the theoretical limit is correctly retrieved:

$$H_{\theta}^{+}(r, \theta, z) = -\frac{M}{2} \frac{R^2}{r^2} \sin \theta \quad (\text{C.38a})$$

$$H_{\theta}^{-}(r, \theta, z) = \frac{M}{2} \sin \theta \quad (\text{C.38b})$$

where the + and – subscripts indicates the component respectively outside and inside the cylinder. The minus sign in the second expression correctly comes from considering the \mathbf{H} field, that gives two fields of opposite sign outside and inside the magnet due to the magnetization present in the latter case. Converting the previous equation to an expression for the field \mathbf{B} using (3.15), the expressions (3.9b) and (3.9d) are retrieved.

C.5.3 The z component

As pointed out in the beginning of this section, $\alpha_{\pm} \rightarrow 0$ when $L \rightarrow \pm\infty$. This trivially leads Equation (C.36) to be null. This result is expected, as the problem addressed by theory allow solutions only in two dimensions, being the cylinder infinitely long in the third dimension. Therefore, the limiting behavior validates the equation found for the z component.

C.5.4 The field on the axis of the cylinder

On the axis of the cylinder, $r = 0$. Therefore, $\gamma \rightarrow -1$ while $k_{\pm} \rightarrow 1$. The result is assumed not to depend on the θ coordinate due to simmetry: therefore, we can set $\theta = 0$ and evaluate the behavior of the radial component only. The integral in (C.9) reduces to:

$$H_{axis} = -\frac{MR}{2\pi R} (\beta_{+} - \beta_{-}) \int_{\frac{\pi}{2}}^{\frac{3}{2}\pi} d\psi \cos^2 2\psi$$

Solving the integral and expressing β_{\pm} in terms of z_{\pm} , the final expression reads:

$$H_{axis}(z) = -\frac{M}{4} \left(\frac{z_{+}}{\sqrt{R^2 + z_{+}^2}} - \frac{z_{-}}{\sqrt{R^2 + z_{-}^2}} \right) \quad (\text{C.39})$$

Converting the \mathbf{H} field to the \mathbf{B} field using (3.15), (3.11) is obtained.

Appendix D

Visualization of the magnetic field generated by magnetized rods

In this Appendix the graphical representations of the magnetic field components as generated by analytical equations and by MagNet are presented. They are comprehensive of all the different cases discussed in Chapter 4.

D.1 Single permanently magnetized rod

D.1.1 Longitudinal magnetization

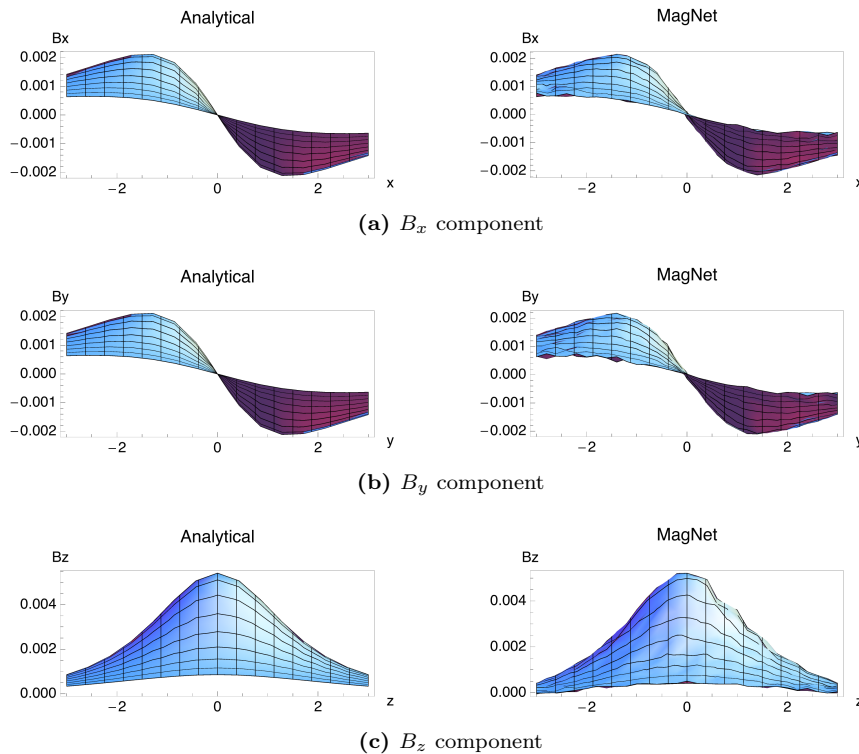


Figure D.1: Graphical representation of the components of the magnetic field \mathbf{B} for a longitudinally magnetized rod. The field is sampled at height $z = -8$

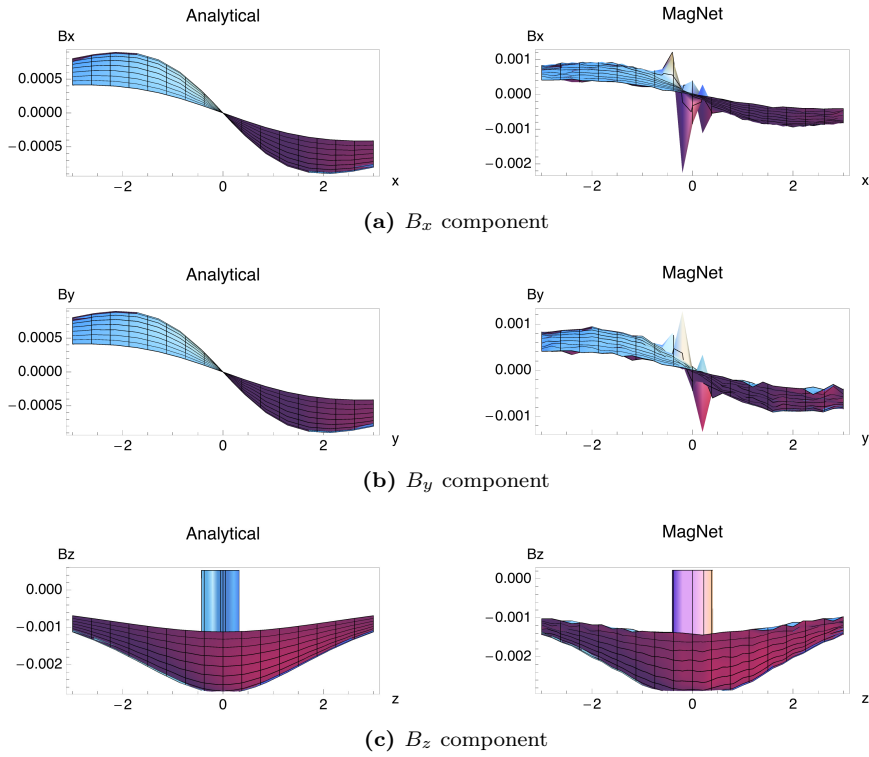


Figure D.2: Graphical representation of the components of the magnetic field \mathbf{B} for a longitudinally magnetized rod. The field is sampled at height $z = -3$

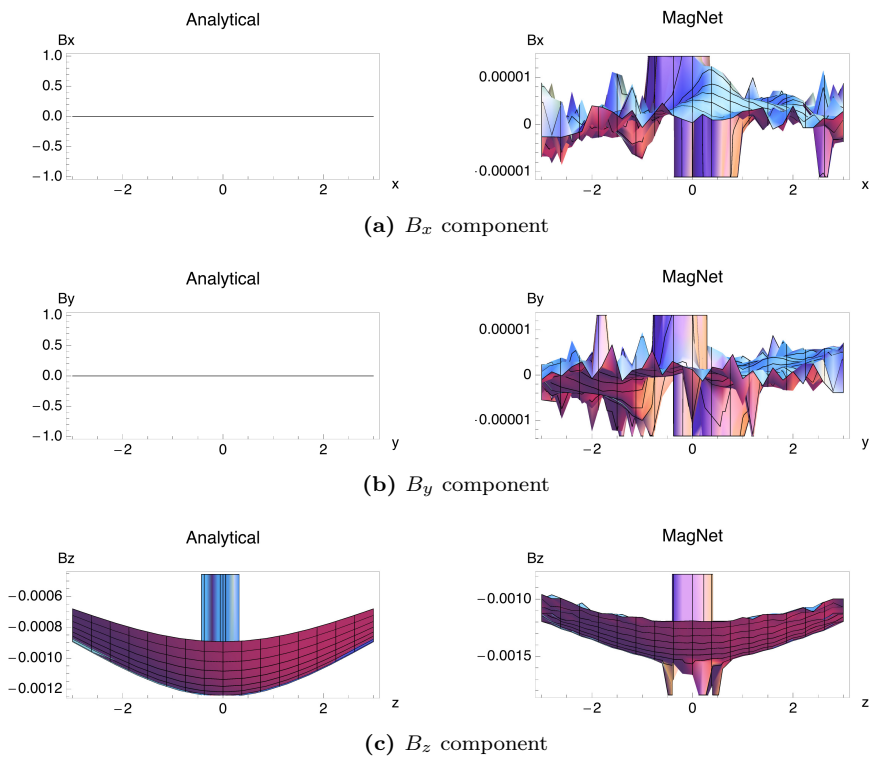


Figure D.3: Graphical representation of the components of the magnetic field \mathbf{B} for a longitudinally magnetized rod. The field is sampled at height $z = 0$

D.1.2 Transverse magnetization

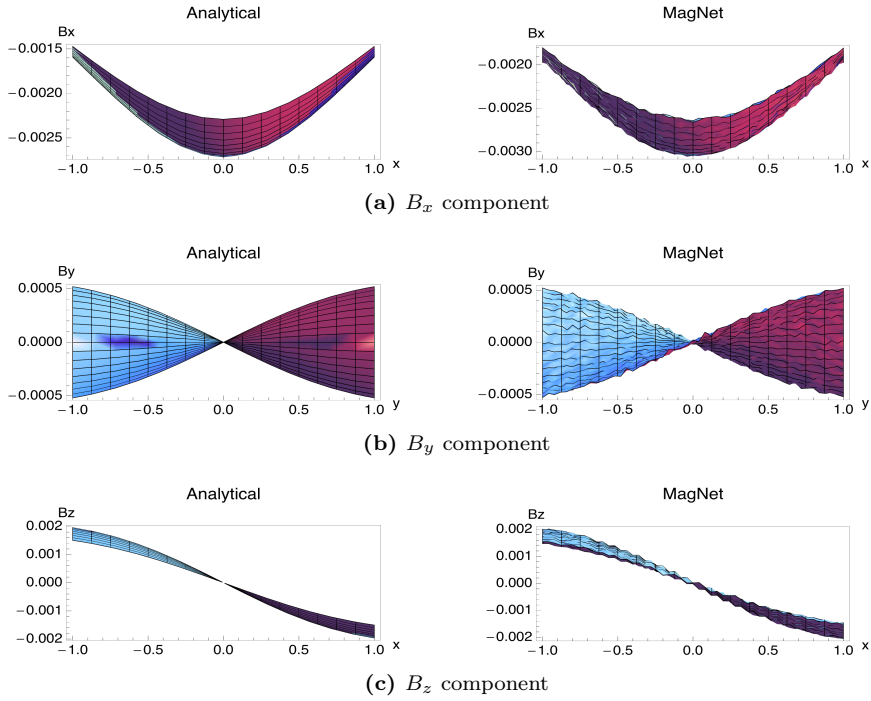


Figure D.4: Graphical representation of the components of the magnetic field \mathbf{B} for a transversally magnetized rod. The field is sampled at height $z = -8$

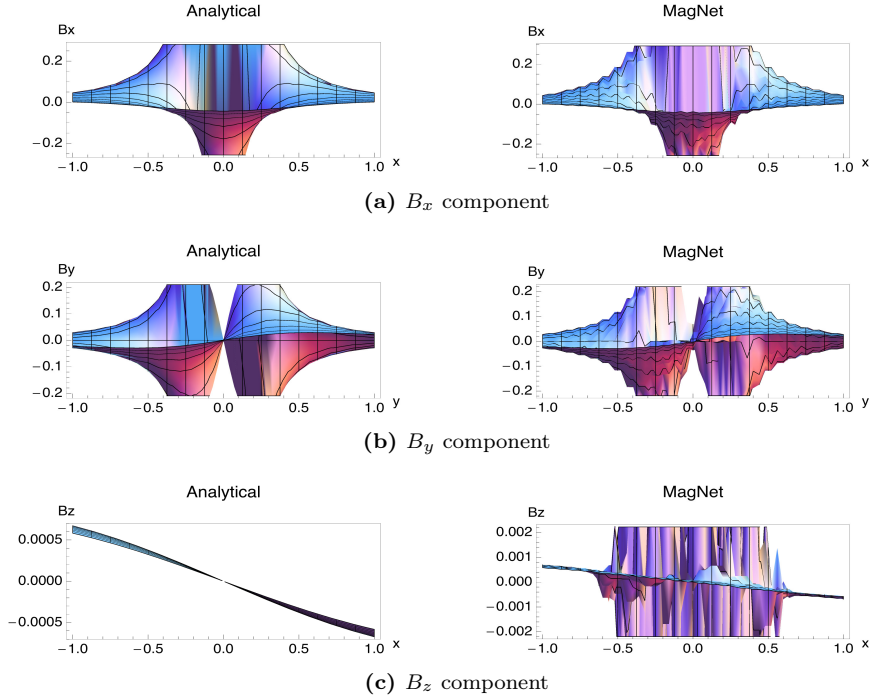


Figure D.5: Graphical representation of the components of the magnetic field \mathbf{B} for a transversally magnetized rod. The field is sampled at height $z = -3$

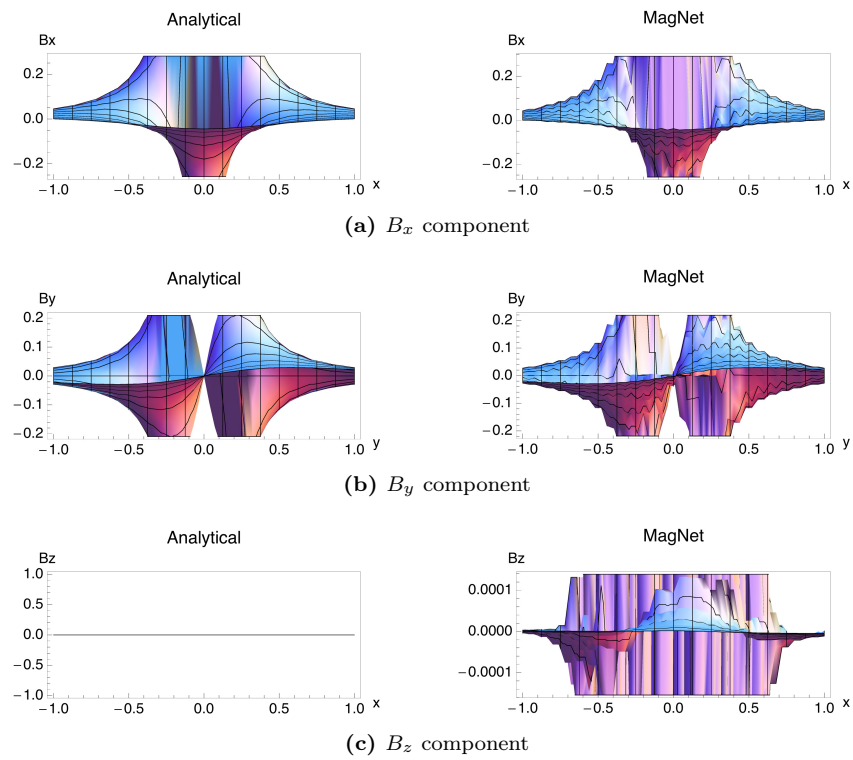


Figure D.6: Graphical representation of the components of the magnetic field \mathbf{B} for a transversally magnetized rod. The field is sampled at height $z = 0$

D.1.3 Mixed magnetization

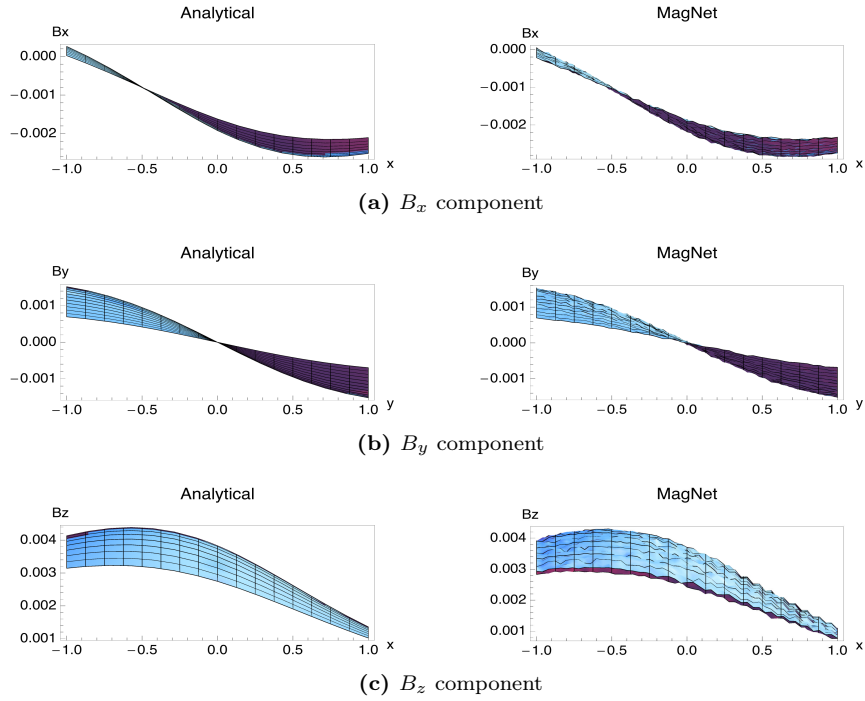


Figure D.7: Graphical representation of the components of the magnetic field \mathbf{B} for a mixed magnetized rod. The field is sampled at height $z = -8$

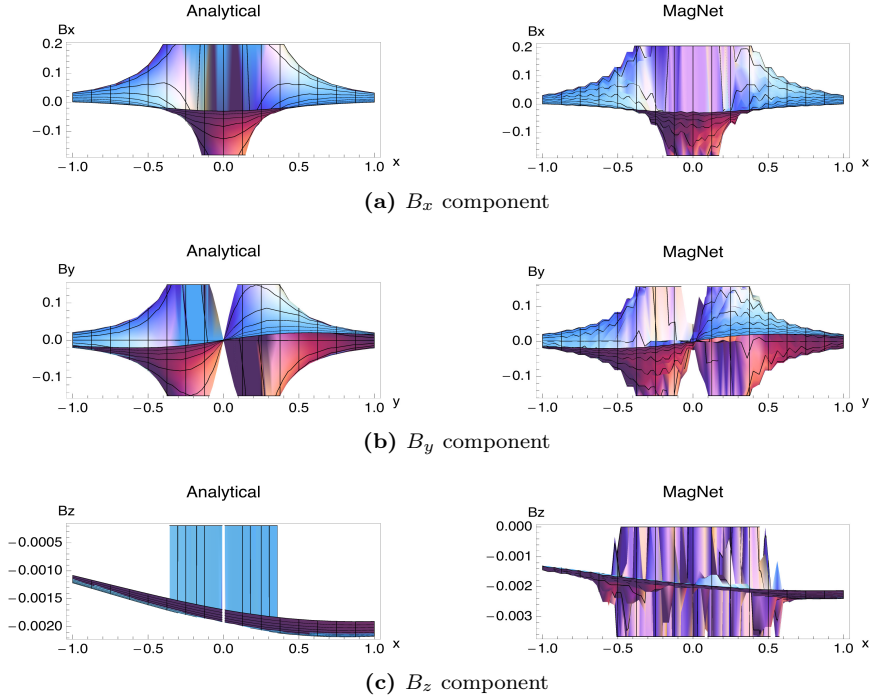


Figure D.8: Graphical representation of the components of the magnetic field \mathbf{B} for a mixed magnetized rod. The field is sampled at height $z = -3$

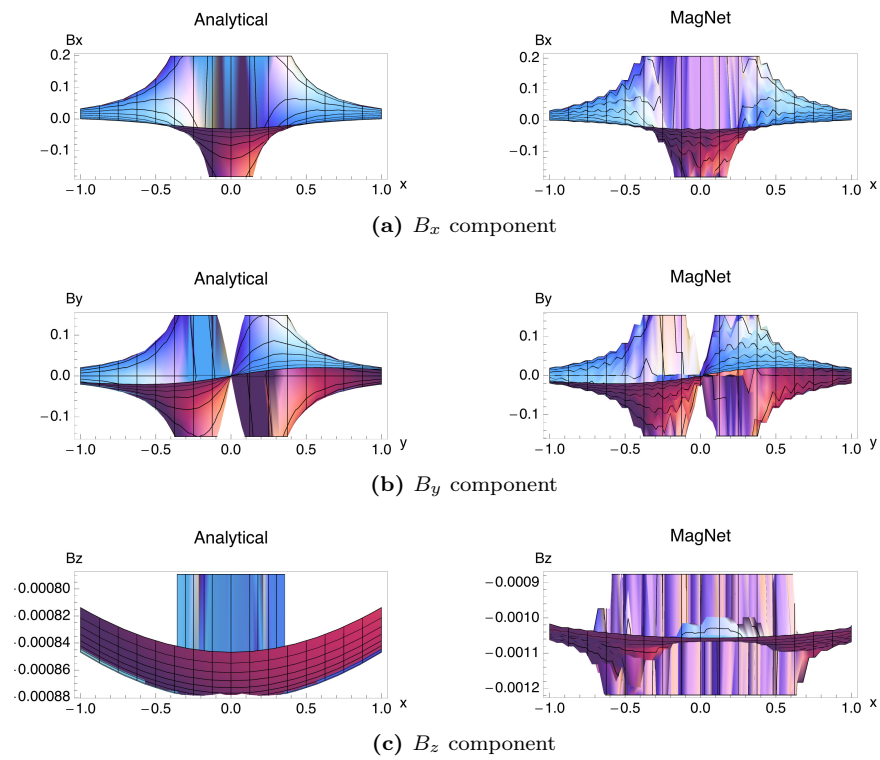


Figure D.9: Graphical representation of the components of the magnetic field \mathbf{B} for a mixed magnetized rod. The field is sampled at height $z = 0$

D.2 Multiple permanently magnetized rods

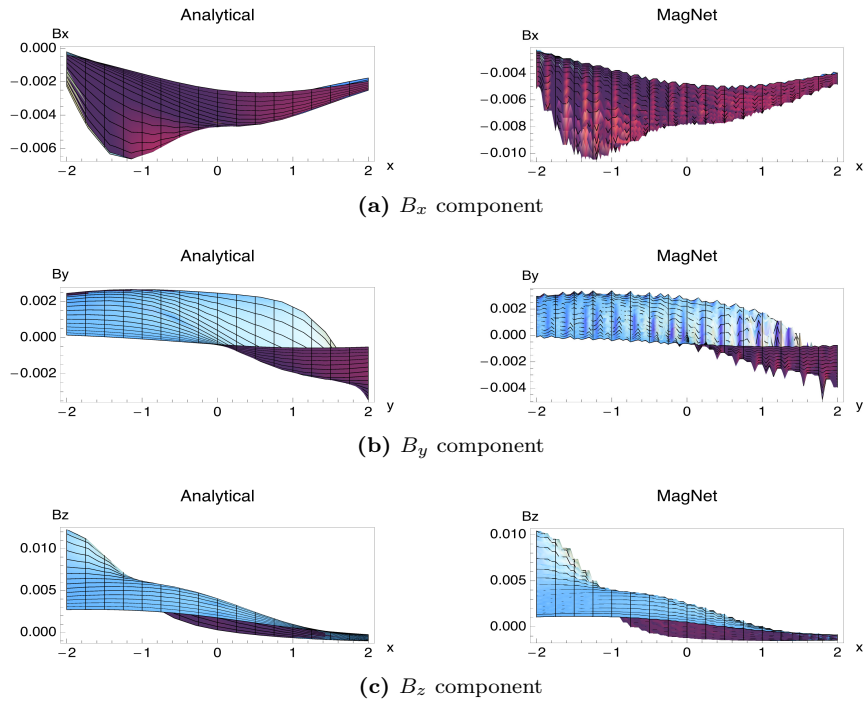


Figure D.10: Graphical representation of the components of the magnetic field \mathbf{B} for a system of three permanently magnetized rod. The field is sampled at height $z = -8$

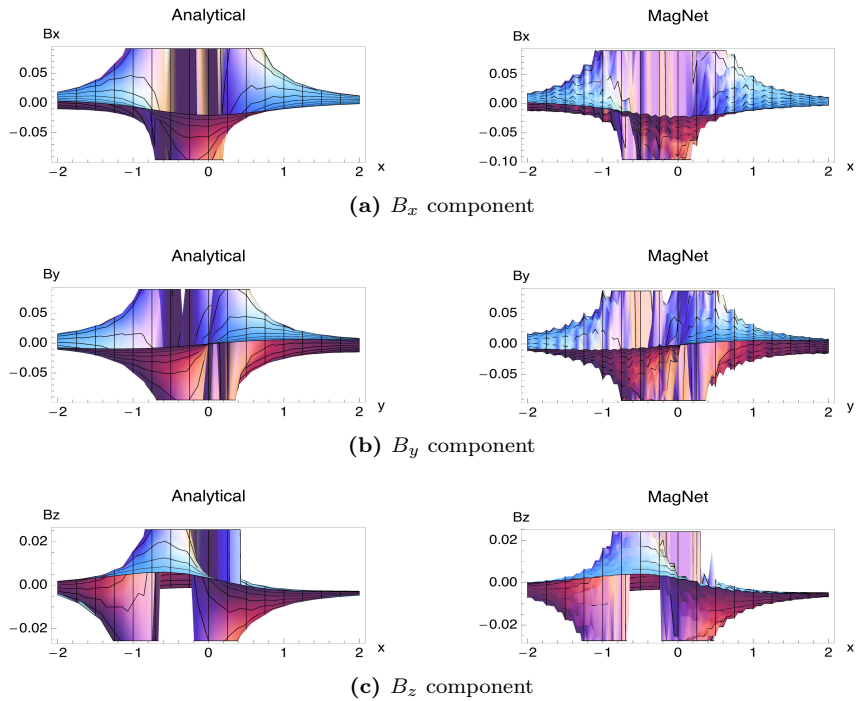


Figure D.11: Graphical representation of the components of the magnetic field \mathbf{B} for a system of three permanently magnetized rod. The field is sampled at height $z = -2$

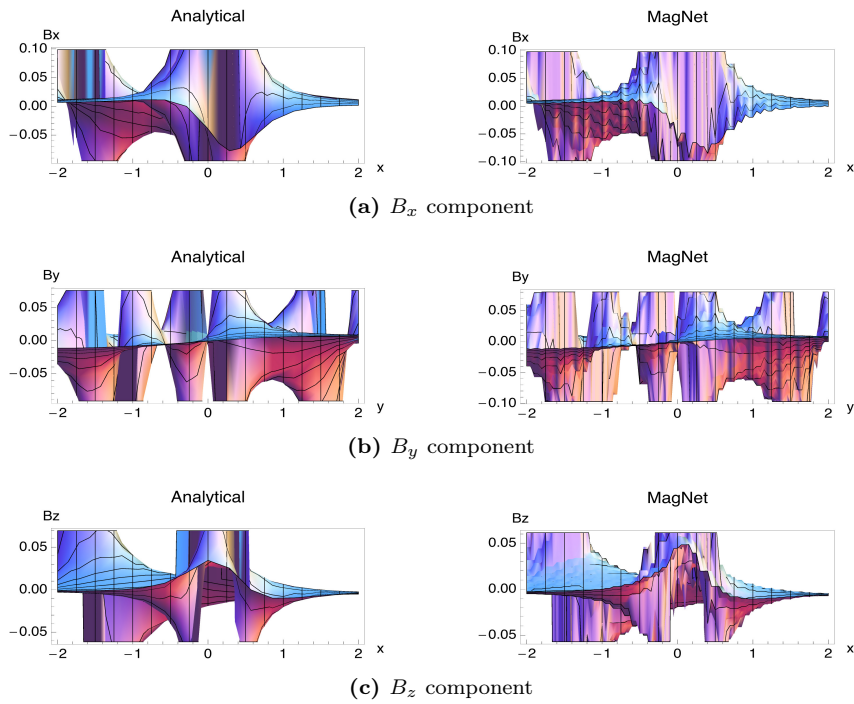


Figure D.12: Graphical representation of the components of the magnetic field \mathbf{B} for a system of three permanently magnetized rod. The field is sampled at height $z = 0$

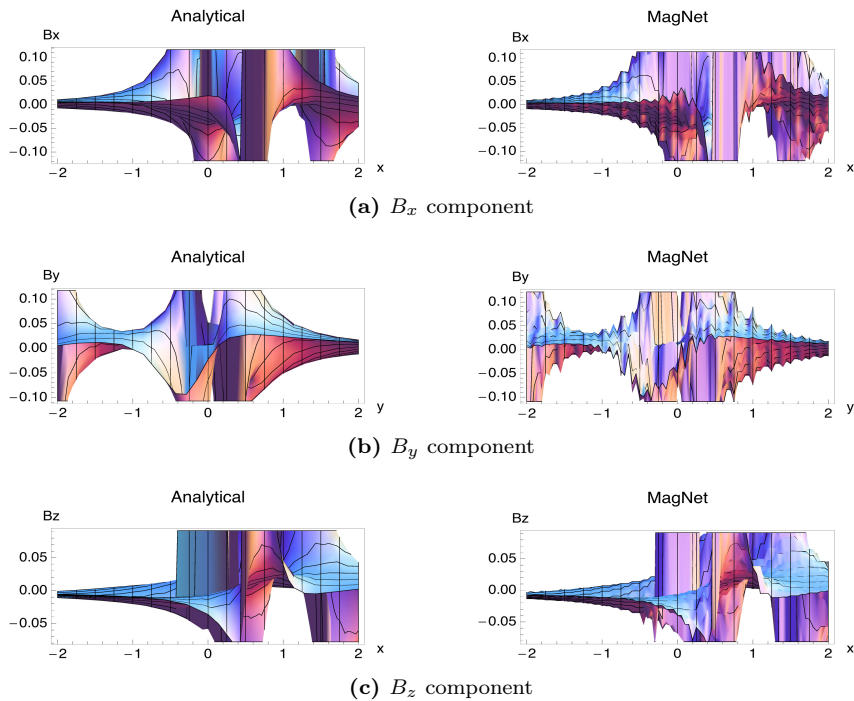


Figure D.13: Graphical representation of the components of the magnetic field \mathbf{B} for a system of three permanently magnetized rod. The field is sampled at height $z = 2$

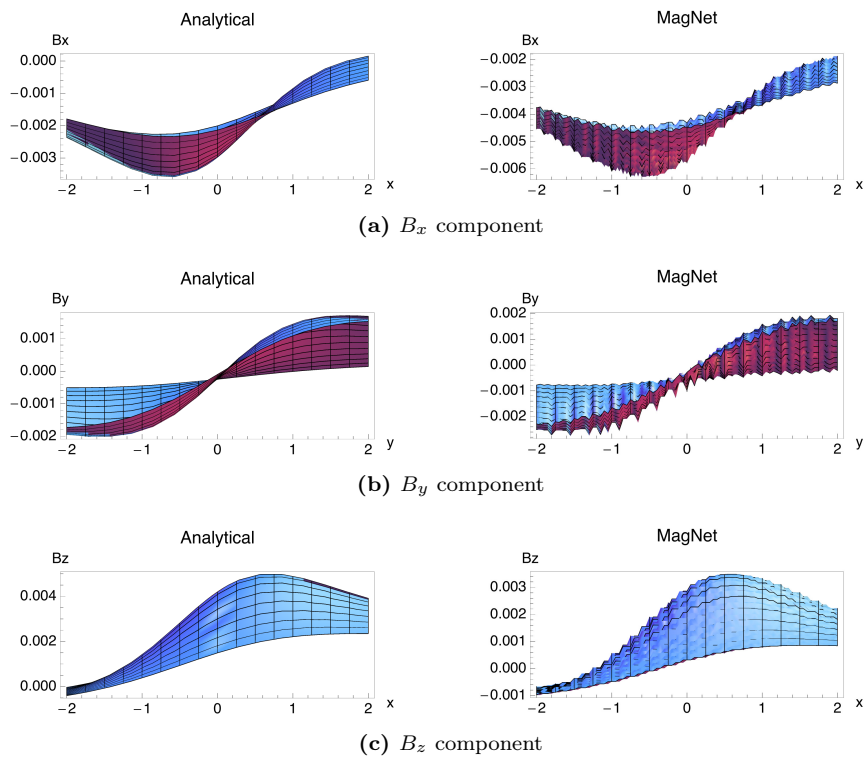


Figure D.14: Graphical representation of the components of the magnetic field \mathbf{B} for a system of three permanently magnetized rod. The field is sampled at height $z = 8$

Bibliography

- [1] K. Mandel and F. Hutter. “The magnetic nanoparticle separation problem”. In: *Nano Today* 7.6 (Dec. 2012), pp. 485–487. ISSN: 17480132. DOI: [10.1016/j.nantod.2012.05.001](https://doi.org/10.1016/j.nantod.2012.05.001) (cit. on pp. 1, 6).
- [2] M. Cooke et al. *Encyclopedia of Separation Science*. Academic Press, 2000. ISBN: 978-0-12-226770-3 (cit. on p. 3).
- [3] G. Mariani. “Theoretical and Experimental Study of the Magnetic Separation of Pollutants from Wastewater”. PhD thesis. University of Bologna, 2010 (cit. on pp. 3, 5).
- [4] J. Segura. “Statistical Mechanics of Superparamagnetic Colloidal Dispersions Under Magnetic Fields”. PhD thesis. Universitat Autònoma de Barcelona, 2013 (cit. on pp. 3–5, 11, 21, 22).
- [5] J. Livingston. *Driving Force: The Natural Magic of Magnets*. Harvard University Press, 1997 (cit. on p. 3).
- [6] C. Yavuz et al. “Magnetic separations: from steel plants to biotechnology”. In: *Chemical Engineering Science* 64.10 (May 2009), pp. 2510–2521. ISSN: 00092509. DOI: [10.1016/j.ces.2008.11.018](https://doi.org/10.1016/j.ces.2008.11.018) (cit. on pp. 3–6).
- [7] M. Berger et al. “Design of a microfabricated magnetic cell separator”. In: *Electrophoresis* 22 (2001), pp. 3883–3892. ISSN: 01730835. DOI: [10.1002/1522-2683\(200110\)22:18<3883::AID-ELPS3883>3.0.CO;2-4](https://doi.org/10.1002/1522-2683(200110)22:18<3883::AID-ELPS3883>3.0.CO;2-4) (cit. on p. 4).
- [8] J. Svoboda and T. Fujita. “Recent developments in magnetic methods of material separation”. In: *Minerals Engineering* 16.9 (Sept. 2003), pp. 785–792. ISSN: 08926875. DOI: [10.1016/S0892-6875\(03\)00212-7](https://doi.org/10.1016/S0892-6875(03)00212-7) (cit. on p. 4).
- [9] H. Kolm et al. “High Intensity Magnetic Filtration”. In: 1972, pp. 949–949. DOI: [10.1063/1.2953948](https://doi.org/10.1063/1.2953948) (cit. on p. 4).
- [10] J. Stratton. *Electromagnetic theory*. New York and London: McGraw-Hill Book Company, 1941 (cit. on pp. 4, 38, 41, 43, 125, 134).
- [11] J. A. Oberteuffer. “Magnetic Separation: A review of Principles, Devices, and Applications”. In: *Ieee Transactions on Magnetics* Mag-10 (1974) (cit. on pp. 5, 38, 41, 43, 134).
- [12] D. Melville, F. Paul, and S. Roath. “High gradient magnetic separation of red cells from whole blood”. In: *IEEE Transactions on Magnetics* 11.6 (Nov. 1975), pp. 1701–1704. ISSN: 0018-9464. DOI: [10.1109/TMAG.1975.1058970](https://doi.org/10.1109/TMAG.1975.1058970) (cit. on p. 5).
- [13] V. A. Kirsh. “Inertial Deposition of Aerosol Particles on Fibrous Filters”. In: *Colloid Journal* 66.5 (Sept. 2004), pp. 547–552. ISSN: 1061-933X. DOI: [10.1023/B:COLL.0000043835.00525.83](https://doi.org/10.1023/B:COLL.0000043835.00525.83) (cit. on p. 6).
- [14] M. Arruebo et al. “Magnetic nanoparticles for drug delivery”. In: *Nano Today* 2.3 (June 2007), pp. 22–32. ISSN: 17480132. DOI: [10.1016/S1748-0132\(07\)70084-1](https://doi.org/10.1016/S1748-0132(07)70084-1) (cit. on p. 6).
- [15] S. C. McBain, H. H. P. Yiu, and J. Dobson. *Magnetic nanoparticles for gene and drug delivery*. 2008. DOI: [10.2147/IJN.S1608](https://doi.org/10.2147/IJN.S1608) (cit. on p. 6).

- [16] Q. A. Pankhurst et al. “Applications of magnetic nanoparticles in biomedicine”. In: *Journal of Physics D: Applied Physics* 36.13 (July 2003), R167–R181. ISSN: 0022-3727. DOI: [10.1088/0022-3727/36/13/201](https://doi.org/10.1088/0022-3727/36/13/201) (cit. on p. 6).
- [17] Q. A. Pankhurst et al. “Progress in applications of magnetic nanoparticles in biomedicine”. In: *Journal of Physics D: Applied Physics* 42.22 (Nov. 2009), p. 224001. ISSN: 0022-3727. DOI: [10.1088/0022-3727/42/22/224001](https://doi.org/10.1088/0022-3727/42/22/224001) (cit. on p. 6).
- [18] C. Sun, J. S. H. Lee, and M. Zhang. *Magnetic nanoparticles in MR imaging and drug delivery*. 2008. DOI: [10.1016/j.addr.2008.03.018](https://doi.org/10.1016/j.addr.2008.03.018) (cit. on p. 6).
- [19] A. K. Gupta and M. Gupta. “Synthesis and surface engineering of iron oxide nanoparticles for biomedical applications.” In: *Biomaterials* 26.18 (June 2005), pp. 3995–4021. ISSN: 0142-9612. DOI: [10.1016/j.biomaterials.2004.10.012](https://doi.org/10.1016/j.biomaterials.2004.10.012) (cit. on p. 6).
- [20] R. V. Ramanujan. “Magnetic particles for biomedical applications”. In: *Biomedical Materials*. 2009, pp. 477–491. ISBN: 9780387848716. DOI: [10.1007/978-0-387-84872-3_17](https://doi.org/10.1007/978-0-387-84872-3_17) (cit. on p. 7).
- [21] E. D. Goluch et al. “A bio-barcode assay for on-chip attomolar-sensitivity protein detection.” In: *Lab on a chip* 6 (2006), pp. 1293–1299. ISSN: 1473-0197. DOI: [10.1039/b606294f](https://doi.org/10.1039/b606294f) (cit. on pp. 6, 8).
- [22] H. E. Knoepfel. *Magnetic Fields. A comprehensive theoretical treatise for practical use*. John Wiley & Sons, 2008. ISBN: 0471322059 (cit. on pp. 9, 41).
- [23] W. D. Callister and D. G. Rethwisch. *Material Science and Engineering: an Introduction*. 8th. John Wiley & Sons, 2010 (cit. on p. 9).
- [24] A. Aharoni and A. Arrott. *Introduction to the Theory of Ferromagnetism*. 2nd. Vol. 50. Oxford University Press, 1997 (cit. on pp. 9, 10, 38, 39, 44, 48, 105).
- [25] D. J. Griffiths. *Introduction to Electrodynamics*. Prentice Hall, 1999 (cit. on pp. 10, 18, 38, 39, 46).
- [26] A. H. Lu, E. L. Salabas, and F. Schüth. “Magnetic nanoparticles: synthesis, protection, functionalization, and application”. In: . . . *Chemie International Edition* (2007), pp. 1222–1244. DOI: [10.1002/anie.200602866](https://doi.org/10.1002/anie.200602866) (cit. on pp. 10, 11).
- [27] C. P. Bean and J. D. Livingston. “Superparamagnetism”. In: *Journal of Applied Physics* 30.4 (1959), S120. ISSN: 00218979. DOI: [10.1063/1.2185850](https://doi.org/10.1063/1.2185850) (cit. on p. 10).
- [28] J. Baumgartner et al. “Formation of magnetite nanoparticles at low temperature: from superparamagnetic to stable single domain particles.” In: *PloS one* 8.3 (Jan. 2013), e57070. ISSN: 1932-6203. DOI: [10.1371/journal.pone.0057070](https://doi.org/10.1371/journal.pone.0057070) (cit. on p. 11).
- [29] K. M. Krishnan. “Biomedical nanomagnetism: A spin through possibilities in imaging, diagnostics, and therapy”. In: *IEEE Transactions on Magnetics* 46 (2010), pp. 2523–2558. ISSN: 00189464. DOI: [10.1109/TMAG.2010.2046907](https://doi.org/10.1109/TMAG.2010.2046907) (cit. on p. 11).
- [30] Y.-W. Du et al. “Magnetic properties of ultrafine nickel particles”. In: *Journal of Applied Physics* 70.10 (1991), p. 5903. ISSN: 00218979. DOI: [10.1063/1.350101](https://doi.org/10.1063/1.350101) (cit. on p. 11).
- [31] M. Reza Barati, C. Selomulya, and K. Suzuki. “Particle size dependence of heating power in MgFe₂O₄ nanoparticles for hyperthermia therapy application”. In: *Journal of Applied Physics* 115.17 (May 2014), 17B522. ISSN: 0021-8979. DOI: [10.1063/1.4867751](https://doi.org/10.1063/1.4867751) (cit. on p. 11).
- [32] S. Oliver et al. “Structure and magnetic properties of magnesium ferrite fine powders”. In: *Scripta Metallurgica et Materialia* 33.10-11 (Dec. 1995), pp. 1695–1701. ISSN: 0956716X. DOI: [10.1016/0956-716X\(95\)00412-0](https://doi.org/10.1016/0956-716X(95)00412-0) (cit. on p. 11).
- [33] M. Knobel et al. “Superparamagnetism and other magnetic features in granular materials: a review on ideal and real systems.” In: *Journal of nanoscience and nanotechnology* 8 (2008), pp. 2836–2857. ISSN: 1533-4880. DOI: [10.1166/jnn.2008.017](https://doi.org/10.1166/jnn.2008.017) (cit. on pp. 11, 12).

- [34] V. Schaller, U Kräling, and C. Rusu. “Motion of nanometer sized magnetic particles in a magnetic field gradient”. In: *Journal of Applied Physics* 104.9 (2008), p. 093918. ISSN: 00218979. DOI: [10.1063/1.3009686](https://doi.org/10.1063/1.3009686) (cit. on pp. [12](#), [24](#), [26](#), [36](#), [81](#), [98](#), [104](#), [105](#)).
- [35] A. Merino-Martos et al. “Setting up High Gradient Magnetic Separation for combating eutrophication of inland waters.” In: *Journal of hazardous materials* 186.2-3 (Feb. 2011), pp. 2068–74. ISSN: 1873-3336. DOI: [10.1016/j.jhazmat.2010.12.118](https://doi.org/10.1016/j.jhazmat.2010.12.118) (cit. on p. [14](#)).
- [36] K. Butter. “Iron (oxide) ferrofluids: synthesis, structure and catalysis”. PhD thesis. Utrecht University, 2003 (cit. on pp. [14](#), [32](#)).
- [37] D. X. Chen, J. A. Brug, and R. B. Goldfarb. “Demagnetizing factors for cylinders”. In: *Ieee Transactions on Magnetics* 27 (1991) (cit. on pp. [16](#), [45](#)).
- [38] D. X. Chen, E. Pardo, and A. Sanchez. “Fluxmetric and magnetometric demagnetizing factors for cylinders”. In: *Journal of Magnetism and Magnetic Materials* 306.1 (Nov. 2006), pp. 135–146. ISSN: 03048853. DOI: [10.1016/j.jmmm.2006.02.235](https://doi.org/10.1016/j.jmmm.2006.02.235) (cit. on pp. [14](#), [68](#)).
- [39] B. C. Dodrill. *Measurements with a VSM*. Tech. rep. 614 (cit. on pp. [16](#), [17](#)).
- [40] M. Urbaniak. *Magnetic hysteresis and basic magnetometry*. 2012 (cit. on p. [17](#)).
- [41] C. Cao et al. “Magnetic characterization of noninteracting, randomly oriented, nanometer-scale ferrimagnetic particles”. In: *Journal of Geophysical Research: Solid Earth* 115 (2010). ISSN: 21699356. DOI: [10.1029/2009JB006855](https://doi.org/10.1029/2009JB006855) (cit. on p. [18](#)).
- [42] J. Jin. *The finite element method in electromagnetics*. John Wiley & Sons, 2014, p. 876 (cit. on pp. [18](#), [19](#), [37](#), [62](#), [70](#)).
- [43] M. K. Haldar. “Introducing the Finite Element Method in electromagnetics to undergraduates using MATLAB”. In: *International Journal of Electrical Engineering Education* 43.3 (July 2006), pp. 232–244. ISSN: 0020-7209. DOI: [10.7227/IJEEE.43.3.4](https://doi.org/10.7227/IJEEE.43.3.4) (cit. on p. [18](#)).
- [44] A. Bermúdez, R. Rodríguez, and P. Salgado. “A finite element method for the magnetostatic problem in terms of scalar potentials”. In: *SIAM Journal on Numerical Analysis* (2008), pp. 1–25 (cit. on p. [18](#)).
- [45] P. P. Silvester and R. L. Ferrari. *Finite Elements for Electrical Engineers*. 3rd. Cambridge University Press, 1996 (cit. on pp. [18](#), [19](#)).
- [46] S. R. H. Hoole. *Computer-aided Design of Electromagnetic Devices*. Elsevier B.V., 1989 (cit. on p. [19](#)).
- [47] <http://www.infolytica.com/en%5Cproducts/magnet/> (cit. on pp. [19](#), [48](#)).
- [48] M. P. Allen and D. J. Tildesley. *Computer simulation of liquids*. 2nd. Clarendon Press - Oxford, 1989 (cit. on pp. [21](#), [23](#), [25](#), [35](#)).
- [49] D. Frenkel and B. Smit. *Understanding Molecular Simulation*. Academic Press, 1996 (cit. on pp. [21](#), [23](#)).
- [50] A. R. Leach. *Molecular Modelling. Principles and Applications*. Prentice Hall, 2001 (cit. on p. [21](#)).
- [51] J. Padding and A. Louis. “Hydrodynamic interactions and Brownian forces in colloidal suspensions: Coarse-graining over time and length scales”. In: *Physical Review E* 74.3 (Sept. 2006), p. 031402. ISSN: 1539-3755. DOI: [10.1103/PhysRevE.74.031402](https://doi.org/10.1103/PhysRevE.74.031402) (cit. on pp. [21](#), [23](#)).
- [52] J. K. G. Dhont. *An introduction to dynamics of colloids*. Ed. by R. Miller and D. Mobius. Elsevier B.V., 1996 (cit. on pp. [22](#), [26–29](#), [91](#)).
- [53] R. Kubo. “The fluctuation-dissipation theorem”. In: *Reports on Progress in Physics* 29.1 (Jan. 1966), pp. 255–284. ISSN: 00344885. DOI: [10.1088/0034-4885/29/1/306](https://doi.org/10.1088/0034-4885/29/1/306) (cit. on p. [22](#)).

- [54] H. Berendsen, D. van der Spoel, and R. van Drunen. *GROMACS: A message-passing parallel molecular dynamics implementation*. 1995. DOI: [10.1016/0010-4655\(95\)00042-E](https://doi.org/10.1016/0010-4655(95)00042-E) (cit. on p. 22).
- [55] S. Plimpton. “Fast Parallel Algorithms for Short-Range Molecular Dynamics”. In: *Journal of Computational Physics* 117 (1995), pp. 1–19. ISSN: 00219991. DOI: [10.1006/jcph.1995.1039](https://doi.org/10.1006/jcph.1995.1039) (cit. on p. 22).
- [56] A. H. Elcock, D. Sept, and J. A. McCammon. “Computer simulation of protein-protein interactions”. In: *The Journal of Physical Chemistry B* 105 (2001), pp. 1504–1518. ISSN: 15206106. DOI: [10.1021/jp003602d](https://doi.org/10.1021/jp003602d) (cit. on p. 23).
- [57] R. G. Larson. *The Structure and Rheology of Complex Fluids*. 1999, p. 688. ISBN: 019512197X. DOI: [10.1029/2006E0230009](https://doi.org/10.1029/2006E0230009) (cit. on p. 24).
- [58] G. Mie. “Zur kinetischen Theorie der einatomigen Körper”. In: *Annalen der Physik* 316.8 (1903), pp. 657–697. ISSN: 00033804. DOI: [10.1002/andp.19033160802](https://doi.org/10.1002/andp.19033160802) (cit. on p. 25).
- [59] J. Jover, A. J. Haslam, and A. Galindo. “Pseudo hard-sphere potential for use in continuous molecular-dynamics simulation of spherical and chain molecules”. In: *The Journal of ...* 137.14 (Oct. 2012), p. 144505. ISSN: 1089-7690. DOI: [10.1063/1.4754275](https://doi.org/10.1063/1.4754275) (cit. on p. 25).
- [60] A. Satoh. “Comparison of Approximations between Additivity of Velocities and Additivity of Forces for Stokesian Dynamics Methods”. In: *Journal of Colloid and Interface Science* 243.2 (Nov. 2001), pp. 342–350. ISSN: 00219797. DOI: [10.1006/jcis.2001.7852](https://doi.org/10.1006/jcis.2001.7852) (cit. on p. 27).
- [61] G. K. Batchelor and J. T. Green. *The hydrodynamic interaction of two small freely-moving spheres in a linear flow field*. 1972. DOI: [10.1017/S0022112072002927](https://doi.org/10.1017/S0022112072002927) (cit. on pp. 27, 29).
- [62] D. J. Jeffrey and Y. Onishi. “Calculation of the resistance and mobility functions for two unequal rigid spheres in low-Reynolds-number flow”. In: *Journal of Fluid Mechanics* 139.-1 (Apr. 2006), p. 261. ISSN: 0022-1120. DOI: [10.1017/S0022112084000355](https://doi.org/10.1017/S0022112084000355) (cit. on p. 27).
- [63] R. B. Jones and R. Schmitz. *Mobility matrix for arbitrary spherical particles in solution*. 1988. DOI: [10.1016/0378-4371\(88\)90111-2](https://doi.org/10.1016/0378-4371(88)90111-2) (cit. on p. 27).
- [64] S. Kim and S. J. Karrila. *Microhydrodynamics: Principles and selected applications*. Vol. 10. Butterworth-Heinemann, 1991 (cit. on p. 28).
- [65] L. Durlofsky, J. F. Brady, and G. Bossis. “Dynamic simulation of hydrodynamically interacting particles”. In: *Journal of fluid mechanics* 180 (1987) (cit. on p. 28).
- [66] J. M. Deutch. “Molecular Theory of Brownian Motion for Several Particles”. In: *The Journal of Chemical Physics* 54.8 (1971), p. 3547. ISSN: 00219606. DOI: [10.1063/1.1675379](https://doi.org/10.1063/1.1675379) (cit. on p. 28).
- [67] A. Satoh. *Introduction to Molecular-Microsimulation of Colloidal Dispersions*. Elsevier B.V., 2003. ISBN: 0444514244 (cit. on p. 29).
- [68] M. Reichert. “Hydrodynamic Interactions in Colloidal and Biological Systems”. PhD thesis. Konstanz University, 2006 (cit. on p. 29).
- [69] D. L. Ermak and J. A. McCammon. “Brownian dynamics with hydrodynamic interactions”. In: *The Journal of Chemical Physics* 69.4 (1978), p. 1352. ISSN: 00219606. DOI: [10.1063/1.436761](https://doi.org/10.1063/1.436761) (cit. on p. 31).
- [70] W. H. Press et al. *Numerical Recipes in C*. 2nd. Cambridge University Press, 1992. ISBN: 0521431085 (cit. on pp. 31, 40, 43).
- [71] B. C. Carlson. “Numerical computation of real or complex elliptic integrals”. In: *Numerical Algorithms* 10.1 (Mar. 1995), pp. 13–26. ISSN: 1017-1398. DOI: [10.1007/BF02198293](https://doi.org/10.1007/BF02198293). arXiv: [9409227](https://arxiv.org/abs/9409227) [math] (cit. on p. 31).

- [72] G. K. Batchelor. *An Introduction to Fluid Dynamics*. 2000. ISBN: 0521663962. DOI: [10.1063/1.3060769](https://doi.org/10.1063/1.3060769) (cit. on pp. [32](#), [115](#), [116](#)).
- [73] S. Jiang, Z. Liang, and J. Huang. “A fast algorithm for Brownian dynamics simulation with hydrodynamic interactions”. In: *Mathematics of Computation* 82.283 (Feb. 2013), pp. 1631–1645. ISSN: 0025-5718. DOI: [10.1090/S0025-5718-2013-02672-5](https://doi.org/10.1090/S0025-5718-2013-02672-5) (cit. on p. [34](#)).
- [74] T. Fukushima. “Fast computation of Jacobian elliptic functions and incomplete elliptic integrals for constant values of elliptic parameter and elliptic characteristic”. In: *Celestial Mechanics and Dynamical Astronomy* 105 (2009), pp. 245–260. ISSN: 09232958. DOI: [10.1007/s10569-008-9177-y](https://doi.org/10.1007/s10569-008-9177-y) (cit. on p. [34](#)).
- [75] T. Fukushima. “Fast computation of a general complete elliptic integral of third kind by half and double argument transformations”. In: *Journal of Computational and Applied Mathematics* 253 (2013), pp. 142–157. ISSN: 03770427. DOI: [10.1016/j.cam.2013.04.015](https://doi.org/10.1016/j.cam.2013.04.015) (cit. on p. [34](#)).
- [76] T. Geyer and U. Winter. “An $O(N^2)$ approximation for hydrodynamic interactions in Brownian dynamics simulations.” In: *The Journal of chemical physics* 130 (2009), p. 114905. ISSN: 1089-7690. DOI: [10.1063/1.3089668](https://doi.org/10.1063/1.3089668). arXiv: [0801.3212](https://arxiv.org/abs/0801.3212) (cit. on p. [34](#)).
- [77] F. Martínez-Pedrero et al. “Formation of magnetic filaments: A kinetic study”. In: *Physical Review E - Statistical, Nonlinear, and Soft Matter Physics* 76 (2007). ISSN: 15393755. DOI: [10.1103/PhysRevE.76.011405](https://doi.org/10.1103/PhysRevE.76.011405) (cit. on pp. [35](#), [104](#)).
- [78] J. S. Andreu, J. Camacho, and J. Farauo. “Aggregation of superparamagnetic colloids in magnetic fields: the quest for the equilibrium state”. In: (Nov. 2010), pp. 2–5. DOI: [10.1039/C0SM01424A](https://doi.org/10.1039/C0SM01424A). arXiv: [1011.4819](https://arxiv.org/abs/1011.4819) (cit. on pp. [35](#), [36](#), [105](#)).
- [79] J. Jackson. *Classical Electrodynamics*. 3rd. Wiley & Sons, 1999 (cit. on p. [38](#)).
- [80] N. Derby and S. Olbert. “Cylindrical magnets and ideal solenoids”. In: *American Journal of Physics* (Sept. 2010), p. 12. arXiv: [0909.3880](https://arxiv.org/abs/0909.3880) (cit. on pp. [38](#), [40](#)).
- [81] J. T. Conway. “Exact solutions for the magnetic fields of axisymmetric solenoids and current distributions”. In: *IEEE Transactions on Magnetics*. Vol. 37. 2001, pp. 2977–2988. ISBN: 0018-9464. DOI: [10.1109/20.947050](https://doi.org/10.1109/20.947050) (cit. on p. [38](#)).
- [82] M. W. Garrett. “Axially symmetric systems for generating and measuring magnetic fields. Part I”. In: *Journal of Applied Physics* 22 (1951), pp. 1091–1107. ISSN: 00218979. DOI: [10.1063/1.1700115](https://doi.org/10.1063/1.1700115) (cit. on p. [38](#)).
- [83] R. C. O’Handley. *Modern Magnetic Materials: Principles and Applications*. 2000, p. 768. ISBN: 0471155667. DOI: [10.1109/MEI.2005.1490004](https://doi.org/10.1109/MEI.2005.1490004) (cit. on pp. [38](#), [39](#)).
- [84] E. C. Stoner and E. P. Wohlfarth. “A mechanism of magnetic hysteresis in heterogeneous alloys”. In: *IEEE Transactions on Magnetics* 27 (1991), pp. 3475–3518. ISSN: 00189464. DOI: [10.1109/TMAG.1991.1183750](https://doi.org/10.1109/TMAG.1991.1183750) (cit. on p. [39](#)).
- [85] Z. Nagy and B. J. Nelson. “Lagrangian Modeling of the Magnetization and the Magnetic Torque on Assembled Soft-Magnetic MEMS Devices for Fast Computation and Analysis”. In: *IEEE Transactions on Robotics* 28.4 (Aug. 2012), pp. 787–797. ISSN: 1552-3098. DOI: [10.1109/TR0.2012.2193230](https://doi.org/10.1109/TR0.2012.2193230) (cit. on p. [39](#)).
- [86] J. Osborn. “Demagnetizing factors of the General Ellipsoid”. In: *Physical Review* (1945) (cit. on p. [39](#)).
- [87] G. M. Wysin. *Demagnetization Fields*. 2012 (cit. on p. [44](#)).
- [88] H. A. Haus and J. R. Melcher. *Electromagnetic Fields and Energy*. 1989. ISBN: 9780132490207 (cit. on p. [45](#)).
- [89] D. V. Berkov, K. Ramstöck, and A. Hubert. “Solving Micromagnetic Problems. Towards an Optimal Numerical Method”. In: *physica status solidi (a)* 207 (1993) (cit. on p. [47](#)).

- [90] A. J. Newell, W. Williams, and D. J. Dunlop. “A generalization of the demagnetizing tensor for nonuniform magnetization”. In: *Journal of Geophysical Research* 98.B6 (1993), p. 9551. ISSN: 0148-0227. DOI: [10.1029/93JB00694](https://doi.org/10.1029/93JB00694) (cit. on p. 48).
- [91] F. Fiorillo. “Measurements of magnetic materials”. In: *Metrologia* 47 (2010), S114 (cit. on p. 66).
- [92] A. Krafčík, P. Babinec, and M. Babincová. “Feasibility of subcutaneously implanted magnetic microarrays for site specific drug and gene targeting”. In: 3.1 (2010), pp. 53–57 (cit. on p. 81).
- [93] S. Bucak et al. “Protein separations using colloidal magnetic nanoparticles”. In: *Biotechnology Progress* 19 (2003), pp. 477–484. ISSN: 87567938. DOI: [10.1021/bp0200853](https://doi.org/10.1021/bp0200853) (cit. on p. 96).
- [94] K. Hounkumnuard, B. Dolwithayakul, and C. Chantrapornchai. “Parallel Simulation of HGMS of Weakly Magnetic Nanoparticles in Irrotational Flow of Inviscid Fluid”. In: *The Scientific World Journal* 2014 (2014). DOI: [10.1155/2014/519654](https://doi.org/10.1155/2014/519654) (cit. on p. 96).
- [95] G. D. Moeser et al. “High-gradient magnetic separation of coated magnetic nanoparticles”. In: *AIChE Journal* 50 (2004), pp. 2835–2848. ISSN: 00011541. DOI: [10.1002/aic.10270](https://doi.org/10.1002/aic.10270) (cit. on pp. 96, 102).
- [96] J. S. Andreu et al. “Simple analytical model for the magnetophoretic separation of superparamagnetic dispersions in a uniform magnetic gradient”. In: *Physical Review E - Statistical, Nonlinear, and Soft Matter Physics* 84 (2011). ISSN: 15393755. DOI: [10.1103/PhysRevE.84.021402](https://doi.org/10.1103/PhysRevE.84.021402) (cit. on pp. 98, 108, 109).
- [97] D. Heinrich, A. R. Goñi, and C. Thomsen. “Dynamics of magnetic-field-induced clustering in ionic ferrofluids from Raman scattering”. In: *Journal of Chemical Physics* 126 (2007). ISSN: 00219606. DOI: [10.1063/1.2713112](https://doi.org/10.1063/1.2713112) (cit. on p. 104).
- [98] G. P. Gajula, M. T. Neves-Petersen, and S. B. Petersen. “Visualization and quantification of four steps in magnetic field induced two-dimensional ordering of superparamagnetic submicron particles”. In: *Applied Physics Letters* 97.2010 (2010), pp. 0–3. ISSN: 00036951. DOI: [10.1063/1.3475770](https://doi.org/10.1063/1.3475770) (cit. on p. 104).
- [99] G. De Las Cuevas, J. Faraudo, and J. Camacho. “Low-gradient magnetophoresis through field-induced reversible aggregation”. In: *Journal of Physical Chemistry C* 112 (2008), pp. 945–950. ISSN: 19327447. DOI: [10.1021/jp0755286](https://doi.org/10.1021/jp0755286) (cit. on pp. 108, 109).
- [100] F. M. White. *Fluid Mechanics*. 4th. Vol. 17. McGraw-Hill Book Company, 2009, p. 864. ISBN: 0071270388. DOI: [10.1111/j.1549-8719.2009.00016.x](https://doi.org/10.1111/j.1549-8719.2009.00016.x). *Mechanobiology* (cit. on pp. 117, 118).
- [101] H. Goldstein, C. P. J. Poole, and J. L. Safko. *Classical Mechanics*. 3rd. Addison-Wesley, p. 2001. ISBN: 978-0201657029 (cit. on p. 122).
- [102] M. Abramowitz and I. Stegun. *Handbook of Mathematical Functions with Formulas, Graphs, and Mathematical Tables*. Vol. 56. Dover Publications, 1964, p. 958. ISBN: 0486612724. DOI: [10.1119/1.15378](https://doi.org/10.1119/1.15378).
- [103] R. Rosenewig. *Ferrohydrodynamics*. Dover Publications, 1985.

Acknowledgements

This thesis has been carried out at the Physical and Colloid Chemistry (FCC) laboratory, Debye Institute of Nanomaterials, Utrecht University, since autumn 2013. A number of people deserve thanks for their support and help. It is therefore my greatest pleasure to express my gratitude to them all in this acknowledgement.

First of all I would like to thank my supervisor Roel Baars. He always provided me with guidance, precious suggestions, sharp observations and honest opinions from the start until the end of my study. Moreover, he boosted my proficiency with the world of computers, terminals and clusters and gave me invaluable tips on how to write, present and ultimately “do” science in the proper way. This is probably the most valuable result of my whole thesis project. I wish you the best for your PhD!

I would like to thank my promoter prof. Albert Philipse, for giving me the opportunity to conduct my research project in his group, and for the precious observations and suggestions during my work. Furthermore, I would like to express my gratitude for his agreement to be my referee in these last months, both for my internship and during my quest to discover what I want to do in my near future. I am really grateful that his door is always open for me.

Thanks to Bonny Kuipers for his invaluable insights, observations and discussions on the physics behind many of the things I have covered in this thesis. Also, I wish to thank him for the help with the VSM, as well as always being ready to help me with the same equipment when something weird (and unphysical) was coming out of it.

I wish to thank the FCC group for the nice atmosphere and the great working environment, as well as for the and for the illuminating and joyful discussions at the coffee table about science, social life and, ultimately, the meaning of existence. I am thankful to the professors, who have been always available for useful and enlightening discussions about different aspects of my work and physical chemistry in general. Moreover, I am thankful to the PhD’s students and postdocs, for the great help, tips and support I received from them in many occasions. Finally, thanks to the FCC master and bachelor students for the cool talks and the fun moments spent together. In particular, I am thankful to Alvaro and Frans, for sharing with me the “Bachelor’s room” and making it a special place to spend the time in, filled with joy and laughter.

Thanks to my friends Stefano and Alvaro, who started with me and faced altogether the challenge of being Master’s students in a foreign country. I could not find better people to live my adventure with. Thanks to my roommate Chiara, with who I shared so many things (and who shouldered the burden of correcting part of my thesis), and all my friends in Utrecht, for making my time in this lovely city one of the best of my life (in particular to Martina, who also endured the correction of parts of my thesis!). Also, thanks to Het Zinkstuk’s waterpolo and swimming team for the good vibrations in the pool and the exciting competitions, tournaments and moments together (Heren... Zwei!!!). Finally, thanks to my old but gold friends back in Rovereto, for always giving me a warm welcoming back in town (in particular to Andrea, who has been part of the correction’s team of my manuscript as well).

A general thanks goes to my relatives, for the support they gave me all along this time. A special thanks goes to my beloved grandparents Alberto, Erminia and Ernesto, who are unfortunately not here to share with me this happy moment but always gave me their love and support. Their memory will be with me in every moment.

Thanks to my brother Lorenzo, a person on which I know I can always count and who gave me a huge help on many things, as well as being a model that pushed me to always strive for more. Thanks for *everything* that helped me get to this day.

A very special thanks goes to *my* Manuela, who always stayed on my side in these long two years. She stood on my side after a difficult decision and a long distance between us, and continued to sail with me through the sun and through the storm. Moreover, she kept myself in one piece in all the bad and stressful moments, saying to me that *yes*, I could do it. *Thank you*, for love and support.

And, last but not least, thanks to my mum and my dad, to who I dedicate this thesis. They have been there all the time, supporting me in every possible way and showing infinite patience for all my bad moments. But, most of all, I cannot thank them enough for showing me what it means to be *strong* people. In these years of sacrifice, they have taught me that, if you really believe in yourself, you can do anything, no matter how much time you will need. I can only hope I will have at most half of their strength in my life. Thank you.

Utrecht, June 2015

A. C.